

Search for  $\eta'$ -nucleus bound states  
from  $^{12}\text{C}(\gamma, p)$  reaction  
with simultaneous detection of decay products



Natsuki Tomida

A dissertation submitted in partial fulfillment of the requirements  
for the degree of Doctor of Science

Department of Physics, Kyoto University

June, 2020



## Abstract

$\eta'(958)$  meson has large mass compared with  $\pi$ ,  $K$  and  $\eta$  mesons because of the axial vector anomaly term in the quantum chromodynamics (QCD) Lagrangian. It is called  $U_A(1)$  anomaly and the effect of the  $U_A(1)$  anomaly might be weakened in a dense matter. A large mass reduction of  $\eta'$  meson in nuclear medium is expected in several model calculations. If the  $\eta'$  mass is reduced in a nucleus, the  $\eta'$  meson and the nucleus can form a bound state. We searched for the  $\eta'$ -nucleus bound states via missing mass spectroscopy of the  $^{12}\text{C}(\gamma, p)$  reaction. The experiment was carried out in the LEPS2 beam line at SPring-8 using photon beam with the energy of 1.3–2.4 GeV. Produced particles were measured using the BGOegg detector system. Missing-mass spectroscopy around  $\eta'$ -mass suffers from numerous background arising from multiple light-meson productions. Thereby, we tagged an  $\eta$ -proton pair, which is expected to be emitted in the  $\eta'N \rightarrow \eta N$  absorption process of a bound  $\eta'$  in a nucleus. Namely, we investigated the  $\gamma + ^{12}\text{C} \rightarrow p + (\eta + p) + X$  reaction. This is the first missing mass spectroscopy around the  $\eta'$  production threshold in coincidence with decay products. Although multi pion backgrounds were suppressed by tagging an  $(\eta + p)$  pair, background events from the  $\gamma + ^{12}\text{C} \rightarrow p + \eta + ^{11}\text{B}$  and  $\gamma + ^{12}\text{C} \rightarrow p + (\eta + \pi^0) + ^{11}\text{B}$  reactions were still observed. We optimized kinematical selection criteria of the  $(\eta + p)$  pair to reduce those backgrounds and to enhance signals from the  $\eta'$ -nucleus bound states. After the kinematical selections, no events were observed in the kinematical region of bound states. The experimental upper limit of the production cross section of the  $\eta'$ -bound nuclei with an  $(\eta + p)$  emission in the  $\eta$ - $p$  opening angle of  $\cos \theta_{lab}^{\eta p} < -0.9$ , was obtained to be 2.2 nb/sr at the 90% confidence level. In addition to the  $\eta'$  absorption process, the missing mass spectrum of the  $\eta'$  escape reaction,  $\gamma + ^{12}\text{C} \rightarrow p + \eta' + X$ , was also measured for the first time. By measuring the missing mass spectrum of the  $\eta'$  escape process, we evaluated the production rate of  $\eta'$  mesons around the kinematical region of the  $\eta'$ -nucleus bound states. The obtained experimental upper limit of the  $(\eta + p)$  coincidence cross section was compared with the theoretical cross sections with different  $\eta'$ -nucleus potential parameters, as a function of the branching fraction of the  $\eta'N \rightarrow \eta N$  absorption process. The uncertainty of the absolute value of the theoretical cross section was suppressed with the measured cross section of the  $\eta'$  escape process. Our result indicates a small branching fraction of the  $\eta'N \rightarrow \eta N$  process and/or a shallow  $\eta'$ -nucleus potential.



# Contents

<b>1</b>	<b>Introduction</b>	<b>1</b>
1.1	The $\eta'$ (958) meson . . . . .	1
1.1.1	Light pseudoscalar mesons . . . . .	1
1.1.2	Mass of octet mesons . . . . .	3
1.1.3	Mass of an $\eta'$ meson . . . . .	5
1.2	The $\eta'$ -nucleus bound state . . . . .	5
1.2.1	$\eta'$ mass modification in a finite nucleus . . . . .	5
1.2.2	$\eta'$ -nucleus potential . . . . .	6
1.3	Theoretical predictions . . . . .	6
1.4	Past experiments . . . . .	8
1.5	Present experiment . . . . .	12
<b>2</b>	<b>Experimental setup</b>	<b>16</b>
2.1	SPring-8/LEPS2 facility . . . . .	16
2.1.1	LEPS2 beam line . . . . .	16
2.1.2	Laser system . . . . .	16
2.1.3	Backward Compton scattering . . . . .	19
2.1.4	Transmission rate . . . . .	20
2.2	Target . . . . .	21
2.3	Detector in LEPS2 . . . . .	22
2.3.1	Tagging counter . . . . .	23
2.3.2	UpVeto counter . . . . .	25
2.3.3	BGOegg calorimeter . . . . .	25
2.3.4	Inner Plastic Scintillator . . . . .	27
2.3.5	Drift Chamber . . . . .	27
2.3.6	Resistive Plate Chamber . . . . .	28
2.3.7	RF signal . . . . .	30
2.4	Electronics . . . . .	30
2.5	Trigger . . . . .	32
2.6	Data summary . . . . .	33

<b>3</b>	<b>Event reconstruction</b>	<b>34</b>
3.1	Photon beam energy measurement . . . . .	34
3.1.1	Tagger track reconstruction . . . . .	34
3.1.2	Photon energy determination . . . . .	35
3.2	Reaction timing reference . . . . .	36
3.3	Measurement of decay products . . . . .	37
3.3.1	BGOegg clustering . . . . .	37
3.3.2	Leak cluster . . . . .	39
3.3.3	Photon energy and polar angle resolution . . . . .	40
3.3.4	Proton kinetic energy and polar angle resolution . . . . .	41
3.4	Charge identification of decay products . . . . .	42
3.4.1	IPS energy deposit and hit timing correction . . . . .	42
3.4.2	Charge identification . . . . .	42
3.5	Forward going-particle detection . . . . .	43
3.6	Forward-going proton momentum measurement . . . . .	45
3.6.1	Hit strip selection . . . . .	45
3.6.2	Timing calibration . . . . .	46
3.6.3	Evaluation of forward proton momentum . . . . .	46
<b>4</b>	<b>Event selection</b>	<b>48</b>
4.1	Outline of the event selection . . . . .	48
4.2	Recoil electron track . . . . .	49
4.3	In-beam $e^+e^-$ veto . . . . .	50
4.4	Decay particle identification . . . . .	51
4.4.1	Identification of gammas . . . . .	51
4.4.2	Identification of $\eta$ and $\eta'$ mesons . . . . .	51
4.4.3	Identification of side-going protons . . . . .	53
4.5	Treatment of additional hit . . . . .	54
4.6	Forward-going particle selection . . . . .	54
4.6.1	Clean track selection . . . . .	54
4.6.2	$e^+e^-$ event suppression . . . . .	54
4.6.3	Energy conservation . . . . .	54
<b>5</b>	<b>The <math>\eta'</math>-nucleus search</b>	<b>58</b>
5.1	Obtained data . . . . .	58
5.2	Outline of the kinematical selection . . . . .	60
5.3	Background source and feature . . . . .	62
5.4	Expected signal kinematics . . . . .	64
5.4.1	Characteristics of signal . . . . .	64
5.4.2	QMD simulation . . . . .	64
5.4.3	Survival probability . . . . .	65
5.5	Cut optimization . . . . .	66
5.5.1	Opening angle cut . . . . .	68

5.5.2	Missing energy cut . . . . .	68
5.5.3	$\eta$ and $p_s$ polar angle cut . . . . .	69
5.6	Expected signal and background yields after the kinematical selection . . . . .	70
5.7	Experimental result . . . . .	71
<b>6</b>	<b>Luminosity, acceptance and efficiency for the cross section measurement</b>	<b>73</b>
6.1	The $(\eta + p_s)$ measurement . . . . .	73
6.1.1	Formulation . . . . .	73
6.1.2	The number of photons weighted with the RPC acceptance and the DAQ efficiency . . . . .	74
6.1.3	Number density of the target . . . . .	76
6.1.4	Acceptance . . . . .	76
6.1.5	Detector efficiencies . . . . .	77
6.1.6	Filling mode correction factor . . . . .	77
6.1.7	Pion contamination to the forward particle . . . . .	78
6.1.8	Branching fraction of $\eta \rightarrow 2\gamma$ mode . . . . .	79
6.1.9	Systematic error . . . . .	79
6.2	The $\eta'$ escape measurement . . . . .	79
6.2.1	Formulation . . . . .	79
6.2.2	The $\eta'$ acceptance . . . . .	80
6.2.3	The $\eta'$ angle region . . . . .	80
6.2.4	Systematic error . . . . .	82
<b>7</b>	<b>Experimental results and discussion</b>	<b>83</b>
7.1	Experimental results . . . . .	83
7.1.1	Upper limit of the production cross section of the $\eta'$ -nucleus bound state with $(\eta + p_s)$ emission . . . . .	83
7.1.2	Cross section of the $\eta'$ escape process . . . . .	83
7.2	Estimation of the $\eta'$ -nucleus potential $V_0$ . . . . .	85
7.2.1	Overview . . . . .	85
7.2.2	Formulation . . . . .	86
7.2.3	Calculation procedure . . . . .	86
7.2.4	Normalization factor of the theoretical cross section . . . . .	88
7.2.5	Cross section of the $(\eta + p_s)$ coincidence reaction . . . . .	90
7.2.6	Result . . . . .	91
7.3	Comparison with theoretical expectations and past experimental results . . . . .	91
<b>8</b>	<b>Summary and prospects</b>	<b>94</b>
<b>A</b>	<b>Filling pattern of the SPring-8 storage ring</b>	<b>98</b>
<b>B</b>	<b>Detector module</b>	<b>101</b>
<b>C</b>	<b>Photon beam energy calibration</b>	<b>103</b>

<b>D</b>	<b>Timing selection criteria</b>	<b>105</b>
D.1	Selection of gammas . . . . .	105
D.2	Selection of protons . . . . .	107
<b>E</b>	<b>QMD model calculation</b>	<b>109</b>
E.1	Basic description . . . . .	109
E.2	Signal simulation . . . . .	109
E.3	Detector acceptance and resolution . . . . .	110
<b>F</b>	<b>Detector acceptance and efficiency</b>	<b>111</b>
F.1	Systematic uncertainty of the acceptance . . . . .	111
F.1.1	Acceptance for $(\eta + p_s)$ . . . . .	111
F.1.2	Acceptance for $p_f$ . . . . .	112
F.2	Efficiency . . . . .	113
F.2.1	Tagger . . . . .	113
F.2.2	UpVeto over veto rate . . . . .	114
F.2.3	DC track reconstruction efficiency . . . . .	114
F.2.4	RPC reconstruction efficiency . . . . .	114
F.3	Transmission rate . . . . .	114
<b>G</b>	<b>Theoretical estimation of the cross section</b>	<b>116</b>
G.1	Overview . . . . .	116
G.2	Nuclear response function $R(E_{\text{ex}})$ . . . . .	117
G.3	Fermi averaging method . . . . .	117
G.3.1	Formalism . . . . .	118
G.3.2	Nucleon momentum distribution . . . . .	120
G.3.3	Elementary cross section in the CM system . . . . .	120
G.3.4	Elementary cross section in the laboratory system . . . . .	121
G.3.5	Numerical result . . . . .	122
G.4	Inclusion of the detector resolution . . . . .	122
G.4.1	The detector resolutions . . . . .	122
G.4.2	The treatment above $E_{\text{ex}} - E_0 = 50$ MeV . . . . .	123
G.4.3	Excitation energy spectra . . . . .	124
G.5	$E_\gamma$ dependence . . . . .	127
G.6	Expected cross section . . . . .	127
G.7	$p_f$ polar angle dependence . . . . .	128
<b>H</b>	<b>The measurement of the <math>\eta'</math> escape process</b>	<b>130</b>
H.1	Definition of the excitation energy . . . . .	130
H.2	$E_\gamma$ dependence of the cross section . . . . .	131
H.3	Comparison with the measurement by CBELSA/TAPS . . . . .	131
	<b>Bibliography</b>	<b>134</b>

# Chapter 1

## Introduction

$\eta'(958)$  meson could be an interesting probe to investigate the origin of hadron masses in a finite density because a large mass reduction of  $\eta'(958)$  meson is expected at the normal nuclear density. If there is a large mass reduction in such environment, the  $\eta'$  meson and a nucleus form a bound state. We looked for the  $\eta'$ -nucleus bound state from the missing mass spectrum of the  $^{12}\text{C}(\gamma, p)$  reaction around the  $\eta'$  production threshold. In this section, we describe the details of the origin of pseudoscalar meson mass spectra, the theoretical models expecting  $\eta'$  mass shift in a finite density, past experiments to examine  $\eta'$ -nucleus potential, and the aim of the present experiment.

### 1.1 The $\eta'(958)$ meson

#### 1.1.1 Light pseudoscalar mesons

$\eta'(958)$  meson is meson with the mass of  $957.78 \text{ MeV}/c^2$ , composed of  $u$ ,  $d$ ,  $s$  quarks and their antiquarks. Its spin-parity is  $J^P = 0^-$ . Mesons having  $J^P = 0^-$  are called pseudoscalar mesons. In the constituent quark model, the light three quarks and their antiquarks generate octet and singlet pseudoscalar mesons as shown in Fig.1.1. In Fig.1.1, the constituent quarks of each meson are also shown. The horizontal and vertical axes of Fig.1.1 are the third component of isospin,  $I_3$ , and hypercharge,  $Y$ , respectively.  $u$  and  $\bar{d}$  quarks have  $I_3 = +1/2$ , and  $d$  and  $\bar{u}$  quarks have  $I_3 = -1/2$ .  $s$  quark has  $Y = -1$  and  $\bar{s}$  quark has  $Y = +1$ . The  $\pi^0$  meson is composed of  $u\bar{u}$  and  $d\bar{d}$  as

$$|\pi^0\rangle = \frac{1}{\sqrt{2}}(|u\bar{u}\rangle - |d\bar{d}\rangle), \quad (1.1)$$

The  $\eta$  and  $\eta'$  mesons are mixed states of the octet  $\eta_8$  and singlet  $\eta_0$  mesons, which are described as follows:

$$|\eta\rangle = \cos\theta |\eta_8\rangle - \sin\theta |\eta_0\rangle, \quad (1.2)$$

$$|\eta'\rangle = \sin\theta |\eta_8\rangle + \cos\theta |\eta_0\rangle, \quad (1.3)$$

$$|\eta_8\rangle = \frac{1}{\sqrt{6}}(|u\bar{u}\rangle + |d\bar{d}\rangle - 2|s\bar{s}\rangle), \quad (1.4)$$

$$|\eta_0\rangle = \frac{1}{\sqrt{3}}(|u\bar{u}\rangle + |d\bar{d}\rangle + |s\bar{s}\rangle), \quad (1.5)$$

where  $\theta = -11.5^\circ$  is the mixing angle of  $\eta_8$  and  $\eta_0$  [1]. Because  $\theta$  is small, we can assume that  $|\eta\rangle \approx |\eta_8\rangle$  and  $|\eta'\rangle \approx |\eta_0\rangle$ . The mass of  $\eta$  meson is  $547.85 \text{ MeV}/c^2$ . The main decay modes of  $\eta'$  and  $\eta$  mesons are shown in Table.1.1 and 1.2. The  $\eta' \rightarrow \gamma\gamma$  and  $\eta \rightarrow \gamma\gamma$  decay processes were measured in the present experiment.

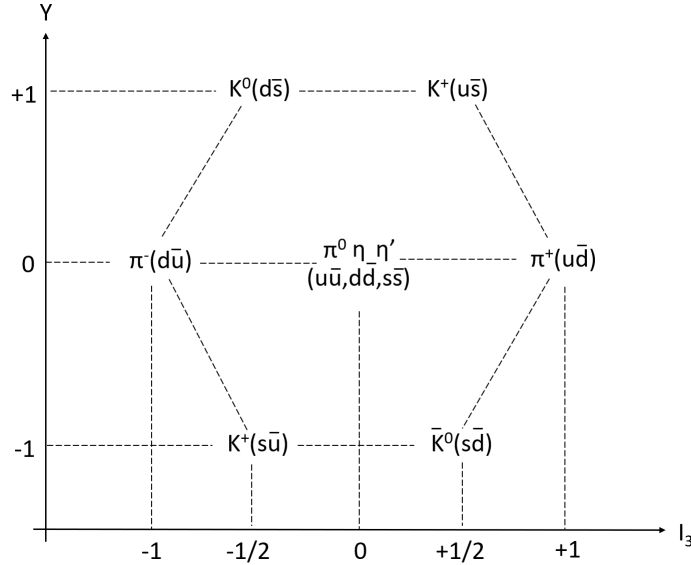


Figure 1.1: The pseudoscalar mesons composed of  $u$ ,  $d$ ,  $s$  quarks and their antiquarks.

Table 1.1: Main decay modes of  $\eta'$  meson [1]. Table 1.2: Main decay modes of  $\eta$  meson [1].

mode	branching fraction	meson	branching fraction
$\pi^+\pi^-\eta$	$(42.6 \pm 0.7)\%$	$\gamma\gamma$	$(39.41 \pm 0.20)\%$
$\rho^0\gamma(\pi^+\pi^-\gamma)$	$(28.9 \pm 0.5)\%$	$3\pi^0$	$(32.68 \pm 0.23)\%$
$\pi^0\pi^0\eta$	$(22.8 \pm 0.8)\%$	$\pi^+\pi^-\pi^0$	$(22.92 \pm 0.28)\%$
$\gamma\gamma$	$(2.22 \pm 0.08)\%$	$\pi^+\pi^-\gamma$	$(4.22 \pm 0.08)\%$

### 1.1.2 Mass of octet mesons

In Table.1.3 and 1.4, we summarize the masses of pseudoscalar and vector ( $J^P = 1^-$ ) mesons composed of  $u$ ,  $d$  and  $s$  quarks and their anti-quarks. As can be seen, the mass differences of octet pseudoscalar mesons are large compared with vector mesons. The light masses of octet mesons are considered to be attributed to the spontaneous breaking of chiral symmetry in the quantum chromodynamics (QCD). The chirality operator  $\gamma^5$  is defined as

$$\gamma^5 \equiv i\gamma^0\gamma^1\gamma^2\gamma^3 \quad (1.6)$$

where  $\gamma^0$ ,  $\gamma^1$ ,  $\gamma^2$  and  $\gamma^3$  are gamma matrices. The eigenstates of chirality of quarks are  $q_L$  and  $q_R$ , which satisfies

$$\gamma^5 q_L(x) = -q_L(x), \quad (1.7)$$

$$\gamma^5 q_R(x) = q_R(x), \quad (1.8)$$

$$q(x) = q_L(x) + q_R(x). \quad (1.9)$$

By using  $q_L(x)$  and  $q_R(x)$ , the QCD Lagrangian for 3 flavors ( $u$ ,  $d$ ,  $s$ ) is described as

$$\begin{aligned} L = & \bar{q}_L(x)i\gamma^\mu D_\mu q_L(x) + \bar{q}_R(x)i\gamma^\mu D_\mu q_R(x) \\ & - \bar{q}_L(x)Mq_R(x) - \bar{q}_R(x)Mq_L(x) - \frac{1}{2}\text{Tr}[G_{\mu\nu}(x)G^{\mu\nu}(x)], \end{aligned} \quad (1.10)$$

$$q_L(x) = \begin{pmatrix} u_L(x) \\ d_L(x) \\ s_L(x) \end{pmatrix}, \quad (1.11)$$

$$q_R(x) = \begin{pmatrix} u_R(x) \\ d_R(x) \\ s_R(x) \end{pmatrix}, \quad (1.12)$$

$$M = \text{diag}(m_u, m_d, m_s). \quad (1.13)$$

Table 1.3: Mass of pseudoscalar mesons [1].

meson	mass [MeV/c <sup>2</sup> ]
$\pi^0$	134.97
$\pi^\pm$	139.57
$K^\pm$	493.68
$K^0, \bar{K}^0$	497.61
$\eta$	547.86
$\eta'$	957.78

Table 1.4: Mass of vector mesons [1].

meson	mass [MeV/c <sup>2</sup> ]
$\rho$	775.3
$K^{*\pm}$	891.7
$K^{*0}, \bar{K}^{*0}$	895.6
$\omega$	782.7
$\phi$	1019.5

The first and second terms in Eq.(1.10) are kinetic terms, and third and fourth terms are mass terms. When  $M \rightarrow 0$ , the Lagrangian is invariant under a  $SU(3)_L \times SU(3)_R$  transformation:

$$q_L \rightarrow U_L q_L, \quad U_L = \exp(i\theta_L^a \frac{\lambda^a}{2}), \quad U_L \in SU(3)_L, \quad (1.14)$$

$$q_R \rightarrow U_R q_R, \quad U_R = \exp(i\theta_R^a \frac{\lambda^a}{2}), \quad U_R \in SU(3)_R. \quad (1.15)$$

where  $\lambda^a$ 's are Gell-Mann matrices. This transformation is called chiral transformation, and thus the QCD Lagrangian has chiral symmetry in the limit of  $M \rightarrow 0$ .

Although the QCD Lagrangian has the chiral symmetry in the massless limit, the ground state of the QCD breaks the chiral symmetry. This is called the breaking of the chiral symmetry. We can see it in the following equations. The Noether currents for the chiral symmetry are described as follows:

$$J_L^{a\mu} = \bar{q}_L(x) \gamma^\mu \frac{\lambda^a}{2} q_L(x), \quad (1.16)$$

$$J_R^{a\mu} = \bar{q}_R(x) \gamma^\mu \frac{\lambda^a}{2} q_R(x), \quad (1.17)$$

The vector and axial vector currents,  $V^{a\mu}$  and  $A^{a\mu}$ , are described as follows:

$$V^{a\mu} = J_R^{a\mu} + J_L^{a\mu} = \bar{q}(x) \gamma^\mu \frac{\lambda^a}{2} q(x), \quad (1.18)$$

$$A^{a\mu} = J_R^{a\mu} - J_L^{a\mu} = \bar{q}(x) \gamma^\mu \gamma^5 \frac{\lambda^a}{2} q(x). \quad (1.19)$$

Then, the vector and axial vector conserved charges,  $Q_V^a$  and  $Q_A^a$ , are expressed as:

$$Q_V^a = \int d^3x V^{a0} = \int d^3x \bar{q}(x) \gamma^0 \frac{\lambda^a}{2} q(x), \quad (1.20)$$

$$Q_A^a = \int d^3x A^{a0} = \int d^3x \bar{q}(x) \gamma^0 \gamma^5 \frac{\lambda^a}{2} q(x). \quad (1.21)$$

Next, we consider an equal time commutation relation of the axial vector conserved charge  $Q_A^a$  and a pseudoscalar operator  $\phi^b$ ;

$$\phi^b \equiv \bar{q}(x) \gamma^5 \frac{\lambda^b}{2} q(x), \quad (1.22)$$

$$[Q_A^a, \phi^b] = \delta^{ab} \bar{q}(x) q(x). \quad (1.23)$$

The expectation value for a vacuum is

$$\langle 0|[Q_A^a, \phi^b]|0 \rangle = \delta^{ab} \langle \bar{q}(x) q(x) \rangle. \quad (1.24)$$

$\langle \bar{q}(x) q(x) \rangle$  is called quark condensate and  $\langle \bar{q}(x) q(x) \rangle \neq 0$  in a QCD vacuum. This means that the vacuum has non zero axial vector current  $Q_A^a$ , and the chiral symmetry is spontaneously broken in the QCD vacuum.

From the Nambu-Goldstone theorem, there are massless particles when a symmetry is spontaneously broken [2]. The massless particles are called Nambu-Goldstone (NG) bosons. The octet mesons are NG bosons associated with the spontaneous breaking of the chiral symmetry. Because quarks have finite masses, the chiral symmetry is an approximate symmetry in the QCD. Thereby, the octet mesons are not massless but their masses are small. Kaons are heavier than pions because an  $s$  quark mass is larger than  $u, d$  quarks.

### 1.1.3 Mass of an $\eta'$ meson

The  $\eta'$  meson could be the ninth NG boson but it is not. As can be seen in Table.1.3, the  $\eta'$  mass is extremely large compared with other pseudoscalar mesons. It is explained with the anomaly of the axial vector current, namely  $U_A(1)$  anomaly. It appears in the divergence of the singlet axial vector current,  $A_\mu^0(x)$ , as

$$A_\mu^0(x) = \sum_f \bar{q}_f(x) \gamma^\mu \gamma^5 q_f(x), \quad (1.25)$$

$$\partial^\mu A_\mu^0 = 2i \sum_f m_f \bar{q}_f \gamma^5 q_f - \frac{N_f g^2}{16\pi^2} G_{\mu\nu}^a \tilde{G}^{a\mu\nu}, \quad (1.26)$$

where  $f$  is flavor of quarks and  $G_{\mu\nu}^a \tilde{G}^{a\mu\nu}$  is a color sum of gluon. The last term does not vanish even quark masses are 0 and thus the axial vector current does not conserve. Because of this  $U_A(1)$  anomaly, the singlet  $\eta^0$  and thus  $\eta'$  has large masses.

## 1.2 The $\eta'$ -nucleus bound state

### 1.2.1 $\eta'$ mass modification in a finite nucleus

As described in section 1.1.2, the chiral symmetry breaking is associated with finite quark condensate  $\langle \bar{q}q \rangle$  in vacuum. The quark condensate is considered to decrease in finite baryon density [3]. Therefore, partial restoration of the chiral symmetry breaking is expected in a nucleus, where density is high. As described in Refs.[4, 5], the effect of the  $U_A(1)$  anomaly to the  $\eta_0$  mass appears under existence of the chiral symmetry breaking. Thus, the  $U_A(1)$  anomaly effect might be weakened together with the partial restoration of the chiral symmetry. If it is weakened, the  $\eta'$  mass can decrease in a nucleus. As described in section 1.3, a large mass reduction of 80–150 MeV at a normal nuclear density is expected by model calculations. Thereby, the  $\eta'$  meson is a good probe to examine hadron masses at high density. The decay width of the  $\eta'$  meson can also change in a nucleus due to the absorption of an  $\eta'$  meson by nucleons. Although there is no theoretical expectation of the change of the width in a nucleus, a small absorption width of 7–19 MeV is derived from the experimental measurement by the CBELSA/TAPS collaboration (see section 1.4).

## 1.2.2 $\eta'$ -nucleus potential

According to Refs.[6, 7], the mass reduction of an  $\eta'$  meson in a nucleus can be translated as an attractive potential between the  $\eta'$  meson and the nucleus. The optical potential of the  $\eta'$ -nucleus system can be described as [6, 7]

$$U(r) = (V_0 + iW_0) \times \frac{\rho(r)}{\rho_0}, \quad (1.27)$$

$$V_0 = \Delta m(\rho_0), \quad (1.28)$$

$$W_0 = -\frac{\Gamma(\rho_0)}{2}, \quad (1.29)$$

where  $\rho(r)$  is the nuclear density distribution,  $\rho_0$  is the normal nuclear density, and  $\Delta m(\rho_0)$  and  $\Gamma(\rho_0)$  are the mass shift and width of the  $\eta'$  meson at  $\rho = \rho_0$ , respectively. The real part of the potential  $V_0$  corresponds to the mass shift in the nucleus.  $\Delta m(\rho_0)$  is defined as  $\Delta m(\rho_0) = m(\rho_0) - m_0$ , where  $m_0$  is the mass in a vacuum. When  $\Delta m(\rho_0)$  is negative, the potential is attractive, and when it is positive, the potential is repulsive. If  $V_0$  is deep enough to have a binding energy, the  $\eta'$  meson and the nucleus form a bound state [8]. The imaginary part of the potential  $W_0$  corresponds to an absorption width of  $\eta'$  meson in the nucleus. If  $W_0$  is too large,  $\eta'$  mesons are immediately absorbed by nucleons and an  $\eta'$ -nucleus bound state cannot be formed. Thereby,  $W_0$  needs to be small to form a bound state. As described in section 1.4, the CBELSA/TAPS collaboration derived  $W_0 = -(13 \pm 3(\text{stat}) \pm 3(\text{syst}))$  MeV [9]. It is small enough to have bound states when there is a large mass shift of  $V_0 = \Delta m(\rho_0) = -80 \sim -150$  MeV. In the present experiment, we examine the real part of the  $\eta'$ -nucleus potential  $V_0$ .

## 1.3 Theoretical predictions

The amount of mass shift in a nucleus, or the depth of the  $\eta'$ -nucleus potential is estimated using different models. The expectation of each model is shown in this section.

### NJL model

In the Nambu-Jona-Lasinio (NJL) model [10, 11], the  $U_A(1)$  anomaly is taken into account through the Kobayashi-Maskawa-'t Hooft interaction [12, 13]. Costa *et al.* and Nagahiro *et al.* examined the mass of an  $\eta'$  meson in a finite density using the NJL model [7, 14]. The strength of the  $U_A(1)$  anomaly term in a vacuum is described using a parameter,  $g_D$ .  $g_D$  was adjusted to reproduce the observed  $\pi, K, \eta'$  masses and  $\pi$  decay constant [15]. They calculated the  $\pi, \eta$  and  $\eta'$  masses as a function of density  $\rho$ , considering several cases of the density dependence of  $g_D$ : (a)  $g_D(\rho) = g_D$ , (b)  $g_D(\rho) = 0$ , and (c)  $g_D(\rho) = g_D \exp(-(\rho/\rho_0)^2)$ . Their calculation results are shown in Fig.1.2. They suggested the mass reduction of  $\eta'$  meson  $\Delta m(\rho_0) = -150$  MeV at  $\rho = \rho_0$  in the case (a). The case (b) corresponds to the calculation without the  $U_A(1)$  anomaly effect, and the masses of  $\eta$  and  $\eta'$  at  $\rho = 0$  are not reproduced. In the case (c), a larger mass reduction  $\Delta m(\rho_0) = -300$  MeV for  $\eta'$  and  $\eta$  mesons at  $\rho = \rho_0$

is expected. The  $\eta$ -nucleus bound states were searched for with  $^{12}\text{C}$  and  $^{27}\text{Al}$  targets by the JINR and COSY-GEM collaborations, respectively, and there are only indications of shallow bound states [16, 17]. Thereby the density dependence of the case (c) is nonpreferred.

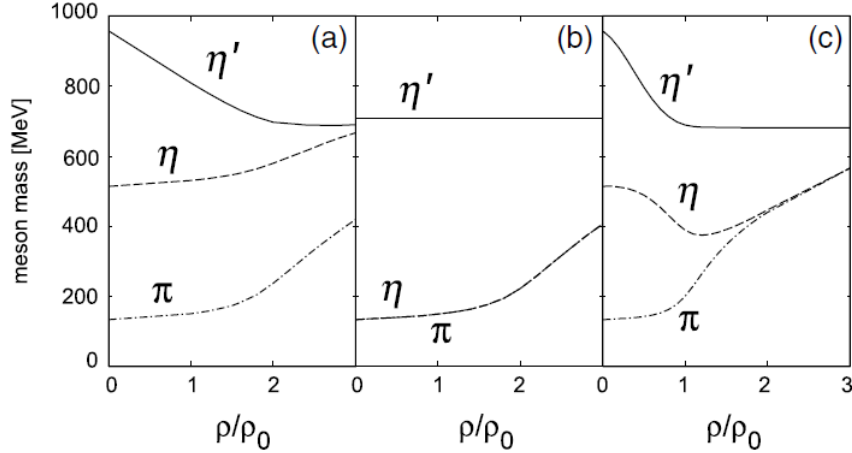


Figure 1.2: The expected mass shift of  $\pi$ ,  $\eta$  and  $\eta'$  using the NJL model [7]. See the text for the difference of (a)–(c).

### Linear sigma model

Sakai and Jido evaluated  $\Delta m(\rho)$  by using the linear sigma model [18]. The fundamental degree of freedom in the linear sigma model is a hadron, and therefore the model can include nucleon fields straightforwardly. The Lagrangian of the model contains a term represents the  $U_A(1)$  anomaly, which corresponds to the Kobayashi-Maskawa-'t Hooft term. The strength parameter of this term ( $B$ ) is determined from decay constants and masses of  $\pi$ ,  $K$ , and masses of  $u$ ,  $d$  quarks. The spontaneous breaking of the chiral symmetry is described with  $\sigma$  condensate as an order parameter. Their calculation result is shown in Fig.1.3. They extracted  $\Delta m(\rho_0 = 0.17 \text{ fm}^{-3}) = -80 \text{ MeV}$  for the  $\eta'$  meson without considering density dependence of the parameter  $B$ . Larger mass reduction is possible if there is density dependence of the  $B$  parameter.

### QMC model

Bass and Thomas calculated  $\eta'$  mass at  $\rho = \rho_0$  by using the Quark-Meson Coupling (QMC) model [19]. They evaluated the  $\eta'$  mass in nuclear matter by solving for an MIT Bag Dirac equations in nuclear medium. Mass reduction  $\Delta m(\rho_0) = -37 \text{ MeV}$  is expected by their model calculation. The  $U_A(1)$  anomaly is not taken into account in the QMC model.

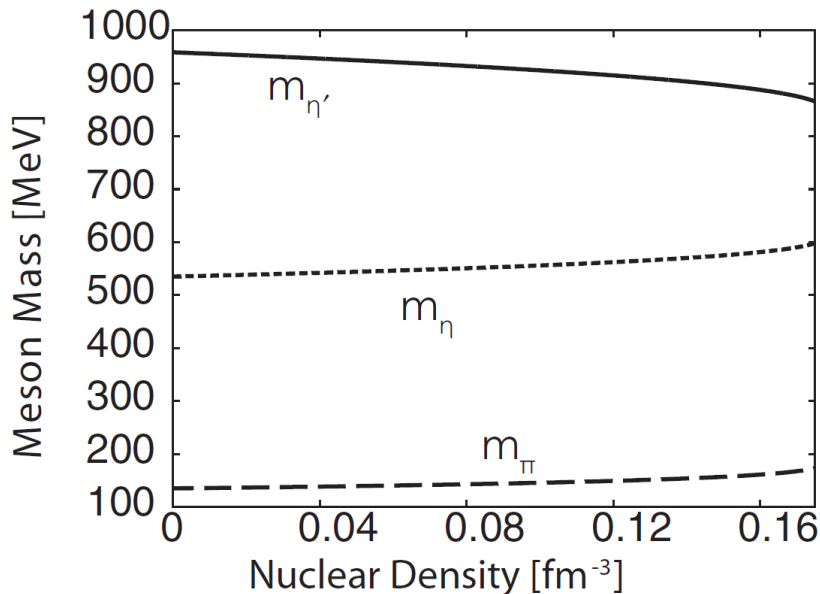


Figure 1.3: The expected mass shift of  $\pi$ ,  $\eta$  and  $\eta'$  using the linear sigma model [18].

### Chiral unitary approach

Nagahiro *et. al.* evaluated the  $\eta'$ -nucleus potential,  $(V_0, W_0)$ , within a chiral unitary approach [8]. They estimated  $(V_0, W_0)$  for several  $\eta'N$  scattering length values. However, later they pointed out in Ref.[20] that there was problems of one of parameters, which is called “subtraction constant”, used for the calculation in Ref.[8]. Different subtraction constants should be used for  $\eta$  and  $\eta'$  mesons but they used the same values in Ref.[8]. In addition, they also pointed out there was a problem of a calculation method of the potential in Ref.[8]. Thus, the expectation in Ref.[8] is not reliable and an updated result is desired.

## 1.4 Past experiments

Experimental information of the  $\eta'$ -nucleus potential is poor. As of now, only the  $\eta$ -PRiME/Super-FRS Collaboration and the CBELSA/TAPS collaboration gave experimental results on the  $\eta'$ -nucleus potential. Their results are summarized in this section. Indirect measurement of the mass modification of  $\eta'$  mesons in heavy ion collision is also reviewed.

### The $\eta$ -PRiME/Super-FRS Collaboration

A straight-forward method of accessing  $(V_0, W_0)$  is missing-mass spectroscopy around the  $\eta'$ -nucleus system. The peak position and width of the  $\eta'$ -nucleus bound state are directly correlated with  $V_0$  and  $W_0$ , respectively. However, the missing-mass spectroscopy around  $\eta'$  bound states suffers from numerous backgrounds arising from multiple production of mesons

having smaller mass than an  $\eta'$  meson. The  $\eta$ -PRiME/Super-FRS Collaboration firstly measured the missing mass spectrum near the  $\eta'$ -meson production threshold in  $p+^{12}\text{C} \rightarrow d+X$  reactions [21, 22]. They used a very high energy resolution spectrometer of  $\sigma = 2.5 \pm 0.1$  MeV, and aimed to measure narrow peaks of bound states above background. The measured excitation energy spectrum of the  $\eta'+^{11}\text{C}$  system  $E_{\text{ex}}$ , relative to the production threshold  $E_0$

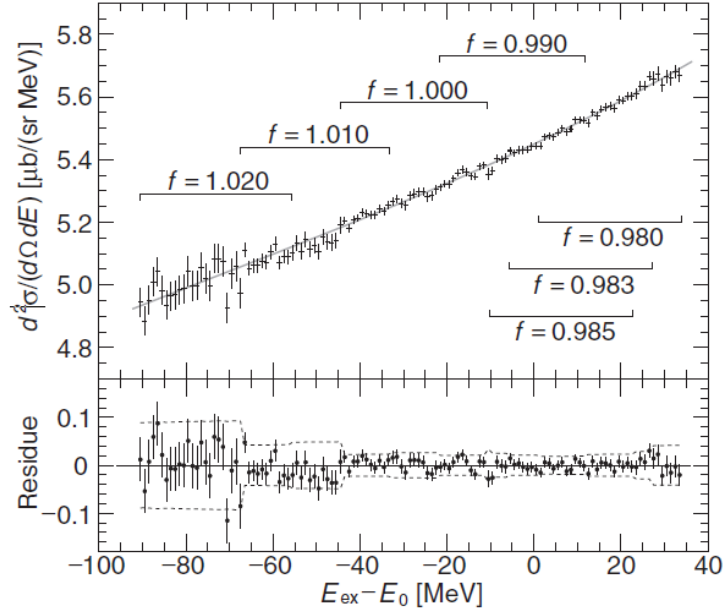


Figure 1.4: The measured excitation energy spectrum  $E_{\text{ex}} - E_0$ . The figure is from Ref.[21].

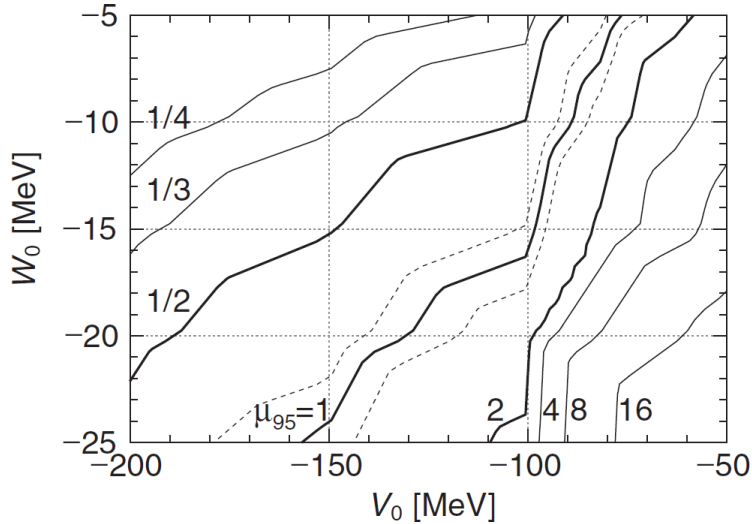


Figure 1.5: The obtained upper limit of  $(V_0, W_0)$  by the  $\eta$ -PRiME/Super-FRS Collaboration [21]. The numbers indicate the normalization factor of the theoretical cross section.

is shown in Fig.1.4. It is an inclusive spectrum and production of  $\eta'$  meson is not tagged. Although the cross sections of background events were as expected, no signals indicating a bound state were observed above backgrounds. An upper limit of  $(V_0, W_0)$  was obtained depending on the normalization factor of the theoretical cross section calculated in the framework of a distorted wave impulse approximation (DWIA) as shown in Fig.1.5 [23, 24]. The lines in Fig.1.5 show the upper limit of  $(V_0, W_0)$  with different normalization factors. Although DWIA calculations nicely describe the spectral shape of bound states such as hyper nuclei and pionic atoms, there is uncertainty in the absolute value of the cross sections and thus normalization factors are needed [25–30]. Furthermore, their theoretical cross section has an uncertainty of a factor of 2 coming from the unknown elementary cross section of the  $pn \rightarrow \eta'd$  reaction. There is no experimental measurement of the  $pn \rightarrow \eta'd$  reaction, and they used estimated value for the input of the DWIA calculation. Thus, large ambiguity coming from the normalization of the theoretical calculation exists in the upper limit of  $(V_0, W_0)$  obtained by the  $\eta$ -PRiME/Super-FRS Collaboration.

### The CBELSA/TAPS Collaboration

The CBELSA/TAPS Collaboration evaluated both  $V_0$  and  $W_0$ . For the evaluation of  $V_0$ , they precisely measured  $\eta'$  mesons escaping from nuclei in the photoproduction process and compared the kinematical distributions with those in a collision model [31] in different  $V_0$  cases. In Ref.[32], they compared the beam energy dependence and the  $\eta'$  momentum dependence of the cross section of the  $\gamma + {}^{12}\text{C} \rightarrow \eta' + \text{X}$  reaction as shown in Fig.1.6. From the comparison, they deduced  $V_0 = -(37 \pm 10(\text{stat}) \pm 10(\text{syst}))$  MeV. In Ref.[33], they performed the same analysis as in Ref.[32] for the  $\gamma + {}^{93}\text{Nb} \rightarrow \eta' + \text{X}$  reaction, and deduced  $V_0 = -(41 \pm 10(\text{stat}) \pm 15(\text{syst}))$  MeV. The weighted average of  $V_0$  measured in Ref.[32] and [33] is  $V_0 = -(39 \pm 7(\text{stat}) \pm 15(\text{syst}))$  MeV. In Ref.[34], they measured  $\gamma + {}^{12}\text{C} \rightarrow \eta' + p + \text{X}$  reaction. By measuring protons in the forward angle, they selected events with low  $\eta'$  kinetic energy of  $\sim 150$  MeV. They can identify protons but they can not measure the momentum of protons, and thus they can not study the missing mass of the  ${}^{12}\text{C}(\gamma, p)$  reaction. From the comparison of the beam energy dependence and the  $\eta'$  kinetic energy dependence of the cross sections with those in the collision model, they deduced  $V_0 = -(44 \pm 16(\text{stat}) \pm 15(\text{syst}))$  MeV. It is consistent with the measurements in Ref.[32] and [33] for the larger average  $\eta'$  momentum of  $\sim 1.1$  GeV/c. The consistency of  $V_0$  evaluated in different measurements is a strong point of their results. However, the collision model has not been calibrated for established bound states, such as hypernuclei and pionic atoms. Therefore, there could be some systematic errors. In addition, there are some questionable points in their cross section measurement as indicated in Appendix H.3.

They estimated  $W_0$  from the measurement of the  $\gamma + A \rightarrow \eta' + A'$  reaction with  ${}^{12}\text{C}$  and  ${}^{93}\text{Nb}$  targets [9]. They derived  $W_0 = -(13 \pm 3(\text{stat}) \pm 3(\text{syst}))$  MeV from the mass number ( $A$ ) dependence of the production cross sections. The  $A$  dependence of the cross section is called “transparency ratio”. Large (small) transparency ratio indicates small (large) absorption rate of the produced hadron in nuclei. The transparency measurement is widely used for evaluating  $W_0$  [35–38]. Thereby, their obtained  $W_0$  is much reliable compared with  $V_0$ .

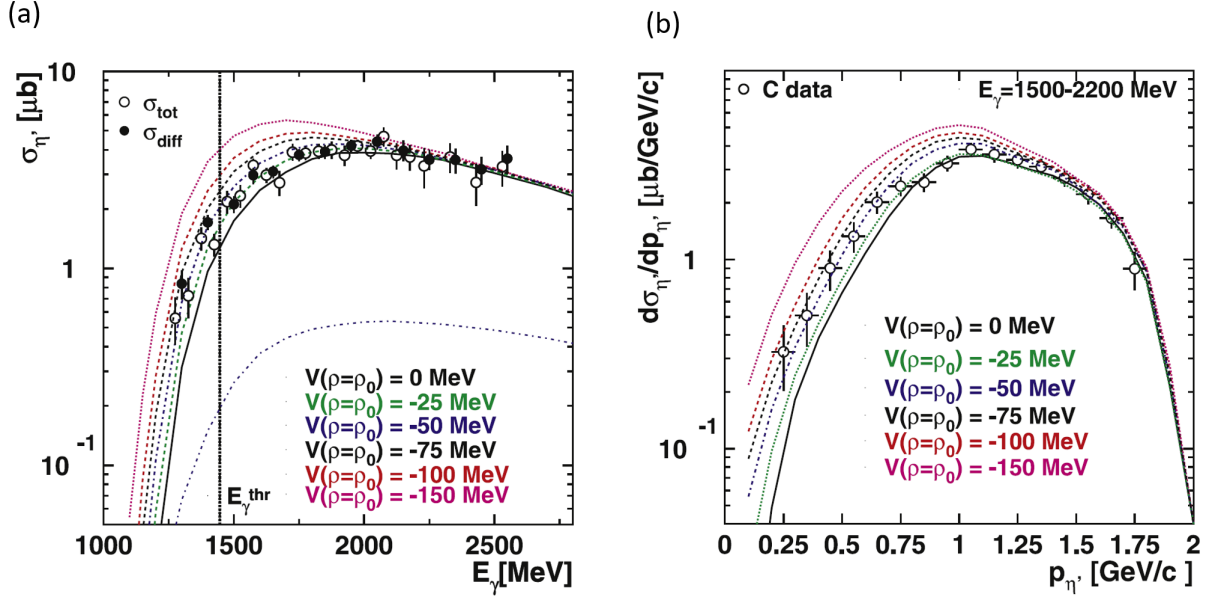


Figure 1.6: (a) The beam energy dependence of the total cross sections and (b) the  $\eta'$  momentum distributions of the  $\gamma + {}^{12}\text{C} \rightarrow \eta' + X$  reaction measured by the CBELSA/TAPS Collaboration [32]. The circles show the experimental values and lines show the calculation results with the collision model.

## Heavy ion collision

The weakening of the  $U_A(1)$  anomaly effect is also expected in a hot matter [39]. T. Csörgő *et al.* claimed that the  $\eta'$  mass is reduced at least 200 GeV/ $c^2$  in  $\sqrt{s_{NN}} = 200$  GeV Au+Au collisions from the analysis of charged pion Bose-Einstein correlation data taken by the PHENIX and STAR Collaborations [40–42]. In thermal models, the production cross section of light mesons are exponentially suppressed by the mass. Thus, if the  $\eta'$  mass is reduced in medium, the  $\eta'$  yield can be increased.  $\eta'$  mesons can decay via  $\eta' \rightarrow \eta + \pi^+\pi^- \rightarrow (\pi^0\pi^+\pi^-) + \pi^+\pi^-$ . The transverse mass ( $m_T$ ) of charged pions from this decay process is small. Since  $\eta'$  mesons mostly decay in halo region of the collision, we may see enhancement (reduction) of charged pion yield at low transverse mass in the halo (core) region when the  $\eta'$  yield increases. T. Csörgő *et al.* examined the transverse mass dependence of the effective intercept parameter of the two-pion Bose-Einstein correlation function,  $\lambda^*$ .  $\lambda^*$  is given by the ratio of the number of events in the core and (core+halo) regions as  $\lambda^* = [N_{\text{core}}^{\pi}/(N_{\text{core}}^{\pi} + N_{\text{halo}}^{\pi})]^2$ . The measured intercept parameter  $\lambda^*(m_T)$  relative to  $\lambda_{\text{max}}^* = \lambda^*(m_T = 0.7 \text{ GeV}/c^2)$  is shown in Fig.1.7. They compared it with theoretical calculations with difference  $\eta'$  mass cases and claimed that the  $\eta'$  mass is reduced at least 200 GeV/ $c^2$ , at the 90% confidence level.

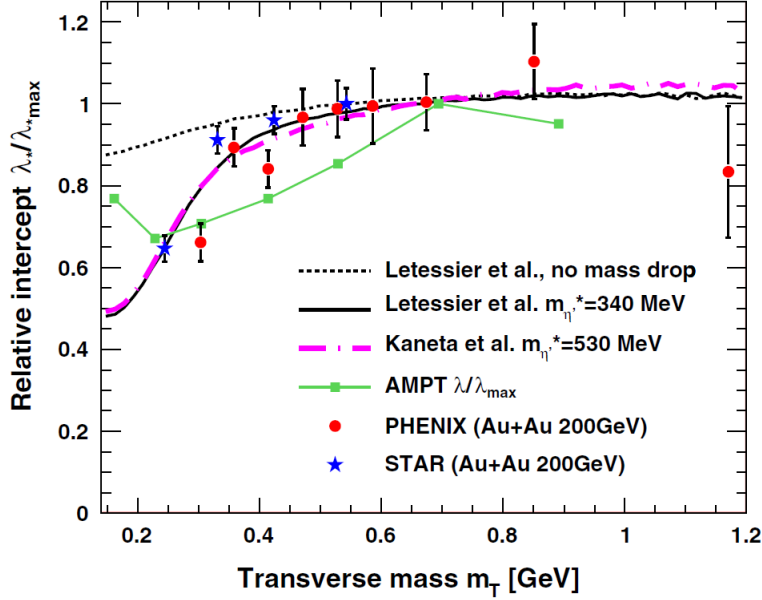


Figure 1.7: The transverse mass dependence of the ratio of  $\lambda^*/\lambda_{\max}^*$  measured by the PHENIX and STAR Collaborations and theoretical calculations with difference  $\eta'$  mass cases in medium.

## 1.5 Present experiment

To search for  $\eta'$ -nucleus bound states and evaluate the  $\eta'$ -nucleus potential, we carried out missing mass spectroscopy of the  $^{12}\text{C}(\gamma, p)$  reaction at the LEPS2 beam line of SPring-8. By using photon beam of 1.3–2.4 GeV and detecting protons in extremely forward angles of  $0.9^\circ - 6.8^\circ$  in the laboratory frame, we investigated the missing mass spectrum in a small momentum transfer kinematics, where  $\eta'$ -nucleus bound states are likely to be produced. The photon energy dependence of the momentum transfer of the  $\gamma + p \rightarrow \eta' + p$  reaction is shown in Fig.1.8. In order to suppress background events from (multi) meson production reactions, such as the  $\gamma + ^{12}\text{C} \rightarrow p + \pi\pi + X$ ,  $\gamma + ^{12}\text{C} \rightarrow p + \pi\pi\pi + X$ ,  $\gamma + ^{12}\text{C} \rightarrow p + \omega + X$ , and  $\gamma + ^{12}\text{C} \rightarrow p + \pi\eta + X$  reactions, possible decay products from the  $\eta'$ -nucleus system were simultaneously measured for the first time, in coincidence with the missing mass spectroscopy. More specifically, we investigated the following two processes; the  $\eta'$  absorption process (Eq.(1.30)) and the  $\eta'$  escape (quasi-free  $\eta'$  production) process (Eq.(1.31)):

$$\gamma + ^{12}\text{C} \rightarrow p_f + \eta' \otimes ^{11}\text{B} \quad (1.30a)$$

$$\hookrightarrow \eta' + p \rightarrow \eta + p_s. \quad (1.30b)$$

$$\gamma + ^{12}\text{C} \rightarrow p_f + \eta' + ^{11}\text{B} \quad (1.31a)$$

$$\hookrightarrow \eta' \rightarrow 2\gamma. \quad (1.31b)$$

Here,  $\eta' \otimes ^{11}\text{B}$  represents a biparticle state of an  $\eta'$  meson and an  $^{11}\text{B}$  nucleus. The forward-going proton,  $p_f$ , is used for the missing-mass spectroscopy. The side-going proton,  $p_s$ , is

emitted in the  $\eta'N \rightarrow \eta N$  reaction, which is one of the most promising absorption processes for an  $\eta'$  meson bound in a nucleus [8, 43]. The  $\eta'$  meson bound to a nucleus hardly escapes from the nucleus and thus decays via an absorption process by a nucleon(s) in nucleus. Thereby, the  $\eta'$ -nucleus bound state was searched for from the reaction in Eq.(1.30). As discussed in the previous section on the past experiment by the  $\eta$ -PRiME/Super-FRS Collaboration, there is uncertainty of the production cross section of the  $\eta'$  off nuclei. By measuring the missing mass spectrum of the  $\eta'$  escape process in Eq.(1.31), we evaluate the  $\eta'$  production rate around the  $\eta'$  production threshold, which is important to confirm that  $\eta'$  mesons are actually produced and to evaluate the normalization factor of the absolute value of the theoretical cross sections.

The  $(\eta + p_s)$  pair was detected with an electromagnetic calorimeter, BGOegg, which covers the polar angle of  $28.5^\circ - 138.5^\circ$ . By tagging an  $(\eta + p_s)$  pair, multi-pion backgrounds were strongly suppressed. Remaining backgrounds are mainly from the  $\gamma + {}^{12}\text{C} \rightarrow p_f + \eta + {}^{11}\text{B}$  and  $\gamma + {}^{12}\text{C} \rightarrow p_f + (\eta + \pi^0) + {}^{11}\text{B}$  reactions. In these events, an  $\eta$  is produced in the primary reaction, and another proton,  $p_s$  is kicked out by either a primary  $\eta$ ,  $\pi^0$  or  $p_f$ . We removed those background events by selecting the kinematical region which is characteristic for signal events. The missing mass resolution of our detector system is 13–30 MeV/c<sup>2</sup>, which is not good enough to observe individual peaks of bound states. Thereby, we searched for events around the production threshold in a very low background condition. Then, the production cross section of the  $\eta'$ -bound nuclei emitting an  $(\eta + p_s)$  pair,  $\left(\frac{d\sigma}{d\Omega_{p_f}}\right)_{exp}^{\eta+p_s}$ , around the production threshold were evaluated.

The  $(\eta + p_s)$  coincidence cross section  $\left(\frac{d\sigma}{d\Omega_{p_f}}\right)_{exp}^{\eta+p_s}$  can be compared with theoretical cross

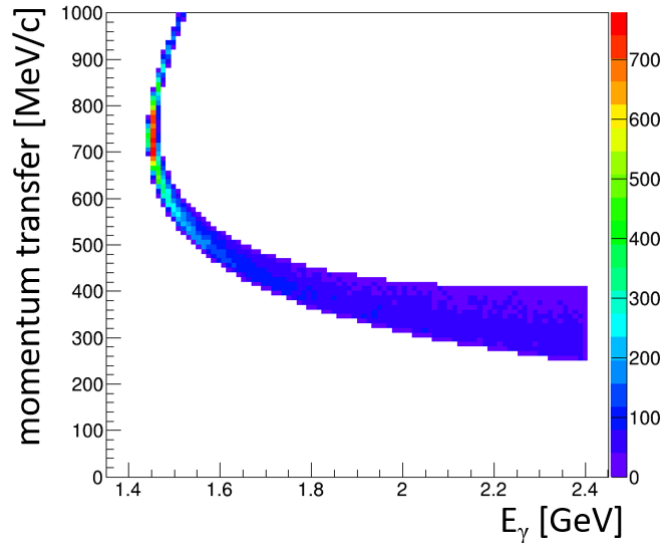


Figure 1.8: The photon energy dependence of the momentum transfer of the  $\gamma + p \rightarrow \eta' + p$  reaction in the forward proton polar angle of  $0.9^\circ - 6.8^\circ$ .

sections,  $\left(\frac{d\sigma}{d\Omega_{p_f}}\right)_{theory}^{\eta+p_s}$ , expected in different  $V_0$  values. For this purpose, we calculated the expected excitation energy of the  $\eta'+^{11}\text{B}$  system  $E_{\text{ex}}$ , relative to the production threshold  $E_0$  in the framework of a DWIA. DWIA calculations are widely used for describing bound states such as hyper nuclei and pionic atoms [25–30]. This is the advantage to the results from the CBELSA/TAPS Collaboration, whose reliability on the theoretical cross section is not established. Typical calculation results within in the DWIA are shown in Fig.1.9. The spectra are decomposed to the  $\eta'$  absorption process and  $\eta'$  escape processes as

$$\left(\frac{d\sigma}{d\Omega_{p_f}}\right)_{theory}^{\gamma+^{12}\text{C}\rightarrow p+\eta'+^{11}\text{B}} = \left(\frac{d\sigma}{d\Omega_{p_f}}\right)_{theory}^{\eta'esc} + \left(\frac{d\sigma}{d\Omega_{p_f}}\right)_{theory}^{\eta'abs}. \quad (1.32)$$

In general, DWIA calculations nicely reproduce spectral shapes of both the bound states and quasi-free processes, but hardly reproduce their absolute cross sections [25–30]. The normalization factor  $F$  of the DWIA calculation was introduced as

$$F = \left(\frac{d\sigma}{d\Omega_{p_f}}\right)_{exp}^{\eta'esc} / \left(\frac{d\sigma}{d\Omega_{p_f}}\right)_{theory}^{\eta'esc}. \quad (1.33)$$

where,  $\left(\frac{d\sigma}{d\Omega_{p_f}}\right)_{exp}^{\eta'esc}$  and  $\left(\frac{d\sigma}{d\Omega_{p_f}}\right)_{theory}^{\eta'esc}$  are the the experimental and theoretical cross sections of the  $\eta'$  escape process, respectively. As summarized in section 1.4, the  $\eta$ -PRiME/Super-FRS Collaboration also used the DWIA calculation to evaluate  $V_0$  and  $W_0$  from a comparison of the experimental and theoretical cross sections. However, they did not measure  $\left(\frac{d\sigma}{d\Omega_{p_f}}\right)_{exp}^{\eta'esc}$  and did not evaluate  $F$ , and thus there is large uncertainty of their upper limit of  $V_0$  and

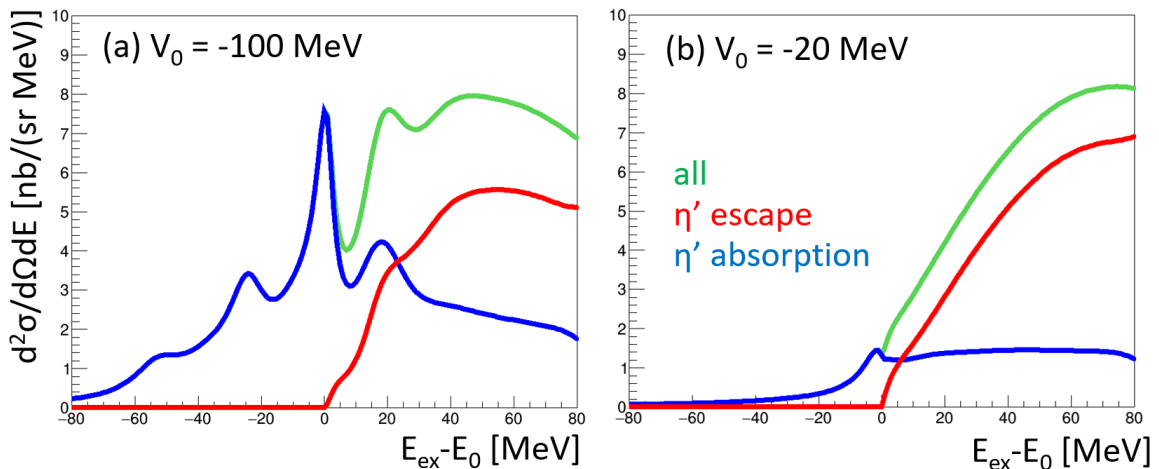


Figure 1.9: The excitation spectra calculated within the DWIA in the cases of  $V_0 = -100$  and  $-20$  MeV,  $W_0 = -12$  MeV,  $\theta_p = 6^\circ$  and photon beam energy = 2.05 GeV.

$W_0$ . Our advantage is that we can confirm that  $\eta'$  mesons are actually produced and the uncertainty of the absolute value of the theoretical cross section is reduced by measuring the  $\eta'$  escape process. The theoretical production cross section of the  $\eta'$  bound states with  $(\eta + p_s)$  emission can be described with the cross section of the  $\eta'$  absorption process as

$$\left(\frac{d\sigma}{d\Omega_{p_f}}\right)_{theory}^{\eta+p_s} = F \times \left(\frac{d\sigma}{d\Omega_{p_f}}\right)_{theory}^{\eta'abs} \times \text{Br}_{\eta'N \rightarrow \eta N} \times P_{srv}^{\eta p_s}. \quad (1.34)$$

Here,  $\text{Br}_{\eta'N \rightarrow \eta N}$  is the unknown branching fraction of the  $\eta'N \rightarrow \eta N$  process in all the  $\eta'$  absorption process and  $P_{srv}^{\eta p_s}$  is the probability that an  $(\eta + p_s)$  pair is emitted from a nucleus after final interactions of the  $(\eta + N)$  pair in the residual nucleus.  $P_{srv}^{\eta p_s}$  can be estimated from a simulation and existing experimental data. If we observe an enough number of  $(\eta + p_s)$  events, we can estimate  $\text{Br}_{\eta'N \rightarrow \eta N}$  from the comparison of  $\left(\frac{d\sigma}{d\Omega_{p_f}}\right)_{exp}^{\eta+p_s}$  and  $\left(\frac{d\sigma}{d\Omega_{p_f}}\right)_{theory}^{\eta+p_s}$  in  $E_{\text{ex}} - E_0 > 0$  MeV. If not,  $\left(\frac{d\sigma}{d\Omega_{p_f}}\right)_{theory}^{\eta+p_s}$  depends on unknown  $\text{Br}_{\eta'N \rightarrow \eta N}$ . Within the DWIA, we calculated the excitation spectra for  $\eta'$  angular momenta up to  $l_{\eta'} = 6$ , which is large enough to have convergence for  $E_{\text{ex}} - E_0 \lesssim 50$  MeV [23, 44]. As can be seen in Fig.1.9, the  $\eta'$  escape process contributes only in  $E_{\text{ex}} - E_0 > 0$  MeV. Thereby, we evaluate  $F$  from  $\left(\frac{d\sigma}{d\Omega_{p_f}}\right)_{exp}^{\eta'esc}$  and  $\left(\frac{d\sigma}{d\Omega_{p_f}}\right)_{theory}^{\eta'esc}$  which are integrated over  $0 \text{ MeV} < E_{\text{ex}} - E_0 < 50 \text{ MeV}$ . After normalizing the theoretical cross sections with  $F$ , we compared  $\left(\frac{d\sigma}{d\Omega_{p_f}}\right)_{exp}^{\eta+p_s}$  and  $\left(\frac{d\sigma}{d\Omega_{p_f}}\right)_{theory}^{\eta+p_s}$  in  $-50 \text{ MeV} < E_{\text{ex}} - E_0 < 50 \text{ MeV}$ .

# Chapter 2

## Experimental setup

The experiment was carried out in the LEPS2 beam line at SPring-8. A photon beam was produced by means of backward Compton scattering (BCS) of UV laser from 8 GeV electrons in the SPring-8 storage ring. Photon beam energy was evaluated by measuring recoil electrons with the tagging counter. The photon beam was transferred to the LEPS2 experimental building and hit a carbon target. Produced particles were measured by the BGOegg detector system. The details of the experimental set up is described in this chapter.

### 2.1 SPring-8/LEPS2 facility

#### 2.1.1 LEPS2 beam line

Figure 2.1 shows the accelerator system of SPring-8 [45]. 100 mA electrons with energies of 8 GeV are stored in the storage ring. The electrons are in packets whose frequency is 508.58 MHz. The beam lines of SPring-8 are shown in Fig.2.2. There are 62 beam lines and four beam lines are in 30 m long straight sectors. The LEPS2 beam line locates in BL31LEP, which is one of the four long sectors. The former LEPS beam line locates in BL33LEP. The electron emittance of long sectors is small compared with ordinary ones, indeed, the average electron emittance in the  $X$  direction in BL31LEP is  $14 \mu\text{rad}$ , whereas it is  $58 \mu\text{rad}$  in BL33LEP. The small emittance of BL31LEP enables us to keep small BCS photon beam size after transferring to the LEPS2 experimental building located 125 m downstream from the collision point. By constructing the experimental building outside of the storage ring building, we installed large detector system covering large acceptance.

#### 2.1.2 Laser system

We used four laser system called TL, BL, TR and BR. They are UV lasers with a wavelength of 355 nm, and substantial output power of each laser was 11, 10, 8 and 8 W, respectively. The details of lasers are summarized in Table.2.1. Figure 2.3 shows the laser injection system. The four UV lasers are shown with blue color. The laser is introduced to the vacuum chamber

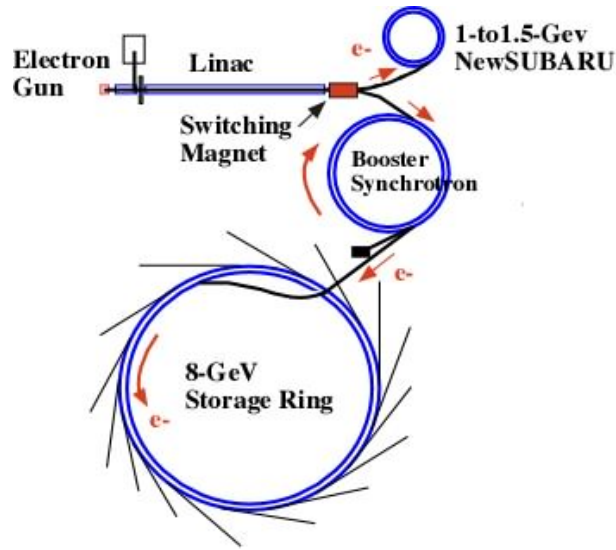


Figure 2.1: SPring-8 accelerators [45].

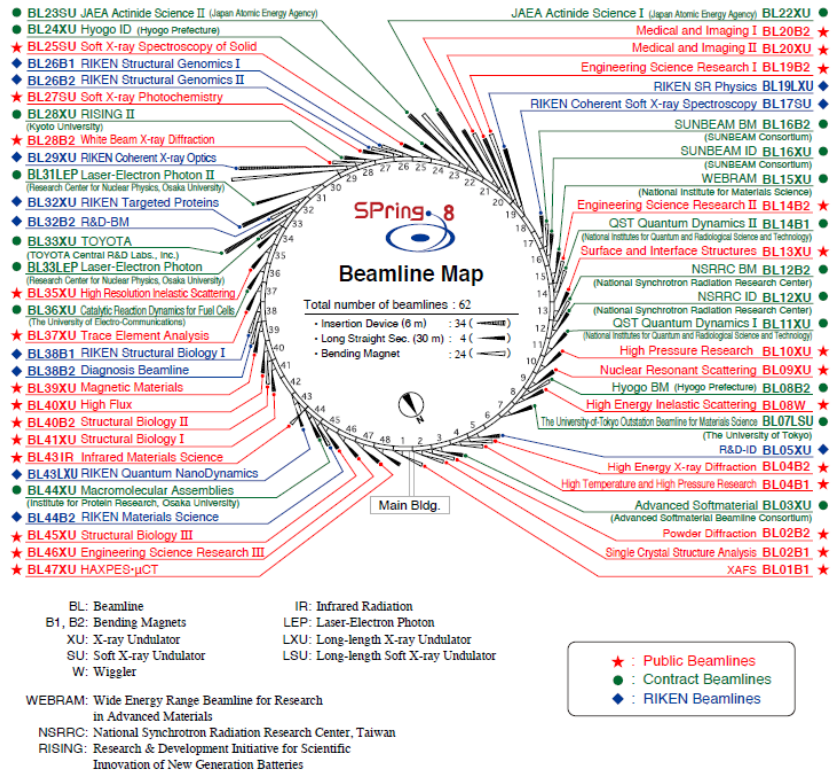


Figure 2.2: The beam line map of SPring-8 [45].

Table 2.1: The details of lasers.

Name	TL	BL	TR	BR		
Laser type	Paladin	Advanced	355-16000	Paladin	Advanced	355-8000
Default output power		>16 W		>8 W		
Substantial output power	11 W	10 W	8 W	8 W		
Wavelength			355 nm			
Repetition rate			80±1 MHz			
Beam divergence		480 $\mu$ rad		550 $\mu$ rad		

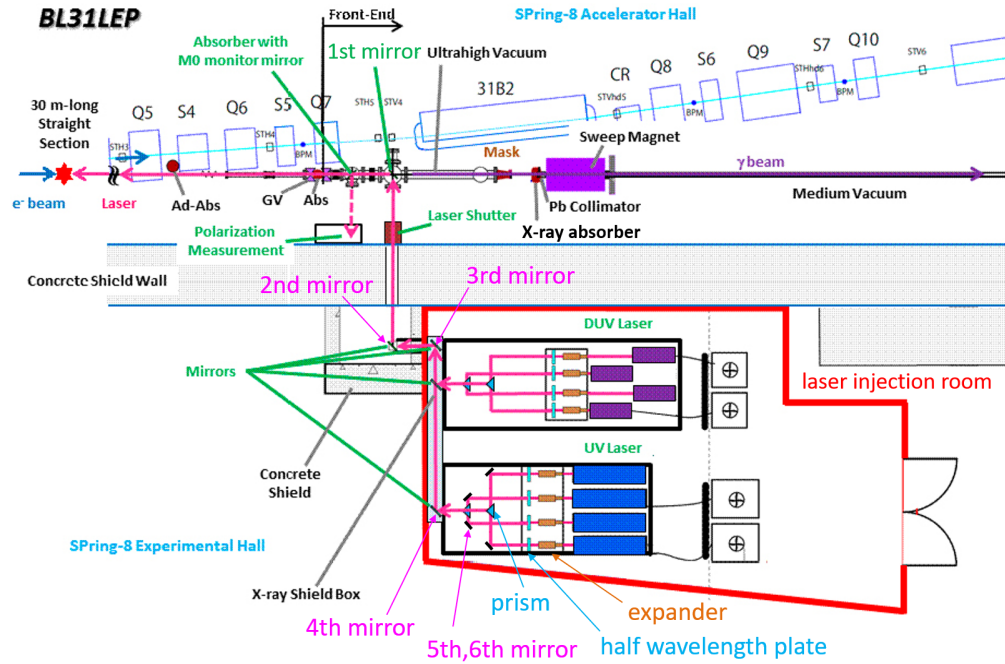


Figure 2.3: The laser injection system of the LEPS2 beam line. The 6th mirror locates above the 5th mirror and they are overlapped in the figure.

of the storage ring using and expander, six mirrors and one prisms. The expander was tuned to focus the laser at the collision point. The 5th mirrors are on micro-stepping motors, and the angles of 5th mirror were tuned during the data taking to obtain high BCS rate. The laser is almost 100% linearly polarized. Orientation of polarization of the laser was controlled by a half-wave plate. The 1-4th mirrors have higher reflectivity for vertically polarized photons than for horizontally polarized photons, and 5-6th mirrors have higher reflectivity for horizontally polarized photons than for vertically polarized photons. In total, the vertically polarized photons give  $\sim 10\%$  higher beam intensity than the horizontally

polarized photon. Therefore, we used vertically polarized lasers in almost all the experimental period.

### 2.1.3 Backward Compton scattering

Figure 2.4 shows a schematic drawing of a backward Compton scattering (BCS) in the laboratory frame. Energy of the BCS photon,  $E_\gamma$  is calculated as [46]

$$E_\gamma = k \frac{1 - \beta \cos \theta_1}{1 - \beta \cos \theta_2 + \frac{k}{E_e}(1 - \cos(\theta_1 - \theta_2))}. \quad (2.1)$$

Here,  $E_e = 7.975 \pm 0.003$  GeV is incoming electron energy [47],  $\beta$  is velocity of the electron, and  $k = 3.49$  eV is energy of a laser photon with a wave length of 355 nm. The angles between an incident electron and, a laser and BCS photon is defined as  $\theta_1$  and  $\theta_2$ , respectively. Below, we assume  $\beta \simeq 1$ ,  $\theta_1 \simeq 180^\circ$  and  $\theta_2 \simeq 0^\circ$ . Then, Eq.(2.1) can be rewritten as

$$E_\gamma = \frac{4E_e^2 k}{m_e^2 + 4E_e k + \theta_2^2 \gamma^2 m_e^2}, \quad (2.2)$$

where  $m_e = 0.511$  MeV/ $c^2$  is electron mass. The maximum BCS photon energy  $E_\gamma^{\max}$  is obtained at  $\theta_2 = 0^\circ$ :

$$E_\gamma^{\max} = \frac{4E_e^2 k}{m_e^2 + 4E_e k} = 2.385 \text{ GeV}. \quad (2.3)$$

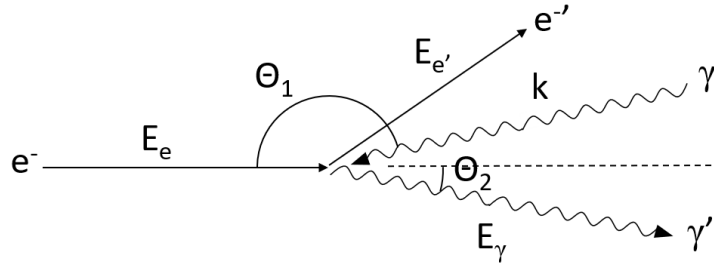


Figure 2.4: A schematic drawing of a backward Compton scattering.

The  $E_\gamma$  dependence of a differential cross section can be described as [48]

$$\frac{d\sigma}{dE_\gamma} = \frac{2\pi r_e^2 a}{E_\gamma^{\max}} (\chi + 1 + \cos^2 \alpha), \quad (2.4)$$

$$a = \frac{m_e^2}{m_e^2 + 4E_e k}, \quad (2.5)$$

$$\chi = \frac{(E_\gamma/E_\gamma^{\max})^2 (1-a)^2}{1 - (E_\gamma/E_\gamma^{\max})(1-a)}, \quad (2.6)$$

$$\cos \alpha = \frac{E_\gamma^{\max} - E_\gamma(1+a)}{E_\gamma^{\max} - E_\gamma(1-a)}. \quad (2.7)$$

In Fig.2.5, the  $E_\gamma$  dependence of the cross section of the BCS process is shown.

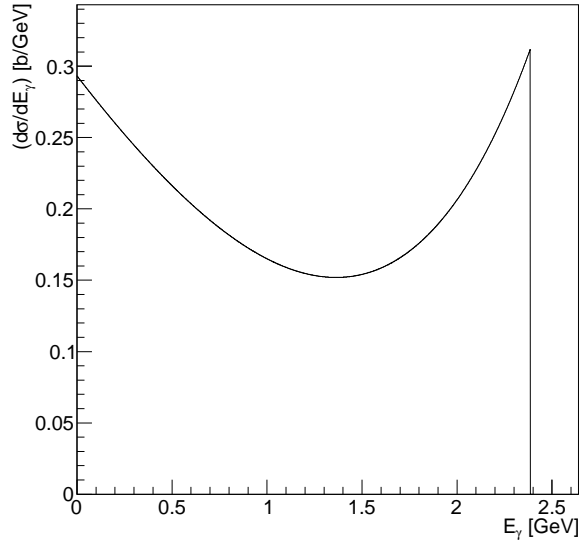


Figure 2.5: The  $E_\gamma$  dependence of the cross section of a BCS process.

### 2.1.4 Transmission rate

In Table.2.2, materials located between the collision point and the target are summarized. Conversion rate of the  $\gamma$  rays to  $e^+e^-$  pairs at each material is also shown. As shown in Fig.2.3, there is an X-ray absorber at the exit of the ultrahigh vacuum chamber. The  $e^+e^-$  pairs generated in the absorber are swept out by a dipole magnet. After the magnet, the  $\gamma$ -rays are transferred to the LEPS2 experimental building through a medium vacuum pipe. In total, 22.8% of the  $\gamma$  rays are converted to  $e^+e^-$  pairs before arriving at the target.

Table 2.2: The materials located between the collision point and the target.

	Material	Radiation length $L_R$ (cm)	Thickness $t$ (cm)	Conversion rate $1 - \exp(-(\frac{7}{9})(\frac{t}{L_R}))$ (%)
Vacuum window 1	Al	8.90	0.20	1.7
X-ray absorber	W	0.35	0.10	19.9
Air 1	Air	30390	170	0.43
Vacuum window 2	Kapton+Aramid	28.6	0.0125	0.03
Vacuum window 3	Kapton+Aramid	28.6	0.0175	0.05
UpVeto counter	Polystyrene	41.3	0.30	0.56
Air 2	Air	30390	310	0.79
Total				22.8

## 2.2 Target

A carbon target used for the experiment is shown in Fig.2.6(a). The thickness is 20.0 mm and the density is 1.73 g/cm<sup>3</sup>. A measurement error for density×thickness is less than 1%. The target holder was made with a 10-mm thick polystyrene form and a 0.125-mm thick kapton foil. They are shown in Fig.2.6(b)(c).

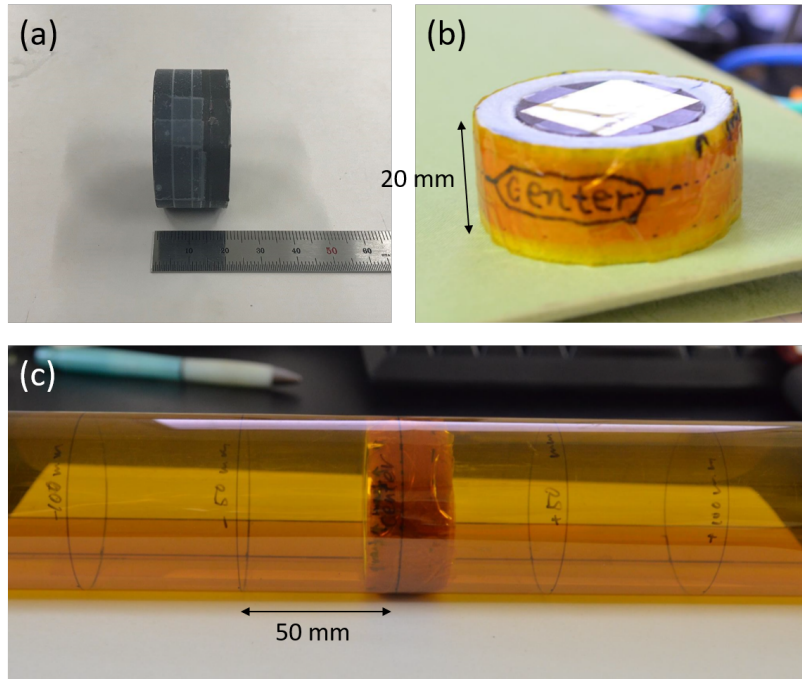


Figure 2.6: (a) A picture of the carbon target. (b)(c) Pictures of the target holder.

## 2.3 Detector in LEPS2

We measured the  $\gamma + {}^{12}\text{C} \rightarrow p_f + (\eta + p_s) + X$  reaction to search for the  $\eta'$ -nucleus bound state. Here,  $p_f$  is the forward-going proton and  $p_s$  is the side-going proton. We also measured  $\gamma + {}^{12}\text{C} \rightarrow p_f + \eta' + X$  reactions to evaluate the production rate of  $\eta'$  meson. The photon beam energy was evaluated by measuring a recoil electron with a tagging counter located near the storage ring. Figure 2.7 shows the experimental set up in the LEPS2 building. Events in which an incident photon were converted to an  $e^+e^-$  pair when it was transmitted to the experimental hall was excluded using an UpVeto counter. The energy of  $p_f$  was measured with Time-Of-Flight (TOF) technique using a resistive plate chamber (RPC) TOF wall. There is the LEPS2 solenoid magnet between the target and the RPC wall, and the acceptance for  $p_f$  is limited with the hole of the solenoid to be polar angle less than  $7.0^\circ$ . The start timing of TOF is determined from RF signal of the SPring-8 storage ring. The  $\eta$  and  $\eta'$  mesons were identified from the invariant mass of  $2\gamma$ s with the BGOegg electromagnetic calorimeter. Particle identification of  $p_s$  was carried out with the energy deposit in the inner plastic scintillators (IPS) and BGOegg. A drift chamber was used to ensure that there is no charged particle other than  $p_f$  in the forward region which is not covered by the BGOegg. Details of each detector are described in the following sections. The coordinates of the experimental set up are defined as shown in Fig.2.7.

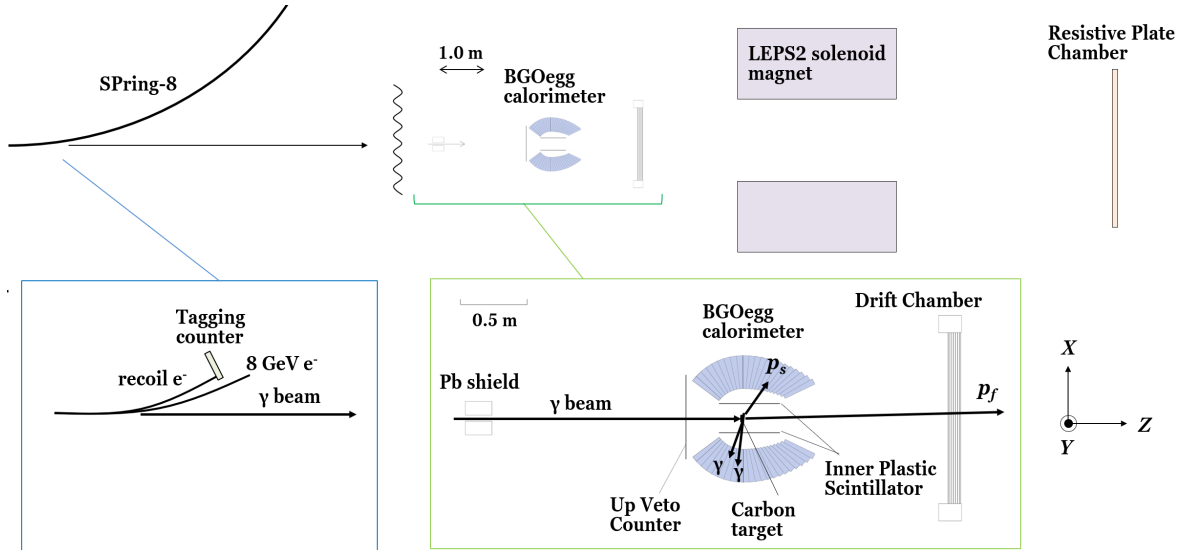


Figure 2.7: A schematic drawing of the detector set up in LEPS2.

### 2.3.1 Tagging counter

#### Installation area

In Fig.2.8(a), schematic drawing of the SPring-8 storage ring around the LEPS2 beam line is shown. The BCS photon is produced upstream of the 31B1 bending magnet. The recoil electrons are bent by the 31B1 magnet to different directions depending on their momentum. The track position of the recoil electron is measured by the 80-mm wide tagging counter made of plastic scintillators. The tagging counter (or tagger) locates at the side of the CR1C chamber downstream of the 31B1 magnet. Figure 2.8(b) shows a schematic drawing of the CR1C chamber. The tagging counter locates in the hatched region. The tagging counter detects electrons coming out from a slit of a tungsten shield shown in Fig.2.8(b)(c). In the

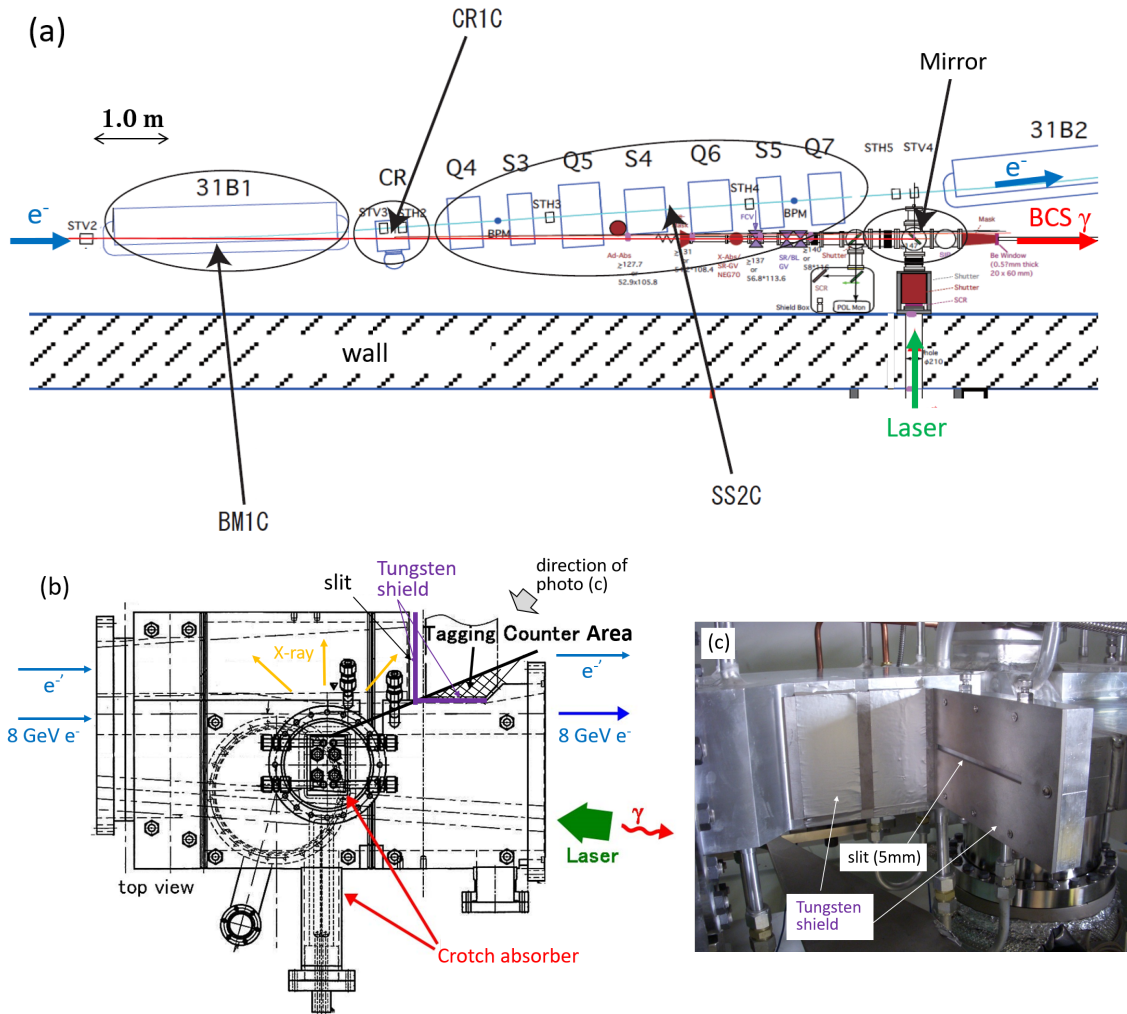


Figure 2.8: (a) A schematic drawing of the LEPS2 beam line. (b) A schematic drawing of the CR1C chamber. (c) A picture of the tungsten shields.

CR1C chamber, there is a crotch absorber. The crotch absorber reflects synchrotron radiation X-rays generated at the 31BL magnet to bottom side to avoid damage on the chamber wall. As can be seen in Fig.2.8(b), the slit for recoil electrons locates downstream side of the crotch absorber whereas it locates upstream in the former LEPS beam line. In downstream side of the crotch absorber, we can place the tagging counter closer to the 8 GeV electron orbit. The lower limit of tagged photon energy of the tagging counter is 1.28 GeV. It is small compared to the one of 1.5 GeV in the LEPS beam line. Note that the  $\eta'$  production threshold for a proton at rest is 1.447 GeV. On the other hand, because the slit locates downstream side of the crotch absorber, X-rays from the absorber are also emitted from the slit and give damage to the tagging counter. Thereby, the tagging counter was designed to be in the hatched region in Fig.2.8(b) where X-rays do not directly hit the counter.

### The detector design

A schematic drawing and picture of the tagging counter are shown in Fig.2.9. The tagging counter consists of two layers of fiber scintillators (tagger-fiber) and pairs of plastic scintillators (tagger-PL). The fiber scintillators are used to measure the recoil electron hit position and the plastic scintillators are used to generate a trigger signal for data acquisition. The fiber scintillator is made of a Kuraray SCSF-78 with a cross section of  $1.0 \times 1.0 \text{ mm}^2$  [49]. Each fiber layer consists of 80 fiber bundles, and each fiber bundle is made of 6 fibers in series. The bundles are placed 1.02 mm-step, in which 0.02 mm for glue. Cladding thickness of the fiber is 0.02 mm, and thus there is  $(0.02(\text{glue}) + 0.02 \times 2(\text{cladding}))/1.02 = 5.9\%$  inefficient area per bundle. We placed the backward bundles so that the center of fibers are 0.5 mm shifted from the one of forward bundles to cover the inefficient region. At the other end, the 6 fibers are bundled in round shape and connected to a single channel of a  $4 \times 4$  channels

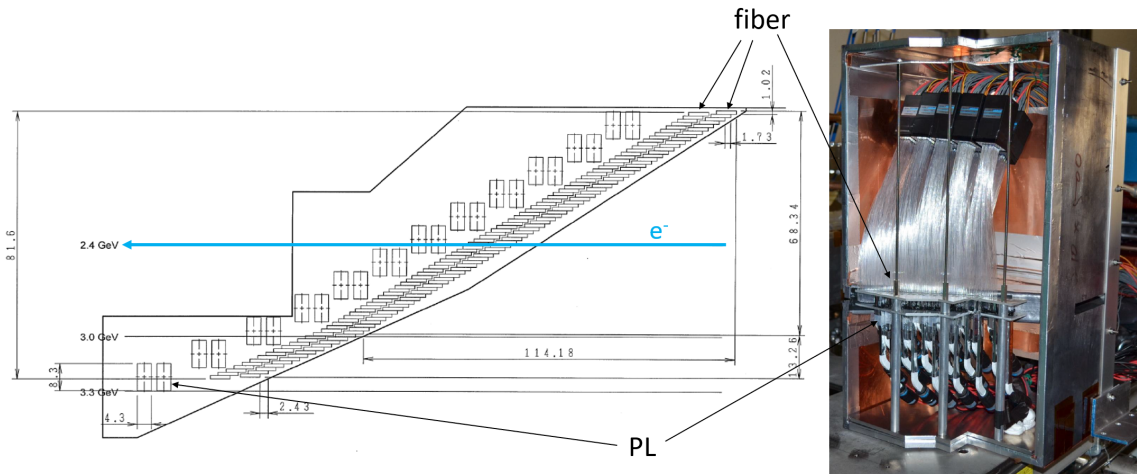


Figure 2.9: A schematic drawing and a picture of the tagging counter. Note that top and bottom of the drawing is opposite with Fig.2.8(b).

photo multiple tube, HAMAMATSU MA-PMT, H6568-200MOD. The plastic scintillator of tagger PL is 4 mm (thick)  $\times$  8 mm (wide)  $\times$  10 mm (height) ELJEN EJ-200. Neighboring pairs of scintillators are overlapped by 1 mm. The plastic scintillator is connected to a HAMAMATSU PMT, R9880U-210, with a light guide.

### 2.3.2 UpVeto counter

The UpVeto counter was installed upstream of the target and used to exclude events in which photon beam is converted to an  $e^+e^-$  pair before arriving at the target. It was also used to detect charged particles going to backward from the target. Figure 2.10 shows a picture of the UpVeto counter. The UpVeto counter is made of a plastic scintillator with 3 mm (thick)  $\times$  620 mm (wide)  $\times$  620 mm (height). It is connected to a HAMAMATSU fine mesh PMT, H6614-70mod, with a light guide.

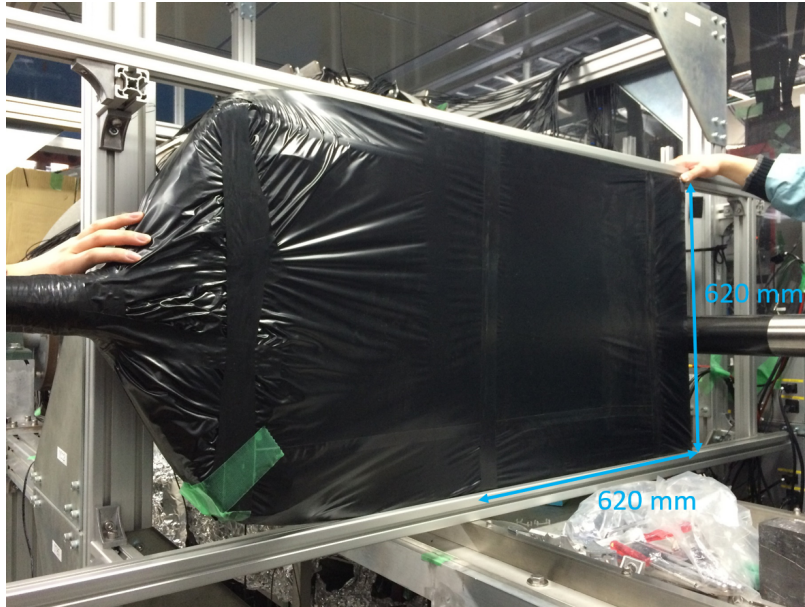


Figure 2.10: A picture of the UpVeto counter.

### 2.3.3 BGOegg calorimeter

Figure 2.11 shows a schematic drawing of the BGOegg calorimeter. It consists of 1,320  $\text{Bi}_{12}\text{GeO}_{20}$  (BGO) crystals. There is no support frame between crystals, and thus there is no dead area. Figure 2.12 shows the cross section of the BGOegg calorimeter. There are 22 layers of the BGO crystals and the polar angle from  $24^\circ$  to  $144^\circ$  is covered. Each layer consists of 60 crystals and covers  $360^\circ$  azimuthal angle. The shape of the crystals are different layer by layer. The length of the crystals is 220 mm which corresponds to 20 radiation length. The

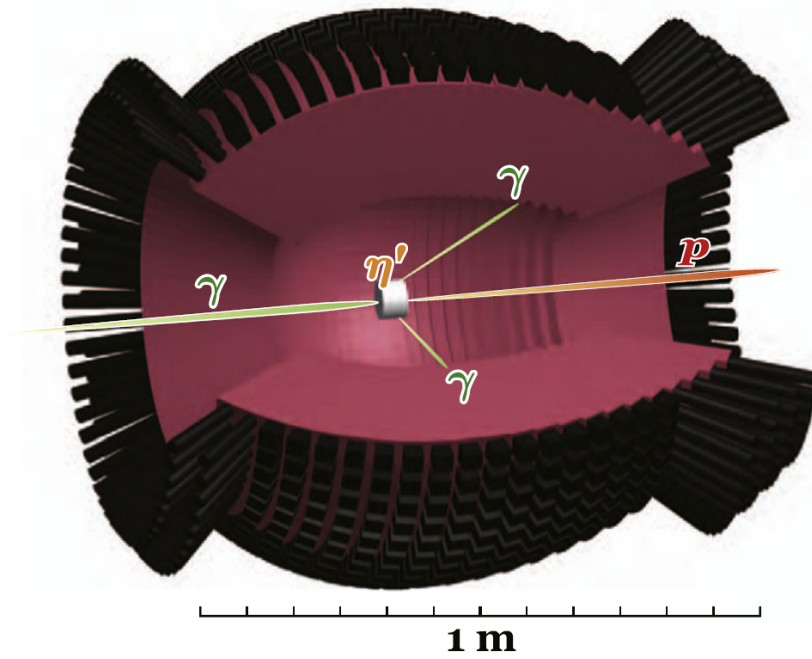


Figure 2.11: A schematic drawing of the BGOegg. The crystals are shown with reddish purple color. The PMTs are shown in black.

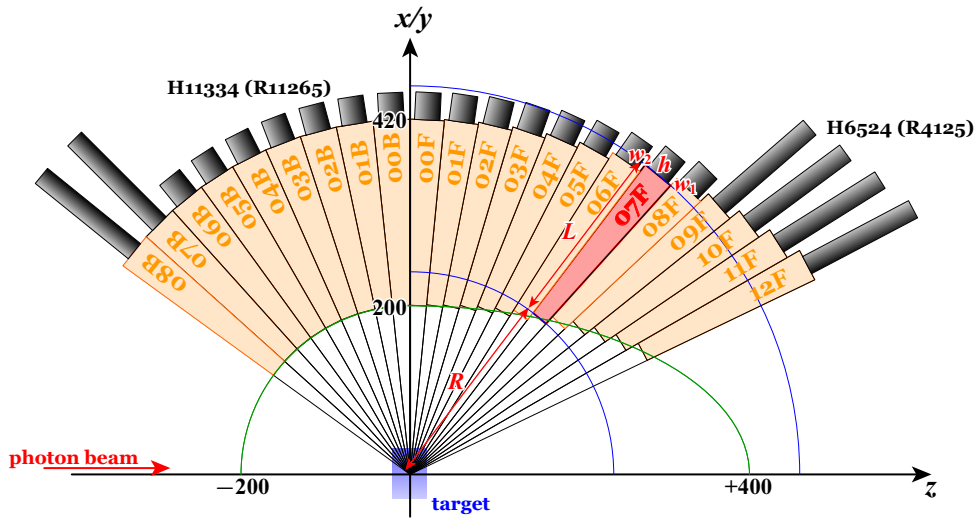


Figure 2.12: The cross section of the BGOegg.

detailed properties of the BGOegg are summarized in Ref.[50]. The crystals of layer 1–4 and 21,22 are read with HAMAMATSU H6524 PMTs. The crystals of layer 5–20 are read with HAMAMATSU H11334 PMTs. The light yield of BGOegg strongly depends on temperature.

Therefore, we installed BGOegg in a thermostatic booth and kept the temperature at 25.0 C°.

### 2.3.4 Inner Plastic Scintillator

Figure 2.13(a)(b) shows schematic drawings of a cross section and front view of the inner plastic scintillators (IPS). The IPS consists of 30 ELJEN EJ-212 plastic scintillators with a size of 453 mm × 26 mm × 5 mm. The neighboring scintillators are overlapped as shown in Fig.2.13(b). The upstream side of the scintillators are connected to HAMAMATSU multi pixel photon counters (MPPCs) S12572-050P. Effective photosensitive area of the MPPC is 3 mm × 3 mm. Five MPPCs are connected to a plastic scintillator. Signals from MPPCs were amplified using LeCroy 612A NIM modules.

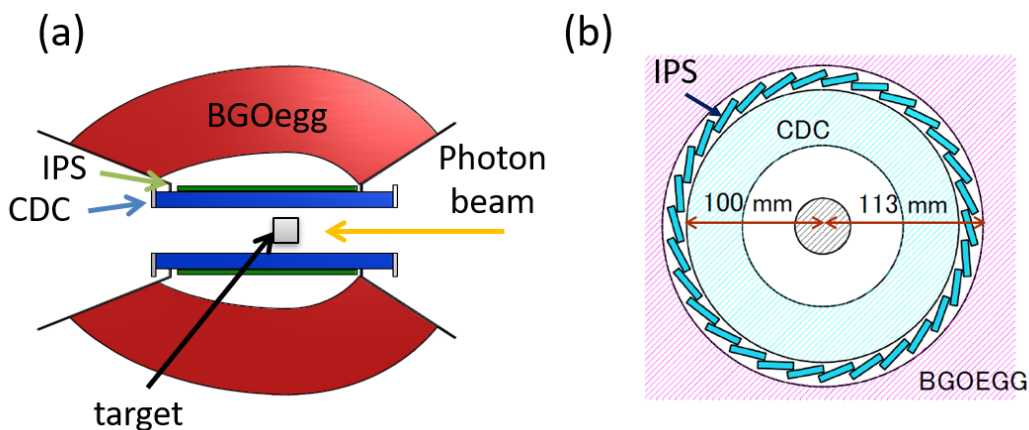


Figure 2.13: A schematic drawing of the IPS (a) from side (b) from upstream. The cylindrical drift chamber (CDC) was installed but it was not used for the analysis.

### 2.3.5 Drift Chamber

Figure 2.14 shows a schematic drawing of the drift chamber (DC). The DC was originally developed to be used in the LEPS2 solenoid magnet, and thus its frame is a round shape. It located 1.6 m downstream from the target. Wire planes are in a hexagonal shape as shown in red-dashed lines in Fig.2.14. The diameter of the inscribed circle of the hexagon is 1300 mm and the diameter of sensitive area is 1280 mm. The sensitive area corresponds to the polar angle from the target center of 21°. Apexes of the hexagon corresponds to the polar angle of 24°. There are 6 planes named X, X', U, U', V and V', in order from upstream. There are 80 wires in a plane. The wires of X, X' planes are aligned horizontally. The wires of U, U' planes are +60° relative to X, X' wires, and wires of V, V' planes are -60° relative to X, X' wires. They are summarized in Table.2.3. Figure 2.15 shows a schematic drawing of a cross section of a plane. The cell size is 16 mm. Cathode layers are made of 25 μm-thick

aluminized Mylar. Sense wires are made of gold-plated tungsten (Au-W) whose diameter is  $30\ \mu\text{m}$ . Potential wires are made of gold-plated beryllium copper (Au-BeCu) whose diameter is  $80\ \mu\text{m}$ . One side of a wire is connected to a Repic RPA-181 preamp card. The gas mixture was 50% Ar and 50% ethane.

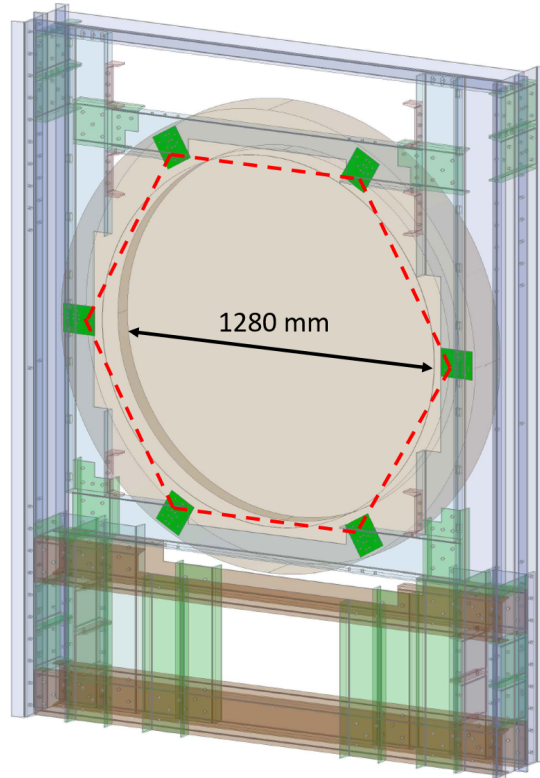


Figure 2.14: A schematic drawing of the DC. The sensitive area is shown by red-dashed lines.

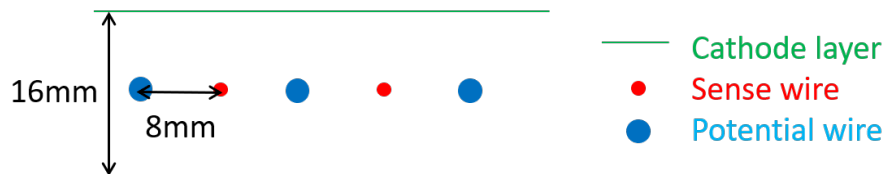


Figure 2.15: The cross section of the DC plane.

### 2.3.6 Resistive Plate Chamber

Figure 2.16 shows a schematic drawing of the resistive plate chamber (RPC) wall. An RPC is a gas chamber consists of multi layers of glasses. The cross section of the RPC chamber

Table 2.3: The angles of the DC wire planes.

Plane	angle
X	$0^\circ$
X'	$0^\circ$
U	$+60^\circ$
U'	$+60^\circ$
V	$-60^\circ$
V'	$-60^\circ$

is shown in Fig.2.17. The width of gas gap is  $260 \mu\text{m}$  and there are 10 gaps in an RPC. There are 8 readout strips in a chamber. The strip is  $1,000 \text{ mm}$  (height)  $\times$   $25.5 \text{ mm}$  (wide) and the gap between strips is  $0.5 \text{ mm}$ . Amplifiers are connected at the both ends of the strips. The gas mixture is 90% R134a, 5% SF6 and 5% butane. The wall consists of 32 RPC chambers. The neighboring chambers in the  $X$  direction are overlapped with a few mm. The RPCs in top row and bottom row are overlap by 70–80 mm. In total, an area of  $3,280 \text{ mm}$  ( $X$ )  $\times$   $1,930 \text{ mm}$  ( $Y$ ) is covered with 256 readout strips. The  $Z$ -position of the RPC module is defined at the middle of 10 gaps and it is  $12,456 \text{ mm}$  (upstream layer of the top row),  $12,496 \text{ mm}$  (downstream layer of the top row),  $12,596 \text{ mm}$  (upstream layer of the bottom row), and  $12,636 \text{ mm}$  (downstream layer of the bottom row). The polar angle is  $4.4^\circ$

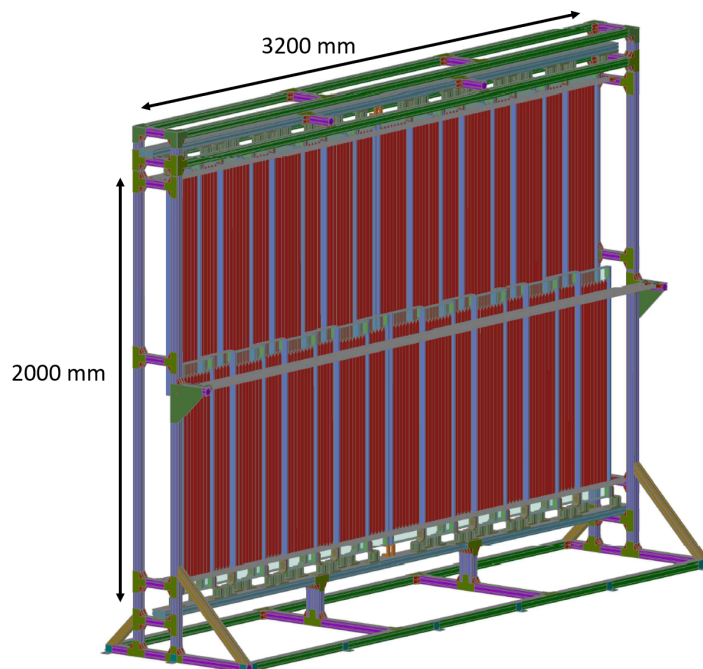


Figure 2.16: A schematic drawing of the RPC wall.

at  $X = 0$  mm and  $7.4^\circ$  at  $X = 1,640$  mm. The acceptance is limited to the polar angle less than  $7.0^\circ$  because of the LEPS2 solenoid magnet as explained in the beginning of section 2.3. The details of the RPCs are described in Refs.[51, 52].

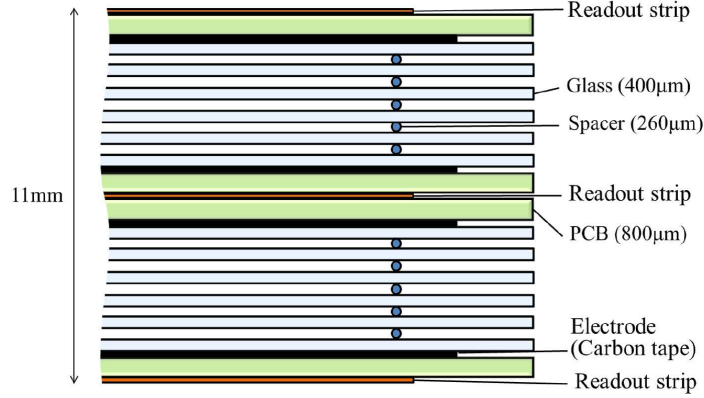


Figure 2.17: The cross section of an RPC.

### 2.3.7 RF signal

The electrons in SPring-8 are in bunches whose interval is 1.966 ns. There are 2436 packets in total but not all packets are used to fill electron bunches. There are several bunch filling modes as summarized in Appendix A and the bunch width varies 14–18 ps depending on the filling modes and bunch currents. By using RF signal from the SPring-8, we can determine the start timing of the TOF with the resolution of the bunch width. The jitter of the RF signal is  $\sim 4$  ps at the LEPS2 experimental hall. Because the RF signal is high frequent, we need to prescale the signal to read it by a time-to-digital converter (TDC). Figure 2.18 shows a schematic drawing of the pre-scale system. We prescaled the RF signal using a 508 MHz synchronous universal counter (SUC) [53] with a factor of 1/84. The 1/84 signal is used to determine the TOF. We also prescaled the RF signal with a factor of 1/2436. Because the interval of the 1/2436 signal is  $4.8 \mu\text{s}$ , we used delay lines so that the 1/2436 signal is recorded in a TDC measurement range. The time resolution of delayed signal is not good enough to be used for TOF measurement. The 1/2436 signal is used to examine events in a specific bunch.

## 2.4 Electronics

In Table.2.4, the number of channels and the readout electronics used for each detector are summarized. We measured signal charge with analog-to-digital converter (ADC) modules and signal timing with TDC modules. We measured both charge and timing of signals from the tagger-PL, UpVeto, BGOegg, IPS and RPC. We measured only timing of signals of the

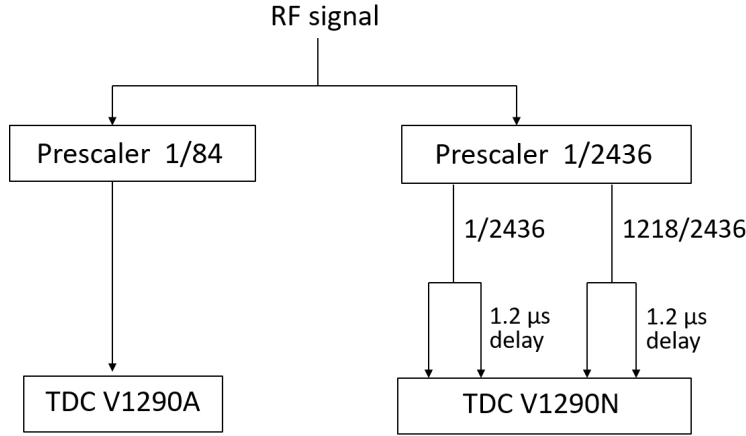


Figure 2.18: A schematic drawing of the RF prescale system.

Table 2.4: The modules used for each detector.

Detector	number of channels	ADC	TDC
Tagger-PL	24	VME V792	VME V1190
Tagger-fiber	160	—	VME V1190
UpVeto	1	VME V792	VME V1290N
BGOegg	1320	FERA 4300B	VME V1190
IPS	30	VME V792	VME V1290A
DC	480	—	LeCroy 3377
RPC	256	FERA 4300B	VME V1290A
RF	5	—	VME V1290A/N

tagger-fiber and DC. For the RPC, we summed up signals from neighboring strips for ADC, and took “or” of two signals from neighboring chambers for TDC, as shown in Fig.2.19. We utilized CAEN VME V792 ADC for the tagger-PL, UpVeto and IPS, and LeCroy FERA (Fast Encoding and Readout ADC) 4300B for the BGOegg and RPC. For the tagger-PL, tagger-fiber and BGOegg, we utilized CAEN VME V1190 TDC with 100 ps bin size. For the UpVeto, IPS, RPC and RF, we utilized CAEN VME V1290 TDC with 25 ps bin size. We utilized LeCroy 3377 with 500 ps bin size for the DC. There is integral nonlinearity in the measurement with VME V1290. The nonlinearity was corrected by offline analysis. The details of power supply, preamplifier and discriminators used for each detector are summarized in Appendix B.

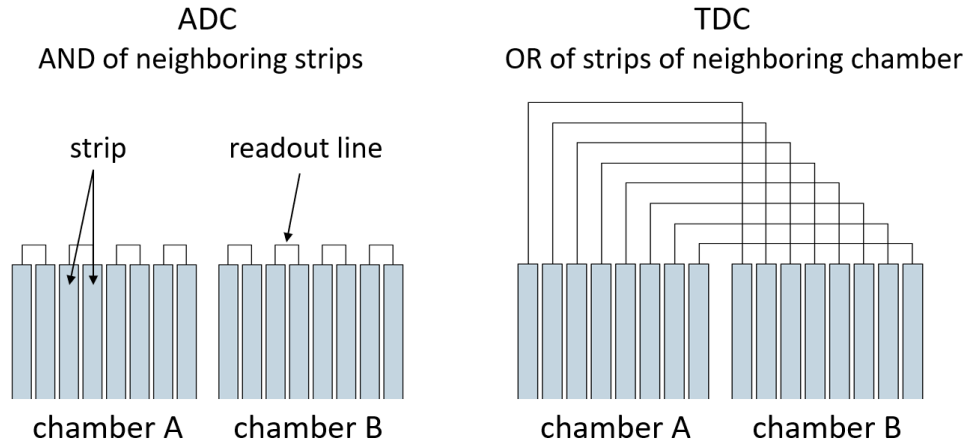


Figure 2.19: A schematic drawing of AND and OR of the readout lines for the RPC.

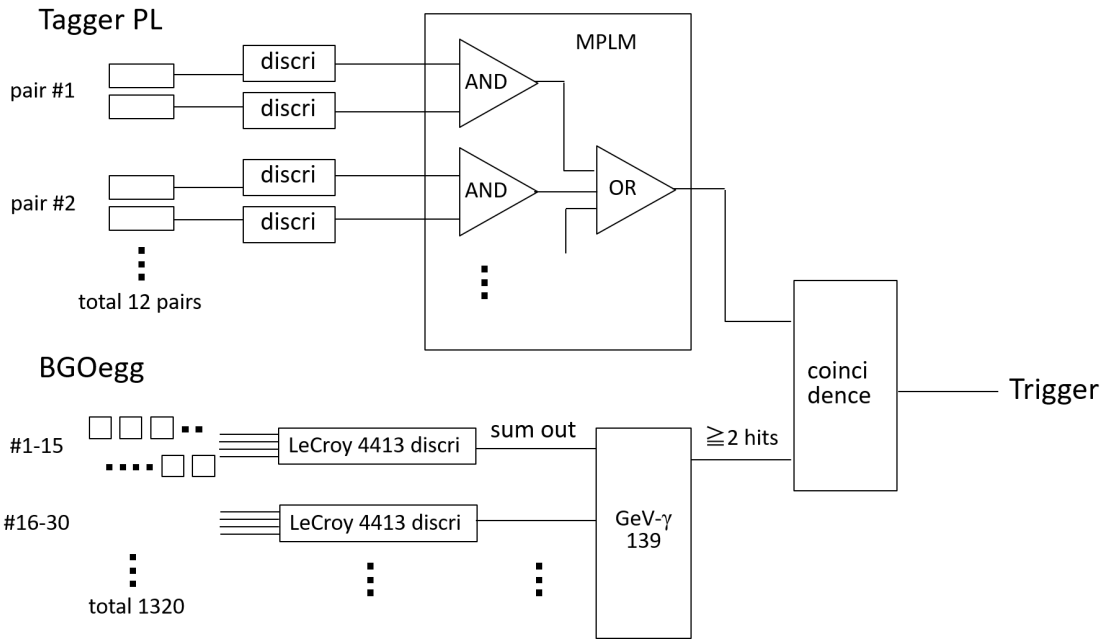


Figure 2.20: The trigger logic.

## 2.5 Trigger

Trigger signals for data acquisition were required that two tagger-PLs in pair have hits and more than one crystal of BGOegg have hits. A schematic drawing of the trigger logic is shown in Fig.2.20. For the tagger, we used a multi-purpose logic module (MPLM4) [54] and generated a trigger signal when both of pair PLs were fired. For the BGOegg, a GeV- $\gamma$  139

module were used for generating trigger signals [55]. The LeCroy 4413 discriminator module used for BGOegg has a current sum output. It gives a signal proportional to the number of channels which exceed the threshold. The output signal is  $-50$  mV/hit channel. The GeV- $\gamma$  139 module sums up signals from all the discriminators. Trigger signal is generated when the sum signal exceeds  $\sim -75$  mV, which corresponds to two-crystals hit. Matching timing hits are required for the tagger signal and the BGOegg signal. With this trigger condition, all reactions which have at least two photons in the final state are recorded. In addition to the  $\gamma + {}^{12}\text{C} \rightarrow p_f + (\eta + p_s) + \text{X}$  and  $\gamma + {}^{12}\text{C} \rightarrow p_f + \eta' + \text{X}$  reactions, which we are interested in, we also analyzed  $\gamma + {}^{12}\text{C} \rightarrow p_f + \eta + \text{X}$  and  $\gamma + {}^{12}\text{C} \rightarrow p_f + (\eta + \pi^0) + \text{X}$  reactions to study backgrounds, and  $\gamma + {}^{12}\text{C} \rightarrow \pi^0 + \text{X}$ ,  $\gamma + {}^{12}\text{C} \rightarrow p + 2\pi^0 + \text{X}$  and  $\gamma + {}^{12}\text{C} \rightarrow p + \omega + \text{X}$  reactions to study detector performance, using the same data set. Here,  $p_f$  is a proton detected with the RPC, and  $p_s$  and  $p$  are protons detected with BGOegg. The  $\pi^0 \rightarrow 2\gamma$ ,  $\eta \rightarrow 2\gamma$ ,  $\eta' \rightarrow 2\gamma$  and  $\omega \rightarrow \pi^0\gamma \rightarrow 3\gamma$  decays were used to identify each meson.

## 2.6 Data summary

The experiment was carried out from April to July in 2015. The total number of incident photons at the target was  $8.5 \times 10^{13}$ . Data which had a problem in a detector were carefully searched for and excluded from the analysis. The data used for the analysis was 72% of the total amount. We also took data with a liquid hydrogen target from November in 2014 to February in 2015. The liquid hydrogen target data is used for calibrations and efficiency measurements of several detectors.

# Chapter 3

## Event reconstruction

We searched for the  $\eta'$ -bound states in the excitation energy spectrum of the  $\gamma + {}^{12}\text{C} \rightarrow p_f + (\eta + p_s) + \text{X}$  reaction. We also measured the  $\gamma + {}^{12}\text{C} \rightarrow p_f + \eta' + \text{X}$  reaction to examine the production rate of  $\eta'$ . The energy of gamma beam was evaluated with the tagger. The momentum of  $p_f$  was measured with the RPC. The consistency of the hit position of  $p_f$  at the DC and RPC was required. The identification and energy measurement of  $\eta$ ,  $p_s$  and  $\eta'$  were carried out with BGOegg and IPS. In this chapter, event reconstruction method for each particle is described.

### 3.1 Photon beam energy measurement

The photon beam energy was evaluated photon by photon by measuring the momentum of a recoil electron after backward Compton scattering. The tagger locates downstream of a bending magnet in the electron storage ring of SPring-8, and the momentum of the recoil electron can be evaluated from the track position. In this section, we describe the algorithm of the tagger track reconstruction and the evaluation of the photon beam energy.

#### 3.1.1 Tagger track reconstruction

The track of recoil electrons was reconstructed in the following procedure. A schematic drawing of the tagger with an example of an electron track is shown in Fig.3.1.

1. Search for PL pairs, which both of them fired.
2. Search for fiber clusters in front of the fired PL pair.
3. Reconstruct an electron track from fiber clusters.

When there were clusters in both of two fiber layers, a tagger track was reconstructed from both of clusters. Since there are some dead regions in each fiber layer, events which have clusters only in one of the two fiber layers were also accepted. In this case, we need to take care cross talks in the MA-PMTs, which consists of  $4 \times 4$  channels. Cross talks in the

MA-PMTs create a fake cluster only in the front or backward fiber near the true cluster. To suppress the cross talk events, clusters satisfying following conditions were excluded from the tracking.

- There is no pair cluster in the another layer.
- There is another track having clusters in both fiber layers.
- The difference of the smallest fiber number of the two clusters in the same layer is less than 6.

An example of a fake cluster is also shown in Fig.3.1. The intrinsic efficiency of the tagger-PL was  $(98.8 \pm 1.2)\%$ . The reconstruction efficiency of the track of recoil electrons depends on event selection criteria. See section 4.2 and Appendix F.2.1 for details.

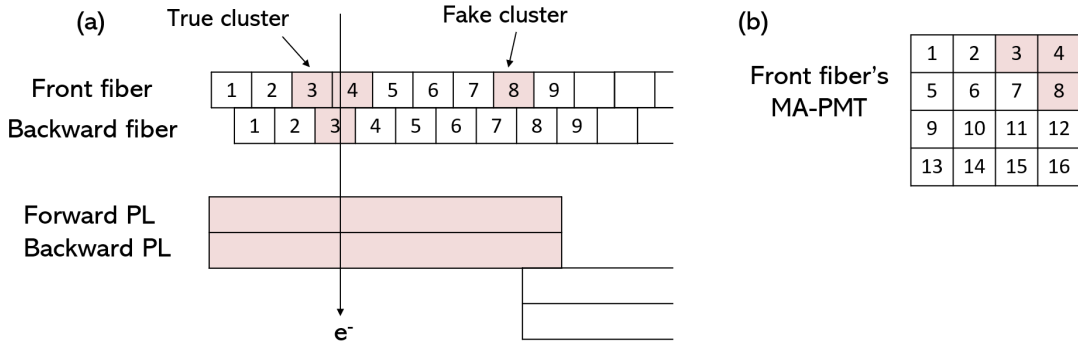


Figure 3.1: (a) A schematic drawing of the tagger and an example of an electron track. (b) A schematic drawing of the MA-PMT of the front fiber. Indicated numbers are fiber numbers. Fired channels are shown with red color. Channel 8 is fired with a cross talk from channel 4.

### 3.1.2 Photon energy determination

A schematic drawing of the recoil electron tracks and the tagger is shown in Fig.3.2. There is a direct relation between the energy of recoil electron  $E_{e'}$  and the  $X$  position of fiber clusters of the electron track. The energy of photon beam  $E_\gamma$  is described as  $E_\gamma = E_e - E_{e'}$ , where  $E_e = 7.975$  GeV is the energy of electrons in the SPring-8 storage ring. Therefore, there is a direct relation between  $E_\gamma$  and the fiber cluster  $X$  hit position. We evaluated  $E_\gamma$  as a function of mean fiber number of the front ( $x_f$ ) and back fiber ( $x_b$ ) clusters, respectively. We used the  $\gamma p \rightarrow 2\pi^0 p$ ,  $\gamma p \rightarrow \pi^0 p$  and  $\gamma p \rightarrow \eta p$  reactions with the liquid hydrogen target data. The details of the evaluation of photon energy function are described in Appendix C. We evaluated the function for front ( $E_{\gamma_f}$ ) and backward ( $E_{\gamma_b}$ ) fiber layer, respectively as

$$E_{\gamma_f} = 1250.7 + 34.912 \times x_f - 0.27172 \times x_f^2 + 5.4498 \times 10^{-3} \times x_f^3 - 7.7346 \times 10^{-5} \times x_f^4 \text{ [MeV]} \quad (3.1)$$

$$E_{\gamma_b} = 1266.0 + 34.486 \times x_b - 0.25291 \times x_b^2 + 4.9325 \times 10^{-3} \times x_b^3 - 7.2442 \times 10^{-5} \times x_b^4 \text{ [MeV]} \quad (3.2)$$

Here,  $x_f$  and  $x_b$  are the mean fiber number of the front and back fiber clusters, respectively. When a track contained both of forward and backward layer clusters, the photon beam energy  $E_\gamma$  was obtained as

$$E_\gamma = (E_{\gamma_f} + E_{\gamma_b})/2. \quad (3.3)$$

Otherwise,  $E_\gamma$  was obtained as

$$E_\gamma = E_{\gamma_f} \quad \text{or} \quad E_\gamma = E_{\gamma_b}. \quad (3.4)$$

The photon energy function evaluated from different reactions were consistent. The photon energy resolution was  $12.0 \pm 0.7$  MeV (see Appendix C).

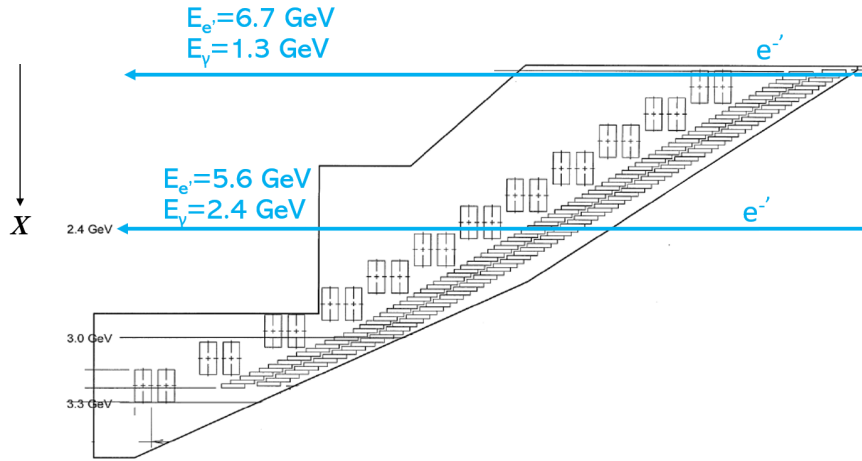


Figure 3.2: A schematic drawing of recoil electron tracks and the tagger.

## 3.2 Reaction timing reference

The timing of the RF signal of the SPring-8 storage ring was used as a reference of the reaction timing. The timing of the RF signal is synchronized with the timing of backward Compton scattering, and thus it is also synchronized with the reaction timing at the target. Because the RF signal was prescaled to  $1/84$ , the RF signal timing was recorded with an ambiguity of  $1.966 \times n$  nsec, where  $1.966$  ns is the electron bunch interval in the SPring-8 storage ring, and  $n = 0$  to  $83$ . We derived  $n$  from the time difference the tagger PL hit and the prescaled RF signal. The distribution of the time difference  $T_{Tag} - T_{RF}$  is shown in Fig.3.3(a).  $1.966 \times n$  nsec was subtracted from the prescaled RF timing, when the RF signal is used for the reference timing of all detectors, the tagger, UpVeto, BGOegg, IPS,

DC and RPC. The distribution  $T_{Tag} - T_{RF}$  after subtraction of  $1.966 \times n$  nsec is shown in Fig.3.3(b). The misidentification probability of  $n$  was 1%. It was taken into account to the tagger reconstruction efficiency (see Appendix F.2.1).

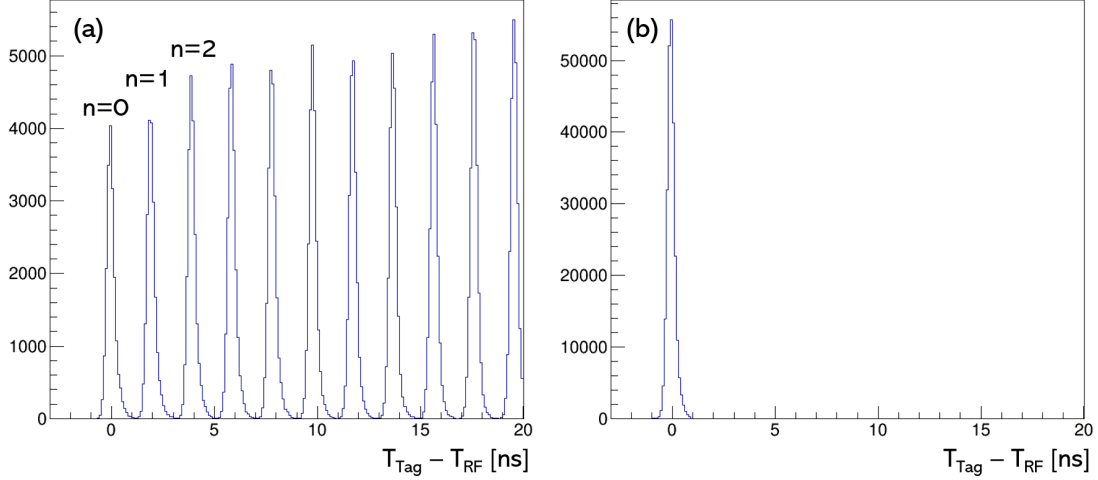


Figure 3.3: The time difference between the tagger PL hit and the RF signal. (a) The raw prescaled RF signal. (b) After subtraction of  $1.966 \times n$  nsec.

### 3.3 Measurement of decay products

The energy and emission angle of  $\eta$ ,  $\eta'$  and  $p_s$  were measured with BGOegg. We measured  $\gamma$ 's from the  $\eta \rightarrow 2\gamma$  and  $\eta' \rightarrow 2\gamma$  decay modes. We describe clustering algorithm of the BGOegg crystals in this section.

#### 3.3.1 BGOegg clustering

When BGOegg crystals have hits, they were clustered as follows. A schematic drawing of the clustering algorithm is shown in Fig.3.4.

- A clustering is carried out when a crystal has a TDC hit (blue crystals).
- The eight neighboring crystals around the hit crystal are included to the cluster (green crystals).
- If one of the eight neighboring crystal has a TDC hit, eight crystals around the hit-crystal are included to the cluster (cluster A in Fig.3.4).

Cluster information is defined as follows.

- Core crystal : the crystal which has the largest energy in a cluster.
- Hit timing : the hit timing of the core crystal.
- Energy : the summation of the energy deposit in all crystals in the cluster.
- Hit position : the weighted average of all crystal positions in the cluster with the weight of energy deposit in each crystal.

The emission angle was determined from the cluster hit position assuming that the particle is from the center of the target. When a crystal belonged to  $n$  clusters like an example in Fig.3.4 ( $n = 2$ ),  $1/n$  of the energy of the crystal was used when we added up the crystal

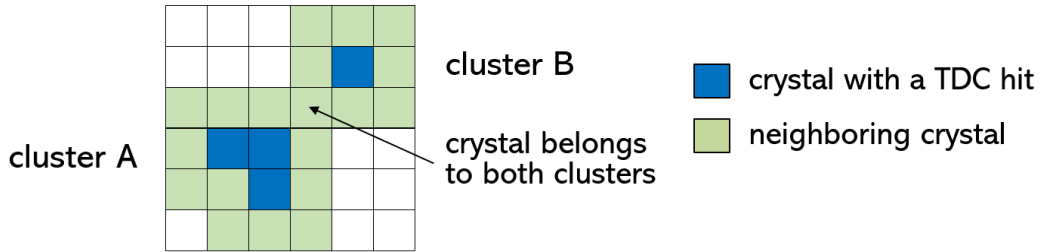


Figure 3.4: A schematic drawing of the BGOegg clustering.

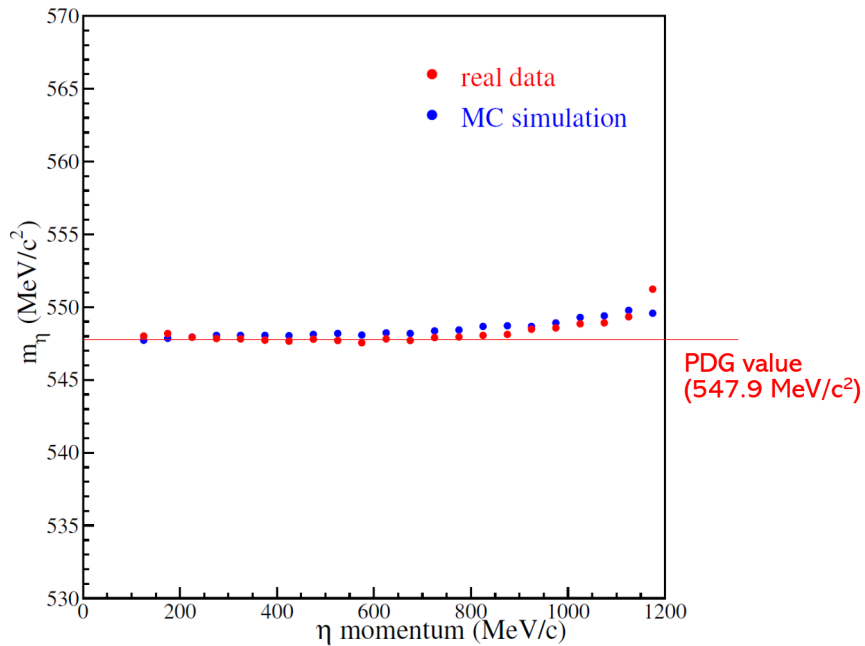


Figure 3.5: The  $\eta$  mass peak position as a function of  $\eta$  momentum.

energy to obtain the cluster energy. The hit timings were calibrated so that the hit timing of  $\gamma$  rays relative to the RF signal,  $T_\gamma - T_{RF}$ , to be 0 ns. The energy was calibrated every about 10 runs so that the invariant mass of  $\eta$  mesons to be the PDG value. The  $\eta$  peak position as a function of  $\eta$  momentum is shown in Fig.3.5. Events in which a core crystal of a cluster is in the first (layer 1) or last layer (layer 22) of BGOegg are excluded from the analysis. In such events, there can be energy leak to out side of BGOegg and the energy of detected particles can not be correctly measured. The polar angle coverage of BGOegg after removing most outer layers is  $29.5\text{--}138.5^\circ$ .

The photon energy resolution of BGOegg crystal measured with positron beam at  $19\text{ C}^\circ$  was

$$(\sigma_E/E)^2 = (0.63\%)^2 + ((1.15 \pm 0.04)\%)/(E/\text{GeV}) + ((0.42 \pm 0.03)\%)/(E/\text{GeV})^2, \quad (3.5)$$

i.e,  $(1.38 \pm 0.05)\%$  for 1-GeV positrons. The position resolution is

$$\sigma_r/mm = (3.07 \pm 0.03)(E/\text{GeV})^{-0.202 \pm 0.008} \quad (3.6)$$

for 1-GeV positrons. We can measure photons from  $\eta$  and  $\eta'$  in any energy.

### 3.3.2 Leak cluster

Cluster A and B in Fig.3.4 are counted as different clusters even if they are induced from one gamma ray. We call such an associated cluster as a “leak cluster”. Leak clusters have small energy and slow hit timing. Figure 3.6 shows cluster energy vs timing, and distance

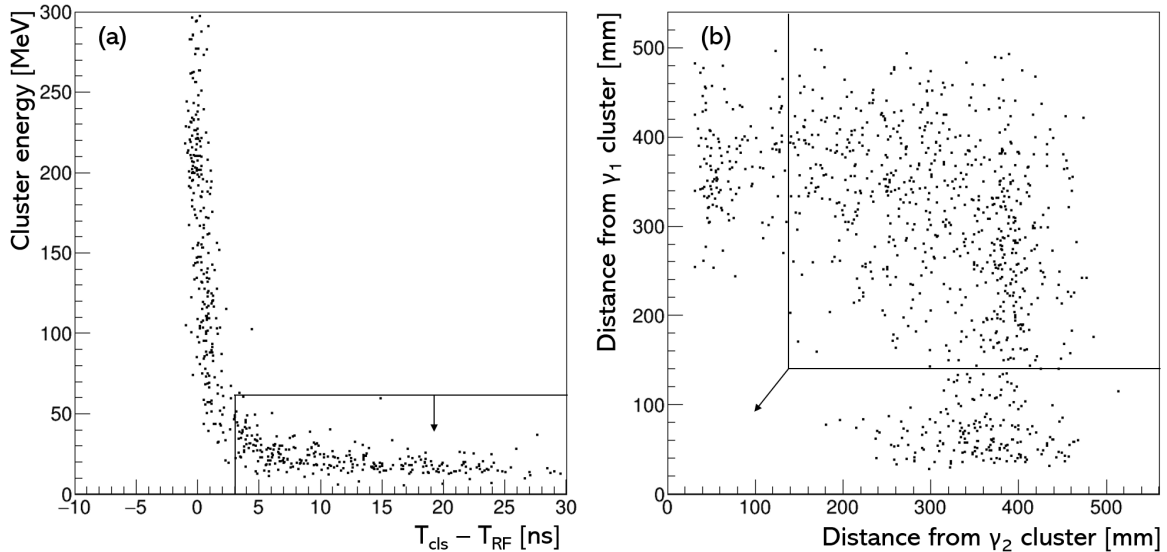


Figure 3.6: Distributions of candidates of leak clusters of the  $\gamma + {}^{12}\text{C} \rightarrow p_f + (\eta + p_s) + X$  data. (a) Cluster energy vs hit timing, (b) distances from gamma clusters.

from gamma clusters of candidates of leak clusters. A cluster is assumed as a leak cluster when the following conditions are satisfied.

- Cluster energy is less than 60 MeV.
- Cluster hit timing relative to the RF signal,  $T_{cls} - T_{RF} > 3$  ns.
- There is a gamma cluster in the distance less than 140 mm.

The cut criteria are shown in Fig.3.6. Leak clusters were excluded when we count the number of clusters. We found that 11.0% of the  $\gamma + {}^{12}\text{C} \rightarrow p_f + (\eta + p_s) + \text{X}$  data have (a) leak cluster(s).

### 3.3.3 Photon energy and polar angle resolution

Although the energy and position resolutions of BGOegg crystal are describes as in Eqs.(3.5) and (3.6), the actual experimental resolutions were worse than Eqs.(3.5) and (3.6) because there is uncertainty of the reaction vertex position. The actual photon energy and polar angle resolutions were estimated using a Monte Carlo simulation, implementing a realistic vertex distribution. The energy and polar angle resolutions are in the range of 5–35 MeV and 1–3°, respectively, which depends on the BGOegg cluster energy and hit layer. As an example, the resolutions of layer 14 are shown in Fig.3.7. The kinetic energy and polar angle resolutions of  $\eta$  meson are quadratic sum of each photon resolution.

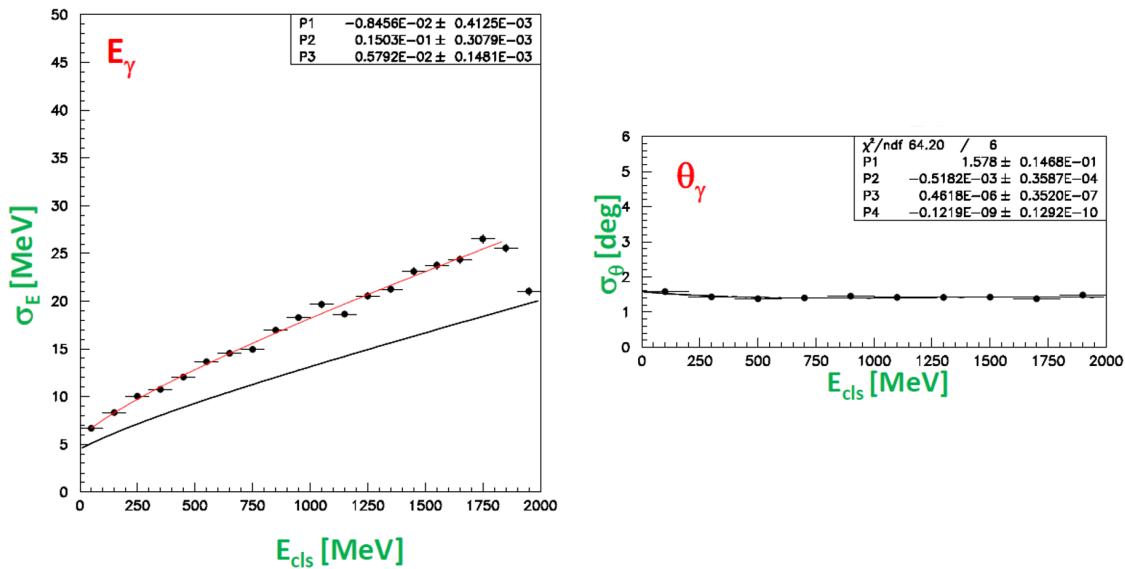


Figure 3.7: The photon energy and polar angle resolutions of the BGOegg layer 14. The black line in the left figure is the resolution when the vertex position is known.

### 3.3.4 Proton kinetic energy and polar angle resolution

The proton kinetic energy was evaluated from the cluster energy. Because there are energy losses in the target and the IPS, the cluster energy is not equal to the proton kinetic energy. The relation between proton kinetic energy and cluster energy were evaluated using the  $\gamma p \rightarrow \eta p$  reactions with the liquid hydrogen target. We carried out kinematical fitting assuming that proton energy is an unmeasured variable. The calculated predicted proton kinetic energy every cluster energy of 50 MeV as shown in Fig.3.8(a). We fitted the black points with a cubic function and obtained the following relation:

$$T_p = 33.704 + 0.75332 \times \text{eCls} + 8.6131 \times 10^{-4} \times \text{eCls}^2 - 1.1902 \times 10^{-6} \times \text{eCls}^3 [\text{MeV}], \quad (3.7)$$

where eCls is the cluster energy of a proton. The proton kinetic energy resolution is shown in Fig.3.8(b) as a function of the cluster energy. Side-going protons with kinetic energy greater than 450 MeV penetrate BGOegg and do not deposit all the energy in BGOegg. Thus, above functions are valid up to 450 MeV. We note that the maximum proton kinetic energy from the  $\eta' N \rightarrow \eta N$  reaction is 250 MeV. The polar angle resolution of proton was estimated in the similar way as photon. The angler resolution for layer 14 is shown in Fig.3.9. The polar angle resolution is in the range of 2–4°, depending on the proton energy and polar angle.

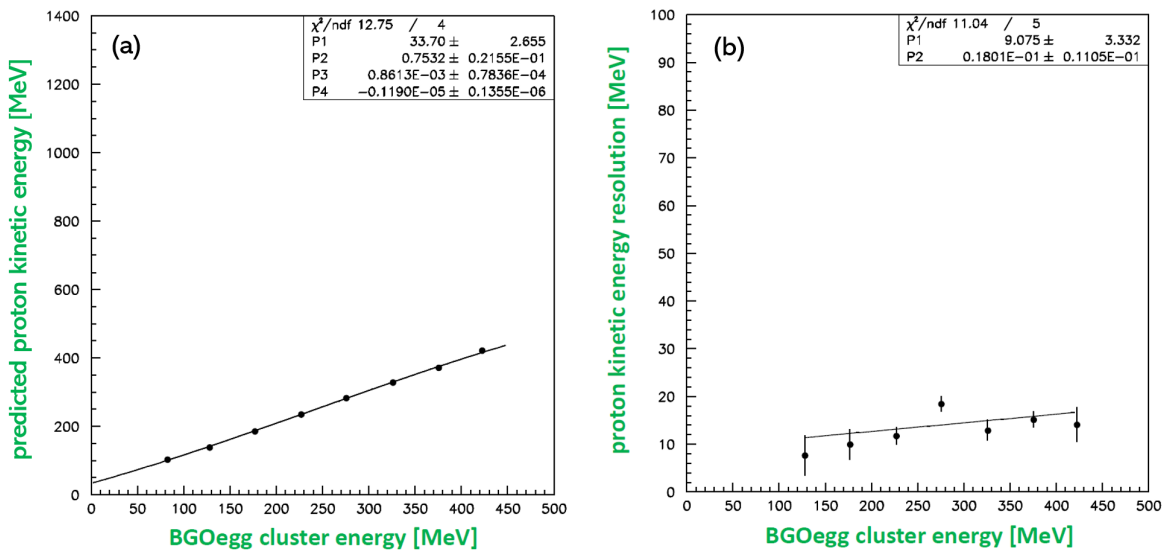


Figure 3.8: (a) The relation between the predicted proton kinetic energy and the BGOegg cluster energy of the  $\gamma p \rightarrow \eta p$  reaction. (b) The proton kinetic energy resolution as a function of the BGOegg cluster energy.

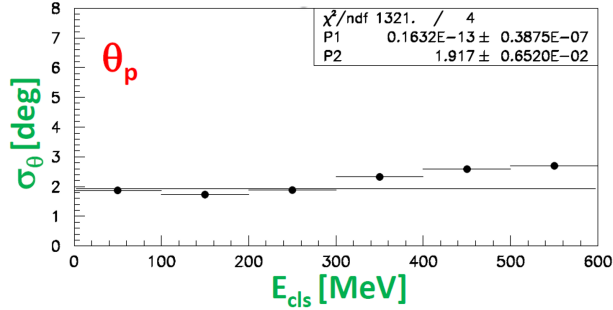


Figure 3.9: The proton polar angle resolution of the BGOegg layer 14 estimated using a MC simulation.

## 3.4 Charge identification of decay products

The charge identification of particles creating BGOegg clusters were carried out using the IPS. In addition, side-going protons were identified from the correlation of the energy deposit in the IPS and the BGOegg cluster energy. The particle identification of protons are described in section 4.4.3. In this section, we describe the calibration method of the energy deposit and hit timing of the IPS, and the criteria of the charge identification.

### 3.4.1 IPS energy deposit and hit timing correction

Energy deposit in the IPS depends on the hit position because the IPS thickness which a particle pass depends on its polar angle. In addition, the IPS signal timing depends on the hit position because signals from scintillators are read at a single end. Thereby, energy deposit and hit timing of the IPS are corrected event by event depending on the emission polar angle of measured with BGOegg. The energy deposit in the IPS is corrected to be 1.0 in all the polar angle region when the corresponding BGOegg cluster energy is in a certain region: 185–245 MeV. The signal timing is also corrected so that the hit timing of the IPS relative to the RF signal,  $T_{IPS} - T_{RF}$ , for the events of this energy region to be 0 ns in all the polar angle region.

### 3.4.2 Charge identification

When there is a cluster in BGOegg, we investigate IPSs in front of the core crystal. A cluster is identified as “charged cluster” created from a charged particle when the energy deposit in the IPS is greater than 0.8 in the calibrated unit. The cut criteria were determined using the  $\gamma p \rightarrow \pi^0 p$  reaction with liquid hydrogen target, in which both the proton and two gammas from the  $\pi^0$  were detected with BGOegg. The energy deposit in the IPS of clusters of protons and gammas is shown in Fig.3.10. There are events that a gamma converted to  $e^+e^-$  in an IPS and created an IPS hit. By requiring some energy deposit in the IPS, we could reduce

the charge misidentification rate of gamma clusters. If the energy deposit in the IPS is less than 0.8, the cluster was identified as a “neutral cluster” created from a neutral particle. The charge misidentification rate of protons and gammas were  $(1.4 \pm 0.1)\%$  and  $(5.5 \pm 1.4)\%$ , respectively. They were taken into account to the acceptance.

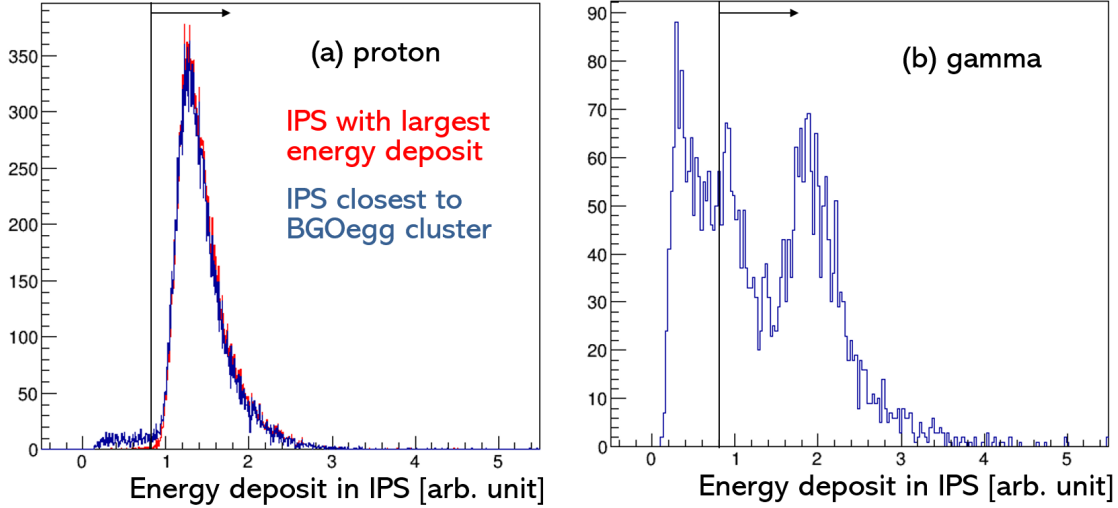


Figure 3.10: The energy deposit distribution in the IPS of protons and gammas of the  $\gamma p \rightarrow \pi^0 p$  data.

### 3.5 Forward going-particle detection

We used the DC to ensure that there is only forward-going proton,  $p_f$ , in the forward region in the polar angle less than  $25^\circ$ , which is not covered by BGOegg. We also required that the track of  $p_f$  measured with the DC and the  $p_f$  hit position at the RPC is consistent. The  $t_0$  and  $xt$  calibrations were carried out every cycle of the SPring-8 storage ring (about every 100 runs). The DC tracking was carried out with the following conditions:

- Carry out the tracking assuming that a track starts from the center of the target.
- Carry out the tracking for all the combination of hit wires.
- The left-right ambiguity is solved by selecting the larger chi-square side.
- When there are more than one track which use a common wire, select the track which has the largest chi-square probability.
- Count as different tracks when there is no common wire used for the tracking.

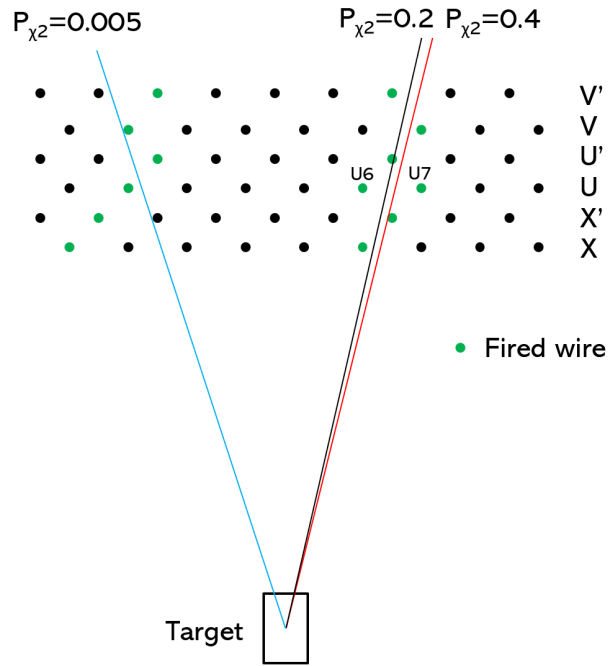


Figure 3.11: A schematic drawing of the DC tracking of a mock data. Green points show fired wires. Blue, black and red lines show the tracking results. The chi-square probability of each track is shown with  $P_{\chi^2}$ .

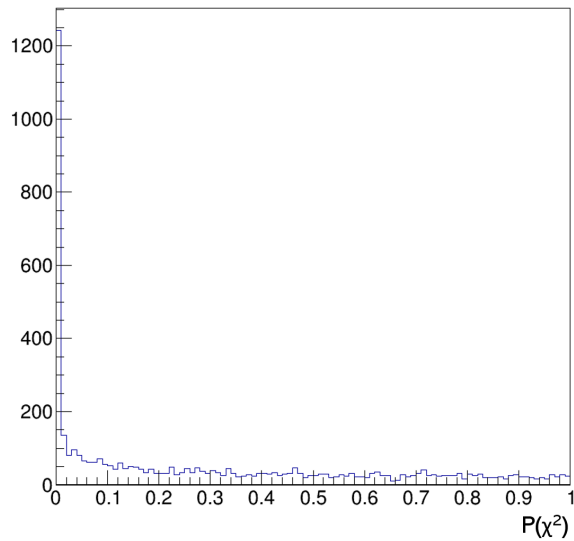


Figure 3.12: The chi-square probability distribution of the DC tracks of  $p_f$  in the  $\gamma + {}^{12}\text{C} \rightarrow p_f + (\eta + p_s) + X$  data.

- Count as a track only when the chi-square probability of the track is greater than 0.01.

In Fig.3.11, a schematic drawing of the tracking method of a mock data is shown. The fired wires are shown with green color. There are two clusters of hit wires. In the right cluster, two wires had a hit in the U plane. The black line is the tracking using the U6 wire and the red one is the U7 wire. We choose the red tracking because its chi-square probability is larger. The particle created the left cluster was not from the target but the tracking is carried out assuming that it is from the target. Thus, the chi-square probability of the blue track is small. We exclude the blue track when we count the number of tracks because its chi-square probability is less than 0.01. In summary, the number of tracks of the mock data is one, and we use the red track for the analysis. The chi-square probability distribution of the DC tracks of  $p_f$  without the chi-square probability cut of the  $\gamma + {}^{12}\text{C} \rightarrow p_f + (\eta + p_s) + X$  data is shown in Fig.3.12. The position resolution of the DC is  $\sigma = 290 - 330 \mu\text{m}$ , depending on the layer. The reconstruction efficiency of tracks with DC is  $(98.2 \pm 0.4)\%$  (see Appendix F.2.3).

## 3.6 Forward-going proton momentum measurement

The momentum of  $p_f$ , used for the missing mass analysis, was measured from the time-of-flight (TOF) from the target to the RPC. In this section, the algorithm to select hit readout strip and the measurement of the particle energy are described.

### 3.6.1 Hit strip selection

As described in section 2.4, we added RPC signals from two neighboring strips for the ADC measurement and two strips from neighbor chambers for the TDC measurement. In addition, there were cross-talks in neighboring strips of a hit strip. Thereby, we constructed an algorithm to select the hit strip. In Fig.3.13, a mock data sample for the strip selection is shown. The hit strip is strip 3 of the chamber 1A. The strips sharing a read out channel are shown in the same color. The hit strip has larger charge and faster timing hit than cross-talk strips. We selected the hit strip when it satisfies the following condition.

	chamber 1A								chamber 1B							
strip	1	2	3	4	5	6	7	8	1	2	3	4	5	6	7	8
charge [pC]	140	140	620	140	140	140	80	80	-30	-30	40	40	-70	-70	10	10
timing [ns]	1.4	0.5	0.3	0.5	1.2	5.0	---	---	1.4	0.5	0.3	0.5	1.2	5.0	---	---

Figure 3.13: A mock data for the hit strip selection of the RPC. The hit strip is strip 3 of chamber 1A.

1. The pair-strips have the largest charge among the 16 strips in the neighboring two chambers.
2. There are TDC hits in all the readout of the pair strips.
3. Faster hit timing than the other pair-strip.

In Fig.3.13, we show one example value for each strip. In the real analysis, data of both the top-end and bottom-end of the strip was used. As described in section 2.3.6, the top-row RPC and bottom-row RPC overlap 70–80 mm. When two strips have hits in the overlapped area in a close timing, the two hits were assumed to be a single hit and the hit timing of the top-row RPC, which located upstream, was used for the analysis. The reconstruction efficiency of the RPC hit was  $(95.9 \pm 2.3)\%$  (see Appendix F.2.4).

### 3.6.2 Timing calibration

We carried out the timing calibration so that the hit timing of the RPC relative to the RF signal,  $T_{RPC} - T_{RF}$ , of the  $e^+e^-$  events to be 0 ns. The velocity of fast  $e^+e^-$  is very close to the speed of light. The time-walk distribution depends on the  $Y$  hit position. Thus, slewing corrections were carried out depending on  $Y$ . The resulting time resolution of TOF measurement was 60 – 90 ps, which also depends on the hit position of the  $Y$  direction of the readout strip [52].

### 3.6.3 Evaluation of forward proton momentum

We evaluated the momentum of  $p_f$  from the TOF and flight length calculated from the RPC hit position. The velocity of  $\beta$  of the forward-going particle was obtained as

$$\beta = \frac{v}{c} = \frac{L}{\left(\frac{L}{c} + T_{RPC} - T_{RF}\right)c}, \quad (3.8)$$

where  $c$  is the speed of light and  $L$  is the flight length.  $\frac{L}{c}$  is the time of flight from the target to the RPC at the speed of light. We obtained the hit position in  $X$  direction from the position of the hit strip. Thus, the position resolution of  $X$  direction was  $26/\sqrt{12} = 7.5$  mm. We evaluated the hit position in  $Y$  direction from the timing difference of signals from top-end and bottom-end of a strip. The position resolution of  $Y$  direction was 16 mm.  $L$  is obtained as  $L = \sqrt{X^2 + Y^2 + Z^2}$ , where  $Z$  is defined chamber by chamber, which is described in section 2.3.6. The momentum of particle was obtained assuming that the particle is a proton with a mass of  $m_p = 938.27$  MeV as

$$p = m_p \beta \gamma \times c_{loss}, \quad (3.9)$$

$$\gamma = \frac{1}{\sqrt{1 - \beta^2}}, \quad (3.10)$$

where,  $c_{loss}$  is the correction factor for the momentum loss in the target and air. We evaluated  $c_{loss}$  by calculating the energy deposit in each material with 1 mm step for a straight track

from the target to the RPC. A two-dimensional plot of the momentum distribution of  $p_f$  and the photon beam energy of the  $\gamma + {}^{12}\text{C} \rightarrow p_f + (\eta + p_s) + X$  data is shown in Fig.3.14. Above the red line, proton momenta exceed the photon beam energy and thus the events there are unphysical. The events above the red lines are mostly pions. They are contaminated since particle identification of forward-going particles was not performed. They were excluded in the event selection described in section 4.6.3. The energy resolution varies from a few MeV to  $\sim 30$  MeV depending on the momentum of  $p_f$ . The energy resolution of  $p_f$  in the  $\gamma p \rightarrow \eta' p$  reaction is shown in Fig.3.15 as a function of the photon beam energy.

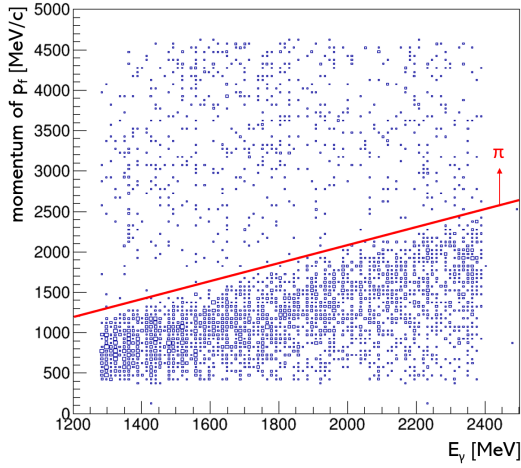


Figure 3.14: The momentum distribution of  $p_f$  vs photon beam energy of the  $\gamma + {}^{12}\text{C} \rightarrow p_f + (\eta + p_s) + X$  data. The unphysical events above the red line are pions.

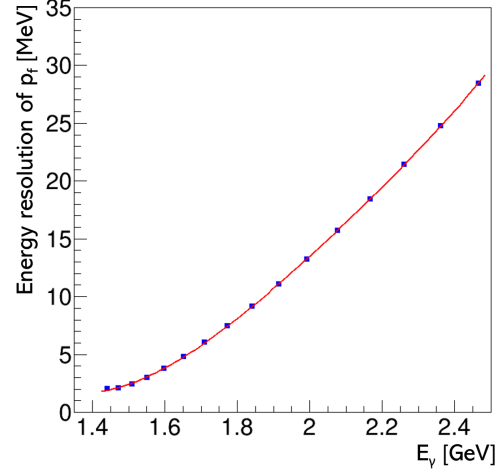


Figure 3.15: The energy resolution of  $p_f$  in the  $\gamma p \rightarrow \eta' p$  reaction as a function of the photon beam energy.

# Chapter 4

## Event selection

We searched for a signal of the  $\eta'$  bound states from the excitation energy spectra of  $^{12}\text{C}(\gamma, p)$  in the  $\gamma + ^{12}\text{C} \rightarrow p_f + (\eta + p_s) + \text{X}$  reaction. Here,  $p_f$  is a forward-going proton detected with the RPC and  $p_s$  is a proton detected with BGOegg. In addition, we measured the  $\gamma + ^{12}\text{C} \rightarrow p_f + \eta' + \text{X}$  reaction to evaluate the production rate of  $\eta'$ . In this chapter, the details of the events selection of above two reactions are described.

### 4.1 Outline of the event selection

Most of event selection criteria are common for the measurements of the  $\gamma + ^{12}\text{C} \rightarrow p_f + (\eta + p_s) + \text{X}$  and  $\gamma + ^{12}\text{C} \rightarrow p_f + \eta' + \text{X}$  reactions. We measured the photon beam energy with the tagger by measuring the position of recoil electron tracks. We required a single recoil electron track from an electron bunch in the tagger. Events having multi-tracks in the tagger were excluded from the analysis because we can not discriminate the beam photon which invoked the reactions above. We required that there is no hit in the UpVeto to exclude events in which a photon beam was converted to  $e^+e^-$  when it was transmitted to the experimental hall. We measured the momentum of  $p_f$  with the time-of-flight (TOF) by assuming the particle is a proton. The start timing of TOF was determined with the RF signal and the flight time was measured with the RPC. We did not carry out the particle-identification of forward-going particles. Most of forward-going pion events give extremely large energy which does not conserve the total energy when the energy is calculated assuming a proton mass. Such events were excluded with the missing energy cut and the pion contamination to the signal region of the excitation energy spectrum is small (see section 6.1.7). We used matching hit positions of  $p_f$  at the DC and RPC. Only the selection criteria of BGOegg and the IPS are different for the  $(\eta + p_s)$  and  $\eta'$  tag analyses. We required that two photons and one proton were detected at BGOegg for the  $(\eta + p_s)$  tag data, and only two photons were detected at BGOegg for the  $\eta'$  tag data. The  $\eta$  and  $\eta'$  mesons were identified from their two gamma invariant mass. The side-going  $p_s$  was identified with the energy deposit and the hit timing in the IPS and BGOegg. In order to suppress events with (an) additional particle(s), we required that there is no other hit in BGOegg, and only a single hit was observed at the

DC and RPC. In summary, we required the following conditions.

- (1) Single recoil electron track in the tagger.
  - (2) No charged particle detected with the UpVeto.
  - (3) Single track at the DC.
  - (4) Single fired strip on the RPC.
  - (5) Matching hit positions at the DC and RPC.
- (6-1) An  $\eta$  meson and one proton are observed at BGOegg ( $(\eta + p_s)$  analysis).
- (6-2) An  $\eta'$  meson are observed at BGOegg ( $\eta'$  analysis).

For the  $\gamma + {}^{12}\text{C} \rightarrow p_f + (\eta + p_s) + \text{X}$  analysis, we required that the events satisfies (1)–(5) and (6-1). For the  $\gamma + {}^{12}\text{C} \rightarrow p_f + \eta' + \text{X}$  analysis, we required that the events satisfies (1)–(5) and (6-2). Details of the event selection of each detector are described in the following sections.

## 4.2 Recoil electron track

To select the certain tagger track corresponding to the beam photon which had the reaction in the target, events satisfying one of the following conditions we used for the analysis.

- The number of reconstructed tracks.
- The number of tracks is one after requiring the time difference between the average timing of PL hits and the average timing of first and second fastest neutral BGOegg clusters is within  $\pm 1.0$  ns.

When the fiber cluster size is large, we cannot measure the photon beam energy correctly. Thereby, the following conditions were also required.

- If there are fiber clusters in both fiber layers, the number of fibers in both clusters is less than 4.
- If there is only a single cluster in one of the fiber layers, the number of fibers in the cluster is less than 3.

The photon energy resolution with above conditions is  $12.0 \pm 0.7$  MeV (see Appendix C). The tagger reconstruction efficiency was  $(89.9 \pm 0.8)\%$  with the above conditions (see Appendix F.2.1).

### 4.3 In-beam $e^+e^-$ veto

Events in which a photon beam converts to an  $e^+e^-$  pair when the beam is transported to the LEPS2 experimental building were excluded by using the UpVeto. The cut criteria were determined from the single bunch events of the H-mode filling pattern. (See Appendix A for the detail of the filling pattern.) Events were selected by using the 1/2436 prescaled RF signal. The single bunch locates 1487 nsec away from other electron bunches. Thereby, there is no event contamination from events in neighboring electron bunches. Figure 4.1(a) shows the signal timing of the UpVeto relative to the RF signal,  $T_{UpVeto} - T_{RF}$ .  $T_{UpVeto} - T_{RF}$ , is expressed in an unit of  $\sigma$  and  $1\sigma$  varies 1.0–1.5 ns depending on run. Two-dimensional plot of  $T_{UpVeto} - T_{RF}$  and the energy deposit in the UpVeto is shown in Fig.4.1(b). The events at around  $T_{UpVeto} - T_{RF} = 0\sigma$  are  $e^+e^-$  pairs from the beam conversion. There is a slow component after the main peak. It is considered to be scattered charged particles from the target to backward. Because we require that there is no produced particles other than the  $p_f + (\eta + p_s)$  or  $p_f + \eta'$ , we excluded events which have the slow hit at the UpVeto. In addition, there is TDC dead time of  $\sim 20$  ns. Thereby, the following conditions were required for the UpVeto.

- No TDC hit in  $|T_{UpVeto} - T_{RF}| < 30\sigma$ .
- Charge deposit smaller than the one of minimum ionization particle.

The selected are are shown with green square in Fig.4.1(b).

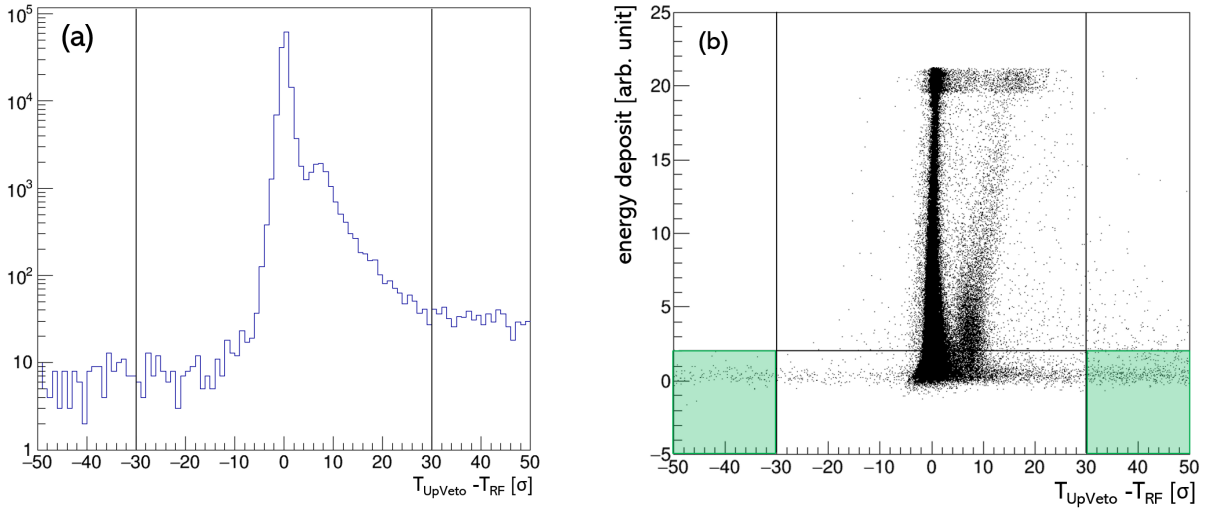


Figure 4.1: (a)  $T_{UpVeto} - T_{RF}$  distribution (b)  $T_{UpVeto} - T_{RF}$  vs energy deposit distribution of the single bunch events. The events in the green area were used for the analysis.

## 4.4 Decay particle identification

The  $(\eta + p_s)$  pair in the  $\gamma + {}^{12}\text{C} \rightarrow p_f + (\eta + p_s) + \text{X}$  reaction and the  $\eta'$  meson in the  $\gamma + {}^{12}\text{C} \rightarrow p_f + \eta' + \text{X}$  reaction were measured at BGOegg and the IPS. We identified  $\eta$  and  $\eta'$  mesons from the invariant mass of two gammas. The gammas were identified from the IPS charge identification and the cluster hit timing.  $p_s$  was identified from the energy deposit in the IPS and BGOegg, and the hit timing of the IPS and BGOegg. We describe details of particle identification of decay products in this section.

### 4.4.1 Identification of gammas

For selecting gamma, neutral clusters identified with the IPS as described 3.4.2 were selected. Neutral clusters are from gammas or neutrons. Neutron takes larger time-of-flight from the target to BGOegg. Thus, we selected gammas by selecting fast timing events as shown in Fig.4.2. Details of the timing selection criterial is described in Appendix D.

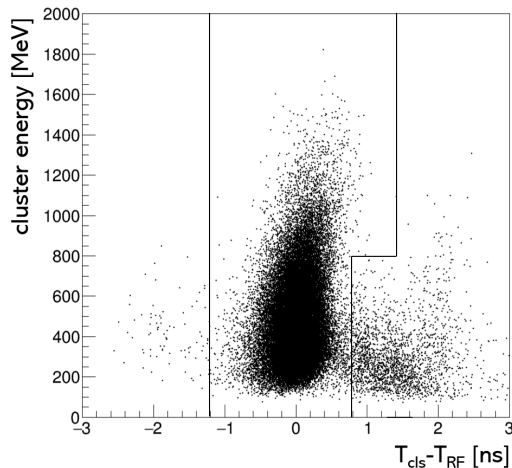


Figure 4.2: A scatter plot of the energy deposit and hit timing of neutral clusters in the (2 neutral + 1 charged + 1 RPC hit) data sample. The selection criteria are shown with black lines.

### 4.4.2 Identification of $\eta$ and $\eta'$ mesons

Figure 4.3 shows the two gamma invariant mass distributions around  $\eta$  and  $\eta'$  masses of the  $\gamma + {}^{12}\text{C} \rightarrow p_f + (\eta + p_s) + \text{X}$  and  $\gamma + {}^{12}\text{C} \rightarrow p_f + \eta' + \text{X}$  data sample, respectively. They are fitted with Gaussian+polynomial functions as shown in Fig.4.4. The peak positions of  $\eta$  and  $\eta'$  are  $(547.2 \pm 0.3) \text{ MeV}/c^2$  and  $(956.4 \pm 1.5) \text{ MeV}/c^2$ , respectively. The PDG values are  $m_\eta = 547.9 \text{ MeV}/c^2$  and  $m_{\eta'} = 957.8 \text{ MeV}/c^2$ . Thus, photon energy and polar angle are calibrated well within the invariant mass resolution of 1 MeV. Events with the invariant

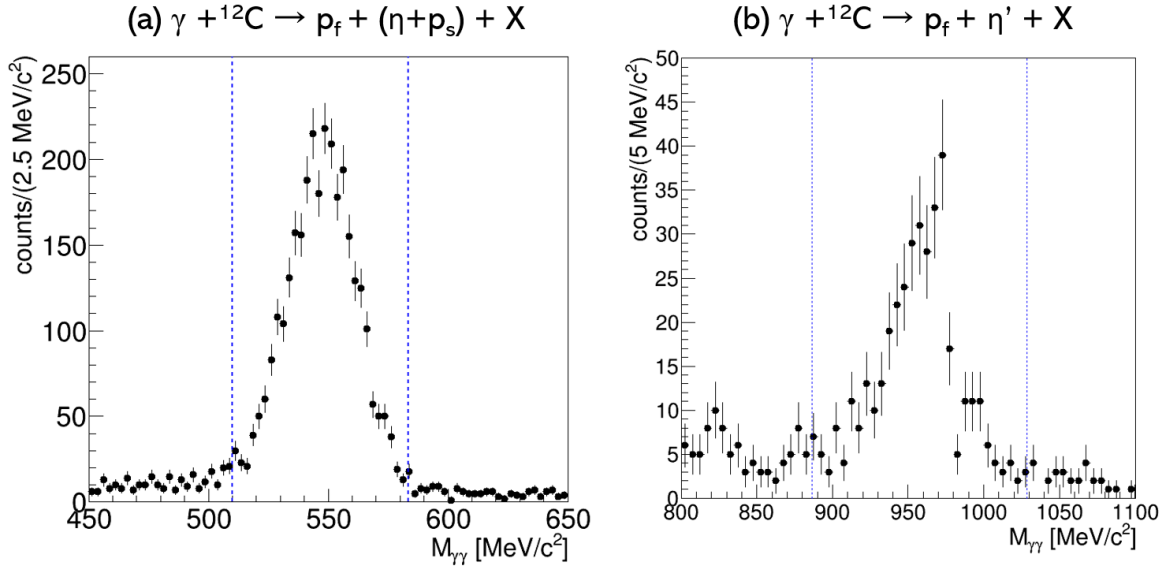


Figure 4.3: The two gamma invariant mass distributions of (a) the  $\gamma + ^{12}\text{C} \rightarrow p_f + (\eta + p_s) + X$  and (b) the  $\gamma + ^{12}\text{C} \rightarrow p_f + \eta' + X$  data sample. Missing energy cut which is explained in the section 4.6.3 is applied for the  $\gamma + ^{12}\text{C} \rightarrow p_f + \eta' + X$  data sample. The selection criteria are shown with blue-dashed lines.

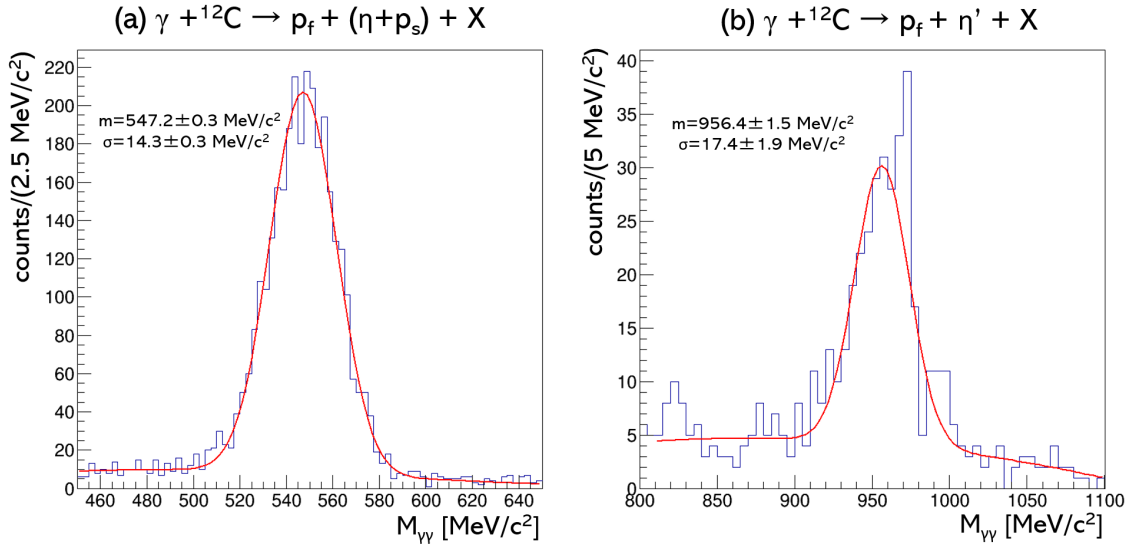


Figure 4.4: The two gamma invariant mass distributions of (a) the  $\gamma + ^{12}\text{C} \rightarrow p_f + (\eta + p_s) + X$  and (b) the  $\gamma + ^{12}\text{C} \rightarrow p_f + \eta' + X$  data sample, fitted with Gaussian+polynomial functions.

mass within  $\pm 2.5\sigma$  and  $\pm 4.0\sigma$  from the peak were selected, for the  $(\eta + p_s)$  and  $\eta'$  tag events, respectively. The selection criteria are shown with blue dashed lines in Fig.4.3.

### 4.4.3 Identification of side-going protons

Side-going protons,  $p_s$ , were identified from the energy deposit in the IPS and BGOegg, and the hit timing of the IPS and BGOegg. The details of the timing selection are described in Appendix D. In this section, the selection criteria with the energy deposit are described. Figure 4.5(a) shows a scatter plot of the energy deposit in the IPS and BGOegg of the charged cluster in the  $\gamma + {}^{12}\text{C} \rightarrow p_f + (\eta + p_s) + X$  data sample, before identifying side-protons. When more than one IPS have hits, we selected the IPS which has the largest energy deposit. We calculated expected energy deposit in the IPS in the case of a proton from the kinetic energy measured with BGOegg using a table of PSTAR by NIST [56]. Figure 4.5(b) shows a scatter plot of the difference of the energy deposit in the IPS and the expected energy deposit, and the BGOegg cluster energy. The region in which the difference is  $-3\sigma \sim +4\sigma$  were selected. Looser selection criteria were used for positive side because the IPS gain was unstable and peak shift up to  $+0.5\sigma$  was observed in some experimental periods. We carried out particle identification of charged particles only when the cluster energy is less than 250 MeV because the expected maximum energy deposit of  $p_s$  in the signal  $\eta' + p \rightarrow \eta + p_s$  reaction is less than 250 MeV. We discarded events in which the charged cluster energy is greater than 250 MeV in the further analysis.

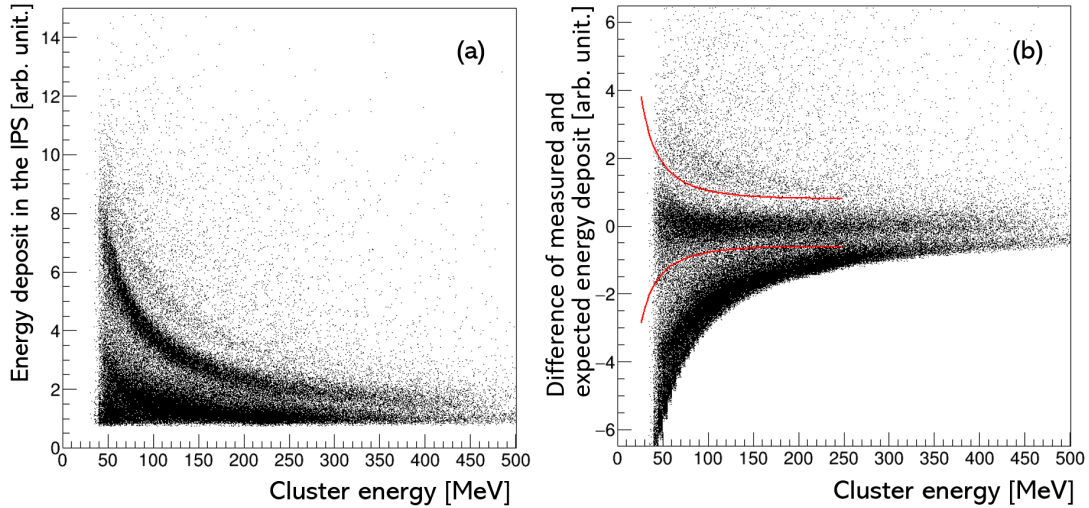


Figure 4.5: A scatter plot of the energy deposit in the IPS and BGOegg of the  $p_f + (\eta + 1$  charged particle) data sample. The selection criteria are shown with red lines.

## 4.5 Treatment of additional hit

We measured the  $\gamma + {}^{12}\text{C} \rightarrow p_f + (\eta + p_s) + X$  and  $\gamma + {}^{12}\text{C} \rightarrow p_f + \eta' + X$  reactions.  $(\eta + p_s)$  and  $\eta'$  were measured with BGOegg, and  $p_f$  was detected with the DC and RPC. In order to exclude events with (an) additional particle(s), events in which other particles were detected at BGOegg, the DC and RPC were excluded from the analysis. On the other hand, events in which the IPS has a hit without corresponding BGOegg cluster were accepted. Protons which have kinetic energy smaller than  $\sim 50$  MeV stop in the IPS and are not detected with BGOegg. Because the residual nucleus after emitting two protons ( $p_f$  and  $p_s$ ) is unstable, low energy protons can be emitted when the unstable nucleus decays. In the  $\gamma + {}^{12}\text{C} \rightarrow p_f + (\eta + p_s) + X$  data sample, 27% of events have (an) IPS hit(s) without a BGOegg cluster. We accepted those events with such very low energy activity.

## 4.6 Forward-going particle selection

Because we do not perform particle identification of forward-going particles, there are contamination of  $e^+e^-$  and pions to forward-going  $p_f$ . To remove  $e^+e^-$  and pions, we applied several cuts. We also required the matching hit positions of  $p_f$  at the DC and RPC.

### 4.6.1 Clean track selection

To ensure that  $p_f$  comes straight from the target, we required that the expected hit position of the RPC from the DC tracking and the actual particle hit position at the RPC are consistent. The selection criteria are shown in Fig.4.6 together with the  $p_f + (\eta + p_s)$  data. The criteria was determined from the  $\gamma p \rightarrow \eta p_f$  data with the liquid hydrogen target after the event selection using a kinematical fitting, in which all events are in these criteria.

### 4.6.2 $e^+e^-$ event suppression

In the forward region near the beam axis, there are  $e^+e^-$  showers coming from the conversion of photon beam. Most of the  $e^+e^-$  can be removed by requiring the particle velocity  $\beta$  is less than 0.98. However,  $e^+e^-$  from different electron bunch of the SPring-8 storage ring cannot be excluded with the  $\beta$  cut. Because  $e^+e^-$  are concentrated around the beam axis, we excluded events in  $R_{RPC} < 200$  mm, where  $R_{RPC} = \sqrt{X_{RPC}^2 + Y_{RPC}^2}$ , and  $X_{RPC}$  and  $Y_{RPC}$  are the  $X$  and  $Y$  hit position measured with the RPC. We also excluded events in  $R_{RPC} > 1500$  mm, where the particle path is close to the wall of the solenoid magnet. The selected area is shown in Fig.4.7. After the  $R_{RPC}$  selection, the RPC coverage for  $p_f$  is  $0.9^\circ < \theta_{lab}^{p_f} < 6.8^\circ$ .

### 4.6.3 Energy conservation

Since we do not perform the particle identification of forward-going particles, the momentum of the forward-going proton  $p_f$  was calculated from TOF assuming the proton mass. In most cases, when the forward-going particle was a pion, the event gives extremely large momentum

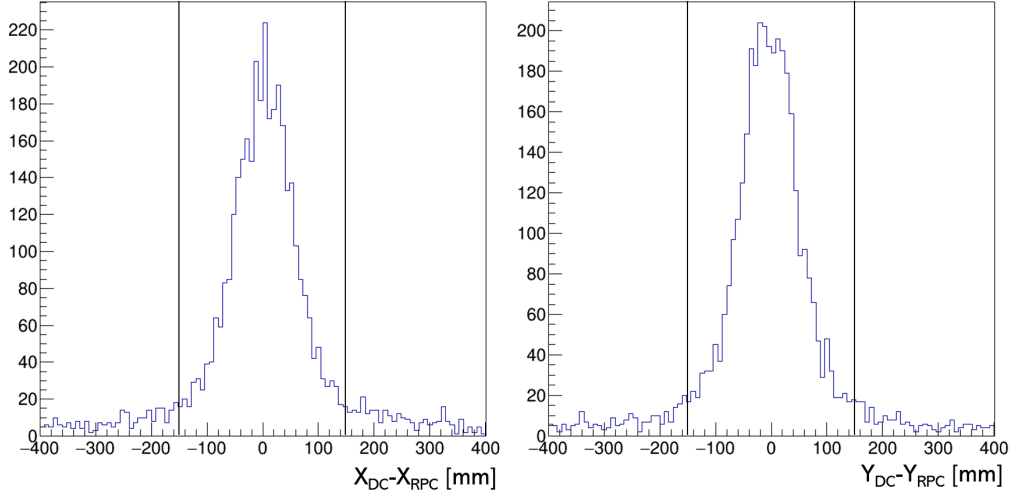


Figure 4.6: The difference of the expected and actual hit positions of  $p_f$  at the RPC for the  $p_f + (\eta + p_s)$  data. The selection criteria are shown with black lines.

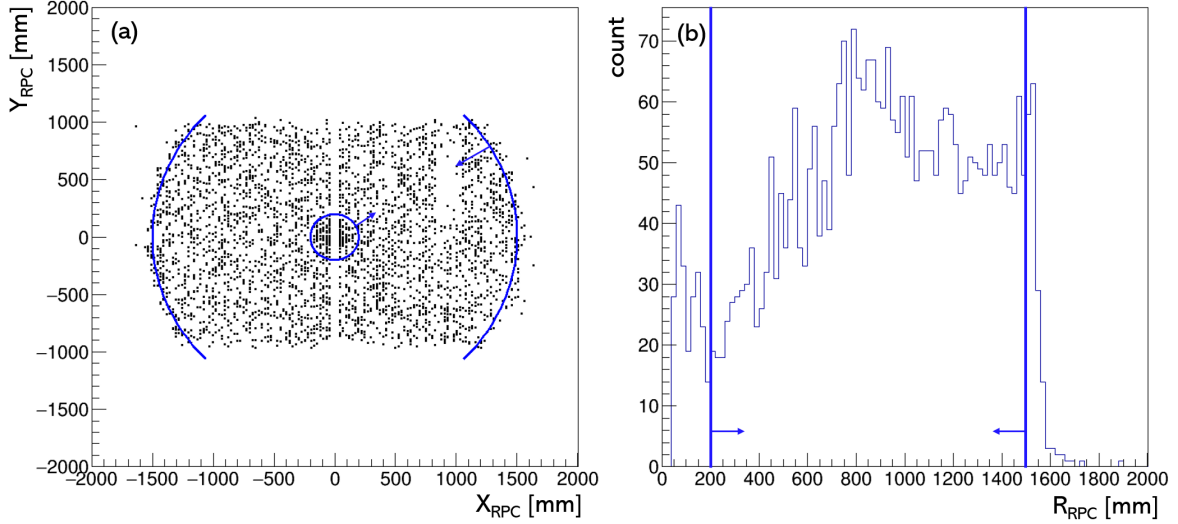


Figure 4.7: (a)  $X_{RPC}$  vs  $Y_{RPC}$  distribution (b)  $R_{RPC}$  distribution of the  $\gamma + {}^{12}\text{C} \rightarrow p_f + (\eta + p_s) + X$  data. The selection criteria  $R_{RPC} > 200$  mm and  $R_{RPC} < 1500$  mm are indicated with blue lines.

of  $p_f$  which breaks the energy conservation rule. To suppress pion events, we applied missing energy cut. The missing energy in the  $\gamma + {}^{12}\text{C} \rightarrow p_f + (\eta + p_s) + X$  reaction,  $E_{miss}^{\eta p_s p_f}$  is defined as

$$E_{miss}^{\eta p_s p_f} = E_\gamma + M_{12\text{C}} - M_{11\text{B}} - E_{\gamma_1} - E_{\gamma_2} - E_{p_s} - E_{p_f}. \quad (4.1)$$

The variables are defined as follows:

- $E_\gamma$  : the photon beam energy,
- $M_{12\text{C}}$  : the mass of a  $^{12}\text{C}$  nucleus,
- $M_{11\text{B}}$  : the mass of a  $^{11}\text{B}$  nucleus,
- $E_{\gamma_1}, E_{\gamma_2}$  : the neutral cluster energies,
- $E_{p_s}$  : the side proton kinetic energy + proton mass,
- $E_{p_f}$  : the forward proton total energy.

The distribution of  $E_{miss}^{\eta p_s p_f}$  of the  $\gamma + ^{12}\text{C} \rightarrow p_f + (\eta + p_s) + \text{X}$  data is shown in Fig.4.8. Negative missing energy indicates that the total energy after the interaction exceeds the initial energy, and thus they are unphysical events coming from that a pion was assumed as a proton. Because of Fermi motion, there are physical events down to  $E_{miss}^{\eta p_s p_f} = -150$  MeV. Therefore, events in  $E_{miss}^{\eta p_s p_f} < -150$  MeV were excluded to suppress pion events.

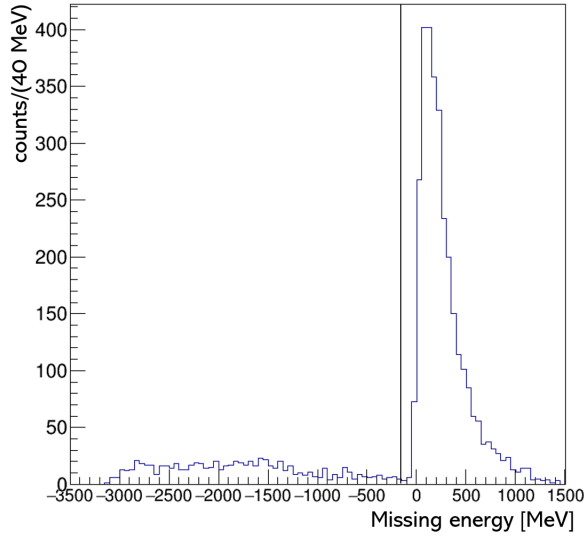


Figure 4.8: The missing energy  $E_{miss}^{\eta p_s p_f}$  distribution of the  $p_f + (\eta + p_s)$  data. The selection criterion is shown with a black line.

The missing energy in the  $\gamma + ^{12}\text{C} \rightarrow p_f + \eta' + \text{X}$  reaction,  $E_{miss}^{\eta' p_f}$  is defined as

$$E_{miss}^{\eta' p_f} = E_\gamma + M_{12\text{C}} - M_{11\text{B}} - E_{\gamma_1} - E_{\gamma_2} - E_{p_f}. \quad (4.2)$$

In addition to  $E_{miss}^{\eta' p_f} > -150$  MeV,  $E_{miss}^{\eta' p_f} < 150$  MeV is required for the  $\eta'$  tag data to exclude events with additional particles, such as  $\gamma + ^{12}\text{C} \rightarrow p_f + \eta' \pi + \text{X}$  reaction, and combinatorial multi meson background events, such as  $\gamma + ^{12}\text{C} \rightarrow p_f + \pi\pi + \text{X}$  reaction. The selection criteria are shown in Fig.4.9.

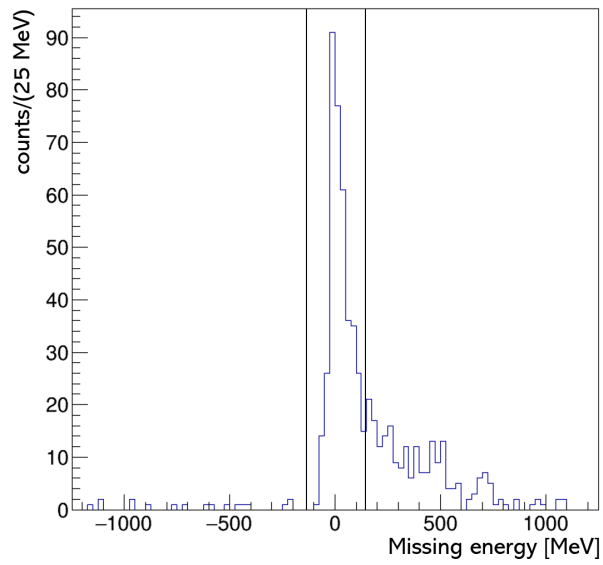


Figure 4.9: The missing energy  $E_{miss}^{\eta' p_f}$  distribution of the  $\eta'$  tag data. The selection criteria are shown with black lines.

# Chapter 5

## The $\eta'$ -nucleus search

To search for the  $(\eta + p_s)$  events from the  $\eta'$ -nucleus bound state, the kinematical selection was applied for the  $(\eta + p_s)$  pair. The optimization of the kinematical selection and the experimental results of the  $\eta'$ -nucleus search are described in this chapter. Note that angles, energies are given in the laboratory frame in this thesis if not specified.

### 5.1 Obtained data

In Fig.5.1 and Fig.5.2 the excitation energy of the  $\eta'+^{11}\text{B}$  system  $E_{\text{ex}}$ , relative to the  $\eta'$  production threshold  $E_0$ , of the  $\gamma + ^{12}\text{C} \rightarrow p_f + (\eta + p_s) + \text{X}$  and the  $\gamma + ^{12}\text{C} \rightarrow p_f + \eta' + \text{X}$  data, are shown respectively. For the  $\gamma + ^{12}\text{C} \rightarrow p_f + (\eta + p_s) + \text{X}$  reaction, the excitation energy is defined as

$$E_{\text{ex}} - E_0^{\eta'} = MM(^{12}\text{C}(\gamma, p_f)) - M_{^{11}\text{B}} - M_{\eta'}, \quad (5.1)$$

where  $MM(^{12}\text{C}(\gamma, p_f))$  is the missing mass in the  $\gamma + ^{12}\text{C} \rightarrow p + \text{X}$  reaction, and  $M_{^{11}\text{B}}$  and  $M_{\eta'}$  represent a mass of an  $^{11}\text{B}$  and an  $\eta'$  meson, respectively. For the  $\gamma + ^{12}\text{C} \rightarrow p_f + \eta' + \text{X}$  reaction, the following definition was used:

$$E_{\text{ex}} - E_0^{\gamma\gamma} = MM(^{12}\text{C}(\gamma, p_f)) - M_{^{11}\text{B}} - M_{\gamma\gamma}. \quad (5.2)$$

Here, we replace  $M_{\eta'}$  in Eq.(5.1) with the invariant mass of two gammas,  $M_{\gamma\gamma}$ . By using  $M_{\gamma\gamma}$ , we can cancel the  $M_{\gamma\gamma}$  dependence of the  $E_{\text{ex}} - E_0$  distribution and we can use side-band events of  $M_{\gamma\gamma}$  for the background evaluation. Details are described in Appendix H. In Fig.5.2, we observed a clean spectrum of the  $\eta'$  escape process, rising from the  $\eta'$  production threshold. On the other hand, in Fig.5.1, we observed a large number of background events rising below the  $\eta'$  production threshold. Huge (multi) meson background events in the  $\gamma + ^{12}\text{C} \rightarrow p_f + \text{X}$  reaction, such as the  $\gamma + ^{12}\text{C} \rightarrow p_f + \pi\pi + \text{X}$ ,  $\gamma + ^{12}\text{C} \rightarrow p_f + \pi\pi\pi + \text{X}$ ,  $\gamma + ^{12}\text{C} \rightarrow p_f + \omega + \text{X}$ , and  $\gamma + ^{12}\text{C} \rightarrow p_f + \pi\eta + \text{X}$  reactions, were suppressed by tagging an  $(\eta + p_s)$  pair, and thus remaining events are background events associating with an  $\eta$  and a side-going proton. To suppress remaining background events, a kinematical selection of  $(\eta + p_s)$  was carried out. The details of the kinematical selection and results after the kinematical selection are described in the following section.

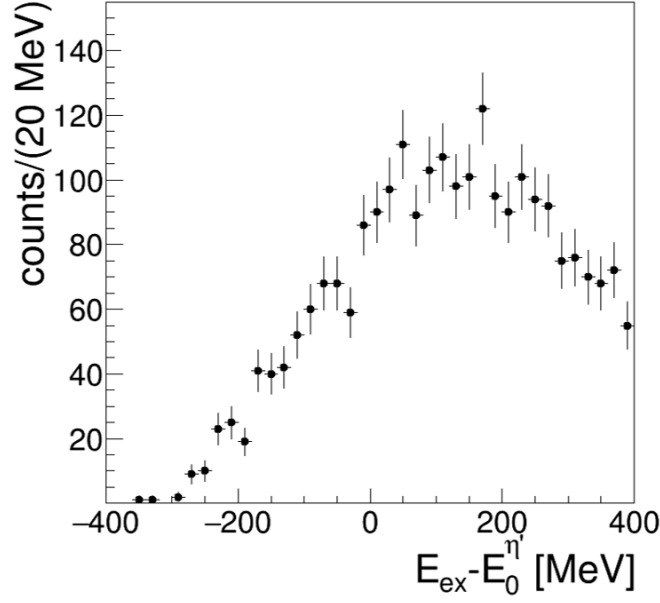


Figure 5.1: The excitation energy spectrum of the  $\gamma + {}^{12}\text{C} \rightarrow p_f + (\eta + p_s) + \text{X}$  data without any kinematical selection cuts for  $\eta$  and  $p_s$ .

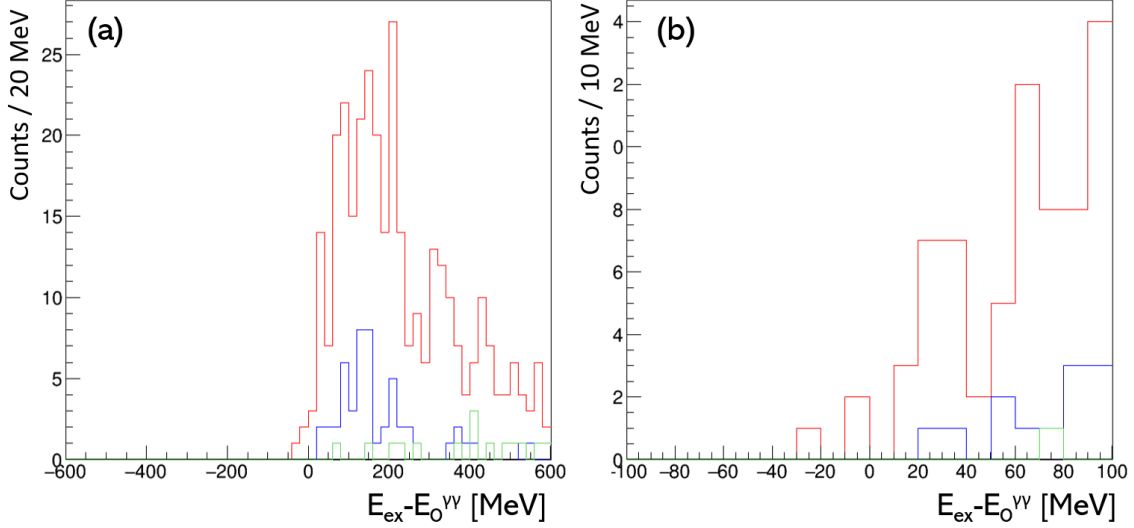


Figure 5.2: The excitation energy distribution of the  $\gamma + {}^{12}\text{C} \rightarrow p_f + \eta' + \text{X}$  reaction (a) in  $-600 \text{ MeV} < E_{\text{ex}} - E_0^{\gamma\gamma} < 600 \text{ MeV}$  and (b) in  $-100 \text{ MeV} < E_{\text{ex}} - E_0^{\gamma\gamma} < 100 \text{ MeV}$ . Red line shows the  $\eta'$  tag events in  $-4\sigma < M_{\gamma\gamma} < +4\sigma$  and blue and green lines show side band events in  $-8\sigma < M_{\gamma\gamma} < -4\sigma$  and  $+4\sigma < M_{\gamma\gamma} < +8\sigma$ , respectively.

## 5.2 Outline of the kinematical selection

Most of events in Fig.5.1 come from background reactions,  $\gamma + {}^{12}\text{C} \rightarrow p_f + \eta + {}^{11}\text{B}$  and  $\gamma + {}^{12}\text{C} \rightarrow p_f + (\eta + \pi^0) + {}^{11}\text{B}$ , where an  $\eta$  meson is produced in a primary reaction and a side-going proton,  $p_s$  is kicked out by either a primary  $\eta$ ,  $\pi^0$  or  $p_f$ . To suppress those background events, we determined kinematical selection criteria of the  $(\eta + p_s)$  pair. The  $(\eta + p_s)$  pair from the bound  $\eta'$  meson is considered to be emitted in a close to back-to-back relation, with an isotropic polar angle distribution in the laboratory frame. On the other hand,  $\eta$  and  $p_s$  from the background reactions are emitted in the forward direction in the

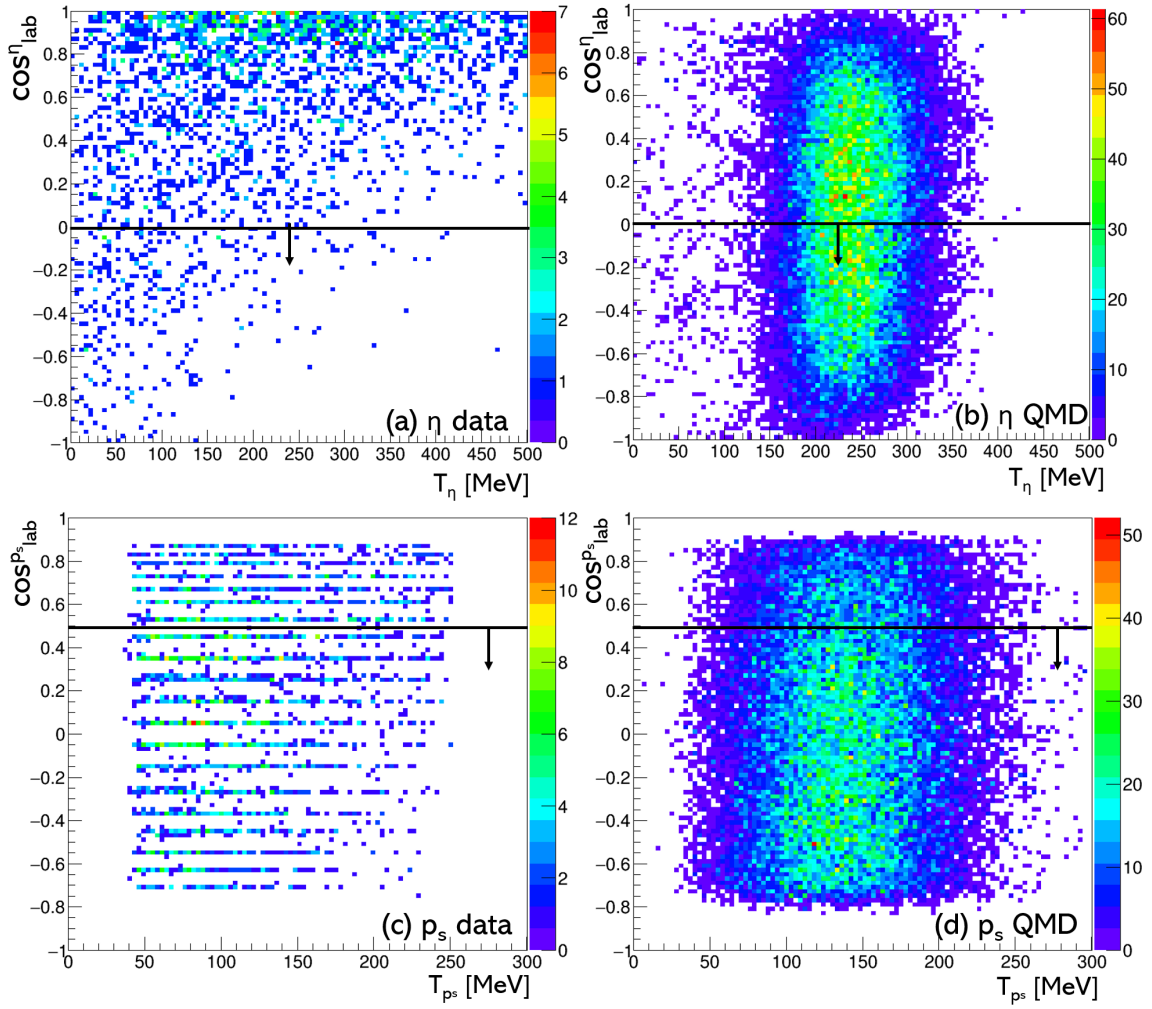


Figure 5.3: The polar angle and kinetic energy distribution of  $\eta$  and  $p_s$ . (a)(c) The  $\gamma + {}^{12}\text{C} \rightarrow p_f + (\eta + p_s) + X$  data in all  $E_{\text{ex}} - E_0$  region, and (b)(d) the QMD signal simulation in  $-50 \text{ MeV} < E_{\text{ex}} - E_0 < 50 \text{ MeV}$ . The kinematical selection criteria are shown with black lines.

laboratory frame because they are Lorentz-boosted as seen in Fig.5.3(a) and (c), in which the polar angle and kinetic energy distribution of  $\eta$  and  $p_s$  of the  $\gamma + {}^{12}\text{C} \rightarrow p_f + (\eta + p_s) + \text{X}$  data are shown. In addition, there is an undetected  $\pi^0$  in the case of the  $\gamma + {}^{12}\text{C} \rightarrow p_f + (\eta + \pi^0) + {}^{11}\text{B}$  background reaction. The opening angle distribution and the missing energy distribution of the  $\gamma + {}^{12}\text{C} \rightarrow p_f + (\eta + p_s) + \text{X}$  data are shown in Fig.5.4(a) and (c). When there is an undetected pion, the missing energy is greater than  $m_{\pi^0} = 135$  MeV. We determined kinematical cuts selecting back-to-back  $(\eta + p_s)$  pairs, backward-going  $p_s$  and  $\eta$ , and events with no additional produced particle to enhance signals. The selection criteria are shown

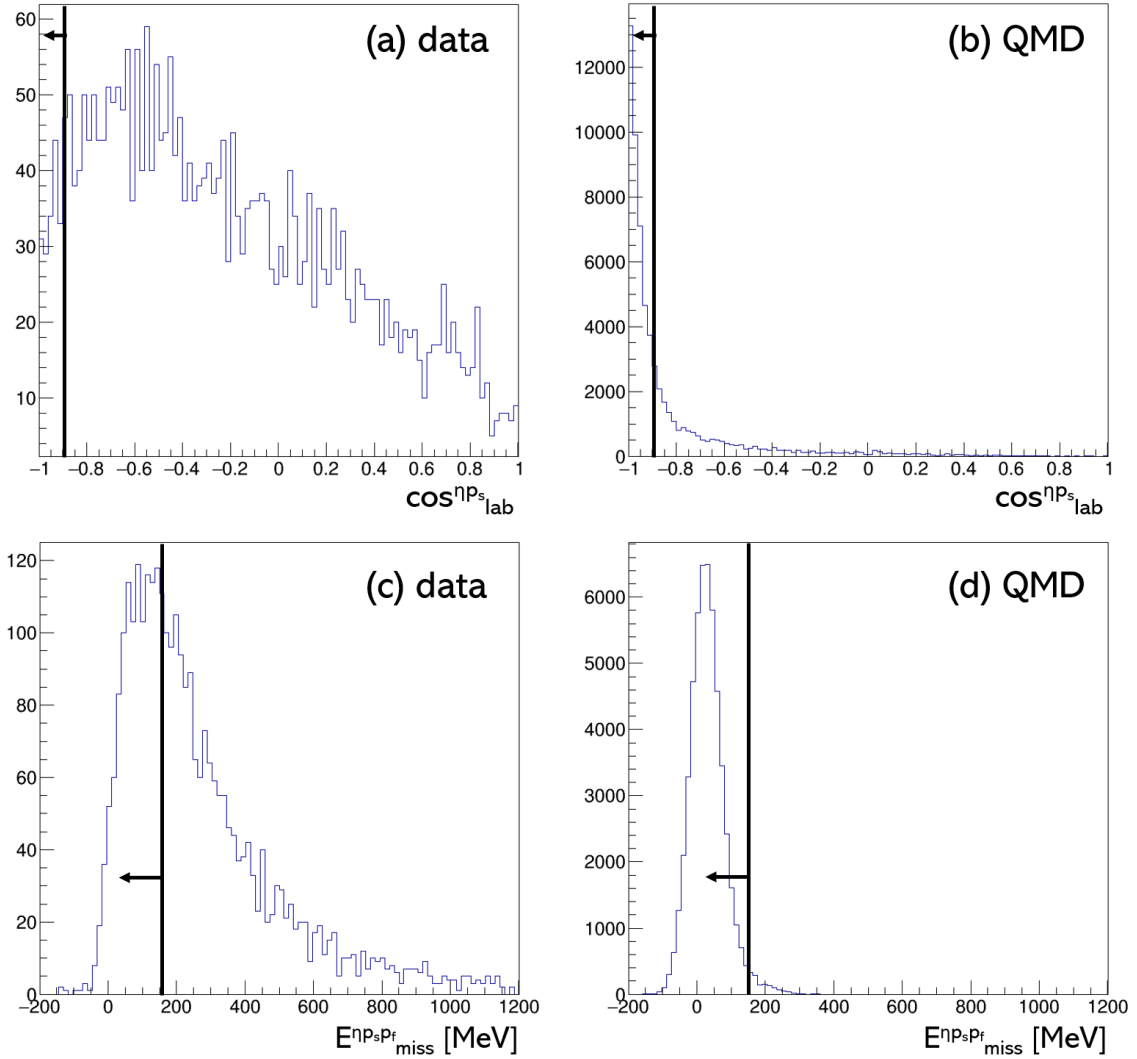


Figure 5.4: The  $\eta - p_s$  opening angle and missing energy distribution. (a)(c) The  $\gamma + {}^{12}\text{C} \rightarrow p_f + (\eta + p_s) + \text{X}$  data in all  $E_{\text{ex}} - E_0$  region, and (b)(d) the QMD signal simulation in  $-50 \text{ MeV} < E_{\text{ex}} - E_0 < 50 \text{ MeV}$ . The kinematical selection criteria are shown with black lines.

with black lines.

Even an  $(\eta + p_s)$  pair from the  $\eta'$  absorption is originally emitted back-to-back, the  $\eta$  and  $p_s$  interact in a nucleus and possibly lose their energy and/or change their direction. We examined the kinematical distribution of the  $(\eta + p_s)$  after the interaction simulated with the QMD model calculation is shown in Fig.5.3(b) and (d). The kinematical distributions of  $\eta$  and  $p_s$  simulated with the QMD model calculation are shown in Fig.5.3(b)(d) and Fig.5.4(b)(d). The kinematics of background events are examined using the experimental data of the  $\gamma + {}^{12}\text{C} \rightarrow p_f + \eta + \text{X}$  and  $\gamma + {}^{12}\text{C} \rightarrow p_f + (\eta + \pi^0) + \text{X}$  reactions. We optimized the kinematical selection criteria using the side band of the excitation energy of the  $\gamma + {}^{12}\text{C} \rightarrow p_f + (\eta + p_s) + \text{X}$  data, requiring  $100 \text{ MeV} < |E_{\text{ex}} - E_0^{\eta'}| < 200 \text{ MeV}$  and  $\eta - p_s$  opening angle  $\cos \theta_{\text{lab}}^{\eta p_s} < -0.9$ . We used the QMD signal simulation and the  $\gamma + {}^{12}\text{C} \rightarrow p_f + \eta + \text{X}$  and  $\gamma + {}^{12}\text{C} \rightarrow p_f + (\eta + \pi^0) + \text{X}$  data as references of the cut optimization. We describe details of the background sources, expected signal kinematics, and optimization of kinematical selection criteria in the following sections.

### 5.3 Background source and feature

We searched for the signals in the following reaction:

$$\gamma + {}^{12}\text{C} \rightarrow p_f + \eta' \otimes {}^{11}\text{B} \quad (5.3a)$$

$$\hookrightarrow \eta' + p \rightarrow \eta + p_s. \quad (5.3b)$$

On the other hand, we found that most of the background events are from the following reactions:

$$\gamma + {}^{12}\text{C} \rightarrow p_f + \eta + {}^{11}\text{B} \quad (5.4a)$$

$$\hookrightarrow \eta + p \rightarrow \eta + p_s, \quad (5.4b)$$

$$\text{or } p_f + p \rightarrow p_f + p_s. \quad (5.4c)$$

$$\gamma + {}^{12}\text{C} \rightarrow p_f + \eta + \pi^0 + {}^{11}\text{B} \quad (5.5a)$$

$$\hookrightarrow \eta + p \rightarrow \eta + p_s, \quad (5.5b)$$

$$\text{or } p_f + p \rightarrow p_f + p_s, \quad (5.5c)$$

$$\text{or } \pi^0 + p \rightarrow \pi^0 + p_s, \quad (5.5d)$$

$$\text{or } \pi^0 + p + n \rightarrow p_s + n. \quad (5.5e)$$

$$\gamma + {}^{12}\text{C} \rightarrow p_f + \eta + \pi^- + {}^{11}\text{C} \quad (5.6a)$$

$$\hookrightarrow \pi^- + p + p \rightarrow p_s + n. \quad (5.6b)$$

In all the background reactions, an  $\eta$  meson is produced in the primary reaction, and  $p_s$  is kicked out by one of the particles produced in the primary reaction. In the single  $\eta$  background reaction (5.3), the particles in the final state are the same as the signal reaction

(5.2). In the  $\eta\pi$  background reactions (5.4) and (5.5), there is an undetected  $\pi^0$  (reactions (5.4b, 5.4c, 5.4d)) or  $n$  (reactions (5.4e, 5.5b)). The  $\gamma$ 's from  $\pi^0$  and  $n$  escape from the measurements when they fly to the holes of BGOegg at  $\theta < 24^\circ$  and  $\theta > 144^\circ$ . In addition, because the detection efficiency for  $n$  of BGOegg is low,  $n$  can escape from the measurement even if it is emitted to  $24^\circ < \theta < 144^\circ$  when it does not react with BGOegg. On the other hand, reactions with an additional charged particle can not be background reactions because all the solid angle is covered with BGOegg, the UpVeto and the DC. Events which had an additional hit in BGOegg, a hit in the UpVeto or an additional track other than  $p_f$  in the DC, are excluded in the event selection. Thereby, in the case of  $\eta\pi^-$  production, only the two nucleon absorption process of the reaction (5.5b), which emits an  $n$ , can be a background.

We examined those background reactions using the  $\gamma + {}^{12}\text{C} \rightarrow p_f + \eta + \text{X}$  and  $\gamma + {}^{12}\text{C} \rightarrow p_f + (\eta + \pi^0) + \text{X}$  data, in which only an  $\eta$  meson or the  $\eta\pi^0$  mesons were detected in BGOegg, respectively. To exclude events with an additional undetected particle, we selected region  $|E_{miss}| < 150$  MeV. Here, we define

$$E_{miss}^{\eta p_f} = E_\gamma + M_{12\text{C}} - M_{11\text{B}} - E_\eta - E_{p_f}, \quad (5.7)$$

$$E_{miss}^{\eta\pi^0 p_f} = E_\gamma + M_{12\text{C}} - M_{11\text{B}} - E_\eta - E_{\pi^0} - E_{p_f}, \quad (5.8)$$

for the  $\eta$  and  $\eta\pi^0$  data, respectively. Except the case that the secondary  $p_s$  is kicked out by  $p_f$  (reaction (5.3c) and (5.4c)), the excitation energy is independent from the secondary reaction. In Fig.5.5, we show the excitation energy distributions of the  $\eta$ ,  $\eta\pi^0$  and  $(\eta + p_s)$  tag data. The distribution of the  $\eta\pi^0$  tag data shows similar distribution as the  $(\eta + p_s)$  tag data. For the  $\eta$  tag data, we require that the  $\eta$  kinetic energy is greater than 100 MeV. It is because that the  $\eta$  needs to have a certain kinetic energy,  $T_\eta$  to have the secondary reaction (5.3b) with  $p_s$  kinetic energy large enough ( $\gtrsim 50$  MeV) to penetrate the IPS and to be detected

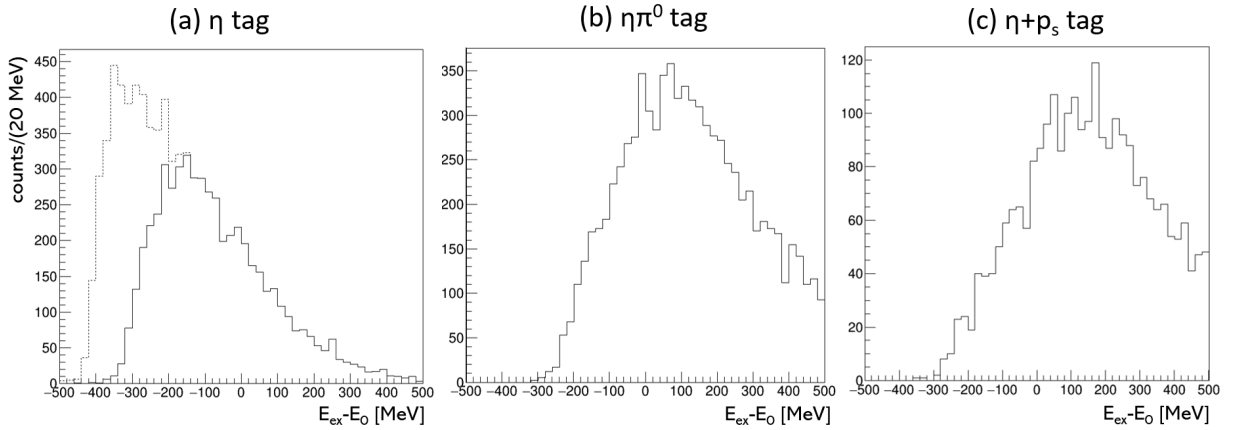


Figure 5.5: The excitation energy spectra of the (a)  $\eta$ , (b)  $\eta\pi^0$  and (c)  $(\eta + p_s)$  tag data. (a) The dashed line shows the distribution without  $T_\eta > 100$  MeV requirement and the solid line with  $T_\eta > 100$  MeV.

with BGOegg. The distributions without and with the requirement of  $T_\eta > 100$  MeV are shown in Fig.5.5(a). The distribution with the requirement of  $T_\eta > 100$  MeV starts to rise at  $E_{\text{ex}} - E_0 = -350$  MeV, which is similar to the distribution of the  $(\eta + p_s)$  tag data. We used the  $\gamma + {}^{12}\text{C} \rightarrow p_f + \eta + X$  and  $\gamma + {}^{12}\text{C} \rightarrow p_f + (\eta + \pi^0) + X$  data, to estimate the distribution of the background after the kinematical selection.

## 5.4 Expected signal kinematics

### 5.4.1 Characteristics of signal

When an  $\eta'$  meson is bound to a nucleus, its momentum is transferred to the nucleus and thus the  $\eta'$  meson is considered to be at rest in the laboratory frame. Therefore, the  $(\eta + N)$  pair from the  $\eta'N \rightarrow \eta N$  absorption process is emitted in a close to back-to-back relation, with an isotropic polar angle distribution, within the fluctuation coming from the Fermi momentum of the nucleon. This is the unique feature of the  $(\eta + N)$  pair from bound  $\eta'$  absorption. However, the emitted  $\eta$  meson and nucleon interact with the nucleus and lose their energy and/or change their direction, or even be absorbed by the nucleus. We examined the effect of the final state interactions in the nucleus using a quantum molecular dynamics (QMD) model calculation. In Fig.5.6, the kinematical distributions of  $\eta$  and  $p_s$  simulated with the QMD calculation are shown. In Fig.5.6, distributions without and with final state interactions are shown with blue and red lines, respectively. Protons with kinetic energy smaller than 50 MeV is mainly from the decay of  ${}^{11}\text{B}$  nucleus. Events with  $T_{p_s} < 50$  MeV are removed in Fig.5.6(a)(b)(c).

### 5.4.2 QMD simulation

To examine the  $\eta - p_s$  opening angle distribution after the interactions and to evaluate the probability that an  $(\eta + p_s)$  pair is emitted back-to-back after the interactions, we simulated the interaction of the  $\eta$  meson and nucleon with nucleons in the nucleus using a QMD model calculation. QMD calculations are widely used for the simulations of nucleus-nucleus collisions and hadron productions in nuclei [57, 58]. We used the same parameters as in Ref.[58], which well reproduce the angular and momentum dependence of differential cross sections of  $\eta$  photoproduction from carbon. In the simulation, we firstly injected a photon to a  ${}^{12}\text{C}$  nucleus. We changed the energy and angle of the forward going proton  $p_f$  to reproduce the kinematics of different  $E_{\text{ex}} - E_0$  cases. Then, the remaining momentum after the forward proton emission was shared with the residual  ${}^{11}\text{B}$  nucleus. The remaining energy was transferred to one of a nucleon in the  ${}^{11}\text{B}$  nucleus and produced a hypothetical  $N^*$  state with a mass of  $\eta'$ +nucleon, which immediately decays to an  $\eta$  and a nucleon. The polar angle distribution of the  $\eta$  and nucleon is assumed to be isotropic. Because the momentum was shared with the nucleus, the  $N^*$  momentum is the order of Fermi motion. The excited nucleon was chosen randomly, thus both the  $N^* \rightarrow \eta p$  and  $N^* \rightarrow \eta n$  processes are included with the weight of 5:6, which is the ratio of the number of  $p$  and  $n$  in the  ${}^{11}\text{B}$  nucleus. We are interested in the case that an  $(\eta + p)$  pair, not an  $(\eta + n)$  pair, which is emitted back-to-back

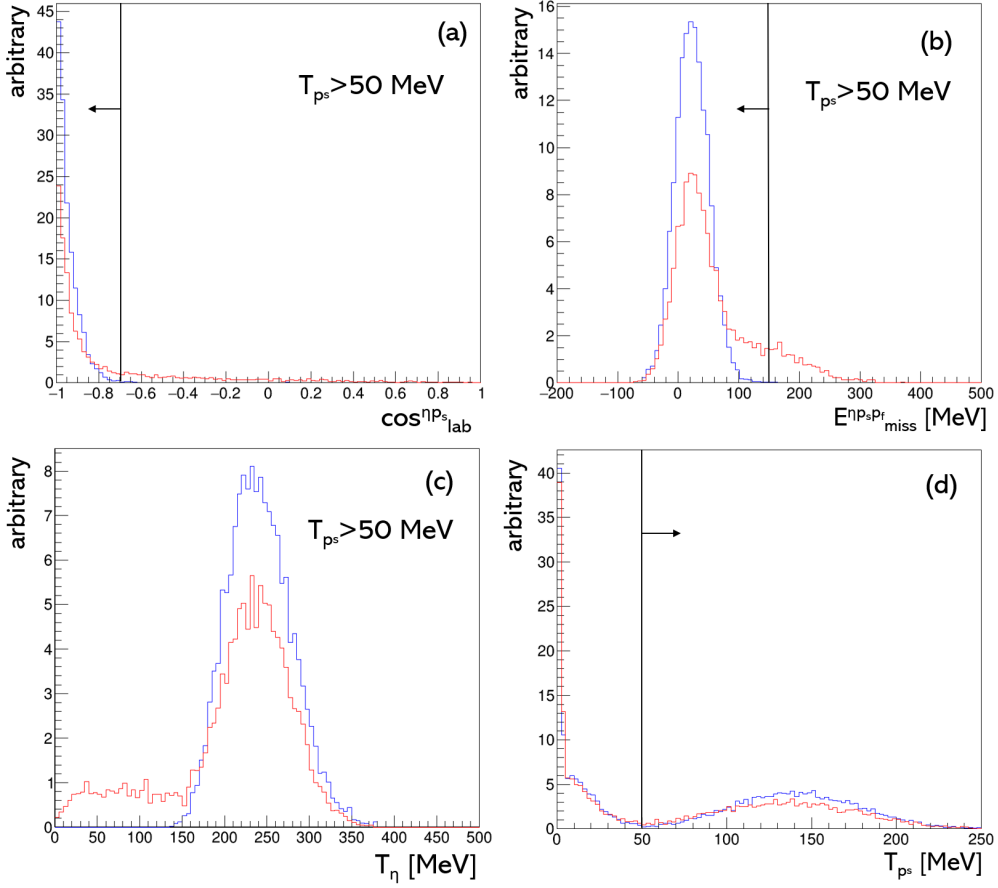


Figure 5.6: Kinematical distributions of the  $(\eta + p_s)$  pair of the QMD simulation in  $-50 \text{ MeV} < E_{\text{ex}} - E_0 < 50 \text{ MeV}$ , without (blue) and with (red) final state interaction. Detector resolution and acceptance are not included in these figures. The selection criteria of the survival sample are shown with black lines.

after the interactions. The details of the QMD simulation are described in Appendix E. The detector acceptance and resolutions were implemented to the simulation.

### 5.4.3 Survival probability

There are cases that the  $\eta$  meson or nucleon is absorbed by a nucleon when they interact, and is not emitted to outside of the nucleus. Even the case that both the  $\eta$  meson and nucleon are emitted, they may lose feature of the kinematics specified for the signal if they lose their energy or change their direction after the interaction in a nucleus. Figure 5.6 shows the kinematical distributions of the  $(\eta + p_s)$  pair in the QMD simulation when both the  $\eta$  and  $p_s$  are emitted outside of the nucleus. The yield decreases when the final state interactions are

implemented and some events lose original kinematical information. We can not distinguish such events from the background reactions anymore. We are interested in only events which keep the original features of signal kinematics. Thus, we defined the events which satisfy the following conditions as a “survival sample” after interactions:

- there are an  $\eta$  meson and a proton in the final state,
- opening angle :  $\cos \theta_{lab}^{\eta p_s} < -0.7$ ,
- missing energy :  $E_{miss}^{\eta p_s p_f} = E_\gamma + M_{12C} - M_{11B} - E_\eta - E_{p_s} - E_{p_f} < 150$  MeV,
- $p_s$  kinetic energy :  $T_{p_s} > 50$  MeV.

Here,  $E$  and  $M$  indicate the total energy and the mass of each particle, respectively. The selection criteria are shown with black lines in Fig.5.6.  $T_{p_s} > 50$  MeV is needed because there are a lot of low energy protons from the decay of residual nuclei as shown in Fig.5.6(c). We should note that the  $p_s$  kinetic energy cut,  $T_{p_s} > 50$  MeV is naturally included in the experimental data because only protons with kinetic energy greater than about 50 MeV can penetrate the IPS and can be detected with BGOegg (see section 4.5). We used the survival sample for estimating the expected signal yield and optimizing the kinematical selection criteria.

We evaluated a survival probability, which is the fraction of the survival sample after the interactions. We used the QMD simulation with the kinematics corresponding to  $-10$  MeV  $< E_{ex} - E_0 < 10$  MeV. In the case that the initial reaction is  $N^* \rightarrow \eta p$ , the fraction of the survival sample is 32.5%. In the case that the initial reaction is  $N^* \rightarrow \eta n$ , we can observe an  $(\eta + p_s)$  pair when a neutron kicked out a proton. The fraction of the survival sample of the  $N^* \rightarrow \eta n$  case is 2.6%. In total, the fraction of survival events was 16.0% of the all the generated events. In the analysis, we optimized the kinematical selection criteria to the opening angle  $\cos \theta_{lab}^{\eta p_s} < -0.9$ . The survival probability  $P_{srv}^{\eta p_s}$  that an  $(\eta + p_s)$  pair is emitted in  $\cos \theta_{lab}^{\eta p_s} < -0.9$  (instead of  $\cos \theta_{lab}^{\eta p_s} < -0.7$ ) is  $P_{srv}^{\eta p_s} = 25.2\%$  for the  $\eta' p \rightarrow \eta p$  case and  $P_{srv}^{\eta p_s} = 1.2\%$  for the  $\eta' n \rightarrow \eta n$  case. Total survival probability is  $P_{srv}^{\eta p_s} = 12.1\%$ . The obtained  $P_{srv}^{\eta p_s}$  for the  $\eta' p \rightarrow \eta p$  is consistent with the measured transparency of carbon nuclei for  $\eta$  ( $\sim 44\%$  [59]) and protons ( $\sim 60\%$  [60–62]). We took into account  $P_{srv}^{\eta p_s}$  when we estimate the expected yield.

## 5.5 Cut optimization

In this section, the optimization of kinematical cut is described. For optimization of the cut criteria, we used the the side band of the interested excitation energy region of the  $(\eta + p_s)$  tag data,  $\eta$ ,  $\eta\pi^0$  tag data, and the QMD survival sample. We determined kinematical cuts selecting back-to-back  $(\eta + p_s)$  pairs, backward-going  $p_s$  and  $\eta$ , and events with no additional produced particles to improve the S/N ratio. The selection criteria are as follows:

- (a) the  $\eta$ - $p_s$  opening angle :  $\cos \theta_{lab}^{\eta p_s} < -0.9$ ,

Table 5.1: Number of the events of the  $(\eta + p_s)$  coincidence data in  $100 \text{ MeV} < |E_{\text{ex}} - E_0^{\eta'}| < 300 \text{ MeV}$ , and the expected number of signal events for the case of  $V_0 = -100 \text{ MeV}$ , after applying each kinematical selection cut.

$E_{\text{ex}} - E_0^{\eta'}$ region [MeV]	[-300, -200]	[-200, -100]	expected signal [-50, 50]	[100, 200]	[200, 300]
no cuts	67	188	$(58.4 \pm 14.7) \times \text{Br}_{\eta'N \rightarrow \eta N}$	507	438
(a): $\cos \theta_{lab}^{\eta p_s} < -0.9$	11	26	$(43.8 \pm 11.0) \times \text{Br}_{\eta'N \rightarrow \eta N}$	24	18
(a), (b): $ E_{miss}^{\eta p_s p_f}  < 150 \text{ MeV}$	11	24	$(43.8 \pm 11.0) \times \text{Br}_{\eta'N \rightarrow \eta N}$	9	4
(a), (b), (c): $\cos \theta_{lab}^{p_s} < 0.5$	9	18	$(35.7 \pm 9.0) \times \text{Br}_{\eta'N \rightarrow \eta N}$	9	4
(a), (b), (c), (d): $\cos \theta_{lab}^{\eta} < 0$	4	1	$(13.1 \pm 3.3) \times \text{Br}_{\eta'N \rightarrow \eta N}$	0	0

(b) missing energy :  $E_{miss}^{\eta p_s p_f} = E_{\gamma} + M_{12C} - M_{11B} - E_{\eta} - E_{p_s} - E_{p_f} < 150 \text{ MeV}$ ,

(c) the  $p_s$  polar angle :  $\cos \theta_{lab}^{p_s} < 0.5$ ,

(d) the  $\eta$  polar angle :  $\cos \theta_{lab}^{\eta} < 0$ .

The number of events of the  $\gamma + {}^{12}\text{C} \rightarrow p_f + (\eta + p_s) + \text{X}$  data in  $100 \text{ MeV} < |E_{\text{ex}} - E_0^{\eta'}| < 300 \text{ MeV}$  after each kinematical selection are summarized in Table.5.1. The numbers of expected signals for the case of  $V_0 = -100 \text{ MeV}$  are also shown as a function of the unknown branching fraction of the  $\eta'N \rightarrow \eta N$  process,  $\text{Br}_{\eta'N \rightarrow \eta N}$ . The details of the calculation of the expected number of signals are described in section 7.2 and Appendix G.

For optimizing cut criteria, we used the side band of the interested excitation energy region of the  $(\eta + p_s)$  tag data,  $100 \text{ MeV} < |E_{\text{ex}} - E_0^{\eta'}| < 200 \text{ MeV}$ . The excitation energy distribution is shown in Fig.5.1. Since kinematical distributions of  $\eta$  and  $p_s$  depend on  $E_{\text{ex}} - E_0^{\eta'}$ , we did not use events in  $200 \text{ MeV} < |E_{\text{ex}} - E_0^{\eta'}|$  for optimizing cut criteria. For optimizing the  $\eta - p_s$  opening angle cut, we used the  $(\eta + p_s)$  data satisfying the following condition:

- excitation energy :  $100 \text{ MeV} < |E_{\text{ex}} - E_0^{\eta'}| < 200 \text{ MeV}$ .

For optimizing other kinematical cut criteria, we used the  $(\eta + p_s)$  data satisfying the following conditions:

- excitation energy :  $100 \text{ MeV} < |E_{\text{ex}} - E_0^{\eta'}| < 200 \text{ MeV}$ ,
- $\eta - p_s$  opening angle :  $\cos \theta_{lab}^{\eta p_s} < -0.9$ .

We required  $\cos \theta_{lab}^{\eta p_s} < -0.9$  because the polar angle distributions of  $\eta$  mesons and protons strongly depends on the opening angle criteria. We call the samples satisfying above conditions as the “ $(\eta + p_s)$  side band sample”.

The resolutions of  $\theta_{lab}^{p_s}$  and  $\theta_{lab}^{\eta}$  are in the range of  $1.4\text{--}4.2^\circ$  and  $1.4\text{--}5.7^\circ$ , respectively, depending on the particle kinetic energy and polar angle. The resolution of  $\theta_{lab}^{\eta p_s}$  is a quadratic

sum of the resolutions of  $\theta_{lab}^{p_s}$  and  $\theta_{lab}^\eta$ . The resolution of  $E_{miss}^{\eta p_s p_f}$  is a quadratic sum of the resolutions of  $E_\gamma$ ,  $E_\eta$ ,  $E_{p_s}$  and  $E_{p_f}$ . It is in the range of 15–40 MeV depending on the energy of  $\eta$ ,  $p_s$  and  $p_f$ .  $E_\gamma$  and BGOegg cluster energy are calibrated so that  $E_{miss}$  to be 0 MeV in the case of proton target. Those resolutions are implemented in the QMD simulation.

The details of the optimization of each cut criterion are described in the following sections.

### 5.5.1 Opening angle cut

First, we determined the criterion of  $\eta - p_s$  opening angle cut. Figure 5.7 shows the  $\eta - p_s$  opening angle distribution of the QMD survival sample and the  $(\eta + p_s)$  side band data. The survival sample is concentrated in  $\cos\theta_{lab}^{\eta p_s} < -0.9$ . On the other hand, the distribution of the side band data is flat. Thereby, we determined the cut condition to  $\cos\theta_{lab}^{\eta p_s} < -0.9$ . As shown in Table.5.1, the opening angle cut suppress background events to 6.6%. The acceptance for the QMD survival event is 75.8%.

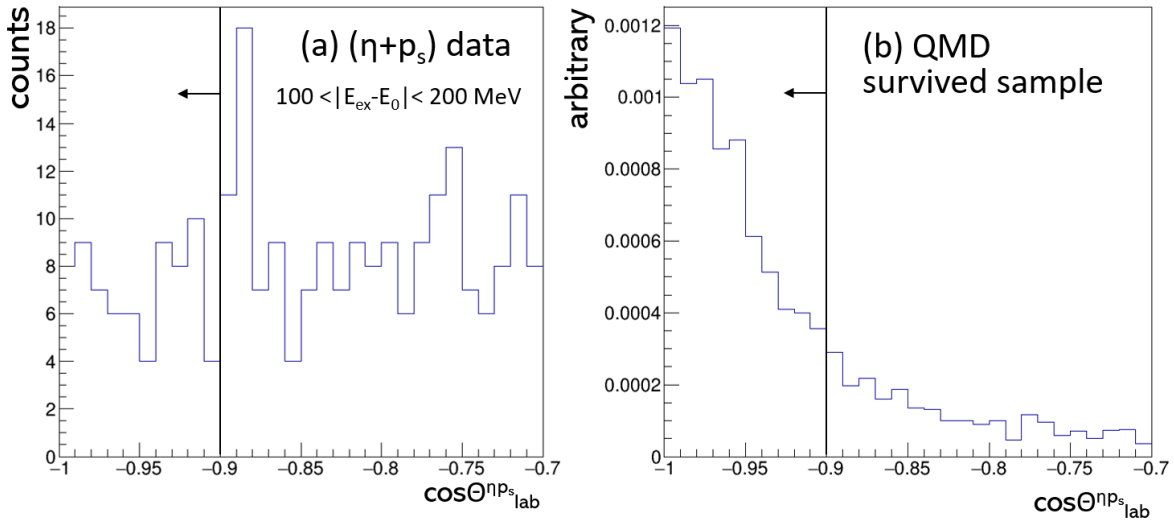


Figure 5.7: The opening angle distributions of the  $(\eta + p_s)$  side band data in  $100 \text{ MeV} < |E_{\text{ex}} - E_0^\eta| < 200 \text{ MeV}$ , and the QMD survival sample.

### 5.5.2 Missing energy cut

Figure 5.8 shows the missing energy distribution of the QMD survival sample (requiring  $T_\eta > 150 \text{ MeV}$  instead of  $E_{miss}^{\eta p_s p_f} < 150 \text{ MeV}$ ) and the  $(\eta + p_s)$  side band data. The missing energy distribution of the  $\gamma + {}^{12}\text{C} \rightarrow p_f + \eta' + \text{X}$  data in the region of  $E_{\text{ex}} - E_0^\eta < 150 \text{ MeV}$

is also shown. Here, the missing energies are defined as follows:

$$(\text{QMD}, (\eta + p_s) \text{ data}) E_{miss}^{\eta p_s p_f} = E_\gamma + M_{12C} - M_{11B} - E_\eta - E_{p_s} - E_{p_f}, \quad (5.9)$$

$$(\eta') E_{miss}^{\eta' p_f} = E_\gamma + M_{12C} - M_{11B} - E_{\eta'} - E_{p_f}, \quad (5.10)$$

for the QMD,  $(\eta + p_s)$  data and  $\eta'$  tag data, respectively. All distributions show the peak at  $E_{miss} = 0$  MeV, which corresponds to events that no other undetected particle was produced. Because the shell structure of the nucleon is not included to the QMD simulation, it is difficult to evaluate the distribution of the tail of the missing energy with the QMD. Thereby, we set a safe missing energy cut criterion as  $|E_{miss}^{\eta p_s p_f}| < 150$  MeV. As shown in Table.5.1, this cut suppress the background events in  $E_{ex} - E_0^\eta > 100$  MeV to 31%, where an additional pion is more likely to be produced. The QMD signal acceptance is more than 99.9%. Note that this cut can suppress the background reactions (5.4b, 5.4c, 5.4d), in which a missing energy larger than the  $\pi^0$  mass ( $M_{\pi^0} = 135$  MeV) is expected. The background reactions (5.4e, 5.5b) survive this cut when the neutron kinetic energy  $T_n$  is smaller than  $\sim 150$  MeV.

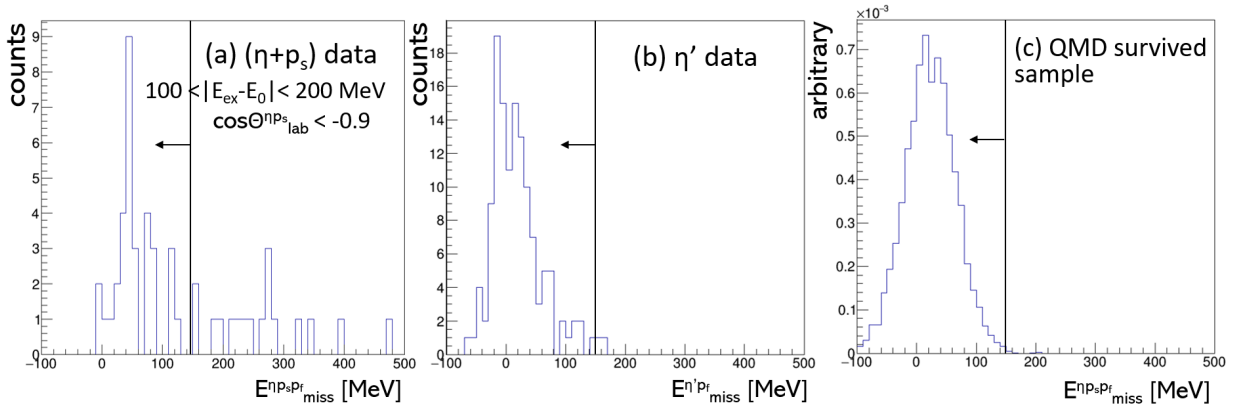


Figure 5.8: The missing energy distributions of the  $(\eta + p_s)$  side band data, the  $\eta'$  tag data, and the QMD survival sample.

### 5.5.3 $\eta$ and $p_s$ polar angle cut

As can be seen in Fig.5.3(a)(c), there are less backgrounds in the  $\eta$  and  $p_s$  backward polar angle region than forward region. However, because of the selection criterion of  $\cos \theta_{lab}^{\eta p_s} < -0.9$ , we can not select the region where both the  $\eta$  meson and  $p_s$  are emitted to backward direction. We optimized the selection criteria of the  $\eta$  and  $p_s$  polar angles simultaneously because there is a correlation between  $\eta$  and  $p_s$  polar angles when we require  $\cos \theta_{lab}^{\eta p_s} < -0.9$ . The number of events in each polar angle region,  $\cos \theta_{lab}^{p_s}$  and  $\cos \theta_{lab}^\eta$ , are summarized in Table.5.2. The expected signal yields for the case of  $V_0 = -100$  MeV in each  $\cos \theta_{lab}^{p_s}$  and  $\cos \theta_{lab}^\eta$  regions are summarized in Table.5.3. We obtain the best  $S/\sqrt{N}$  ratio when we select

the region of  $[\cos \theta_{lab}^{p_s} < 0.5 \text{ and } \cos \theta_{lab}^\eta < 0]$  ( $(13.2 \times \text{Br}_{\eta' N \rightarrow \eta N})/\sqrt{1}$ ). Thus, we determined the  $\eta$  and  $p_s$  polar angle cut to be  $[\cos \theta_{lab}^{p_s} < 0.5 \text{ and } \cos \theta_{lab}^\eta < 0]$ . The signal acceptance with the cut of  $[\cos \theta_{lab}^{p_s} < 0.5 \text{ and } \cos \theta_{lab}^\eta < 0]$  is 30.0%. As can be seen in Table.5.1, the background events are reduced to 10.4% with the polar angle cuts.

Table 5.2: The number of background events in each  $\cos \theta_{lab}^{p_s}$  and  $\cos \theta_{lab}^\eta$  region. The number of events in  $-200 \text{ MeV} < E_{\text{ex}} - E_0^{\eta'} < -100 \text{ MeV}$  and  $100 \text{ MeV} < E_{\text{ex}} - E_0^{\eta'} < 200 \text{ MeV}$  is shown before and after slash, respectively. The selected region with the kinematical cut is shown with thick letters.

	$-1 < \cos \theta_{lab}^\eta < -0.5$	$-0.5 < \cos \theta_{lab}^\eta < 0$	$0 < \cos \theta_{lab}^\eta < 0.5$	$0.5 < \cos \theta_{lab}^\eta < 1$
$0.5 < \cos \theta_{lab}^{p_s} < 1$	4/0	2/0	0/0	0/0
$0 < \cos \theta_{lab}^{p_s} < 0.5$	<b>0/0</b>	<b>1/0</b>	1/0	0/0
$-0.5 < \cos \theta_{lab}^{p_s} < 0$	<b>0/0</b>	<b>0/0</b>	6/4	4/2
$-1 < \cos \theta_{lab}^{p_s} < -0.5$	<b>0/0</b>	<b>0/0</b>	2/0	4/3

Table 5.3: The expected signal yield in  $-50 \text{ MeV} < E_{\text{ex}} - E_0^{\eta'} < 50 \text{ MeV}$  for the case of  $V_0 = -100 \text{ MeV}$  in each  $\cos \theta_{lab}^{p_s}$  and  $\cos \theta_{lab}^\eta$  region. The selected region with the kinematical cut is shown with thick letters.

	$-1 < \cos \theta_{lab}^\eta < -0.5$	$-0.5 < \cos \theta_{lab}^\eta < 0$	$0 < \cos \theta_{lab}^\eta < 0.5$	$0.5 < \cos \theta_{lab}^\eta < 1$
$0.5 < \cos \theta_{lab}^{p_s} < 1$	$5.6 \times \text{Br}_{\eta' N \rightarrow \eta N}$	$2.7 \times \text{Br}_{\eta' N \rightarrow \eta N}$	0	0
$0 < \cos \theta_{lab}^{p_s} < 0.5$	<b><math>1.3 \times \text{Br}_{\eta' N \rightarrow \eta N}</math></b>	<b><math>9.7 \times \text{Br}_{\eta' N \rightarrow \eta N}</math></b>	$3.6 \times \text{Br}_{\eta' N \rightarrow \eta N}$	0
$-0.5 < \cos \theta_{lab}^{p_s} < 0$	<b>0</b>	<b><math>2.2 \times \text{Br}_{\eta' N \rightarrow \eta N}</math></b>	$9.6 \times \text{Br}_{\eta' N \rightarrow \eta N}$	$2.7 \times \text{Br}_{\eta' N \rightarrow \eta N}$
$-1 < \cos \theta_{lab}^{p_s} < -0.5$	<b>0</b>	<b>0</b>	$2.2 \times \text{Br}_{\eta' N \rightarrow \eta N}$	$5.0 \times \text{Br}_{\eta' N \rightarrow \eta N}$

## 5.6 Expected signal and background yields after the kinematical selection

The numbers of background events in  $100 \text{ MeV} < |E_{\text{ex}} - E_0^{\eta'}| < 300 \text{ MeV}$  and expected signal yields  $-50 \text{ MeV} < E_{\text{ex}} - E_0^{\eta'} < 50 \text{ MeV}$  after each kinematical selection are summarized in Table.5.1. With all the kinematical selection, the background events are reduced to 0.4%, while 23% of the signal events is preserved. The background events remained only in  $E_{\text{ex}} - E_0^{\eta'} < -100 \text{ MeV}$ . In the small  $E_{\text{ex}} - E_0^{\eta'}$  region, the missing energy and the kinetic energies of  $\eta$  and  $p_s$  are small and those events are hardly removed with kinematical selections. The remained numbers of events are 4 in  $-300 \text{ MeV} < E_{\text{ex}} - E_0^{\eta'} < -200 \text{ MeV}$  and 1 in  $-200 \text{ MeV} < E_{\text{ex}} - E_0^{\eta'} < -100 \text{ MeV}$ . Figure 5.9 shows the excitation energy distribution of the single  $\eta$ ,  $\eta\pi^0$  and  $(\eta + p_s)$  tag sample with no  $\cos \theta_{lab}^\eta$  cut (black),  $\cos \theta_{lab}^\eta < 0.5$  (blue) and  $\cos \theta_{lab}^\eta < 0$  (red). We require  $\cos \theta_{lab}^{\eta p_s} < -0.9$  for the  $(\eta + p_s)$  tag data but do not

require  $|E_{miss}^{\eta p_s p_f}| < 150$  MeV to increase statistics. An identical or smaller background level in  $-100 \text{ MeV} < E_{ex} - E_0^{\eta'} < 100 \text{ MeV}$  as  $-200 \text{ MeV} < E_{ex} - E_0^{\eta'} < -100 \text{ MeV}$  is indicated for the case of  $\cos\theta_{lab}^{\eta} < 0$ . Thereby, the expected background level in  $-50 \text{ MeV} < E_{ex} - E_0^{\eta'} < 50 \text{ MeV}$  is  $1 \pm 1$  events or less after the kinematical selection. On the other hand, the expected number of signal events is  $(13.1 \pm 3.3) \times \text{Br}_{\eta' N \rightarrow \eta N}$ . If  $\text{Br}_{\eta' N \rightarrow \eta N}$  is the order of a few tenth %, we can observe signals above backgrounds.

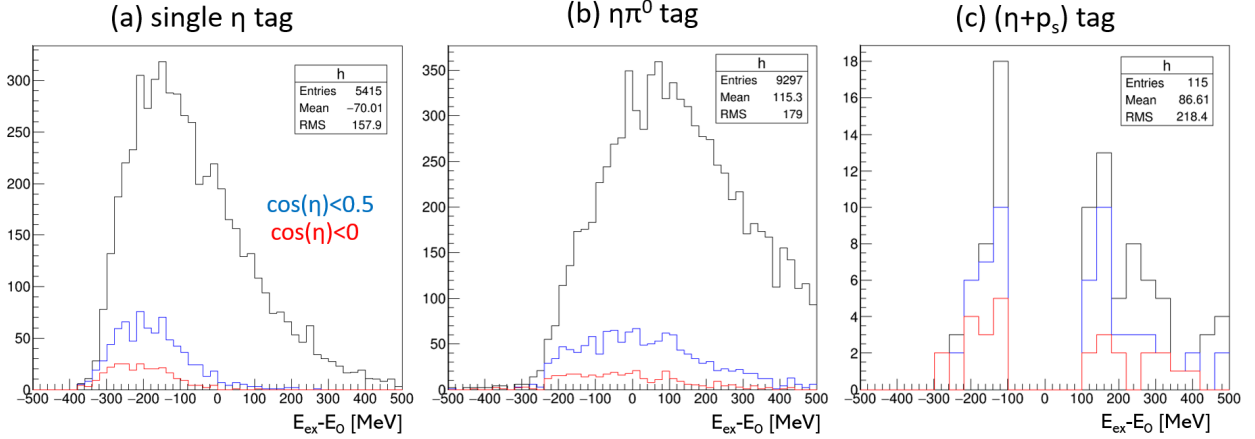


Figure 5.9: The excitation energy distributions of the single  $\eta$ ,  $\eta\pi^0$  and  $(\eta + p_s)$  tag data with different  $\cos\theta_{lab}^{\eta}$  cut criteria.

## 5.7 Experimental result

In Fig.5.10, we show a two dimensional plot of each variable used for the kinematical selection and  $E_{ex} - E_0^{\eta'}$  of the  $\gamma + {}^{12}\text{C} \rightarrow p_f + (\eta + p_s) + X$  data. The black dots show the events without any kinematical selection and blue circles show events after kinematical selections except for the kinematical selection with the variable used in the vertical axis. The red rectangles indicate the regions to search for the signals. There is no event satisfying all the cut conditions, therefore, we do not observe  $(\eta + p_s)$  events from bound- $\eta'$  absorption via the  $\eta' N \rightarrow \eta N$  process. The events observed in  $E_{ex} - E_0^{\eta'} < -50$  MeV are considered to be from the  $\gamma + {}^{12}\text{C} \rightarrow p_f + \eta + {}^{11}\text{B}$  and  $\gamma + {}^{12}\text{C} \rightarrow p_f + (\eta + \pi^0) + {}^{11}\text{B}$  background reactions. In chapter 6 and 7, we evaluate the experimental upper limit of the production cross section of the  $\eta'$ -nucleus bound state with  $(\eta + p_s)$  emission. The excitation energy spectrum of the  $\gamma + {}^{12}\text{C} \rightarrow p_f + \eta' + X$  was measured with very low background condition as shown in Fig.4.3(b) and Fig.5.2. We also evaluate the cross section of the  $\eta'$  escape process depending on the excitation energy.

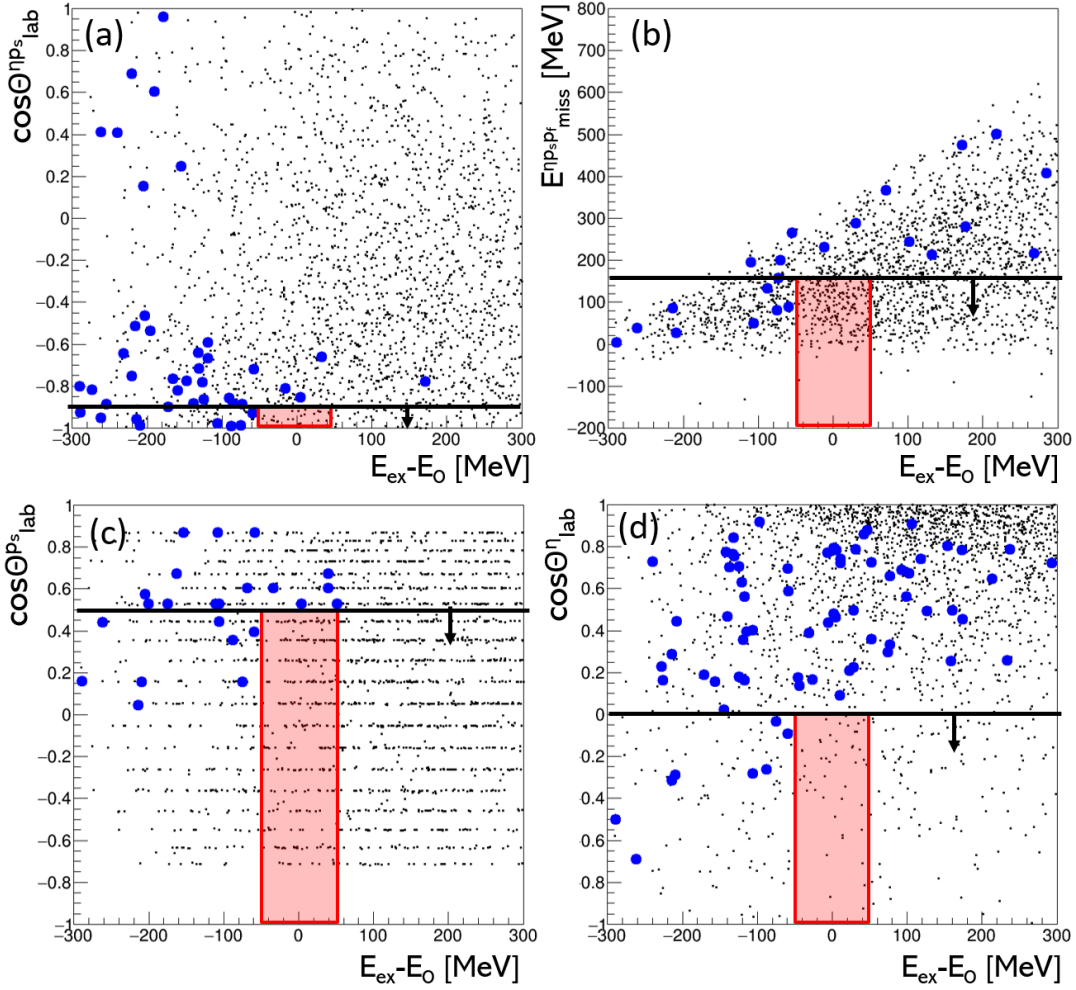


Figure 5.10: The two dimensional plot of each variable used for the kinematical selection and  $E_{ex} - E_0^{\eta'}$  of the  $\gamma + {}^{12}\text{C} \rightarrow p_f + (\eta + p_s) + X$  data. The black dots show events without the kinematical selections and blue circles show events after the kinematical selections except for the kinematical selection with the variable used in the vertical axis. The red rectangles indicate the regions to search for signals.

# Chapter 6

## Luminosity, acceptance and efficiency for the cross section measurement

In this section, we describe the details of the cross section evaluation for the  $\eta'$ -bound states with an  $(\eta + p_s)$  emission. We also describe the cross section measurements of the  $\eta'$  escape process.

### 6.1 The $(\eta + p_s)$ measurement

#### 6.1.1 Formulation

The experimental cross section of the  $\eta'$ -bound states with  $(\eta + p_s)$  emission averaged in  $\theta_p = 0.9 - 6.8^\circ$  and  $E_\gamma = 1.28 - 2.4$  GeV is expressed as

$$\overline{\left(\frac{d\sigma}{d\Omega_{p_f}}\right)^{(\eta+p_s)}} = \frac{N}{\Sigma(N_\gamma \times \varepsilon_{DAQ} \times \Omega_{RPC}) \times \rho_N \times Acc \times \varepsilon_{detector} \times \varepsilon_{filling} \times \text{Br}_{\eta \rightarrow 2\gamma}} \quad (6.1)$$

Here, the meaning of the variables are as follows:

- $N$  : the observed number of events after the kinematical selection
- $N_\gamma$  : the number of beam photons in 1.28-2.4 GeV
- $\varepsilon_{DAQ}$  : the DAQ efficiency
- $\Omega_{RPC}$  : the solid angle covered with the RPC
- $\rho_N$  : the number density of target nucleons
- $Acc$  : the acceptance of the BGOegg, IPS and DC for the  $(\eta + p_s)$  pair and  $p_f$  including the events selection and kinematical selection
- $\varepsilon_{detector}$  : the detector efficiency and over veto rate (Tagger, UpVeto, DC and RPC)

- $\varepsilon_{filling}$  : the correction factor of the electron filling mode dependence
- $\text{Br}_{\eta \rightarrow 2\gamma}$  : the branching fraction of the  $\eta \rightarrow 2\gamma$  process

Because  $\varepsilon_{DAQ}$  depends on the photon beam rate and the storage ring electron filling pattern, and the RPC has problematic chamber depending on run period,  $(N_\gamma \times \varepsilon_{DAQ} \times \Omega_{RPC})$  was evaluated run by run and summed up over all runs.  $\varepsilon_{detector}$  and  $\varepsilon_{filling}$  are averaged value over all data taking periods. Other variables are independent from run periods. We summarize the values in Table.6.1. We describe details of the variables in the following subsections.

Table 6.1: The summary of values used for the calculation of the cross sections.

	value	error
$\Sigma(N_\gamma \times \varepsilon_{DAQ} \times \Omega_{RPC})$	$1.59 \times 10^{11}$	
$\rho_N$	$1.74 \times 10^{23}$	$0.02 \times 10^{23}$
$Acc$	13.2%	0.7%
$\varepsilon_{detector}$	81.9%	2.9%
$\varepsilon_{filling}$	91.1%	1.2%
$\text{Br}_{\eta \rightarrow 2\gamma}$	39.41%	0.20%

## 6.1.2 The number of photons weighted with the RPC acceptance and the DAQ efficiency

### The number of photons

We evaluated the number of photons hit the target from the following equation:

$$N_\gamma = N_{scaler} \times f_{dead\ time} \times f_{not\ shower} \times T_{trans}. \quad (6.2)$$

$N_{scaler}$  is the number of beam photon counted with a scaler. When there are hits in both of pair tagger PLS, a logic signal is sent to the scaler. The width of the logic signal for the scaler is 20 ns. Thereby, photons coming from the same electron bunch or coming in the 20 ns dead time are not counted with the scaler. We evaluated the dead time correction factor  $f_{dead\ time}$  using a Monte Carlo (MC) simulation.  $f_{dead\ time}$  depends on the electron bunch filling pattern and the laser-electron collision rate. It varies between around 1.0 and 1.5. We evaluated  $N_{scaler} \times f_{dead\ time}$  run by run.

There are some events that an recoiled electron hit the box wall of the tagger or the vacuum chamber and create an electron shower, and the shower electrons hit PLS. Such events are not used in the analysis and should be excluded when we count the number of photons. We evaluated the fraction of events not from such showers  $f_{not\ shower}$ , using a special data taken with a lead glass counter. We measured the photon beam energy using the lead glass counter and evaluated the number of photons from the showers. The energy of photon beam

associated with a shower is smaller than 1.3 GeV, which is the lowest energy of in the tagger acceptance for recoil electrons without shower. We obtained  $f_{not\ shower} = (95.75 \pm 0.06)\%$ .

$T_{trans}$  is the photon transmission rate from the collision point to the target. It is 77.2% as described in section 2.1.4.

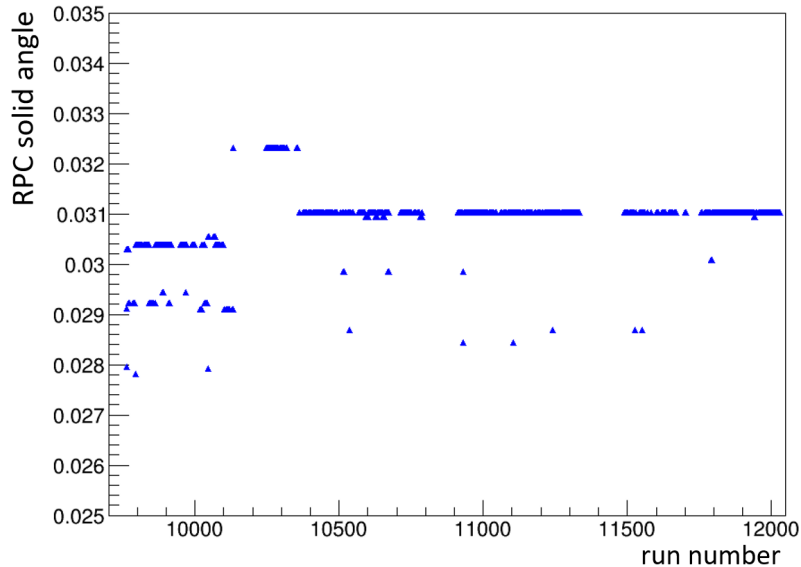
The total number of photon is  $N_\gamma = 5.87 \times 10^{12}$  when we sum up over 1129 runs used for the analysis.

### The DAQ efficiency

The DAQ efficiency,  $\varepsilon_{DAQ}$ , depends on the laser-electron collision rate. We corrected  $\varepsilon_{DAQ}$  run by run. A typical value of  $\varepsilon_{DAQ}$  was 83 – 97%.

### The RPC solid angle

There are 32 RPC chambers. Some of them suffered from occasional oscillation of amplifiers during data taking. In addition, the amplifier and the readout strip sometimes disconnected because of weak soldering. We excluded those problematic chambers from the analysis. The problematic chamber was defined run by run, thus the solid angle covered with the RPC depends on run. Figure 6.1 shows the run dependence of the solid angle of the RPC.



### 6.1.3 Number density of the target

We evaluated the number density of target nucleons  $\rho_N$  as

$$\rho_N = \frac{d_{target} \times N_A \times x}{A}. \quad (6.3)$$

Here,  $d_{target} = 1.73 \text{ g/cm}^3$  is the target density,  $N_A = 6.02 \times 10^{23} \text{ mol}$  is the Avogadro constant,  $x = 2.00 \text{ cm}$  is the target thickness, and  $A = 12.01$  is the standard atomic weight of C. We obtained  $\rho_N = (1.74 \pm 0.02) \times 10^{23}$ . The error mainly comes from the uncertainty of the measurement of  $d_{target}$  and  $x$ .

### 6.1.4 Acceptance

The acceptance for  $(\eta + p_s)$  pairs and  $p_f$  was evaluated using a Monte Carlo (MC) simulation based on Geant 4 [63]. All the detector system including support structures was implemented in the simulation. The same event selection and kinematical selection criteria described in chapter 4 and 5 were applied to the MC. We evaluated the acceptance for an  $(\eta + p_s)$  pair and  $p_f$  separately in different simulations.

#### Acceptance for $(\eta + p_s)$

For evaluation of the acceptance for  $(\eta + p_s)$ , we generated an hypothetical  $N^* \rightarrow \eta p$  reaction with the MC simulation, in which we implemented Fermi motion of carbon nucleus to the momentum of the  $N^*$  [64]. Both the  $\eta$  and proton are assumed to have isotropic angler distributions. We changed the mass of  $N^*$  in the range between 1850 and 1950 MeV. This energy corresponds to the excitation energy region around  $-50 \text{ MeV} < E_{ex} - E_0 < 50 \text{ MeV}$  for the case of the signal  $\eta' p \rightarrow \eta p$  reaction. We obtained the acceptance for the  $(\eta + p)$  pair in  $\cos \theta_{lab}^{p_s} < 0.5$  and  $\cos \theta_{lab}^{\eta} < 0$  to be  $Acc_{\eta+p_s} = (13.9 \pm 0.6)\%$ . The systematic error mainly comes from differences of the detector response between the MC and the real data. Details of the systematic error are described in Appendix F.

#### Acceptance for $p_f$

As explained in section 6.1.2, we evaluated the acceptance for  $p_f$  of the RPC run by run. We examined the acceptance for  $p_f$  of the DC by using a MC simulation. We generated an  $\gamma + p \rightarrow \eta' + p_f$  reaction, in which the proton flights to  $\theta_{lab}^{p_f} < 7^\circ$ , which roughly corresponds to the RPC acceptance. When  $p_f$  interacts in the target,  $p_f$  changes the direction and/or kicks out another particle. Then there can be no track in the DC or an additional track/cluster in the DC/BGOegg. Those events are excluded at the event selection stage. We evaluated the probability to pass the event selection criteria, which the number of DC track is one and no additional particle hit in the BGOegg. We obtained the acceptance for  $p_f$  of the DC,  $Acc_{DC_{p_f}} = (94.7 \pm 0.5)\%$ . Details are described in Appendix F.

## Total acceptance

In total, we obtained  $Acc = Acc_{\eta+p_s} \times Acc_{DC_{fp}} = (13.2 \pm 0.7)\%$ . This value includes the BGOegg, IPS reconstruction efficiencies and the over veto rate of the DC.

### 6.1.5 Detector efficiencies

In Table.6.2, we summarize the reconstruction, detection efficiencies of the tagger, DC and RPC and the over veto rate of the UpVeto. We evaluated the tagger PL intrinsic efficiency using events in which recoil electrons pass overlap regions of neighboring PLs. The tagger track reconstruction efficiency and the UpVeto over veto rate are evaluated using the  $\gamma + {}^{12}\text{C} \rightarrow 2\pi^0 + p_s + X$  data sample. We estimated the reconstruction efficiencies of these detectors from the  $\gamma + p \rightarrow \omega + p$ ,  $\gamma + p \rightarrow \eta + p$  data samples with the liquid hydrogen target after kinematical fitting. Details of the evaluation of the efficiencies are described in Appendix F. In total, we obtained  $\varepsilon_{detector} = (81.9 \pm 2.9)\%$ .

Table 6.2: The detector efficiencies and the over veto rate.

	value	error
Tagger PL intrinsic efficiency	98.8%	1.2%
Tagger track reconstruction efficiency	89.90%	0.81%
UpVeto over veto rate	97.84%	0.27%
DC reconstruction efficiency	98.24%	0.44%
RPC reconstruction efficiency	95.89%	2.32%
Total	81.9%	2.9%

### 6.1.6 Filling mode correction factor

Figure 6.2 shows the run dependence of the ratio of the number of measured events and  $N_\gamma \times \varepsilon_{tag}$  for the  $\gamma + {}^{12}\text{C} \rightarrow (\pi^0 + \eta) + p_f + X$  and  $\gamma + {}^{12}\text{C} \rightarrow (\omega + p_s) + X$  reactions. Here,  $(\pi^0 + \eta)$  and  $(\omega + p_s)$  were detected with BGOegg, and  $p_f$  was detected with the RPC. The electron filling modes of the storage ring are indicated with Alphabets. The tagger reconstruction efficiency  $\varepsilon_{tag}$  depends on the electron filling mode and thus the tagger efficiency depending on the cycle is taken into account. The electron bunch structure of each filling mode is summarized in Appendix A. We normalized the ratio so that the ratio of the first C-mode data (shown with thick letters) to be one. The red and blue points shows the ratios of events with  $E_\gamma > 1.8$  GeV and  $E_\gamma < 1.8$  GeV, respectively. We observe smaller ratio in the first A-mode (yellow letters) and D, E and H-mode (green letters). In the first A-mode cycle, we observed smaller transmission rate of beam photons than other periods because of bad focus point of lasers. The low transmission rate was also observed in the liquid hydrogen target data taken in 2014 and there were  $E_\gamma$  dependence. On the other hand, the  $E_\gamma$  dependence of the transmission rate of the first A-mode of the carbon

data is small and negligible when we count the total number of photons. The details of the drop of the transmission rate is described in Appendix F.3. The D, E and H-mode have concentrated train bunches as described in Appendix A. The smaller ratios of the D, E and H-modes are considered to be from smaller event reconstruction efficiencies at the concentrated bunch regions. We evaluated an correction factor of this filling mode dependence from the  $\gamma + {}^{12}\text{C} \rightarrow (\omega + p_s) + X$  data. We used all C-mode and 2nd A-mode cycle data (indicated with black colors) as a reference. The evaluated correction factor is  $\varepsilon_{filling} = \frac{\omega + p_s}{N_\gamma \times \varepsilon_{tag}}(\text{all cycle}) / \frac{\omega + p_s}{N_\gamma \times \varepsilon_{tag}}(\text{reference cycle}) = (91.10 \pm 1.19)\%$ .

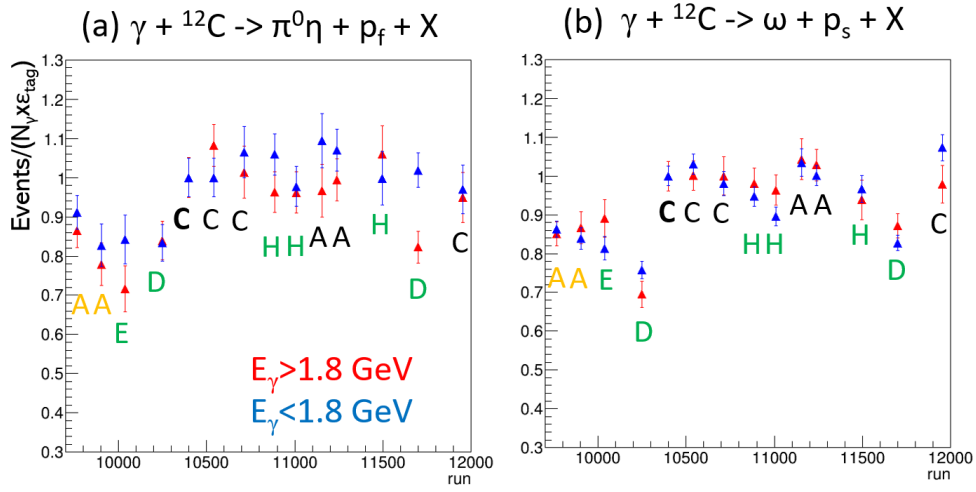


Figure 6.2: The filling mode dependence of the ratio of the number of measured events and  $N_\gamma \times \varepsilon_{tag}$  of the  $\gamma + {}^{12}\text{C} \rightarrow (\pi^0 + \eta) + p_f + X$  and  $\gamma + {}^{12}\text{C} \rightarrow (\omega + p_s) + X$  reactions.

### 6.1.7 Pion contamination to the forward particle

Since we do not have the particle identification capability in the forward going particles, pions can be contaminated to forward going protons. We investigated the contamination rate of pions as follows. Figure 6.3 shows a scatter plot of  $T_{RPC} - T_{RF}$  and the missing energy  $E_{miss}^{\eta' p_f}$  of the  $\gamma + {}^{12}\text{C} \rightarrow p_f + \eta' + X$  data. The events in  $E_{miss}^{\eta' p_f} < -150$  MeV are pions. The number of events in  $-1000$  MeV  $< E_{miss}^{\eta' p_f} < -200$  MeV is 14 events in the  $\eta'$  tag data and 9 events in the  $\eta'$  invariant mass side band data. Thus, the pion contamination rate per 300 MeV of  $E_{miss}^{\eta' p_f}$  (corresponds to the missing energy cut of  $-150$  MeV  $< E_{miss} < 150$  MeV, which we selected with the event and kinematical selections) is  $1.9 \pm 1.8$  events. This is  $(0.7 \pm 0.7)\%$  of the total 265  $\eta'$  events. We set the upper limit of the pion contamination to 1.4%.

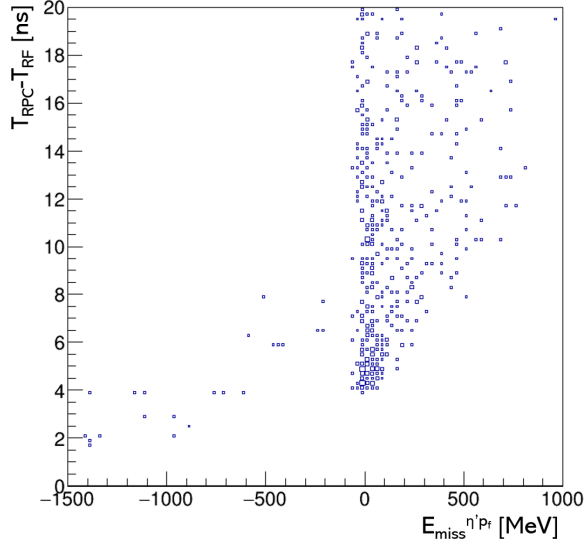


Figure 6.3: A scatter plot of  $T_{RPC} - T_{RF}$  and the missing energy  $E_{miss}^{\eta'p_f}$  of the  $\gamma + {}^{12}\text{C} \rightarrow p_f + \eta' + \text{X}$  data.

### 6.1.8 Branching fraction of $\eta \rightarrow 2\gamma$ mode

According to the summary table by Particle Data Group (PDG) [1], the branching fraction of the  $2\gamma$  decay mode of the  $\eta$  meson is  $\text{Br}_{\eta \rightarrow 2\gamma} = (39.41 \pm 0.20)\%$ . We used this value for the calculation of the cross section.

### 6.1.9 Systematic error

The systematic uncertainty of the cross section measurement was evaluated from a quadratic sum of the systematic errors shown in Table.6.1 and the pion contamination fraction. The obtained value is  $\sigma_{syst} = 5.4\%$ .

## 6.2 The $\eta'$ escape measurement

### 6.2.1 Formulation

The acceptance for the  $\eta'$  meson depends on its kinetic energy ( $T_{\eta'}$ ) and polar angle ( $\theta_{lab}^{\eta'}$ ). Because there are final state interactions, it is difficult to reproduce the experimental kinetic energy and polar angle distributions with a Monte Carlo (MC) simulation. Therefore, we made an acceptance correction event by event according to the measured  $T_{\eta'}$  and  $\theta_{lab}^{\eta'}$ . The cross section of the  $\eta'$  escape process averaged in  $\theta_p = 0.9 - 6.8^\circ$  and  $E_\gamma = 1.28 - 2.4$  GeV is

expressed as

$$\overline{\left(\frac{d\sigma}{d\Omega_{p_f}}\right)^{\eta'esc}} = \left(\sum_{i=0}^N \frac{1}{Acc[i]}\right) \times \frac{1}{\Sigma(N_\gamma \times \varepsilon_{DAQ} \times \Omega_{RPC}) \times \rho_N \times \varepsilon_{detector} \times \varepsilon_{filling} \times Br_{\eta' \rightarrow 2\gamma}} \quad (6.4)$$

Here,  $i$  is the event number and  $N$  is the total number of events.  $Acc[i]$  is the acceptance for  $\eta'$  meson of the  $i$ th event. Other variables are described in section 6.1.1. They are common to the  $(\eta + p_s)$  measurement, except for the branching fraction of the  $\eta' \rightarrow 2\gamma$  process,  $Br_{\eta' \rightarrow 2\gamma} = (2.20 \pm 0.08)\%$  [1]. When we estimate cross sections with different  $E_\gamma$  regions,  $N_\gamma$  in each  $E_\gamma$  bin was estimated assuming the photon beam energy distribution of a backward Compton scattering shown in Fig.2.5. To subtract the contribution of the combinatorial background, the cross section of the side band of the invariant mass ( $4\sigma < |M_{\gamma\gamma}| < 8\sigma$ ) was subtracted. The statistical error of the cross section is described as

$$\sigma_{stat}^{\eta'esc} = \sqrt{\left(\sum_{i=0}^N \frac{1}{Acc[i]^2}\right)} \times \frac{1}{\Sigma(N_\gamma \times \varepsilon_{DAQ} \times \Omega_{RPC}) \times \rho_N \times \varepsilon_{detector} \times \varepsilon_{filling} \times Br_{\eta' \rightarrow 2\gamma}} \quad (6.5)$$

## 6.2.2 The $\eta'$ acceptance

We estimated the acceptance of BGOegg and the IPS for the  $\eta'$  meson as a function of  $T_{\eta'}$  and  $\theta_{lab}^{\eta'}$  by using a MC simulation. The procedure is common to the MC simulation for the  $(\eta + p_s)$  measurement described in section 6.1.4. Instead of the  $N^* \rightarrow \eta p$  reaction, we implemented a  $\gamma + p \rightarrow \eta' + p$  reaction. In the MC simulation, the Fermi motion of a target proton was taken into account but the final state interaction of  $\eta'$  and  $p$  was not taken into account. In Table.6.3, we show the acceptance for  $\eta'$  in each  $T_{\eta'}$  and  $\theta_{lab}^{\eta'}$  region evaluated with the MC simulation. Several kinematical regions show very small acceptance.

Since the final state interaction was not taken into account in the MC simulation, there can be discrepancy between the MC and the experimental data in the  $T_{\eta'}$  and  $\theta_{lab}^{\eta'}$  distributions. Figure 6.4 shows the  $\theta_{lab}^{\eta'}$  distribution in  $T_{\eta'} < 100$  MeV and  $T_{\eta'}$  distribution in  $\cos \theta_{lab}^{\eta'} > 0.9$ , of the accepted events in the MC and the experimental data. The  $\eta'$  polar angle distributions are consistent within the statistical error. On the other hand, the kinetic energy distributions are inconsistent. Because the angle distributions are consistent, we evaluated acceptance as only a function of  $T_{\eta'}$  with the weight of the  $\cos \theta_{lab}^{\eta'}$  distribution of the MC. It is summarized in Table.6.4. As the statistical error is described in Eq.(6.5), a small acceptance gives a large statistical error. The averaged acceptance over  $\cos \theta_{lab}^{\eta'}$  helped to reduce the statistical error coming from the small acceptance regions.

## 6.2.3 The $\eta'$ angle region

Figure 6.5 shows the two-dimensional plot of the  $\eta'$  polar angle  $\theta_{lab}^{\eta'}$  and kinetic energy  $T_{\eta'}$  of the  $\eta'$  tag events (red) and the invariant mass side band events (blue). They are plotted on the acceptance table same as Table.6.3. Although we have several events in  $\cos \theta_{lab}^{\eta'} < 0$

Table 6.3: The acceptance of BGOegg and the IPS for  $\eta'$  meson as a function of the  $\eta'$  kinetic energy ( $T_{\eta'}$ ) and polar angle ( $\theta_{lab}^{\eta'}$ ) estimated with a MC simulation. “0” means no accepted events and “-” means no generated events.

$T_{\eta'}$ [MeV]	0–	100–	200–	300–	400–	500–	600–	700–	800–	900–
$\cos \theta_{lab}^{\eta'}$	100	200	300	400	500	600	700	800	900	1000
0.8 – 1.0	0.687	0.613	0.524	0.414	0.286	0.166	0.089	0.055	0.027	0.013
0.6 – 0.8	0.667	0.513	0.035	0.009	0.007	0	0	0	–	–
0.4 – 0.6	0.656	0.354	0	0	–	–	–	–	–	–
0.2 – 0.4	0.629	0.250	–	–	–	–	–	–	–	–
0.0 – 0.2	0.609	–	–	–	–	–	–	–	–	–
-0.2 – 0.0	0.652	–	–	–	–	–	–	–	–	–
-0.4 – -0.2	0.444	–	–	–	–	–	–	–	–	–
-0.6 – -0.4	0	–	–	–	–	–	–	–	–	–
-0.8 – -0.6	0.167	–	–	–	–	–	–	–	–	–
-1.0 – -0.8	–	0	–	–	–	–	–	–	–	–

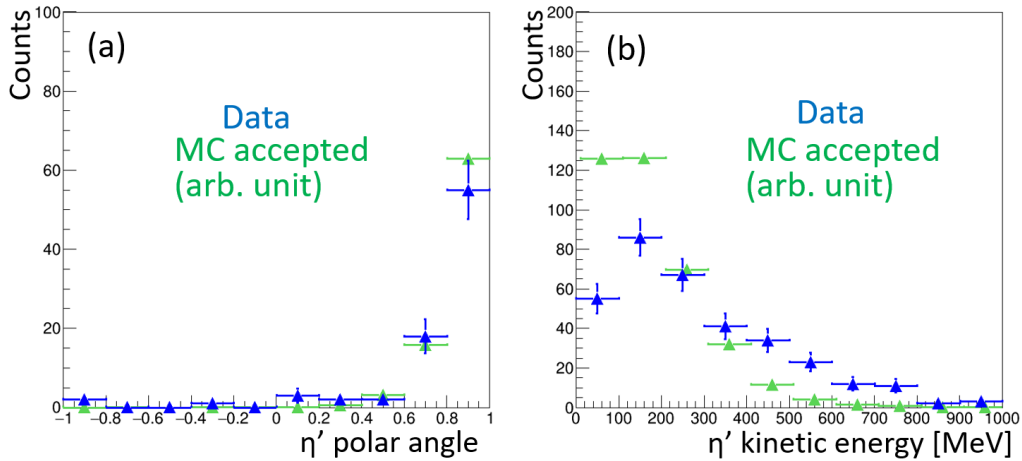


Figure 6.4: The  $\eta'$  polar angle distributions and kinetic energy distributions of the experimental data (blue) and the MC (green).

in the experimental data, there were almost no generated events in the MC. The number of events in  $\cos \theta_{lab}^{\eta'} < 0$  is the same for the  $\eta'$  tag data and side band data. This means that the combinatorial background events from multi pions are dominant in  $\cos \theta_{lab}^{\eta'} < 0$ . We evaluated the  $\eta'$  coincidence cross section only in  $\cos \theta_{lab}^{\eta'} > 0$ .

Table 6.4: The acceptance of BGOegg and the IPS for  $\eta'$  meson as a function of the  $\eta'$  kinetic energy.

$\eta'$ kinetic energy	acceptance
0–100 MeV	68.1%
100–200 MeV	60.7%
200–300 MeV	51.5%
300–400 MeV	40.3%
400–500 MeV	27.7%
500–600 MeV	16.3%
600–1000 MeV	5.3%

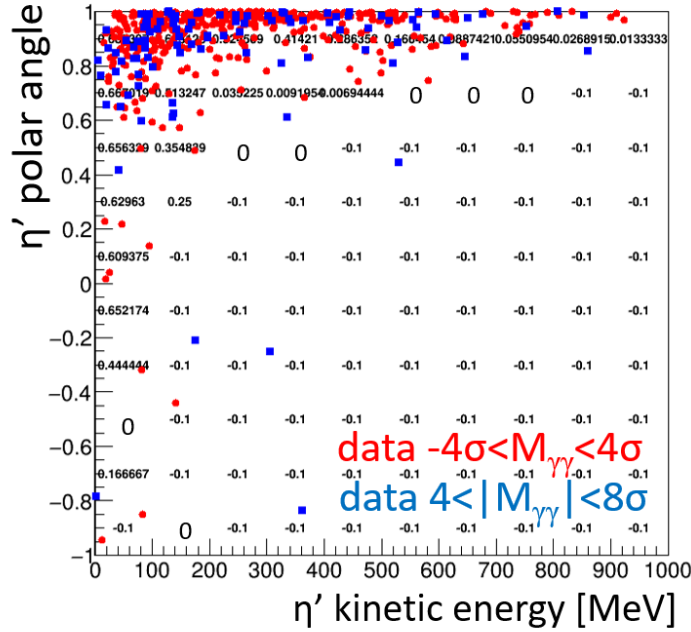


Figure 6.5: The two-dimensional plot of the  $\eta'$  polar angle and kinetic energy of the  $\eta'$  tag events (red) and side band events (blue) plotted on the acceptance table. “-0.1” means no generated events.

### 6.2.4 Systematic error

The systematic uncertainty of the  $\eta'$  cross section evaluation was estimated in the similar way as  $(\eta + p_s)$  measurement. The obtained value is  $\sigma_{syst} = 6.7\%$ .

# Chapter 7

## Experimental results and discussion

### 7.1 Experimental results

#### 7.1.1 Upper limit of the production cross section of the $\eta'$ -nucleus bound state with $(\eta + p_s)$ emission

As shown in chapter 5, no  $(\eta + p_s)$  events from  $\eta'$ -nucleus bound states were observed in  $-50 \text{ MeV} < E_{\text{ex}} - E_0 < 50 \text{ MeV}$  after the kinematical cut. Assuming a Poisson distribution, an upper limit of the number of events for a null result at the 90% confidence level is assigned as [65]

$$N_{up} = 2.30 \times (1 + 2.30 \times \sigma_{syst}^2/2), \quad (7.1)$$

where  $\sigma_{syst}$  is the systematic error of the measurement. Then, the upper limit of the production cross section of the  $\eta'$ -nucleus bound state in coincidence with an  $(\eta + p_s)$  emission is given as

$$\overline{\left(\frac{d\sigma}{d\Omega_{p_f}}\right)}_{up}^{(\eta+p_s)} = \frac{N_{up}}{\Sigma(N_\gamma \times \varepsilon_{DAQ} \times \Omega_{RPC}) \times \rho_N \times Acc \times \varepsilon_{detector} \times \varepsilon_{filling} \times \text{Br}_{\eta \rightarrow 2\gamma}} \quad (7.2)$$

The meaning and value of the variables are described in section 6.1. We obtained that the upper limit of the production cross section of the  $\eta'$ -bound state in coincidence with an  $(\eta + p_s)$  pair emission in  $\cos \theta_{lab}^{\eta p_s} < -0.9$ ,  $-50 \text{ MeV} < E_{\text{ex}} - E_0 < 50 \text{ MeV}$  and  $\theta_{lab}^{p_f} = 0.9 - 6.8^\circ$ , under photon beam distribution of a backward Compton scattering in 1.28-2.4 GeV to be 2.2 nb/sr, at the 90% confidence level.

#### 7.1.2 Cross section of the $\eta'$ escape process

Figure 7.1 shows the excitation energy dependence of the cross section for the  $\eta'$  escape process in five different  $E_\gamma$  regions. We observed enhancement at  $1.6 \text{ GeV} < E_\gamma < 1.8 \text{ GeV}$ . This comes from the large transformation factor of the cross section from the center-of-mass frame to the laboratory frame near the production threshold ( $E_\gamma = 1.447 \text{ GeV}$  for a

proton at rest). At  $E_\gamma < 1.6$  GeV,  $\sqrt{s}$  can be smaller than the  $\eta'$  production threshold ( $\sqrt{s} = 1.896$  GeV) even above  $E_\gamma = 1.447$  GeV because of the Fermi motion of the target proton, and thus the cross section decrease. The peak position of the excitation energy spectrum moves to lower excitation energy with increasing  $E_\gamma$ . This is because of small momentum transfer at lower  $E_\gamma$ . These behaviors are clearly understood by seeing  $E_\gamma$  vs excitation energy distribution of a MC simulation. Figure 7.2(a) shows a two dimensional plot of  $E_\gamma$  and excitation energy distribution of the experimental data. Figure 7.2(b) and (c) show the distributions of MC simulations of the  $\gamma p \rightarrow \eta' p$  reaction (b) with and (c) without Fermi motion. The distributions in (a) and (b) are quite similar. From Fig.7.2(c), we can see that the distributions moves to higher excitation energy with lower  $E_\gamma$ . The  $E_\gamma$  dependence of the momentum transfer is shown in Fig.1.8. We can see that the shift of the peak position of the excitation energy is correlated with the momentum transfer. The events in  $E_{\text{ex}} - E_0^{\gamma\gamma} < 200$  MeV in Fig.7.2(c) corresponds to events in  $\cos\theta_{\eta'}^{CM} < 0$  and events in  $E_{\text{ex}} - E_0^{\gamma\gamma} > 200$  MeV corresponds to events in  $\cos\theta_{\eta'}^{CM} > 0$ . Supplements of the  $\eta'$  escape cross section measurement is describe in Appendix H.

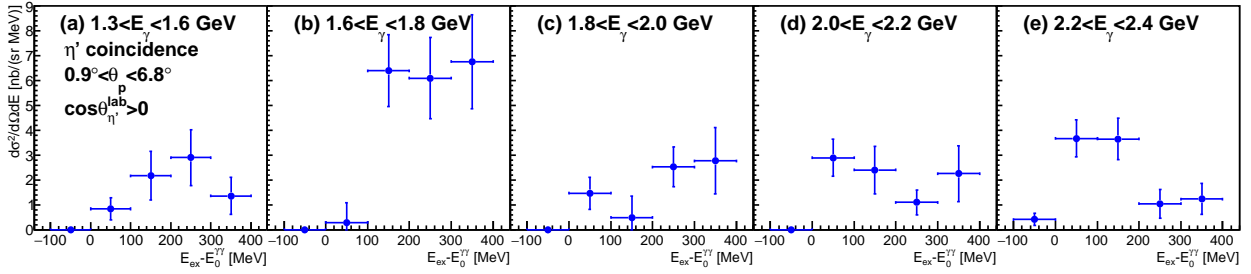


Figure 7.1: The excitation energy spectra of the  $\eta'$  escape reaction in five different  $E_\gamma$  region.

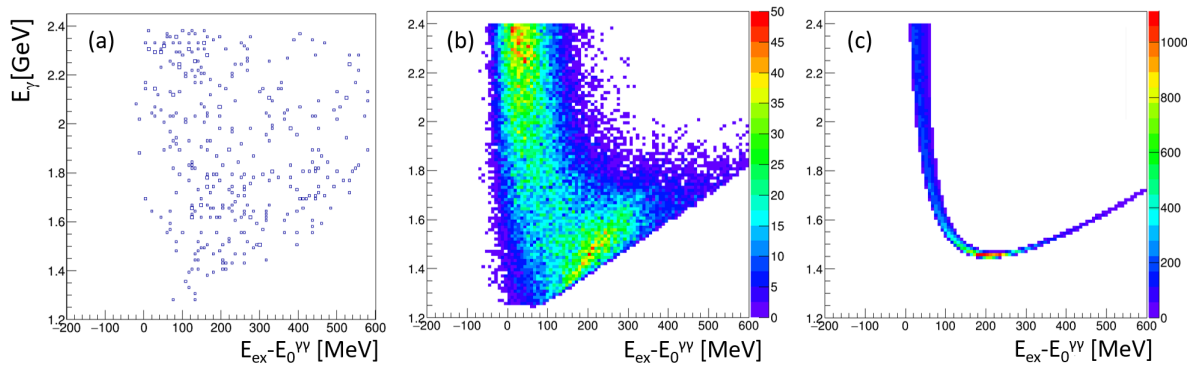


Figure 7.2: The  $E_\gamma$  vs excitation energy distributions. (a) experimental data, (b) MC simulation with Fermi motion, (c) MC simulation without Fermi motion.

As described in section 1.5, for the evaluation of the normalization factor  $F$  of the theoretical cross section, the  $\eta'$  escape cross section integrated over  $0 \text{ MeV} < E_{\text{ex}} - E_0^{\gamma\gamma} < 50 \text{ MeV}$ , and averaged in  $E_\gamma = 1.3 - 2.4 \text{ GeV}$  is used. As can be seen in Fig.5.2, the observed number of events in this region is  $17.0 \pm 4.4$  events. (19 events in the  $\eta'$  tag data and 2 events in the  $\eta'$  side band data.) It is only 6% of all observed  $\eta'$  events. From Eq.(6.4), the cross section of  $\eta'$  escape events in  $\theta_{lab}^{p_f} = 0.9 - 6.8^\circ$ , integrated in  $0 \text{ MeV} < E_{\text{ex}} - E_0^{\gamma\gamma} < 50 \text{ MeV}$ , and averaged over  $E_\gamma = 1.28 - 2.4 \text{ GeV}$  was obtained as

$$\overline{\left(\frac{d\sigma}{d\Omega_{p_f}}\right)}_{exp}^{\eta'esc} = 60.2 \pm 15.4(stat) \pm 4.1(syst) \text{ nb/sr}. \quad (7.3)$$

## 7.2 Estimation of the $\eta'$ -nucleus potential $V_0$

In this section, we estimate the real part of the  $\eta'$ -nucleus potential  $V_0$ . We estimate  $V_0$  from the experimental upper limit of the cross section and the theoretical expected cross section calculated within a distorted wave impulse approximation (DWIA). We estimate  $V_0$  as a function of the branching fraction of the  $\eta'N \rightarrow \eta N$  absorption process.

### 7.2.1 Overview

We calculated the expected excitation energy spectrum  $E_{\text{ex}} - E_0$  of the  $\eta'$ - $^{11}\text{B}$  nucleus bound state in the framework of a distorted wave impulse approximation (DWIA) [23, 44]. The calculation was carried out for the case of  $V_0 = -100$  and  $-20 \text{ MeV}$ , and  $W_0 = -12 \text{ MeV}$ . We chose  $W_0$  consistent with the measured value by the CBELSA/TAPS Collaboration,  $W_0 = -(13 \pm 3(stat) \pm 3(syst)) \text{ MeV}$  [9]. The obtained spectrum is integrated in  $-50 \text{ MeV} < E_{\text{ex}} - E_0 < 50 \text{ MeV}$  and averaged over  $E_\gamma = 1.28 - 2.4 \text{ GeV}$  to compare with the obtained experimental upper limit of the cross section. The DWIA calculation is decomposed in two processes; the  $\eta'$  escape and  $\eta'$ absorption. Although DWIA calculations nicely represent spectral shapes of bound states, it hardly reproduces their absolute cross sections [25–30]. We evaluated normalization factor  $F$  of the theoretical cross section from the  $\eta'$  escape process. The branching fraction of the  $\eta'N \rightarrow \eta N$  absorption process in all the  $\eta'$  absorption process,  $\text{Br}_{\eta'N \rightarrow \eta N}$ , is unknown. In addition, the  $(\eta + N)$  pair can be absorbed by nucleons due to final state interaction even they were produced. We evaluated the probability  $P_{srv}^{\eta p_s}$  that an  $(\eta + p_s)$  pair is emitted in  $\cos \theta_{lab}^{\eta p_s} < -0.9$  using a quantum molecular dynamics (QMD) transport model calculation. The experimental upper limit of the cross section of the  $\eta'$ -bound states with  $(\eta + p_s)$  emission is compared with the theoretical cross section in different  $V_0$  cases as a function of  $\text{Br}_{\eta'N \rightarrow \eta N}$ . In section 7.2.2 and 7.2.3, we describe the formulation and procedure of the calculation. Details of the calculations are described in Appendix G. In section 7.2.4, we describe the evaluation of the normalization factor  $F$ . We evaluate  $V_0$  from the comparison of the experimental upper limit of the cross section with theoretical cross section in section 7.2.5 and 7.2.6.

## 7.2.2 Formulation

Within a DWIA, an excitation energy spectrum of the  $\eta'$ - $^{11}\text{B}$  nucleus bound state can be described as

$$\left(\frac{d^2\sigma}{d\Omega_{p_f}dE_{\text{ex}}}\right)_{\text{theory}}^{\gamma+^{12}\text{C}\rightarrow p+\eta'+^{11}\text{B}} = \overline{\left(\frac{d\sigma}{d\Omega_{p_f}}(E_{\text{ex}})\right)_{\text{lab}}^{\gamma+p\rightarrow p+\eta'}} \times R(E_{\text{ex}}). \quad (7.4)$$

Here,  $E_{\text{ex}}$  is the excitation energy,  $\overline{\left(\frac{d\sigma}{d\Omega}(E_{\text{ex}})\right)_{\text{lab}}^{\gamma+p\rightarrow p+\eta'}}$  the Fermi-averaged cross section of the elementary  $\gamma + p \rightarrow p + \eta'$  reaction [66], and  $R(E)$  the nuclear response function. An example of results of  $\left(\frac{d^2\sigma}{d\Omega_{p_f}dE_{\text{ex}}}\right)_{\text{theory}}^{\gamma+^{12}\text{C}\rightarrow p+\eta'+^{11}\text{B}}$  for the case of  $E_\gamma = 2.05$  GeV are shown in Fig.7.3 (same figure as in Fig.1.9). The calculation results are decomposed into the  $\eta'$  escape and absorption processes as

$$\left(\frac{d^2\sigma}{d\Omega_{p_f}dE_{\text{ex}}}\right)_{\text{theory}}^{\gamma+^{12}\text{C}\rightarrow p+\eta'+^{11}\text{B}} = \left(\frac{d^2\sigma}{d\Omega_{p_f}dE_{\text{ex}}}\right)_{\text{theory}}^{\eta' \text{ esc}} + \left(\frac{d^2\sigma}{d\Omega_{p_f}dE_{\text{ex}}}\right)_{\text{theory}}^{\eta' \text{ abs}}. \quad (7.5)$$

The  $\eta'$  absorption process contributes below and above the production threshold  $E_{\text{ex}} - E_0 = 0$  MeV. On the other hand, the  $\eta'$  escape process contributes only above the production threshold.

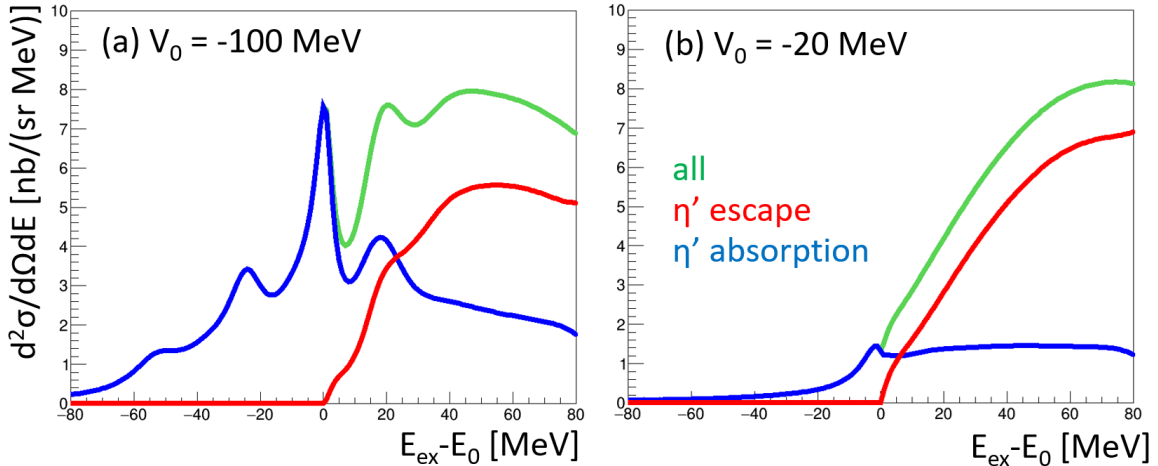


Figure 7.3: The excitation spectra calculated within the DWIA in the cases of  $V_0 = -100$  and  $-20$  MeV,  $W_0 = -12$  MeV,  $\theta_p = 6^\circ$  and  $E_\gamma = 2.05$  GeV.

## 7.2.3 Calculation procedure

We integrated the theoretical cross sections over  $E_{\text{ex}}$ , and averaged over  $E_\gamma$  to compare with the experimental upper limit of the cross section. We calculated the theoretical cross section in the following procedure.

1. Calculate  $R(E_{\text{ex}})$ .
2. Calculate  $\overline{\left(\frac{d\sigma}{d\Omega_{p_f}}(E_{\text{ex}})\right)_{lab}^{\gamma+p \rightarrow p+\eta'}}$ .
3. Integrate over  $E_{\text{ex}}$ .
4. Average over  $E_\gamma$ .

Then, we evaluated the expected cross section of the  $(\eta + p_s)$  coincidence process as follows.

5. Evaluate the normalization factor  $F$  of the theoretical cross section from the  $\eta'$  escape process.
6. Evaluate the probability  $P_{srv}^{\eta p_s}$  in which an  $(\eta + p_s)$  pair is emitted in  $\cos\theta_{lab}^{\eta p_s} < -0.9$  after the  $\eta'N \rightarrow \eta N$  absorption process.

The nuclear response function  $R(E)$  is calculated by Nagahiro for the cases of  $V_0 = -20$ ,  $-100$  MeV,  $W_0 = -12$  MeV,  $E_\gamma = 1.5, 2.05, 2.5$  GeV, and  $\theta_{lab}^{p_f} = 6^\circ$  [44]. For the calculation of  $\overline{\left(\frac{d\sigma}{d\Omega_{p_f}}(E_{\text{ex}})\right)_{lab}^{\gamma+p \rightarrow p+\eta'}}$ , we used the elementary cross section in the center-of-mass frame,  $\left(\frac{d\sigma}{d\Omega}\right)_{c.m.}^{\gamma+p \rightarrow p+\eta'} = 40$  nb/sr in  $\cos\theta_{c.m.}^{\eta'} < -0.9$  and  $\sqrt{s} < 2.4$  GeV, measured by the LEPS [67] and CBELSA/TAPS [68] Collaborations. When we integrated over  $E_{\text{ex}}$ , we took into account the experimental detector resolutions. The integrated ranges of  $E_{\text{ex}}$  were  $-50$  MeV  $< E_{\text{ex}} - E_0 < 50$  MeV and  $0$  MeV  $< E_{\text{ex}} - E_0 < 50$  MeV for the  $\eta'$  absorption and  $\eta'$  escape processes, respectively:

$$\left(\frac{d\sigma}{d\Omega_{p_f}}\right)_{theory}^{\eta'abs} = \int_{-50}^{+50} \left(\frac{d^2\sigma}{d\Omega_{p_f}dE_{\text{ex}}}\right)_{theory}^{\eta'abs} dE_{\text{ex}}, \quad (7.6)$$

$$\left(\frac{d\sigma}{d\Omega_{p_f}}\right)_{theory}^{\eta'esc} = \int_0^{+50} \left(\frac{d^2\sigma}{d\Omega_{p_f}dE_{\text{ex}}}\right)_{theory}^{\eta'esc} dE_{\text{ex}}. \quad (7.7)$$

Then, they are averaged over  $E_\gamma$ , with the experimental  $E_\gamma$  distribution of a backward Compton scattering (BCS),  $I(E_\gamma)$ , shown in Fig.2.4.

$$\overline{\left(\frac{d\sigma}{d\Omega_{p_f}}\right)_{theory}^{\eta'abs}} = \int_{1.28}^{2.4} \left(\frac{d\sigma}{d\Omega_{p_f}}\right)_{theory}^{\eta'abs} I(E_\gamma) dE_\gamma / \int_{1.28}^{2.4} I(E_\gamma) dE_\gamma, \quad (7.8)$$

$$\overline{\left(\frac{d\sigma}{d\Omega_{p_f}}\right)_{theory}^{\eta'esc}} = \int_{1.28}^{2.4} \left(\frac{d\sigma}{d\Omega_{p_f}}\right)_{theory}^{\eta'esc} I(E_\gamma) dE_\gamma / \int_{1.28}^{2.4} I(E_\gamma) dE_\gamma \quad (7.9)$$

We evaluated the normalization factor  $F$  by comparing the experimental and theoretical cross sections of the  $\eta'$  escape process:

$$F = \overline{\left(\frac{d\sigma}{d\Omega_{p_f}}\right)_{exp}^{\eta'esc}} / \overline{\left(\frac{d\sigma}{d\Omega_{p_f}}\right)_{theory}^{\eta'esc}}. \quad (7.10)$$

$F$  is common for all  $E_{\text{ex}}$  region as long as the DWIA calculation reproduces the experimental spectrum shape, and is common to the  $\eta'$  escape and  $\eta'$  absorption process. The theoretical production cross section of the  $\eta'$  bound states with  $(\eta + p_s)$  emission can be described as

$$\overline{\left(\frac{d\sigma}{d\Omega_{p_f}}\right)}_{theory}^{\eta+p_s} = F \times \overline{\left(\frac{d\sigma}{d\Omega_{p_f}}\right)}_{theory}^{\eta'abs} \times \text{Br}_{\eta'N \rightarrow \eta N} \times P_{srv}^{\eta p_s}. \quad (7.11)$$

Here,  $F$  is the normalization factor of the theoretical cross section.  $\text{Br}_{\eta'N \rightarrow \eta N}$  is the unknown branching fraction of the  $\eta'N \rightarrow \eta N$  process in all the  $\eta'$  absorption process. The  $(\eta + N)$  pair is originally emitted back-to-back. They interact with nucleons in nucleus and can change their direction or be absorbed by (a) nucleon(s). We are interested in a case that an  $(\eta + p_s)$  pair, not an  $(\eta + n)$  pair, is emitted in  $\cos\theta_{lab}^{\eta p_s} < -0.9$ . We evaluated the probability  $P_{srv}^{\eta p_s}$  that an  $(\eta + p_s)$  pair is emitted in  $\cos\theta_{lab}^{\eta p_s} < -0.9$  after interactions of an  $(\eta + N)$  pair in the residual nucleus. We evaluated  $P_{srv}^{\eta p_s}$  using a quantum molecular dynamics (QMD) transport model calculation [57].

We describe the details of the procedure 1–4 in Appendix G. We describe the details of the procedure of the calculation of the cross section with  $(\eta + p_s)$  emission (procedure 5 and 6) in the following sections.

## 7.2.4 Normalization factor of the theoretical cross section

### Comparison of the $E_\gamma$ dependence

Because we use the average cross section over  $E_\gamma$  for evaluating  $F$ , we compared the  $E_\gamma$  dependence of the experimental and theoretical cross sections of the  $\eta'$  escape process before evaluation of  $F$ . In Fig.7.4, black circles show the experimental cross section and red points show the theoretical cross sections. Red lines are the fitting results of three points by quadratic functions. The  $E_\gamma$  dependence of the experimental and theoretical cross sections agree, and thus we can compare the average cross section over  $E_\gamma$ . We note that, in Ref.[44], the elementary cross section for a proton at rest is used in Eq.(7.4) instead of the Fermi-averaged cross section. As shown by the blue line in Fig.7.4, the calculation without Fermi motion is divergent near the production threshold because of a large CM-to-laboratory transformation factor of the cross section. It is clearly unsuitable to use the calculation result without Fermi motion for describing the observed  $E_\gamma$  dependence, and therefore we adopted the Fermi averaged cross section in Eq.(7.4).

### Evaluation of $F$

By averaging the red lines in Fig.7.4 over  $E_\gamma = 1.28 - 2.4$  GeV, with weight of the BCS photon beam energy distribution, we obtained the expected theoretical cross sections of the

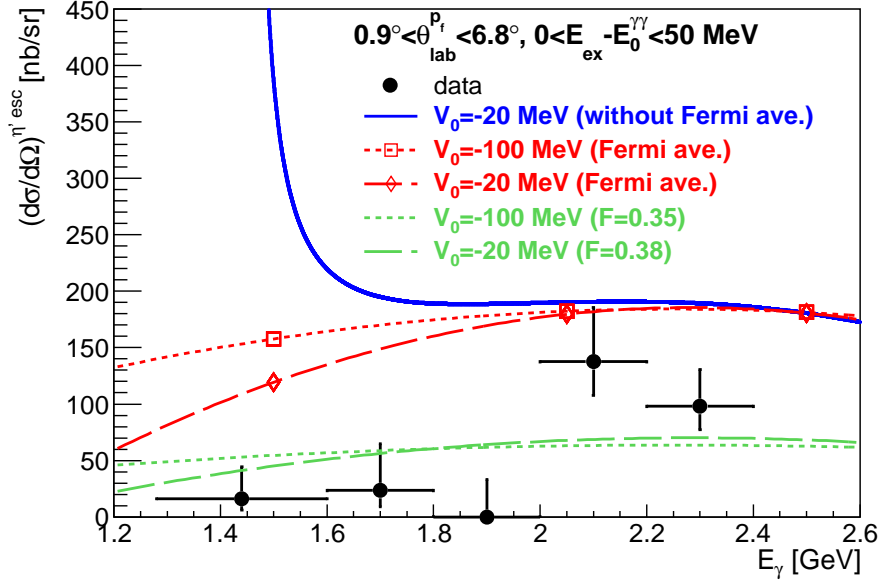


Figure 7.4: The  $E_\gamma$  dependence of  $\left(\frac{d\sigma}{d\Omega_{p_f}}\right)_{exp}^{\eta' esc}$  (black circles) and  $\left(\frac{d\sigma}{d\Omega_{p_f}}\right)_{theory}^{\eta' esc}$  (red lines) in  $0 \text{ MeV} < E_{ex} - E_0^{\gamma\gamma} < 50 \text{ MeV}$ . The original  $\left(\frac{d\sigma}{d\Omega_{p_f}}\right)_{theory}^{\eta' esc}$  based on Ref.[44] without using the Fermi averaging method is shown by the blue line. The theoretical calculations after the normalization are shown in green lines.

$\eta'$  escape process:

$$\overline{\left(\frac{d\sigma}{d\Omega_{p_f}}\right)_{theory}^{\eta' esc}} = 173.8 \text{ nb/sr} \quad (V_0 = -100 \text{ MeV}), \quad (7.12)$$

$$\overline{\left(\frac{d\sigma}{d\Omega_{p_f}}\right)_{theory}^{\eta' esc}} = 159.1 \text{ nb/sr} \quad (V_0 = -20 \text{ MeV}). \quad (7.13)$$

As shown in the previous section, the experimental cross section in  $0 < E_{ex} - E_0 < 50 \text{ MeV}$ , averaged over  $E_\gamma = 1.28 - 2.4 \text{ GeV}$  is

$$\overline{\left(\frac{d\sigma}{d\Omega_{p_f}}\right)_{exp}^{\eta' esc}} = 60.2 \pm 15.4(stat) \pm 4.1(syst) \text{ nb/sr}. \quad (7.14)$$

By substituting the above values and the experimental cross section in Eq.(7.14) to Eq.(7.10), we obtained

$$F = 0.35 \pm 0.09(stat) \pm 0.02(syst) \quad (V_0 = -100 \text{ MeV}), \quad (7.15)$$

$$F = 0.38 \pm 0.10(stat) \pm 0.03(syst) \quad (V_0 = -20 \text{ MeV}). \quad (7.16)$$

The theoretical cross sections after the normalization correction are shown with green lines in Fig.7.4. The difference between two  $V_0$  cases is too small to distinguished each other.

### 7.2.5 Cross section of the $(\eta + p_s)$ coincidence reaction

As described in section 7.2.3, the theoretical production cross section of the  $\eta'$  bound states coincidence with  $(\eta + p_s)$  emission can be described as

$$\overline{\left(\frac{d\sigma}{d\Omega_{p_f}}\right)_{theory}^{\eta+p_s}} = F \times \overline{\left(\frac{d\sigma}{d\Omega_{p_f}}\right)_{theory}^{\eta'abs}} \times \text{Br}_{\eta'N \rightarrow \eta N} \times P_{srv}^{\eta p_s}. \quad (7.17)$$

$F$  is obtained as in Eq.(7.15) and (7.16). We describe the details of other variables in this section.

#### The cross section of the $\eta'$ absorption process

The calculation results of the theoretical cross section of the  $\eta'$  absorption process integrated over  $-50 \text{ MeV} < E_{\text{ex}} - E_0 < 50 \text{ MeV}$  and averaged over  $E_\gamma = 1.28 - 2.4 \text{ GeV}$  indicated in Eq.(7.8) are

$$\overline{\left(\frac{d\sigma}{d\Omega_{p_f}}\right)_{theory}^{\eta'asb}} = 292.2 \text{ nb/sr} \quad (V_0 = -100 \text{ MeV}), \quad (7.18)$$

$$\overline{\left(\frac{d\sigma}{d\Omega_{p_f}}\right)_{theory}^{\eta'abs}} = 79.7 \text{ nb/sr} \quad (V_0 = -20 \text{ MeV}). \quad (7.19)$$

#### Branching fraction of the $\eta'N \rightarrow \eta N$ process

The branching fraction of the  $\eta'N \rightarrow \eta N$  process in all the absorption process,  $\text{Br}_{\eta'N \rightarrow \eta N}$ , is unknown. An  $\eta'$  is mainly absorbed through either single-nucleon absorption ( $\eta'N \rightarrow MB$ ) or two-nucleon absorption ( $\eta'NN \rightarrow NN$ ) processes [69]. Here,  $M$  and  $B$  denote a meson and a baryon, respectively. From the calculation within a chiral unitary approach in Ref.[69], the fraction of the single-nucleon absorptions process is expected to be between 40–97%. Thereby, we expect that the fraction of the single-nucleon absorptions process is similar or larger compared with the fraction of the two-nucleon absorption process. From the same chiral unitary approach calculation in Ref.[43], the  $\eta'N \rightarrow \eta N$  process is considered to account 80% the single-nucleon absorption processes. For example, if the proportion of single-nucleon absorptions is 50% of all absorption processes and the  $\eta'N \rightarrow \eta N$  process accounts for 80% of the single-nucleon absorption processes,  $\text{Br}_{\eta'N \rightarrow \eta N}$  is given by  $50\% \times 80\% = 40\%$ . Because the reliability of the evaluation of the branching fraction within the chiral unitary approach is unknown, we treated  $\text{Br}_{\eta'N \rightarrow \eta N}$  is an unknown value when we evaluate the  $\eta'$ -nucleus potential. We assumed that  $\text{Br}_{\eta'N \rightarrow \eta N}$  is independent on  $E_{\text{ex}}$  in  $-50 \text{ MeV} < E_{\text{ex}} - E_0 < 50 \text{ MeV}$ .

## Survival probability of $(\eta + p_s)$ pair

We evaluated the survival probability of  $\eta$  and  $p_s$ ,  $P_{srv}^{\eta p_s}$  for  $\cos \theta_{lab}^{\eta p_s} < -0.9$  by the quantum molecular dynamics (QMD) transport model calculation [57]. The details of the QMD simulation is described in Appendix E. The primary reactions are  $\eta'p \rightarrow \eta p$  or  $\eta'n \rightarrow \eta n$ . In the case of the  $\eta'p \rightarrow \eta p$  reaction,  $P_{srv}^{\eta p_s}$  is 25.2%, which is consistent with the measured transparency of carbon nuclei for  $\eta$  ( $\sim 44\%$  [59]) and protons ( $\sim 60\%$  [60–62]). In the case of the  $\eta'n \rightarrow \eta n$  reaction,  $P_{srv}^{\eta p_s}$  is 1.2%. By taking a weighted average with the ratio of  $p/n$  in a residual  $^{11}\text{B}$  nucleus,  $P_{srv}^{\eta p_s}$  for the  $\eta'N \rightarrow \eta N$  reaction was deduced to be

$$P_{srv}^{\eta p_s} = 12.1\%. \quad (7.20)$$

The uncertainties of the transparency of  $\eta$  and  $p$  are considered to be several %. Because they are multiplied and weighted with the  $p/n$  ratio, the uncertainty of  $P_{srv}^{\eta p_s}$  is considered to be the level of 1%.

## 7.2.6 Result

In Fig.7.5, we compare the experimental upper limit of the cross section of the  $\eta'$  bound states with  $(\eta + p_s)$  emission  $\left(\frac{d\sigma}{d\Omega_{p_f}}\right)_{exp}^{\eta+p_s}$  and theoretical cross section  $\left(\frac{d\sigma}{d\Omega_{p_f}}\right)_{theory}^{\eta+p_s}$ , as a function of  $\text{Br}_{\eta'N \rightarrow \eta N}$ . For  $\left(\frac{d\sigma}{d\Omega_{p_f}}\right)_{theory}^{\eta+p_s}$ , we substituted Eqs.(7.15), (7.16), (7.18), (7.19) and (7.20) to Eq.(7.17). We exclude  $V_0 = -100$  MeV in  $\text{Br}_{\eta'N \rightarrow \eta N} > 24\%$  at the 90% confidence level. The upper limit of  $\text{Br}_{\eta'N \rightarrow \eta N}$  in the case of  $V_0 = -20$  MeV is 80% at the 90% confidence level.

## 7.3 Comparison with theoretical expectations and past experimental results

### Comparison with the original DWIA calculation

As shown in section 7.2.4, we found that the DWIA calculation gave larger cross section with a factor of 2.0–4.3 compared with the experimental measurement. In the original DWIA calculation in Ref.[44], a larger  $\gamma p \rightarrow \eta'p$  elementary cross section of 50 nb/sr in the center-of-mass system (1.25 times larger) was used. In addition, the Fermi averaged elementary cross section in the laboratory system was not used in Ref.[44]. Thereby, the DWIA calculation in Ref.[44] gave  $\sim 1.7$  times larger cross section than the value shown in this chapter. Thus, the measured cross section was  $\sim 1/3.4$ – $1/7.3$  of the original expectation in Ref.[44].

The expected number of  $(\eta + p_s)$  events in  $-50$  MeV  $< E_{\text{ex}} - E_0 < 50$  MeV using the original DWIA results in Ref.[44] and  $\text{Br}_{\eta'N \rightarrow \eta N} = 40\%$  is 24 and 6.5 events, for the case of  $V_0 = -100$  MeV and  $V_0 = -20$  MeV, respectively. It is large enough to determine  $\text{Br}_{\eta'N \rightarrow \eta N}$  in  $0$  MeV  $< E_{\text{ex}} - E_0 < 50$  MeV, where  $\eta'$  absorption events are expected in any  $V_0$  cases (see Fig.7.3). We found the  $\eta'$  cross section is much small compared with the original DWIA

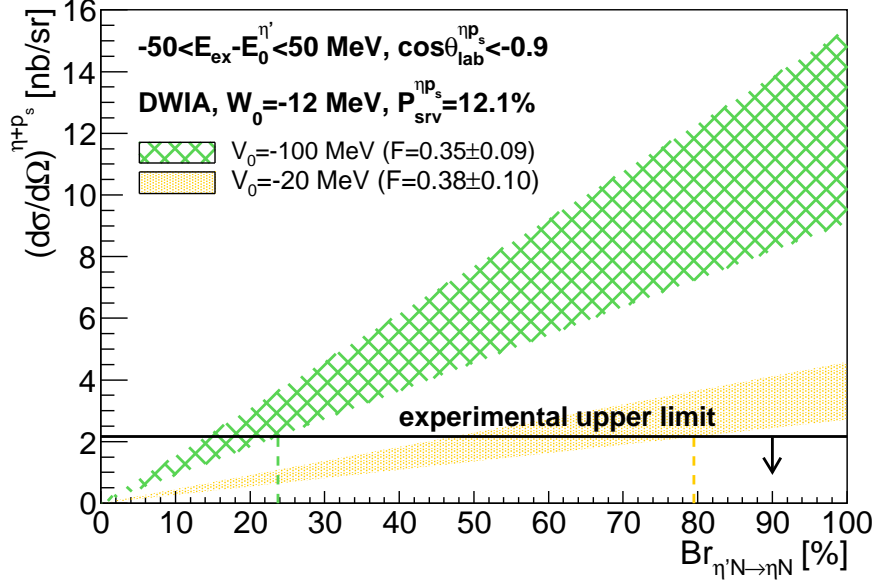


Figure 7.5: The experimental upper limit of  $\left(\frac{d\sigma}{d\Omega_{p_f}}\right)_{exp}^{\eta+p_s}$  at the 90% confidence level, and  $\left(\frac{d\sigma}{d\Omega_{p_f}}\right)_{theory}^{\eta+p_s}$  as a function of  $Br_{\eta'N \rightarrow \eta N}$ .

calculation and we did not observe any events in  $-50 \text{ MeV} < E_{ex} - E_0 < 50 \text{ MeV}$ . Thus, we treated  $Br_{\eta'N \rightarrow \eta N}$  as an unknown variable.

### Comparison with theoretical expectations

As described in section 1.3, the NJL model and linear sigma model calculations expect a deep  $\eta'$ -nucleus potential,  $V_0 = -150$  and  $-80$  MeV, respectively, owing to the  $U_A(1)$  anomaly term. When we assume the naive expectation of the  $\eta'N \rightarrow \eta N$  branching fraction,  $Br_{\eta'N \rightarrow \eta N} > 40\%$ , our results reject such deep potentials. Both theoretical calculations assume that the strength parameter of the  $U_A(1)$  anomaly term is independent from the density. A modification of the strength parameter leads different  $V_0$ . Thus, our result indicates smaller  $Br_{\eta'N \rightarrow \eta N}$  than the naive expectation  $Br_{\eta'N \rightarrow \eta N} > 40\%$  and/or a need of modification of parameters used in the theoretical calculation.

### Comparison with the result of the $\eta$ -PRiME/Super-FRS Collaboration

The  $\eta$ -PRiME/Super-FRS Collaboration evaluated the upper limits of  $V_0$  and  $W_0$  by comparing their experimental upper limit of the cross section of the  $p + {}^{12}\text{C} \rightarrow d + X$  reaction and the theoretical calculation within the same DWIA calculation as ours as shown in Fig.7.6. [21, 22, 24]. In the DWIA calculation, they used an estimated elementary cross section of

the  $pn \rightarrow \eta'd$  process because there is no experimental measurement. They estimated the uncertainty of the elementary cross section is a factor of  $\sim 2$ . In addition, they were not able to evaluate the normalization factor  $F$  of the DWIA calculation itself because they did not tag decay products. Our result indicates that there is uncertainty of  $F$  with a factor of 2.0–4.3 even if we use the measured elementary cross section. In total, the uncertainty of the absolute value of their theoretical cross section is  $\sim 4.0$ –8.6. Thereby, the total normalization factor can be smaller than  $1/4$ , which is out of their evaluation range shown in Fig.7.6. The uncertainty of our measurement is much smaller compared with the ones by the  $\eta$ -PRiME/Super-FRS Collaboration because we obtained  $F$  from the elementary cross section of the  $\gamma p \rightarrow \eta'p$  process.

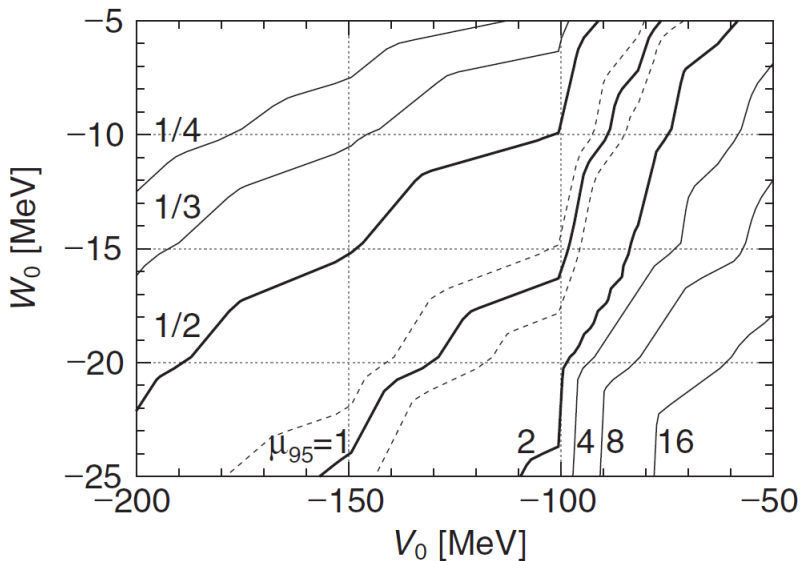


Figure 7.6: The obtained upper limit of  $(V_0, W_0)$  by the  $\eta$ -PRiME/Super-FRS Collaboration [21]. The numbers indicate the normalization factor of the theoretical cross section.

### Comparison with the result of the CBELSA/TAPS Collaboration

The CBELSA/TAPS Collaboration deduced  $V_0 = -(39 \pm 7(\text{stat}) \pm 15(\text{syst}))$  MeV by comparing their experimental cross sections of the  $\eta'$  escape process with the theoretical cross sections calculated with a collision model. Our result is consistent with their result. Although the DWIA calculations are widely used for describing bound states, such as hypernuclei and pionic atoms, the collision model is not. Thereby, the reliability and the uncertainty of the collision model are unknown. The reproducibility of the known bound states is the advantage of the DWIA calculation used for our analysis.

# Chapter 8

## Summary and prospects

An  $\eta'$  meson is an interesting probe to investigate hadron masses in a finite density, where the partial restoration of chiral symmetry is expected. Several model calculations expect large mass reduction of 80 – 150 MeV of an  $\eta'$  meson in a nucleus, owing to the reduction of the  $U_A(1)$  anomaly. If there is large mass reduction, the system of an  $\eta'$  meson and a nucleus may have a light mass as a bound state. The amount of mass shift can be described with the real part of the  $\eta'$ -nucleus potential,  $V_0$ .

We searched for an  $\eta'$ -nucleus bound state by using a missing-mass spectroscopy of the  $^{12}\text{C}(\gamma, p)$  reaction. The missing-mass spectroscopy around  $\eta'$ -mass threshold suffers from numerous backgrounds arising from multiple light-meson productions. Therefore, we tagged an  $(\eta + p)$  pair which is the most promising decay mode in one-nucleon absorption of  $\eta'$  meson in a nucleus,  $\eta'N \rightarrow \eta N$  [43]. This is the first measurement of the missing mass spectrum around the  $\eta'$  production threshold in coincidence with decay products. We carried out the experiment in 2015 at the SPring-8/LEPS2 beam line, using the BGOegg detector system. We measured the  $\gamma + ^{12}\text{C} \rightarrow p_f + (\eta + p_s) + X$  reaction, where  $p_f$  is the forward-going proton emitted in  $0.9^\circ < \theta_{lab}^{p_f} < 6.8^\circ$ , used for the missing mass analysis, and  $p_s$  is the side-going proton emitted in  $28.5^\circ < \theta_{lab}^{p_s} < 138.5^\circ$ .  $5.9 \times 10^{12}$  photon beams in the energy range of 1.3 – 2.4 GeV hit a 2.0-cm thick carbon target.

Although we succeeded to suppress huge background from multi pion production by tagging an  $(\eta + p_s)$  pair, we found that there still remained large background events accompanying an  $\eta$  meson and a side-going proton in the experimental data. Above the large background, no enhancement was observed around the  $\eta'$  production threshold. We found that the remaining backgrounds are mainly from the  $\gamma + ^{12}\text{C} \rightarrow p_f + \eta + ^{11}\text{B}$  and  $\gamma + ^{12}\text{C} \rightarrow p_f + (\eta + \pi^0) + ^{11}\text{B}$  reactions, in which an  $\eta$  is produced in the primary reaction, and another proton,  $p_s$  is kicked out by either a primary  $\eta$ ,  $\pi^0$  or  $p_f$ . We investigated the kinematics of the  $(\eta + p_s)$  pair from those background reactions and optimized kinematical selection criteria to suppress the background events and to enhance the signal events from the  $\eta'$ -nucleus bound state. With the kinematical selections, we reduced the background events associated with an  $(\eta + p_s)$  pair to 0.4%, while 23% of signal events is preserved. After the kinematical selection, we observed no signal events in the excitation energy region,  $-50 \text{ MeV} < E_{\text{ex}} - E_0 < 50 \text{ MeV}$ , the region to search for the signal. The upper limit of the production cross section of the  $\eta'$ -nucleus

bound state with emission of an  $(\eta + p_s)$  pair in the opening angle of  $\cos\theta_{lab}^{\eta p_s} < -0.9$  was obtained to be 2.2 nb/sr at the 90% confidence level.

In addition to the measurement of the  $\eta'$  absorption process to search for the bound state, the missing mass spectrum of the  $\eta'$  escape process,  $\gamma + {}^{12}\text{C} \rightarrow p_f + \eta' + \text{X}$ , was also measured for the first time. By measuring the missing mass dependence of the cross section of the  $\eta'$  escape process, we evaluated the production rate of  $\eta'$  meson around the bound state region.

The obtained experimental upper limit of the  $(\eta + p_s)$  coincidence cross section was compared with the theoretical cross section calculated within a distorted wave impulse approximation (DWIA) in the case of  $V_0 = -100$  and  $-20$  MeV, and  $W_0 = -12$  MeV. The calculated cross section is decomposed to the  $\eta'$  absorption and escape processes. The DWIA calculations nicely represent spectral shapes of bound states such as hypernuclei but hardly reproduce their absolute cross sections. Thereby, we evaluated the normalization factor of the theoretical cross section by comparing the experimental and theoretical cross sections of the  $\eta'$  escape process. The obtained normalization factor is in the range of 0.23–0.50, within the statistical and systematic errors. We compared the theoretical and experimental cross sections of the  $\eta'$  absorption process for different  $V_0$  cases as a function of  $\text{Br}_{\eta'N \rightarrow \eta N}$ , the branching fraction of the  $\eta'N \rightarrow \eta N$  process in all the  $\eta'$  absorption process. We exclude  $V_0 = -100$  MeV in  $\text{Br}_{\eta'N \rightarrow \eta N} > 24\%$  at the 90% confidence level. The upper limit of  $\text{Br}_{\eta'N \rightarrow \eta N}$  in the case of  $V_0 = -20$  MeV is 80% at the 90% confidence level. Our result indicates smaller  $\text{Br}_{\eta'N \rightarrow \eta N}$  than a naive expectation of  $\text{Br}_{\eta'N \rightarrow \eta N} = 40\%$  and/or a shallow  $V_0$ , while theories based on the  $U_A(1)$  anomaly predict a deep  $V_0$ .

If the branching fraction of the one nucleon process is small, we can expect that the branching fraction of the two nucleon absorption process,  $\eta'NN \rightarrow NN$  is large. The measurement of the  $\eta'pp \rightarrow pp$  process is planned in GSI by the  $\eta$ -PRiME/Super-FRS Collaboration [21]. It is also possible to analyze the  $\eta'pp \rightarrow pp$  mode with the existing BGOegg data although it is challenging because the protons from the  $\eta'pp \rightarrow pp$  process penetrate BGOegg, and particle identification and energy measurement are difficult. The measurement of the two nucleon absorption process will help to differentiate the two possibilities; small  $\eta'N \rightarrow \eta N$  branching fraction and shallow potential.

In the case of  $\Sigma$  hyper nuclei, one derives the  $\Sigma$ -nucleus potential by comparing the theoretical and experimental cross sections in wide excitation energy range above threshold [25]. The DWIA calculation used in the present analysis is for the excitation energy in  $E_{\text{ex}} - E_0 \lesssim 50$  MeV. In this region, there is only 6% of all the experimentally observed  $\eta'$  meson. Because of small statistics of observed  $\eta'$  escape events, we were not able to distinguish different  $V_0$  cases of the theoretical expected excitation energy spectra. By extending the DWIA calculation to higher  $\eta'$  angular momentum and large excitation energy, we can compare the experimental and theoretical excitation energy spectra with larger statistics. Then, we will be able to evaluate the  $\eta'$ -nucleus potential from our  $\eta'$  escape data.

# Acknowledgements

I would like to show my greatest appreciation to Prof. Masayuki Niiyama. He has trained me since I was a master student. His instruction has been always careful and I learned a lot from him.

I would like to express my gratitude to Prof. Norihito Muramatsu. He led the BGOegg collaboration as a leader. He helped me a lot on the data analysis. He also carefully proofed the submitted paper many times.

I would like to thank Prof. Tomofumi Nagae, the leader of the Experimental Nuclear and Hadronic Physics Laboratory in Kyoto University. We could develop the RPC detector since he let me go to the RPC2012 workshop when I was a master student. He also gave me a lot of suggestions to improve this thesis.

I am grateful to Prof. Masaru Yosoi. He taught and helped me many times when we started the BGOegg experiment and when we took the experimental data.

I appreciate Prof. Hiroaki Ohnishi. We could build the RPC detector thanks to him. He often encouraged me cheerfully.

I would like to express my gratitude to Prof. Takashi Nakano. The published paper was much improved thank to the suggestion from him. He also supported my life as a scientist from many aspects.

I greatly appreciate Prof. Hajime Shimizu. He has started the BGOegg experiment. He gave me a lot of suggestion to improve the published paper. In addition, he often takes care of my life.

I would particularly like to thank Prof. Tomoyuki Maruyama. He helped me a lot for the QMD simulation. We could carry out the simulation thanks to him.

I am deeply grateful to Prof. Hideko Nagahiro. We could derive the result thanks to her calculation. She discussed a lot with us and taught us the details of the calculation.

I appreciate Prof. Toru Harada and Prof. Hiroyuki Noumi. They taught me how to carry out the calculation of the Fermi averaging method.

I thank Prof. Megumi Naruki. She gave me a lot of suggestions to improve this thesis. She also has been taken care of my analysis as a PAC leader.

I particularly thank Prof. Yuki Nozawa. We have been classmates since we were undergraduate students. I could spend a good time in SPring-8 thanks to him.

I owe my gratitude to Dr. Tran Hai Nam, Mr. Toshikazu Hashimoto, Mr. Yuji Matsumura, Mr. Hiroto Hamano, Mr. Takuya Shibukawa and Dr. Keigo Miztani. They carried out important calibrations of detectors needed for this experiment.

I would like to show my appreciation to the member of the BGOegg collaboration. We could start and carry out the experiment thank to the collaborators. I especially thank Prof. Takatsugu Ishikawa, Prof. Manabu Miyabe, Prof. Hirohito Yamazaki, Prof. Atsushi Tokiyasu and Dr. Yusuke Tsuchikawa. They conducted the start-up of the BGOegg experiment. I also thank Prof. Stokovsky, Prof. Wen-Chen Chang, Prof. Jung Keun Ahn, Prof. Yohei Morino and Prof. Kenneth Hicks. They gave me a lot of suggestions to improve the published paper. I also appreciate Prof. Takeshi Ohta and Mr. Yuto Kasamatsu and shift takers who helped to take the experimental data.

I want to thank Prof. Sunyoung Ryu and Prof. Kotaro Shirotori. They cheered me a lot in my long analysis period at RCNP.

I thank the members of the Experimental Nuclear and Hadronic Physics Laboratory in Kyoto University. I spent the best time there to carry out researches.

Last but not least, I express my appreciation to my family for their support.

# Appendix A

## Filling pattern of the SPring-8 storage ring

In Table.A.1, we summarize the electron filling patterns of the SPring-8 storage ring in the present experimental period. In Table.A.1, “filling” means that bunches are in series of every 1.966 ns. We also show illustrations of each filling mode in Fig.A.1–A.5. The figures are from SPring-8 web site [70].

Table A.1: The electron filling pattern of the SPring-8 storage ring.

mode	bunch	bunch period
A mode	203 bunches	23.6 ns
C mode	11 bunch train $\times$ 29	165.2 ns
D mode	1/7-filling $\times$ 5 bunches	684.3 ns
E mode	2/29-filling $\times$ 26 bunches	165.2 ns
H mode	11/29-filling $\times$ 1 bunch	1486 ns

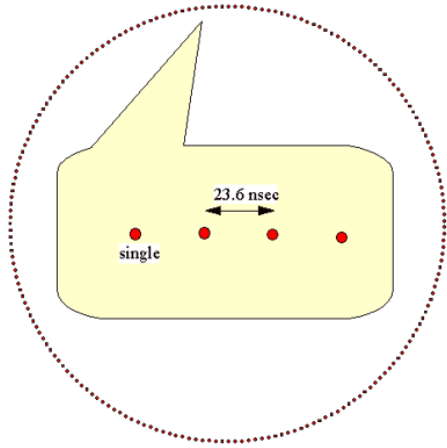


Figure A.1: A-mode.

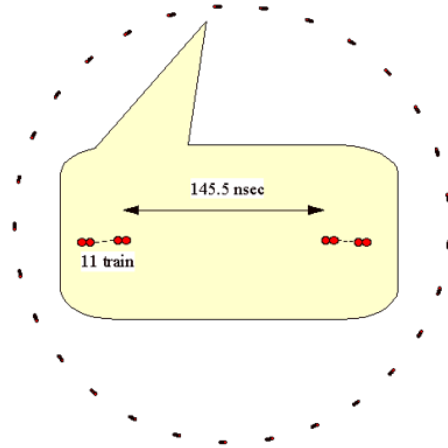


Figure A.2: C-mode.

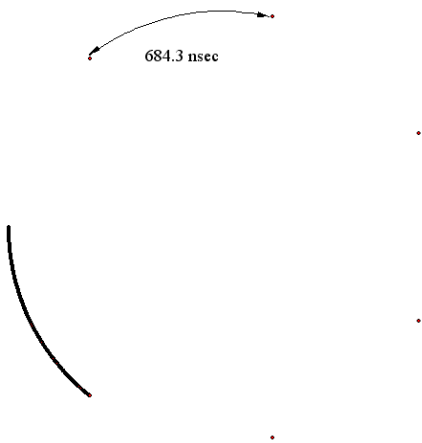


Figure A.3: D-mode.

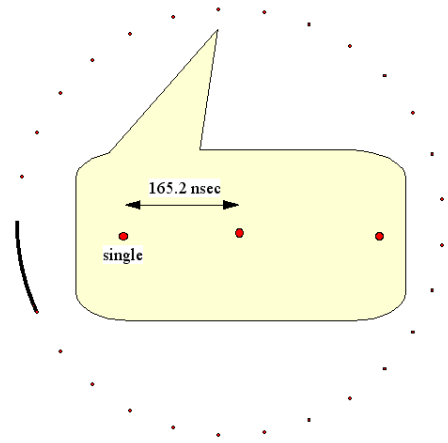


Figure A.4: E-mode.

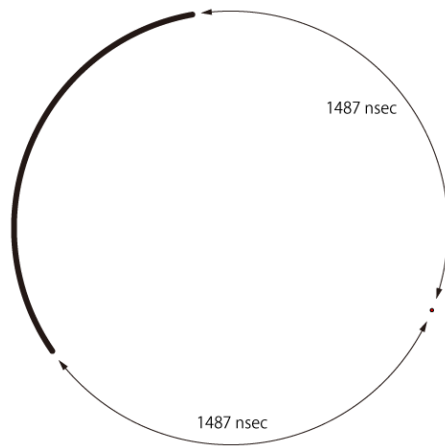


Figure A.5: H-mode.

# Appendix B

## Detector module

In Table.B.1 and B.2, we summarize the supplied power, preamplifier, attenuator and discriminator of each detector. We adjusted the high voltage for the tagger-PL and the BGOegg channel by channel. We adjusted the high voltage for the tagger-fiber PMT by PMT, thus it was common for 16 channels. The power supply value of other detectors was common for all channels or chambers. For the BGOegg and IPS, we used attenuators for charge measurement to reduce charge to meet with a range of analog-to-digital converter (ADC) modules. The threshold level of discriminators was common for all channels of each detector except for the tagger-PL.

Table B.1: The supplied voltage, preamplifier and attenuator used for each detector.

Detector	power supply	preamplifier	attenuator
Tagger-PL	channel by channel	—	—
Tagger-fiber	PMT by PMT	—	—
UpVeto	+2200 V	—	—
BGOegg	channel by channel	—	30 dB (1/31.2)
IPS	common (+67.9 V)	LeCroy 612A	channel by channel
DC	sense: +2200 V, potential: +100 V	RPA-181	—
RPC	common (13.5 kV)	Ref.[51]	—

Table B.2: The discriminator module and threshold of each detector.

Detector	discriminator	threshold
Tagger-PL	OULNS	channel by channel
Tagger-fiber	LeCroy 4413	common (-20 mV)
UpVeto	Phillips 711	-20 mV
BGOegg	LeCroy 4413	common (-20 mV)
IPS	LeCroy 4413	common (-60 mV)
DC	RPA-181	common (-600 mV)
RPC	Ref.[51]	common (-50 mV)

# Appendix C

## Photon beam energy calibration

The photon beam energy was evaluated from the track of recoil electrons from backward Compton scattering. We evaluated the relation of the photon beam energy and tagger fiber hit position as Eq.(3.1) and (3.3). We derived Eq.(3.1) and (3.3) by simultaneously fitting expected photon energy of (a) the  $\gamma + p \rightarrow 2\pi^0 + p$  reaction, (b) the  $\gamma + p \rightarrow \pi^0 + p_f$  and  $\gamma + p \rightarrow \eta + p_f$  reactions, and (c) the maximum photon beam energy, using the liquid hydrogen target data. Here,  $\pi^0, \eta, p$  are detected with BGOegg and  $p_f$  with the RPC. In the analysis of the  $\gamma + p \rightarrow 2\pi^0 + p$  reaction, we used kinematical fitting and evaluated expected photon beam energy. In the analysis of the  $\gamma + p \rightarrow \pi^0 + p_f$  and  $\gamma + p \rightarrow \eta + p_f$  reactions, we evaluated the missing mass of the  $p(\gamma, p_f)$  reaction and estimated the photon energy which gives the mass of an  $\eta$  or  $\pi^0$  meson. As described in section 2.1.3, the maximum photon beam energy is 2.385 GeV. It is called Compton edge, and the maximum tagger fiber number which had entries corresponds to the Compton edge. In Fig.C.1, we show the two-dimensional plot of the predicted photon beam energy from the analysis (a)-(c), and fiber hit position. We fitted data points with quartic functions and obtained Eq.(3.1) and (3.3).

The photon energy resolution was evaluated using the  $\gamma + p \rightarrow \pi^0\eta + p_f$  reaction with the liquid hydrogen target. The photon beam energy was predicted with a kinematical fitting using measured momentum of  $\pi^0, \eta$  and  $p_f$ . The sigma of the difference of the measured photon beam energy and the predicted photon beam energy was  $16.8 \pm 0.9$  MeV. The contribution of the detector resolution was estimated to be  $11.8 \pm 0.2$  MeV using a Monte Carlo simulation. By subtracting the detector resolution, the photon beam energy resolution was estimated to be  $12.0 \pm 0.7$  MeV.

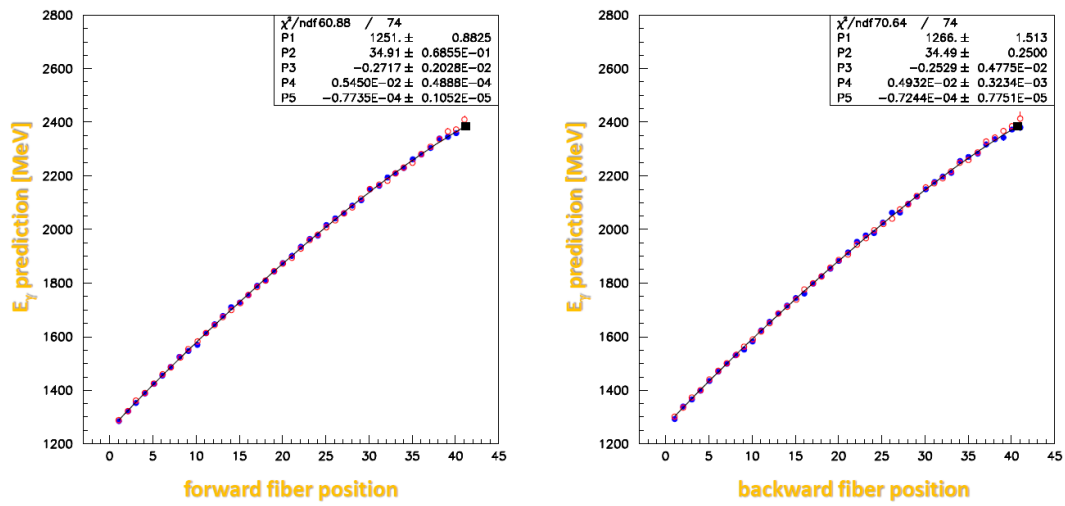


Figure C.1: The two-dimensional plot of the predicted photon beam energy and fiber hit position. Red open circles are from the analysis (a), blue full circles from (b), and black square from (c). Lines are fitting results with quartic functions. The error bars are shown although most of them are smaller than the size of circles.

# Appendix D

## Timing selection criteria

In this Appendix, we describe the timing selection criteria of BGOegg and the IPS for particle identifications of  $\gamma$  and  $p_s$ .

### D.1 Selection of gammas

the following timing cut conditions were required for neutral clusters to select events from gammas.

#### Clusters in layer 2–20

For the neutral clusters whose core crystal is in layer 2–20, the following timing cut conditions were required.

- $-1.2 \text{ ns} < T_{cls} - T_{RF}$ ,
- $T_{cls} - T_{RF} < 1.4 \text{ ns}$  (clusters with energy greater than 800 MeV).
- $T_{cls} - T_{RF} < 0.8 \text{ ns}$  (clusters with energy smaller than 800 MeV).

The cut conditions were optimized using a data set having two neutral cluster and one charged cluster in BGOegg and a hit in the RPC. The selection criteria are shown in Fig.D.1 together with the distribution of the neutral clusters of the (2 neutral + 1 charged + 1 RPC hit) data sample. By applying those timing cuts, we removed clusters from neutrons which locates around  $T_{cls} - T_{RF} = 1 \sim 2 \text{ ns}$ . This cut also removed events at around  $\pm 2 \text{ ns}$  which indicates misselection of the RF signal. The cut conditions for events with cluster energy greater than 800 MeV was loosened because the time-walk correction does not work well at large energy deposit region.

#### Clusters in layer 21

For the neutral clusters whose core crystal is in layer 21, the following timing cut conditions were required.

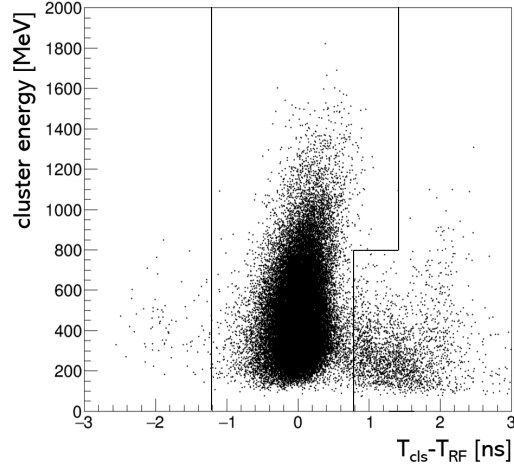


Figure D.1: A scatter plot of the energy deposit and hit timing of neutral clusters in layer 2-20, in the (2 neutral + 1 charged + 1 RPC hit) data sample. The selection criteria are shown with black lines.

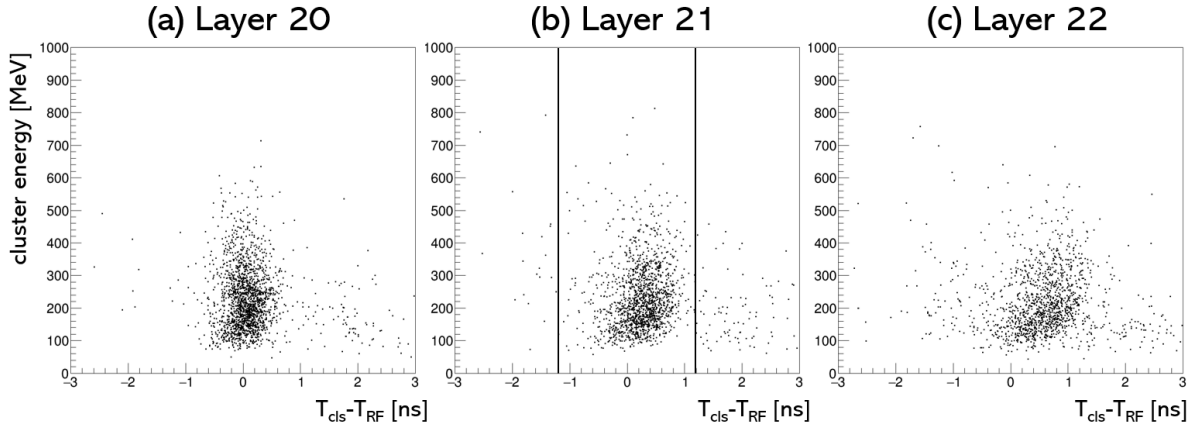


Figure D.2: A scatter plot of the energy deposit and hit timing of neutral clusters in layer 20, 21 and 22, in the (2 neutral + 1 charged + 1 RPC hit) data sample. The selection criteria for layer 21 are shown with black lines.

- $-1.2 \text{ ns} < T_{cls} - T_{RF} < 1.2 \text{ ns}$ .

Figure D.2 shows a scatter plot of the energy deposit and hit timing of neutral clusters in layer 20, 21, 22 of the (2 neutral + 1 charged + 1 RPC hit) data sample. Because of low statistics, the time-walk corrections do not properly work for backward layers, the layer 21 and 22. Thereby, we applied looser cut for layer 21 than ones for other layers. The cut criteria are shown in Fig.D.2 (b). As described in section 3.3, clusters in the most outer layer 22 were not used for the analysis.

## D.2 Selection of protons

### BGOegg timing selection

Figure D.3 shows a scatter plot of the hit timing and the energy deposit of the charged cluster of the ( $\eta + 1$  charged + 1 RPC hit) data sample after the energy deposit selection described in chapter 4. There are some events around  $T_{cls} - T_{RF} = 0$  ns. They are considered to be events in which a proton had kinetic energy greater than 450 MeV and penetrated the BGOegg. We removed such events at  $-3\sigma$  shown with a red line in Fig.D.3. The cut is applied when the cluster energy is greater than 60 MeV. Below 60 MeV, the BGOegg crystal response is slow and thus timing cuts were not applied. The cluster energy dependent timing resolution  $\sigma$  is evaluated using the  $\gamma + {}^{12}\text{C} \rightarrow (\omega + p_s) + \text{X}$  data sample.

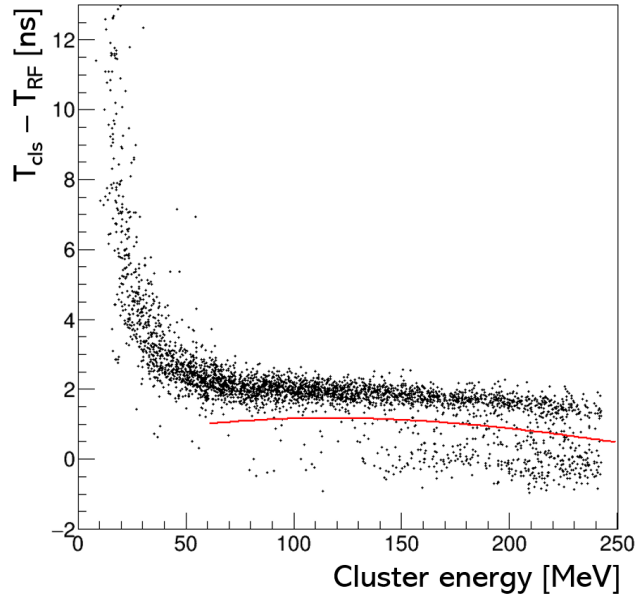


Figure D.3: A scatter plot of the hit timing and the energy deposit of the charged cluster of the ( $\eta + 1$  charged + 1 RPC hit) data sample. The  $-3\sigma$  selection criterion is shown with a red line.

### IPS timing selection

Figure D.4(a) shows a scatter plot of the hit timing and the energy deposit of the IPS of the charged particle of the ( $\eta + 1$  charged + 1 RPC hit) data sample after the energy deposit selection and the BGOegg cluster timing selection. The time-walk correction of the IPS was carried out period by period and channel by channel at a cluster energy in the range of 185–245 MeV. The correction obviously does not work properly at high energy deposit region. Thereby, an additional time-walk correction were carried out which uses a common

parameter for all periods and all channels. The distribution after the additional time-walk correction is shown in Fig.D.4(b). We select the region in  $\pm 1$  ns.

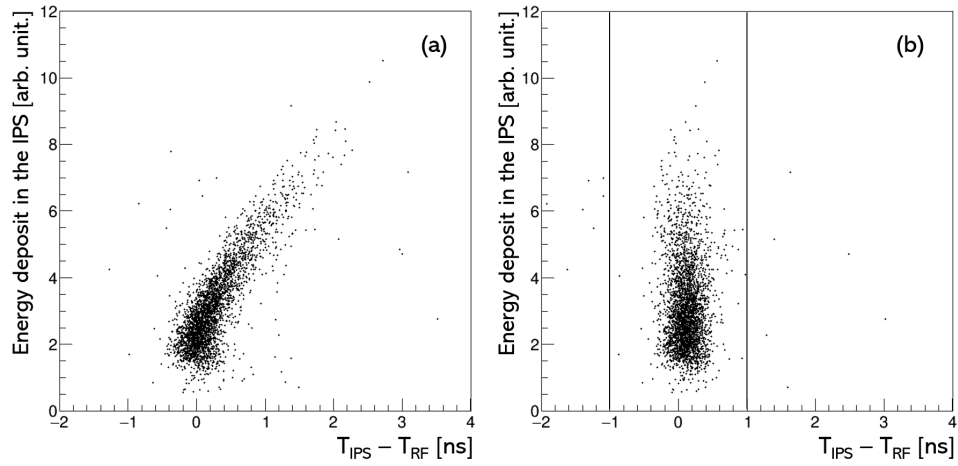


Figure D.4: A scatter plot of the energy deposit and the hit timing of the IPS before (a) after (b) an additional time-walk correction. The selection criteria are shown with black lines.

# Appendix E

## QMD model calculation

In this Appendix, we describe the details of the quantum molecular dynamics (QMD) model calculation used for evaluating the probability  $P_{srv}^{\eta p}$  that an  $(\eta + p_s)$  pair is emitted back-to-back after interactions in a nucleus.

### E.1 Basic description

The quantum molecular dynamics (QMD) model is originally developed to simulate behavior of particles in heavy ion collisions. In the QMD model, the time evolution of particles is calculated taking into account a Newtonian equation and two body interactions. The QMD calculation is used together with the statistical decay model (SDM). The QMD model is for dynamical process such as direct reactions in  $10^{-22}$  s, and the SDM model is for statistical process such as nuclear fissions and decays in  $10^{-21} - 10^{-15}$  s. The details of the QMD simulation is described in Ref.[57]. In the original QMD package in Ref.[57], only the interaction of nucleons, pions and excited states of nucleons are implemented and the interaction of  $\eta$  mesons is not implemented. Kinoshita *et al.* implemented the interaction of  $\eta$  mesons to the QMD simulation to describe photoproduction of  $\eta$  off nuclei targets [58]. We used the program developed by Kinoshita *et al.* and studied the interaction of  $\eta$  meson and nucleons from the  $\eta'N \rightarrow \eta N$  process.

### E.2 Signal simulation

We implemented the reaction in Eq.(1.29) as follows. A photon beam is injected to a  $^{12}\text{C}$  target, and then a forward going proton  $p_f$  is emitted. The remaining momentum after the emission of  $p_f$  is shared with the residual  $^{11}\text{B}$  nucleus. The remaining energy is given to a nucleon and the nucleon become a  $N^*$  state. Then, the  $N^*$  decays to an  $\eta$  meson and a nucleon back-to-back in the center of mass (CM) frame. Because the remaining momentum is shared with the  $^{11}\text{B}$  nucleus, the momentum of  $N^*$  is small. Thereby, the initial opening angle of  $\eta - N$  is back-to-back even in the laboratory system. We simulated the interaction of the  $\eta$  and  $N$  in the nucleus with the QMD model and evaluated the probability  $P_{srv}^{\eta p_s}$  that

an  $(\eta + p)$  pair is emitted in  $\cos\theta_{lab}^{\eta p} < -0.9$  after the interaction. Most of such events are from  $N^* \rightarrow \eta p$ .  $N^* \rightarrow \eta n$  events are also included, in which the neutron kicked out a proton when they interacted.

The input variables of the simulation are the photon beam energy and momentum of  $p_f$ . The kinematics of the  $(\eta + N)$  depends only on the difference of the incident photon momentum and the forward proton momentum. Thereby, we fixed the incident photon energy to 2.4 GeV. We varied the  $p_f$  kinetic energy in 1.10–1.72 GeV, which corresponds to the excitation energy of  $-300 \text{ MeV} < E_{\text{ex}} - E_0 < 300 \text{ MeV}$ . We changed the  $p_f$  initial polar angle in  $-12.6 \sim +12.6$  degree. The angle can be changed after the interaction of the  $p_f$  with the nucleus. We selected the events in the RPC acceptance after the interaction with nuclei.

### E.3 Detector acceptance and resolution

The detector acceptance and resolution were implemented as follows. First, the events in which the  $p_f$  angle is in the RPC acceptance is selected. The two gamma decay of  $\eta$  mesons is simulated by using TGenPhaseSpace of ROOT [71]. The events in which two gammas and  $p_s$  are in the polar angle of 27.5–138.5 degree, corresponding to the BGOegg layer 2–21, were selected. We implemented the gamma and  $p_s$  energy resolution depending on the particle energy, which is evaluated from the  $\gamma + p \rightarrow \eta + p$ ,  $\gamma + p \rightarrow \omega + p$  and  $\gamma + p \rightarrow 2\pi^0 + p$  reactions with the liquid hydrogen target. We implemented the photon beam energy resolution of 12.0 MeV. The RPC time resolution is 80 ps and the  $p_f$  energy resolution depends on the energy of  $p_f$ . We evaluated the  $p_f$  energy resolution with the weight of  $p_f$  energy distribution with the BCS photon beam energy distribution.

# Appendix F

## Detector acceptance and efficiency

In this Appendix, we describe the details of the systematic uncertainty of the detector acceptance and how we evaluated the detector efficiencies.

### F.1 Systematic uncertainty of the acceptance

#### F.1.1 Acceptance for $(\eta + p_s)$

We evaluated the acceptance including the reconstruction efficiency of  $(\eta + p_s)$  using a Monte Carlo (MC) simulation. We carefully compared the MC and experimental data and found that there are differences in the fraction of the leak cluster, charge misidentification rate with the IPS, and energy deposit calibration of the IPS. We took into account the differences when we calculate the acceptance.

#### Leak cluster

As described in section 3.3.2, the number of BGOegg clusters can be more than 3 even when only 3 particles ( $2\gamma$ 's and a proton) entered to BGOegg, because of the interactions in the detector. In the present analysis, we assumed that clusters satisfying the following conditions are leak cluster and excluded when we count the number of clusters:

- Cluster energy is less than 60 MeV.
- Cluster hit timing  $T_{cls} - T_{RF} > 3$  ns.
- There is a gamma cluster in the distance less than 140 mm.

We examined the fraction of events having (a) leak cluster(s) and it is  $(8.9 \pm 1.5)\%$  in the experimental data and 11.0% in the MC data. We note that we do not require  $T_{cls} - T_{RF} > 3$  ns in the MC. There is a large difference of  $T_{cls} - T_{RF}$  distribution between the MC and experimental data. In the MC, all events are in  $T_{cls} - T_{RF} < 3$  ns, whereas most of events are in  $T_{cls} - T_{RF} > 3$  ns in the experimental data. We took into account the difference of the fraction  $11.0 - (8.9 - 1.5) = 4.0\%$ , as a systematic uncertainty coming from the cluster counting.

## Charge misidentification rate

When we identify that a particle in BGOegg is neutral, we required that the energy deposit in the IPS is smaller than certain value. (See section 3.4). However, there are cases that a  $\gamma$  is converted to an  $e^+e^-$  pair in the target or the IPS and identified as a charged particle. We examined the probability that a  $\gamma$  is identified as a charged particle using the  $\gamma + {}^{12}\text{C} \rightarrow p_f + \eta' + \text{X}$  reaction in both the experimental and MC data. In the experimental data, we required  $-100 \text{ MeV} < E_{miss}^{\eta'p_f} = E_\gamma + M_{12\text{C}} - M_{11\text{B}} - E_{\eta'} - E_{p_f} < 0 \text{ MeV}$ , where sample is clean even we remove the charge identification information of  $\gamma$ 's. The probability that one of  $\gamma$  from an  $\eta'$  meson is identified as a charged particle is  $(89.12 \pm 2.65)\%$  in the experimental data and  $92.11\%$  for the MC data. Thereby, we derived the correction factor of the acceptance on the charge misidentification rate to be  $(89.12 \pm 2.65)/92.11 = (96.75 \pm 1.57)\%$ .

## Energy deposit in the IPS

As described in section 4.4.3, we carried out the particle identification of side-going proton by using the difference of the energy deposit in the IPS and expected energy deposit from a PSTAR calculation. The conversion factor of the unit of the PSTAR calculation (MeV) to the unit used for the IPS of the MC was optimized to reproduce the distribution of the experimental data. We tested two extreme cases of the conversion factor and the resulting acceptance was  $14.2\%$  and  $14.1\%$ . We took into account this difference to the systematic uncertainty.

### F.1.2 Acceptance for $p_f$

As describe in section 6.1.4,  $p_f$  can interact in the target and can change its direction or create an additional particle. We evaluated the acceptance for  $p_f$  of the DC using a MC simulation. We generated the  $\gamma + p \rightarrow \eta' + p$  reaction requiring that the original forward proton angle is less than  $7^\circ$  which is the region covered with the RPC. The fraction of events that the number of DC tracks equals one was  $94.7\%$ .  $2.2\%$  of events had no track in the DC and  $3.3\%$  of events have more then one track.

We compared the fraction of events with more than one track in the MC and experimental data using a clean sample of the  $\gamma + p \rightarrow \eta' + p$  reaction. We required that the number of BGOegg cluster is two and the invariant mass of  $2\gamma$  is more than  $700 \text{ MeV}/c^2$ . In the MC, the fraction of events with more than one track is  $1.5\%$ . On the other hand, it is  $(2.0 \pm 0.1)\%$  in the experimental data. We took in to account the difference ( $0.5\%$ ) to the systematic error of the DC acceptance for  $p_f$ .

## F.2 Efficiency

### F.2.1 Tagger

#### Tagger PL intrinsic efficiency

We evaluated the intrinsic efficiency of the tagger-PL using the liquid hydrogen target data. Because a pair-PL hit is required at the trigger of the data acquisition, we used events with two tracks. An example of events used for the efficiency measurement is shown in Fig.F.1. When we measured the efficiency of the forward PL 3 (blue), we required two fiber clusters consist of both fiber layers, another pair PL hit and a hit in the backward PL 3 (red). We evaluated the efficiency PL by PL, and electron filling pattern by pattern. We found that the PL dependence and the filling pattern dependence of the PL intrinsic efficiency is small. We derived the PL intrinsic efficiency to be  $(98.8 \pm 1.2)\%$  by averaging the obtained efficiency over all PL and all experimental period.

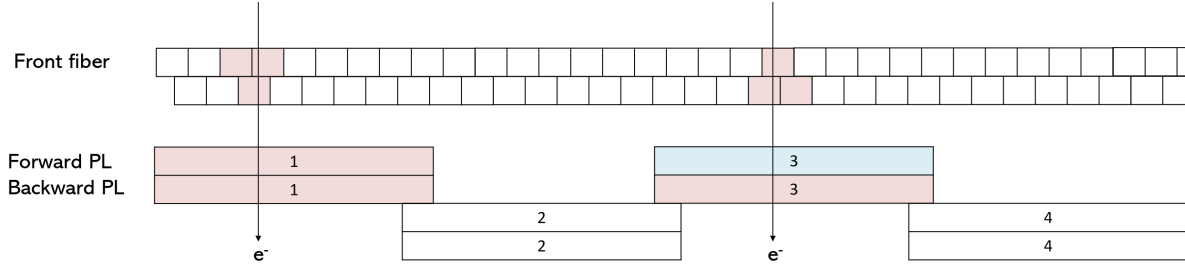


Figure F.1: A schematic drawing of the tagger with an example data for the intrinsic PL efficiency measurement.

#### Tagger track reconstruction efficiency

We evaluated the tagger track reconstruction efficiency using the  $\gamma + {}^{12}\text{C} \rightarrow 2\pi^0 + p + X$  reaction. Because the tagger reconstruction efficiency strongly depends on the tagger hit rate and the filling pattern, we need to evaluate the tagger track reconstruction efficiency using the carbon target data not the liquid hydrogen target data. For the evaluation of the tagger track reconstruction efficiency, we used two data samples; the loose cut sample and the tight cut sample. Both samples detected  $2\pi^0 + p$  with BGOegg. The loose cut sample did not use the RF signal because we require a tagger track when we select the RF signal. Because we need the RF signal for the particle identification, we did not carry out the particle identification of charged particles in the loose cut sample and thus there were contamination of pions to protons. In the tight sample, we selected the RF signal by using the BGOegg hit timing. In addition, very tight kinematical cut and kinematical fitting were applied. The tight cut sample is very clean but the statistics is 1/10 of the loose cut sample. Table.F.1 shows the tagger reconstruction efficiency measured using both samples. The measurements

of two data samples are consistent within the statistical error. In addition, there is no  $E_\gamma$  dependence. We used the average efficiency obtained from the tight sample,  $(89.9 \pm 0.8)\%$ .

Table F.1: The tagger reconstruction efficiency.

mode	loose sample	tight sample
$E_\gamma < 1.6$ GeV	$(90.0 \pm 0.5)\%$	$(90.4 \pm 1.5)\%$
$1.6$ GeV $< E_\gamma < 1.8$ GeV	$(90.8 \pm 0.4)\%$	$(90.9 \pm 1.8)\%$
$1.8$ GeV $< E_\gamma < 2.0$ GeV	$(90.1 \pm 0.5)\%$	$(87.9 \pm 2.8)\%$
$2.0$ GeV $< E_\gamma < 2.2$ GeV	$(91.6 \pm 0.7)\%$	$(91.6 \pm 2.0)\%$
$2.2$ GeV $< E_\gamma < 2.4$ GeV	$(91.6 \pm 1.0)\%$	$(88.9 \pm 1.6)\%$
all	$(90.6 \pm 0.2)\%$	$(89.9 \pm 0.8)\%$

## F.2.2 UpVeto over veto rate

We measured the rate that the UpVeto over veto events with accidental hits. For the evaluation, we used the tight  $2\pi^0 + p$  sample used for the tagger reconstruction efficiency measurement. The obtained over veto rate is  $(97.84 \pm 0.27)\%$ .

## F.2.3 DC track reconstruction efficiency

We evaluated the DC track reconstruction efficiency using the  $\gamma + p \rightarrow \omega + p$  reaction with the liquid hydrogen target. We used kinematical fitting and required that the proton angle to be in the DC acceptance. We obtained the DC track reconstruction efficiency to be  $(98.24 \pm 0.44)\%$ .

## F.2.4 RPC reconstruction efficiency

We evaluated the RPC reconstruction efficiency using the  $\gamma + p \rightarrow \eta + p$  reaction with the liquid hydrogen target. We used kinematical fitting and required a track of proton in the DC in the RPC acceptance. We obtained the RPC reconstruction efficiency to be  $(95.89 \pm 2.32)\%$ .

## F.3 Transmission rate

In Fig.F.2, we show the run dependence of the ratio of the number of  $\pi^0$  tagged with BGOegg and the number of photons counted with the tagger. We required that the number of tagger tracks is one and the ratio is shown in ten different colors for different photon energies. The electron filling pattern of the SPring-8 storage ring is shown with Alphabets. The ratio is low in E and D modes because of low detector efficiencies. (See section 6.1.6.) In the first A-mode, we observed drop of the ratio depending on the photon energy. This is considered to come from the low transmission rate of photon beam coming from bad tuning of the 5th

mirror angle for laser injection (see section 2.1.2). When the mirror angle is bad and the electron-laser collision point is downstream of the straight line, electrons and laser do not collide at  $180^\circ$  because electrons are bent at the downstream of the straight line. Then, the scattered photon angle is also change and some of photons do not pass the collimator in the beam line (see Fig.2.3). As in Eq.(2.1), the photon energy depends on the scattered angle of the photon beam. Therefore, there is  $E_\gamma$  dependence of the transmission rate in the first A-mode. The overall drop of the transmission rate in A-mode is corrected with the filling mode dependence correction factor described in section 6.1.6, which is independent with  $E_\gamma$ . We ignored the  $E_\gamma$  dependence of the transmission of the first A-mode because its fraction (0.2%) is negligibly small compared with the statistical uncertainty of the  $E_\gamma$  dependence of the filling mode correction factor (5%).

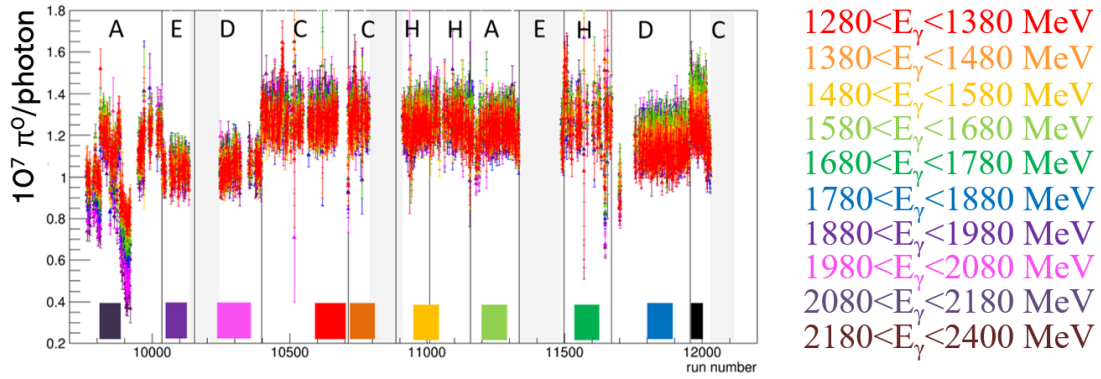


Figure F.2: The run dependence of the ratio of the number of  $\pi^0$  tagged with BGOegg and the number of photons counted with the tagger.

# Appendix G

## Theoretical estimation of the cross section

We evaluated the expected production cross section of the  $\eta'$ -nucleus bound state in a framework of a distorted wave impulse approximation (DWIA). In this Appendix, we describe how we calculated the expected cross section.

### G.1 Overview

As described in section 7.2, we calculated the excitation energy spectra within DWIA as

$$\left( \frac{d^2\sigma}{d\Omega_{p_f} dE_{\text{ex}}} \right)_{\text{theory}}^{\gamma+^{12}\text{C} \rightarrow p+\eta'+^{11}\text{B}} = \overline{\left( \frac{d\sigma}{d\Omega_{p_f}}(E_{\text{ex}}) \right)_{\text{lab}}^{\gamma+p \rightarrow p+\eta'}} \times R(E_{\text{ex}}). \quad (\text{G.1})$$

Here,  $E_{\text{ex}}$  is the excitation energy,  $\overline{\left( \frac{d\sigma}{d\Omega_{p_f}}(E_{\text{ex}}) \right)_{\text{lab}}^{\gamma+p \rightarrow p+\eta'}}$  the Fermi-averaged cross section of the elementary  $\gamma + p \rightarrow p + \eta'$  reaction [66], and  $R(E)$  the nuclear response function. The excitation energy spectra are calculated for the cases of  $V_0 = -20, -100$  MeV and  $E_\gamma = 1.5, 2.05, 2.5$  GeV. We evaluated expected cross section averaged over  $E_\gamma$  in the following procedure.

1. Calculate  $R(E_{\text{ex}})$ ,
2. Calculate  $\overline{\left( \frac{d\sigma}{d\Omega_{p_f}}(E_{\text{ex}}) \right)_{\text{lab}}^{\gamma+p \rightarrow p+\eta'}}$ ,
3. Integrate over  $E_{\text{ex}}$ ,
4. Average over  $E_\gamma$ .

We describe the details of each procedure in the following sections.

## G.2 Nuclear response function $R(E_{\text{ex}})$

The nuclear response function  $R(E_{\text{ex}})$  is calculated by Nagahiro with Green's function method as described in Ref.[44]. The Green's function  $G(E_{\text{ex}})$  of the  $\gamma + {}^{12}\text{C} \rightarrow p + \eta' \otimes {}^{11}\text{B}$  reaction is defined as

$$G(E_{\text{ex}}; \mathbf{r}, \mathbf{r}') = \langle p^{-1} | \phi_{\eta'}(\mathbf{r}) \frac{1}{E_{\text{ex}} - H_{\eta'} + i\epsilon} \phi_{\eta'}^\dagger(\mathbf{r}') | p^{-1} \rangle, \quad (\text{G.2})$$

where  $\phi_{\eta'}^\dagger$  is an  $\eta'$  creation operator and  $|p^{-1}\rangle$  is a proton hole state. The Hamiltonian  $H_{\eta'}$  contains the  $\eta'$ -nucleus potential  $U$  in Eq.(1.26). The response function  $R(E)$  is calculated as

$$R(E_{\text{ex}}) = -\frac{1}{\pi} \text{Im} \sum_f \int d\mathbf{r} d\mathbf{r}' \mathcal{T}_f^\dagger(\mathbf{r}) G(E_{\text{ex}}; \mathbf{r}, \mathbf{r}') \mathcal{T}_f(\mathbf{r}' \mathbf{s}), \quad (\text{G.3})$$

where the summation is inclusively taken over all possible final states. The amplitude  $\mathcal{T}_f$  describes the transition of the incident photon to a proton hole and the outgoing proton;

$$\mathcal{T}_f((r)) = \chi_f^*(\mathbf{r}) [Y_{l_{\eta'}}^*(\hat{r}) \otimes \psi_{j_p}(\mathbf{r})]_{JM} \chi_i(\mathbf{r}), \quad (\text{G.4})$$

where  $\psi_{j_p}$  is a proton hole wave function,  $\chi_i$  and  $\chi_f$  are distorted wave functions of initial and final particles, and  $Y_{l_{\eta'}}(\hat{r})$  is an  $\eta'$  angular function. The calculation is carried out up to  $l_{\eta'} = 6$ . The calculation results for  $E_\gamma = 2.5$  GeV and several  $\theta_p$  and  $V_0$  cases shown in Ref.[44] is shown in Fig.G.1. Note that in Fig.G.1, the elementary cross section in the laboratory frame without Fermi averaging,  $\left(\frac{d\sigma}{d\Omega_{p_f}}(E_{\text{ex}})\right)_{\text{lab}}^{\gamma+p \rightarrow p+\eta'} = 519$  nb/sr ( $1^\circ$ ), 504 nb/sr ( $6^\circ$ ) and 472 nb/sr ( $11^\circ$ ) is multiplied in the Y axis. We can see  $R(E_{\text{ex}})$  by multiplying  $1/\left(\frac{d\sigma}{d\Omega_{p_f}}(E_{\text{ex}})\right)_{\text{lab}}^{\gamma+p \rightarrow p+\eta'}$ .

$R(E_{\text{ex}})$  contains both  $\eta'$  escape and absorption processes. The decomposed calculation was done only for  $V_0 = 0, -100$  MeV,  $E_\gamma = 2.5$  GeV and the forward proton angle  $\theta_{p\text{Forward}} = 1^\circ$  case. If  $V_0$  is the same, the peak position of each  $\eta'$  and proton hole orbit is the same for different  $E_\gamma$  and different proton angle. Only peak heights change depending on the  $E_\gamma$  and proton angle. We assumed that the  $\eta'$  escape and absorption ratio is the same for the same orbit of different  $E_\gamma$  and different proton angle. Then, we obtained  $\eta'$  escape spectra and  $\eta'$  absorption spectra separately for  $E_\gamma = 1.5, 2.05$  GeV and  $\theta_{p\text{Forward}} = 6^\circ$  cases. We used the escape/absorption ratio of  $V_0 = 0$  MeV case to obtain  $V_0 = -20$  MeV spectra.

## G.3 Fermi averaging method

As described in section 7.2.4, we found that the Fermi averaging method is necessary to obtain  $E_\gamma$  dependence similar to the experimentally observed one. We calculate the Fermi averaged cross section by weighting the elementary cross section in the laboratory frame with the Fermi momentum distribution. The cross section in the laboratory frame is obtained by

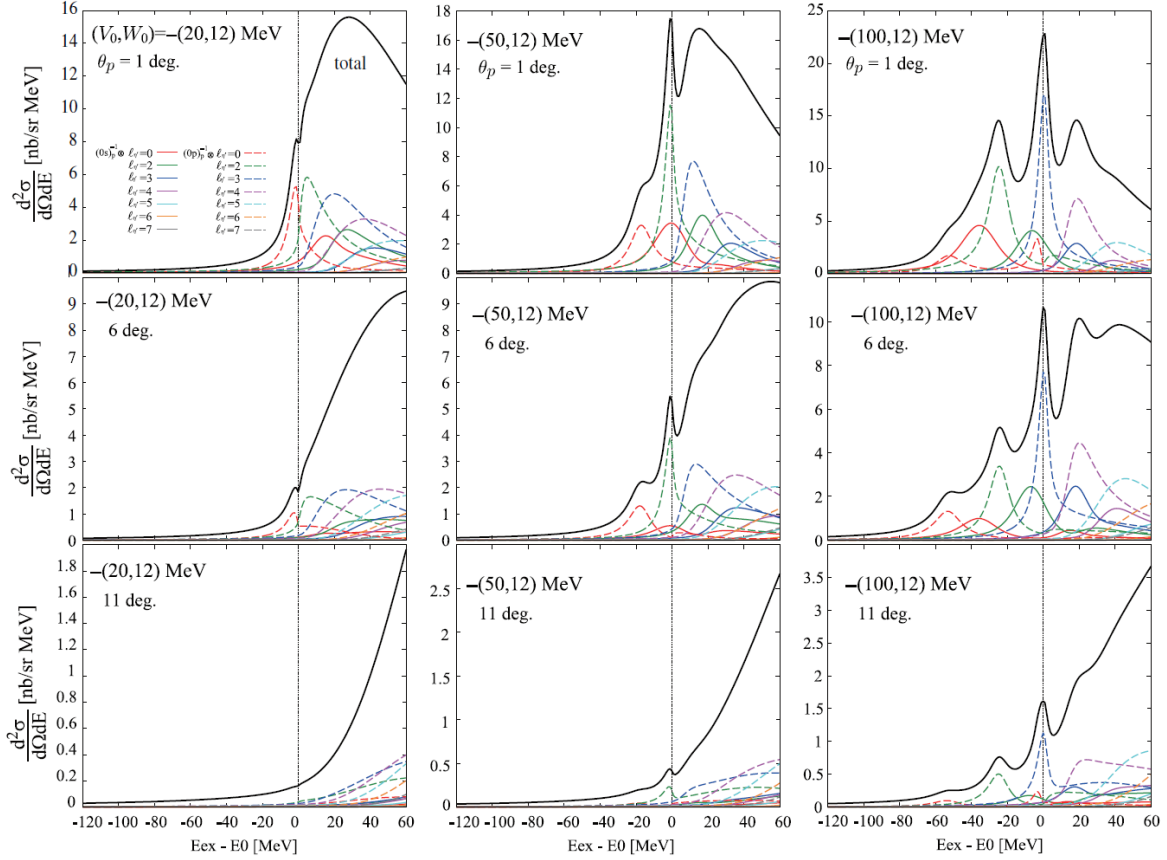


Figure G.1: The calculation result shown in [44].

transforming the cross section in the center-of-mass frame taking into account the target proton Fermi momentum. We describe details of the calculation of the Fermi averaged cross section.

### G.3.1 Formalism

In Fig.G.2, we illustrate  $\gamma + p \rightarrow \eta' + p$  reaction with Fermi motion. “pFermi” indicates the target proton which have Fermi motion and “pForward” indicates the scattered proton. The

Fermi averaged cross section is calculated as

$$\begin{aligned}
& \overline{\left( \frac{d\sigma}{d\Omega_{p_f}}(E_\gamma, \omega, \mathbf{q}) \right)_{lab}}^{\gamma p \rightarrow \eta' p} \\
&= \frac{\int_0^\pi \sin \theta_{pFermi} d\theta_{pFermi} \int_0^\infty dp_{pFermi} p_{pFermi}^2 \rho(p_{pFermi}) \left( \frac{d\sigma}{d\Omega_{p_f}}(E_\gamma, \mathbf{p}_{pFermi}, \omega, \mathbf{q}) \right)_{lab}^{\gamma p \rightarrow \eta' p}}{\int_0^\pi \sin \theta_{pFermi} d\theta_{pFermi} \int_0^\infty dp_{pFermi} p_{pFermi}^2 \rho(p_{pFermi})} \Bigg|_{\mathbf{p}_{pFermi} = \mathbf{p}_{pFermi}^*} \quad (G.5)
\end{aligned}$$

where

$$\omega = E_\gamma - E_{pForward}, \quad (G.6)$$

$$\mathbf{q} = \mathbf{p}_\gamma - \mathbf{p}_{pForward}. \quad (G.7)$$

$\rho(p_{pFermi})$  is the nucleon momentum distribution, and  $\mathbf{p}_{pFermi}^*$  is a solution of the following equation:

$$\begin{aligned}
\omega &= \sqrt{(\mathbf{p}_{pFermi}^* + \mathbf{q})^2 + m_{\eta'}^2} - \sqrt{(\mathbf{p}_{pFermi}^* + m_p^2)} \\
&\simeq m_{\eta'} - m_p + \frac{\mathbf{q}^2}{2m_p} + \frac{\mathbf{p}_{pFermi}^* \cdot \mathbf{q}}{m_{\eta'}} - \frac{m_{\eta'} - m_p}{m_{\eta'}} \frac{\mathbf{p}_{pFermi}^{*2}}{2m_p}. \quad (G.8)
\end{aligned}$$

$\left( \frac{d\sigma}{d\Omega_{p_f}} \right)_{lab}^{\gamma p \rightarrow \eta' p}$  is the elementary cross section of the  $\gamma + p \rightarrow \eta' + p$  reaction in the laboratory system.

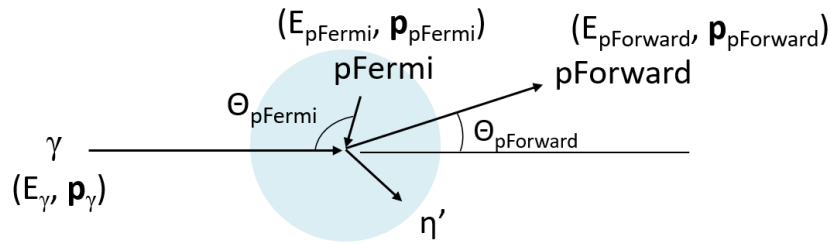


Figure G.2: The illustration of the  $\gamma + p \rightarrow \eta' + p$  reaction with Fermi motion.

### G.3.2 Nucleon momentum distribution

For nucleon momentum distribution  $\rho(p_{pFermi})$ , we used the harmonic oscillator model used in [64]. For the case of carbon nuclei,

$$\rho(p_{pFermi}) = 2 \times \frac{4b^3}{\sqrt{\pi}} \exp(-b^2 k^2) + 4 \times \frac{2}{3} \times \frac{4b^3}{\sqrt{\pi}} b^2 k^2 \exp(-b^2 k^2), \quad (\text{G.9})$$

$$b = 1.93, \quad (\text{G.10})$$

$$p_{pFermi} = \hbar k. \quad (\text{G.11})$$

### G.3.3 Elementary cross section in the CM system

#### Interest kinematical region

We calculated  $\left(\frac{d\sigma}{d\Omega_{p_f}}\right)_{lab}^{\gamma p \rightarrow \eta' p}$  from the cross section in the center-of-mass system,  $\left(\frac{d\sigma}{d\Omega_{p_f}}\right)_{CM}^{\gamma p \rightarrow \eta' p}$ , measured by the LEPS and the CBELSA/TAPS collaboration. When we include the Fermi motion, the center-of-mass energy,  $\sqrt{s}$ , and the center-of-mass angle,  $\theta_{\eta'}^{CM}$ , regions involved in the reaction are wider than the case of a proton target at rest with the same beam energy and detector acceptance. Thereby, we examined the  $\sqrt{s}$  and  $\theta_{\eta'}^{CM}$  regions involved in our measurement when Fermi motion is taken into account. Figure G.3 shows two dimensional plots of  $\sqrt{s}$  and  $\theta_{\eta'}^{CM}$  vs  $E_{ex} - E_0$  satisfying Eq.(G.8) for the case of highest beam energy  $E_\gamma = 2.4$  GeV, and the proton angle at  $6^\circ$ . The distributions are weighted with the Fermi momentum distribution in Eq.(G.9). We can see that the events in  $\sqrt{s} < 2.5$  GeV and  $\theta_{\eta'}^{CM} > 160^\circ$  ( $\cos\theta_{\eta'}^{CM} < -0.94$ ) are dominant when we weight with Fermi momentum.

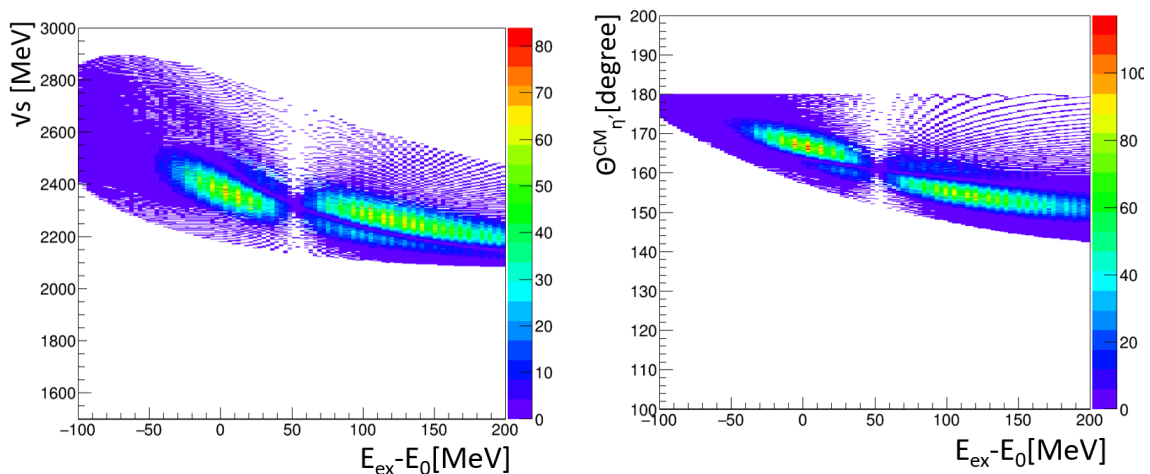


Figure G.3: The  $\sqrt{s}$  and  $\theta_{\eta'}^{CM}$  vs missing mass distributions satisfying Eq.(G.8) with the Fermi weight for the case of  $E_\gamma = 2.4$  GeV and the proton angle at  $6^\circ$ .

## Elementary cross section

Figure G.4 shows the differential cross section of the  $\gamma + p \rightarrow \eta' + p$  reaction in CM system in  $-1.0 < \cos \theta_{\eta'}^{CM} < -0.9$  reported by the LEPS and the CBELSA/TAPS collaborations [67, 68]. Those measurements cover the kinematical region discussed in the previous section. The LEPS data shows bump at around  $\sqrt{s} = 2.35$  GeV and decrease with increasing  $\sqrt{s}$  although the error is large. There is no bump structure in the CBELSA/TAPS data. There is a strong correlation between  $\sqrt{s}$  and the excitation energy as can be seen in Fig.G.3. The bump structure of the cross section depending on  $\sqrt{s}$  leads a bump structure in the excitation energy spectrum. We have the value of  $R(E)$  only for discrete  $E_\gamma$ , 1.5, 2.05, 2.5 GeV, and obtain the expected yield from these three points. It is not appropriate to reflect a bump structure in the small  $\sqrt{s}$  region to estimate yield in wide  $E_\gamma$  region. Thus, we assumed that the differential cross section is constant at 40 nb/sr in the CM system when we calculate  $\left(\frac{d\sigma}{d\Omega_{p_f}}\right)_{lab}^{\gamma p \rightarrow \eta' p}$  (shown by the green line in Fig.G.4).

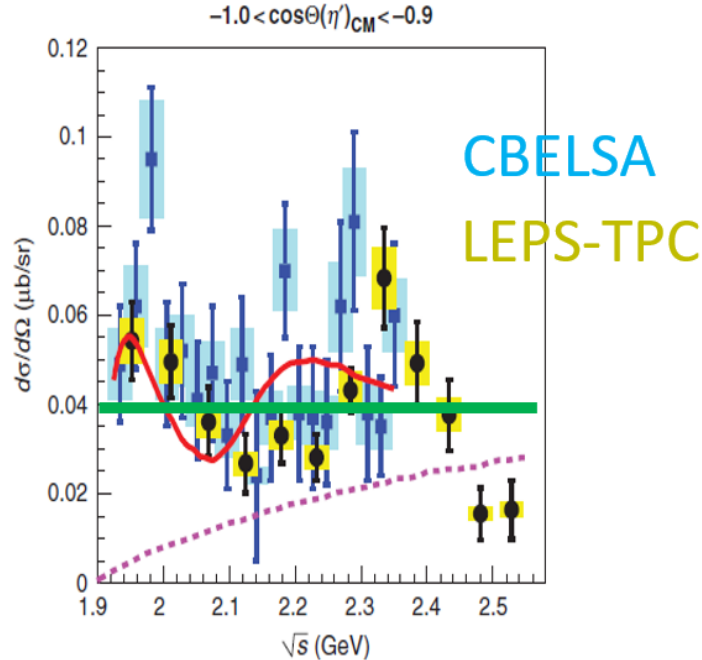


Figure G.4: The differential cross section of  $\gamma + p \rightarrow \eta' + p$  in  $-1.0 < \cos \theta_{\eta'}^{CM} < -0.9$  measured by the LEPS and CBELSA group. The figure is from [67].

### G.3.4 Elementary cross section in the laboratory system

Even the cross section in the CM system is constant in the kinematical region interested in, the cross section in the laboratory system is not. The transformation factor of the cross section from the CM system to the laboratory system depends on  $E_\gamma$ ,  $\mathbf{p}_{pFermi}$  and  $\mathbf{p}_{pForward}$ .

The transformation is done using the generalized CM to laboratory transformation factor of the cross section as

$$\left(\frac{d\sigma}{d\Omega_{p_f}}\right)_{lab}^{\gamma p \rightarrow \eta' p} = \frac{p_{pForward}}{p_{pForward}^{CM}} \frac{\sqrt{s}}{E_\gamma + E_{pFermi} - (E_\gamma \cos \theta_{pForward} + p_{pFermi} \cos \theta_{pFermi}) \frac{E_{pForward}}{p_{pForward}}} \left(\frac{d\sigma}{d\Omega_{p_f}}\right)_{CM}^{\gamma p \rightarrow \eta' p}$$

$$\sqrt{s} = \sqrt{(E_\gamma + E_{pFermi})^2 - ((p_{pFermi} \sin \theta_{pFermi})^2 + (E_\gamma + p_{pFermi} \cos \theta_{pFermi})^2)}. \quad (\text{G.12})$$

### G.3.5 Numerical result

Figure G.5 shows the numerical results of the Fermi-averaged cross section,  $\overline{\left(\frac{d\sigma}{d\Omega_{p_f}}(E_\gamma, \omega, \mathbf{q})\right)_{lab}^{\gamma p \rightarrow \eta' p}}$ , as a function of the excitation energy.

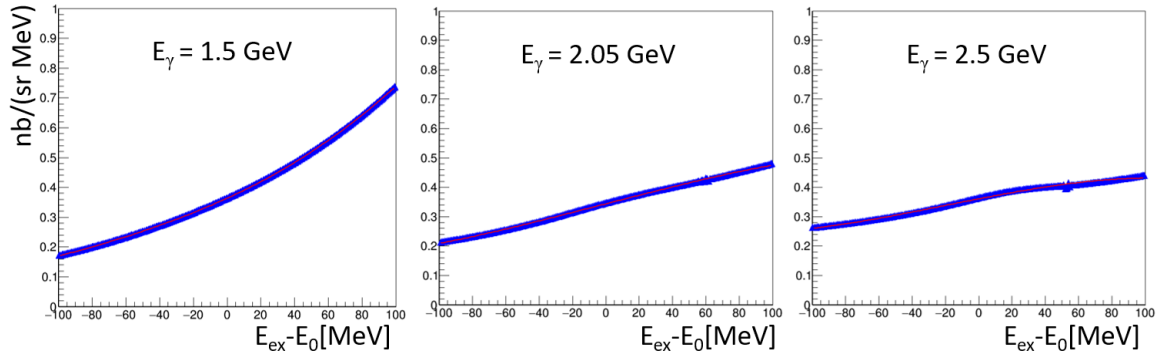


Figure G.5: The excitation energy dependence of the Fermi averaged cross section for different  $E_\gamma$  cases. The forward proton angle is  $6^\circ$ .

## G.4 Inclusion of the detector resolution

The green lines of Fig.G.6 and Fig.G.7 shows the calculation results of  $\left(\frac{d^2\sigma}{d\Omega_{p_f} dE_{ex}}\right)^{\eta' abs}$  and  $\left(\frac{d^2\sigma}{d\Omega_{p_f} dE_{ex}}\right)^{\eta' esc}$ , respectively. We substituted  $R(E_{ex})$  and  $\left(\frac{d\sigma}{d\Omega_{p_f}}\right)_{lab}^{\gamma p \rightarrow \eta' p}$  in Eq.(G.12) to Eq.(G.1). To compare the theoretical expected cross section with the experimental cross section, we included detector resolution to the theoretical excitation energy spectra. The details of the inclusion of the detector resolution is described in the following sections.

### G.4.1 The detector resolutions

The following detector resolutions were implemented to the theoretical excitation energy spectra:

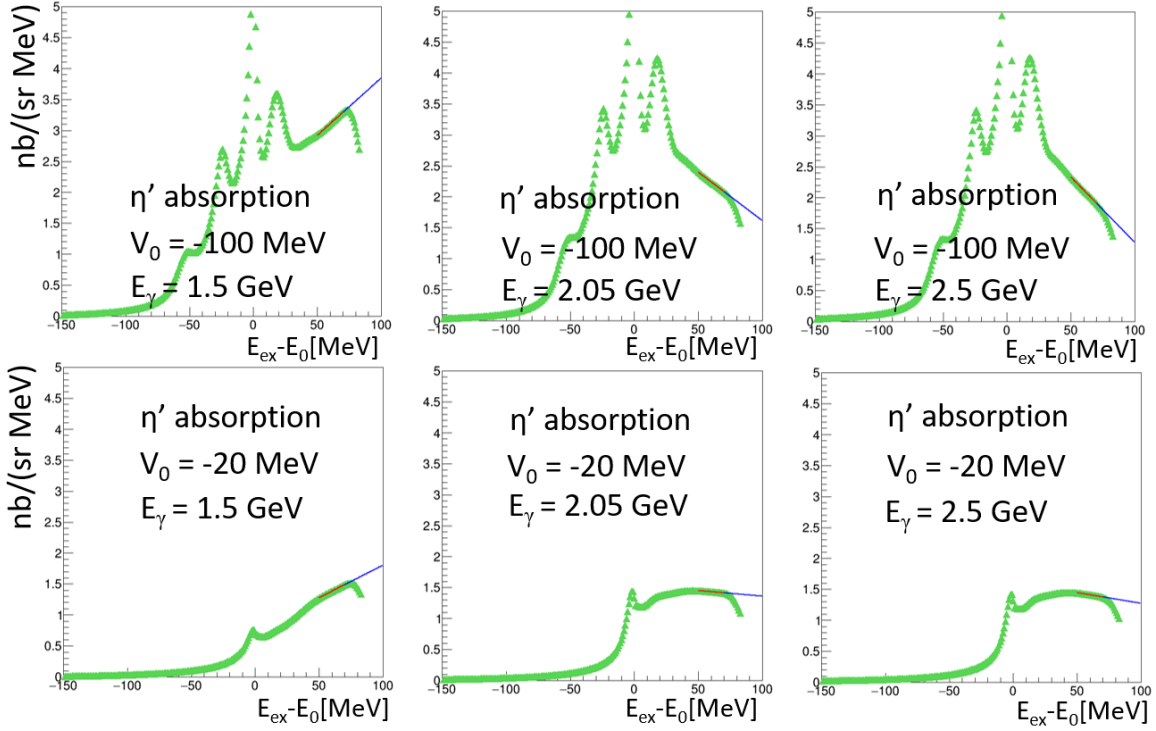


Figure G.6: Calculation results of  $\left(\frac{d^2\sigma}{d\Omega_{p_f}dE_{ex}}\right)^{\eta'abs}$ . The lines are the fitting results in  $50 \text{ MeV} < E_{ex} - E_0 < 70 \text{ MeV}$  by linear functions.

- $E_\gamma$  resolution = 12.0 MeV,
- TOF time resolution for  $E_{pForward}$  measurement = 80 ps,
- the ambiguity of the energy deposit in the target = 1.8–3.6 MeV depending on the forward proton momentum.

The excitation energy resolution as a function of  $E_\gamma$  is shown in Fig.G.8.

For the  $\eta'$  escape measurement, we use  $E_{ex} - E_0^{\eta'} = MM(^{12}\text{C}(\gamma, p)) - M_{11\text{B}} - M_{\gamma\gamma}$  instead of  $MM(^{12}\text{C}(\gamma, p)) - M_{11\text{B}} - M_{\eta'}$ . We used

- $M_{\gamma\gamma}$  resolution = 17.8 MeV,

which is the measured value.

#### G.4.2 The treatment above $E_{ex} - E_0 = 50 \text{ MeV}$

After including the detector resolution, events in  $E_{ex} - E_0 > 50 \text{ MeV}$  contaminate to  $E_{ex} - E_0 < 50 \text{ MeV}$ . Thus, we need the expected cross section above  $E_{ex} - E_0 = 50 \text{ MeV}$ . For the

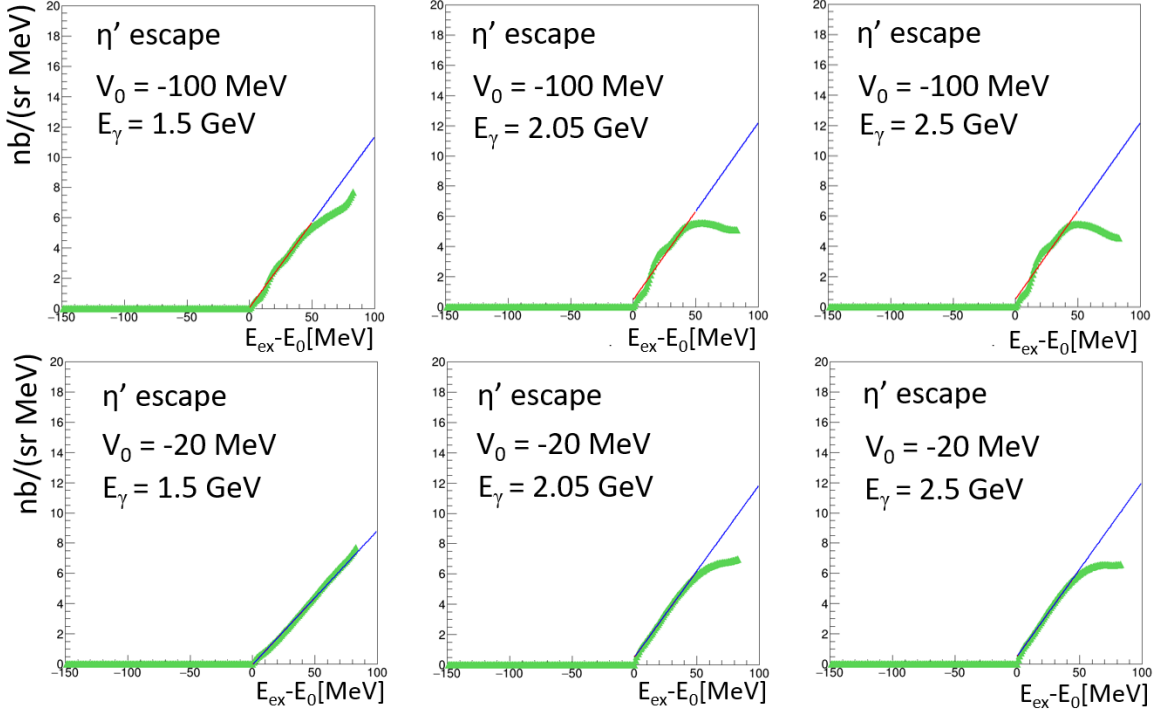


Figure G.7: Calculation results of  $\left(\frac{d^2\sigma}{d\Omega_{p_f} dE_{ex}}\right)^{\eta'esc}$ . The lines are the fitting results in  $0 \text{ MeV} < E_{ex} - E_0 < 50 \text{ MeV}$ . by linear functions.

escape spectra, we fit  $0 \text{ MeV} < E_{ex} - E_0 < 50 \text{ MeV}$  by linear functions and extend the value up to  $E_{ex} - E_0 = 100 \text{ MeV}$ . For the absorption spectra, we fit  $50 \text{ MeV} < E_{ex} - E_0 < 70 \text{ MeV}$  by linear functions and extend the value up to  $E_{ex} - E_0 = 100 \text{ MeV}$ . The fitting results are shown by the red and blue lines in Fig.G.6 and G.7.

### G.4.3 Excitation energy spectra

Figure G.9 and Fig.G.10 show the excitation spectra after including the detector resolutions for the  $\eta'$  absorption mode and the  $\eta'$  escape mode, respectively. For the case of  $\eta'$  escape mode, we have more events below  $0 \text{ MeV}$  with larger  $E_\gamma$  because of the bad excitation resolution at large  $E_\gamma$ . We integrated the cross sections after inclusion of the detector resolution, over  $-50 \text{ MeV} < E_{ex} - E_0 < 50 \text{ MeV}$  and  $0 \text{ MeV} < E_{ex} - E_0 < 50 \text{ MeV}$ , for the  $\eta'$  absorption and escape process, respectively.

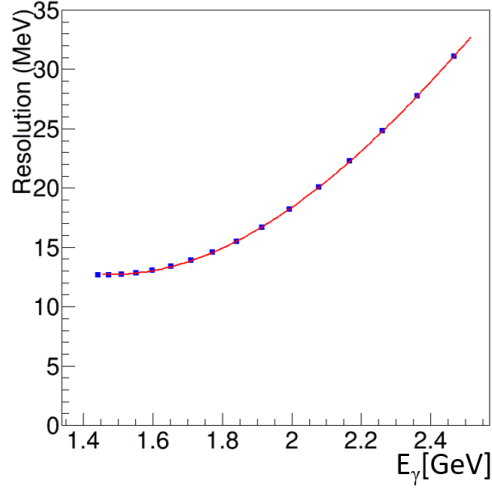


Figure G.8: The excitation energy resolution as a function of  $E_\gamma$  used for the  $\eta'$  absorption mode.

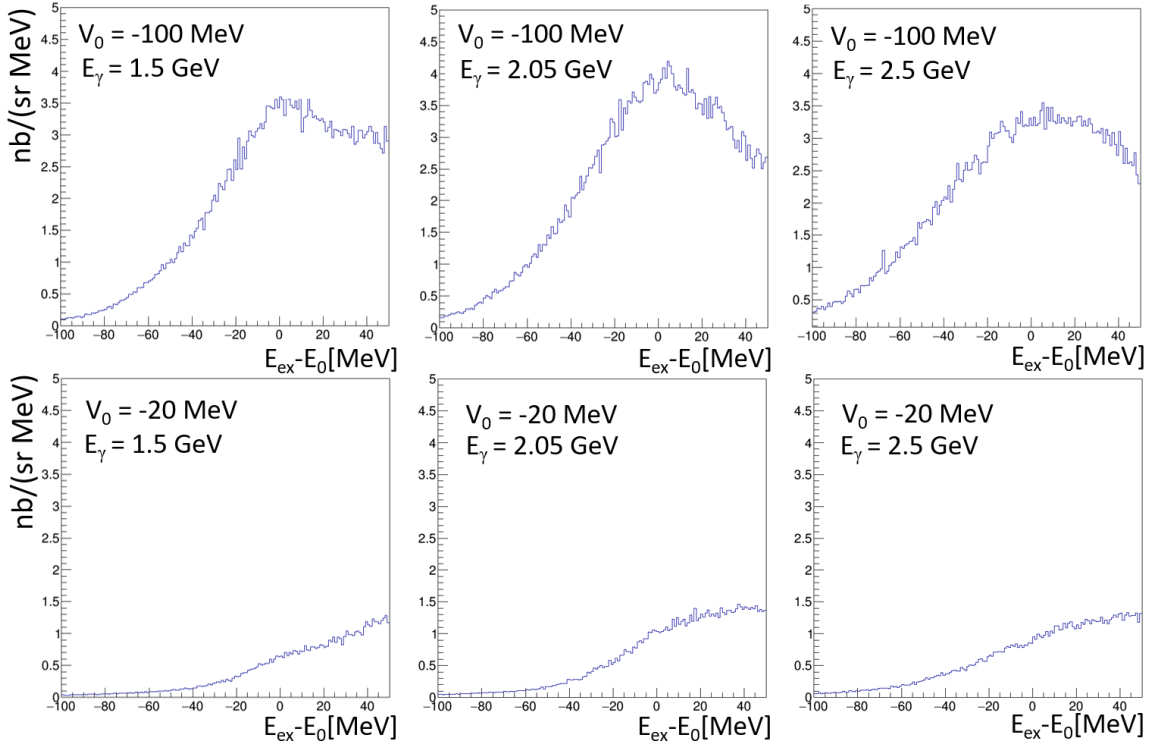


Figure G.9:  $\left(\frac{d^2\sigma}{d\Omega_{p_f} dE_{ex}}\right)^{\eta'abs}$  including the detector resolutions.

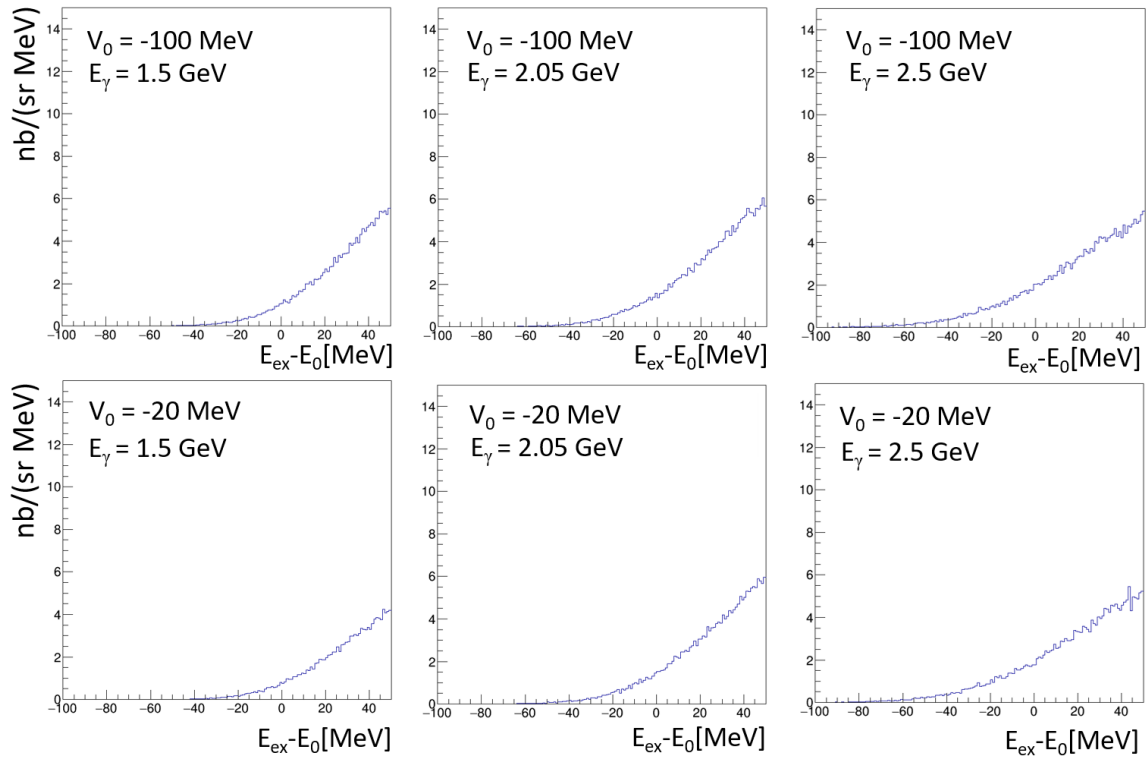


Figure G.10:  $\left(\frac{d^2\sigma}{d\Omega_{p_f} dE_{\text{ex}}}\right) \eta'^{\text{esc}}$  including the detector resolutions.

## G.5 $E_\gamma$ dependence

The  $E_\gamma$  dependence of the integrated cross section and the experimental cross section of the  $\eta'$  escape process are shown in section 7.2.4. They have consistent  $E_\gamma$  dependence. The  $E_\gamma$  dependence of the integrated cross section of the  $\eta'$  absorption process is shown in Fig.G.11. We fit the 3 points with a quadratic function. The fitted function is used for evaluating the average cross section over  $E_\gamma$ .

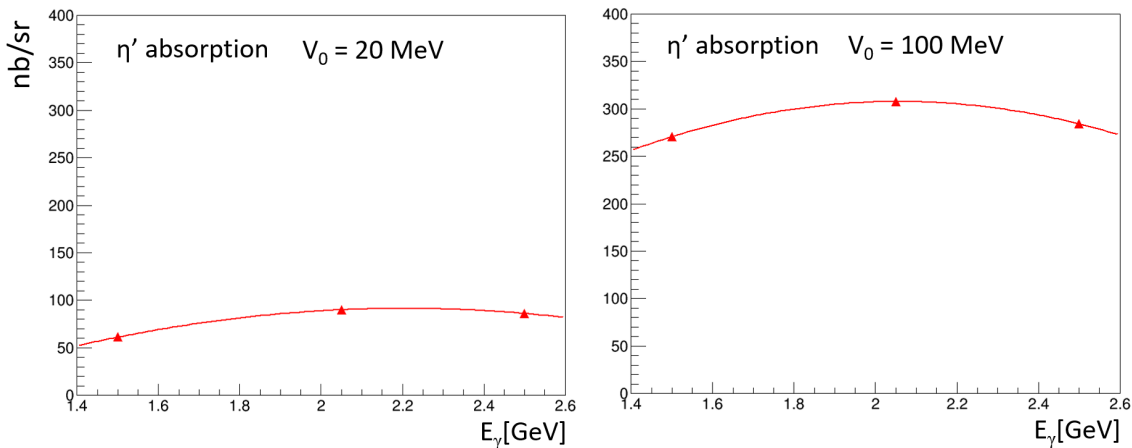


Figure G.11: The  $E_\gamma$  dependence of the integrated cross section of the  $\eta'$  absorption process of the DWIA calculation.

## G.6 Expected cross section

We evaluated the expected cross section by averaging the fitted function in Fig.7.4 and Fig.G.11 over  $E_\gamma = 1.28 - 2.4$  GeV, with the weight of the  $E_\gamma$  distribution of the backward Compton scattering shown in Fig.2.5. The obtained cross section is summarized in Table.G.1.

Table G.1: The expected cross section with the DWIA calculation.

mode	$V_0 = -20$ MeV	$V_0 = -100$ MeV
$\eta'$ escape ( $0 \text{ MeV} < E_{\text{ex}} - E_0 < 50 \text{ MeV}$ )	159.1 nb/sr	173.8 nb/sr
$\eta'$ absorption ( $-50 \text{ MeV} < E_{\text{ex}} - E_0 < 50 \text{ MeV}$ )	79.7 nb/sr	292.2 nb/sr

## G.7 $p_f$ polar angle dependence

Figure G.12 shows the excitation energy distributions of the  $\eta'$  escape events of the experimental data at  $\theta_{pForward} < 3^\circ$  and  $\theta_{pForward} > 5^\circ$  in  $E_\gamma > 1.8$  GeV. The number of events is increasing together with excitation energy in  $0 \text{ MeV} < E_{ex} - E_0 < 100 \text{ MeV}$ . Figure G.13 shows the excitation energy distributions of the  $\eta'$  escape events of the DWIA calculation at  $\theta_{pForward} = 1^\circ$  and  $6^\circ$  at  $E_\gamma = 2.5$  GeV. In the case of  $\theta_{pForward} = 1^\circ$ , the cross section starts

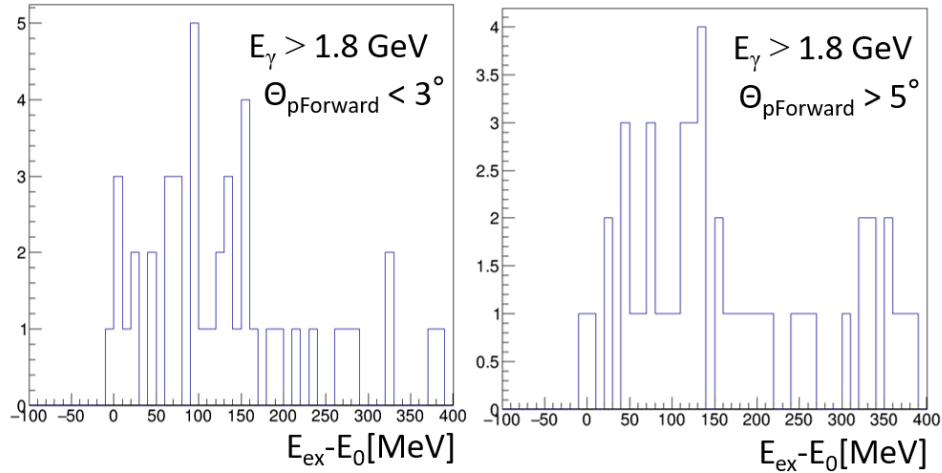


Figure G.12: The excitation energy distributions of the  $\eta'$  escape events of the experimental data in  $\theta_{pForward} < 3^\circ$  and  $\theta_{pForward} > 5^\circ$  in  $E_\gamma > 1.8$  GeV.

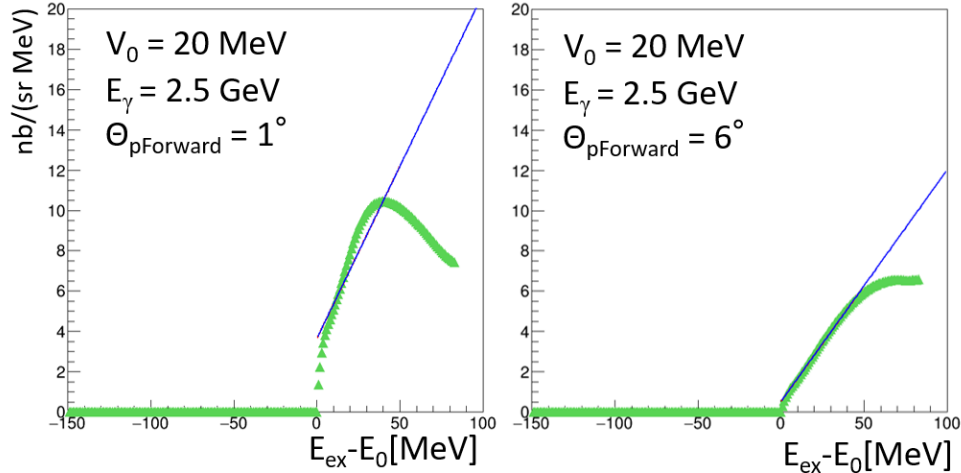


Figure G.13: The expected excitation energy distributions at  $\theta_{pForward} = 1^\circ$  and  $6^\circ$  at  $E_\gamma = 2.5$  GeV based on the DWIA calculation.

to decrease at around  $E_{\text{ex}} - E_0 = 30$  MeV. It is not consistent with the measurement. Thus, we used only the calculation of  $\theta_{p\text{Forward}} = 6^\circ$  for the yield estimation.

# Appendix H

## The measurement of the $\eta'$ escape process

In this Appendix, we describe the details of the cross section measurement of the  $\eta'$  escape process. We also show the comparison of the cross section measured by the CBELSA/TAPS Collaboration.

### H.1 Definition of the excitation energy

The definition of the excitation energy used for the  $(\eta + p_s)$  measurement is as follows:

$$E_{\text{ex}} - E_0^{\eta'} = MM(^{12}\text{C}(\gamma, p_f)) - M_{11\text{B}} - M_{\eta'}, \quad (\text{H.1})$$

As described in chapter 5, instead of Eq.(H.1), we used the following definition of the excitation energy for the  $\eta'$  escape measurement:

$$E_{\text{ex}} - E_0^{\gamma\gamma} = MM(^{12}\text{C}(\gamma, p_f)) - M_{11\text{B}} - M_{\gamma\gamma}. \quad (\text{H.2})$$

Here, we replaced the  $\eta'$  mass,  $M_{\eta'}$ , with the invariant mass of two  $\gamma$ s,  $M_{\gamma\gamma}$ . We used the definition in Eq.(H.2) so that we can use the side band events of the invariant mass peak for evaluating background events. It is clearly shown in Fig.H.1. In Fig.H.1(a) and (b), we show two dimensional plots of the invariant mass of two  $\gamma$ s and the excitation energy with the definition in Eq.(H.1) and (H.2), respectively. When we use the definition in Eq.(H.1), there is a correlation between the invariant mass and the excitation energy. Therefore, we cannot use the side band events of the invariant mass peak when we evaluate the background events depending on the excitation energy. On the other hand, when we used the definition in Eq.(H.2), we can use the invariant mass sideband events for evaluating background contamination. The energy resolution of the definition in Eq.(H.2) is worse than in Eq.(H.1) with the invariant mass resolution,  $\sigma_{M_{\gamma\gamma}} = 17.8$  MeV. This resolution is taken into account for the theoretical cross section described in Appendix G.

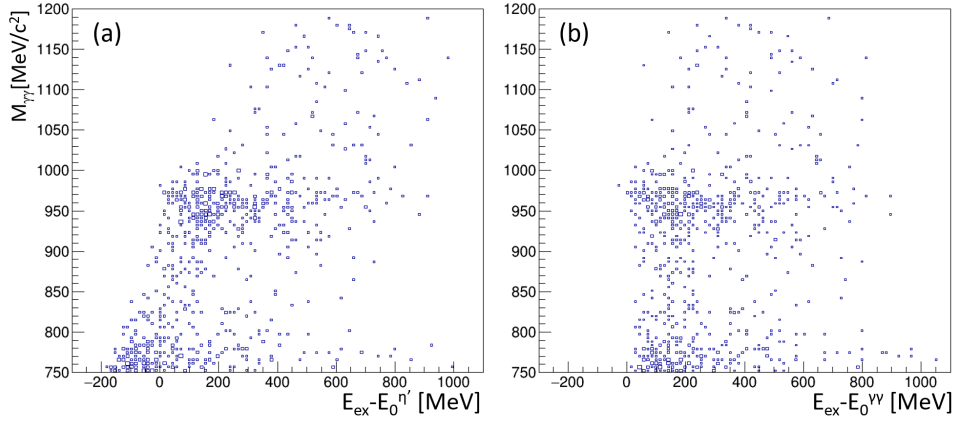


Figure H.1: The two dimensional plots of the invariant mass of two  $\gamma$ s and the excitation energy with the definition in Eq.(H.1)(a) and (H.2)(b).

## H.2 $E_\gamma$ dependence of the cross section

The  $E_\gamma$  dependence of the cross section in different excitation energy region is shown in Figure H.2. The data points are common to Fig.7.1 and just the axis is different.

## H.3 Comparison with the measurement by CBELSA/TAPS

The CBELSA/TAPS Collaboration measured the cross section of the  $\gamma + {}^{12}\text{C} \rightarrow p + \eta' + X$  reaction in  $2^\circ < \theta_p < 11^\circ$  [34]. They did not measure the proton momentum and thus their cross section is an integrated cross section over all the excitation energy region. Although the proton polar angle region is slightly different from our measurement, we compared our cross section with the one measured by the CBELSA/TAPS Collaboration. In Fig.H.3, we show the  $E_\gamma$  dependence of the cross section for all excitation energy region of our measurement in  $\cos\theta_{\eta'}^{lab} > 0$ , and the measurement by CBELSA/TAPS Collaboration [34]. In order to compare with the measurement by CBELSA/TAPS, we used the same requirements as ones of CBELSA/TAPS. We required the  $\eta'$  kinetic energy  $< 500$  MeV,  $\cos\theta_{\eta'}^{CM} < 0$ , and multiplied a shadowing factor = 15%. The shadowing factor represents the absorption of the incoming photon beam by nucleons. It is introduced just to compare their cross section with theoretical calculations which are lines in Fig.H.3.

There are several questionable points in the CBELSA/TAPS results. Firstly, the definition of  $\cos\theta_{\eta'}^{CM}$  is ambiguous. In Ref.[34], it is described that they calculated  $\cos\theta_{\eta'}^{CM}$  from  $E_\gamma$  and the  $\eta'$  energy, assuming that the target proton is at rest. In this case,  $\cos\theta_{\eta'}^{CM}$  can not be defined below the production threshold at  $E_\gamma = 1.447$  GeV. However, there is an data point below  $E_\gamma = 1.447$  GeV in Fig.H.3. Secondary, the selection range of  $\cos\theta_{\eta'}^{CM}$

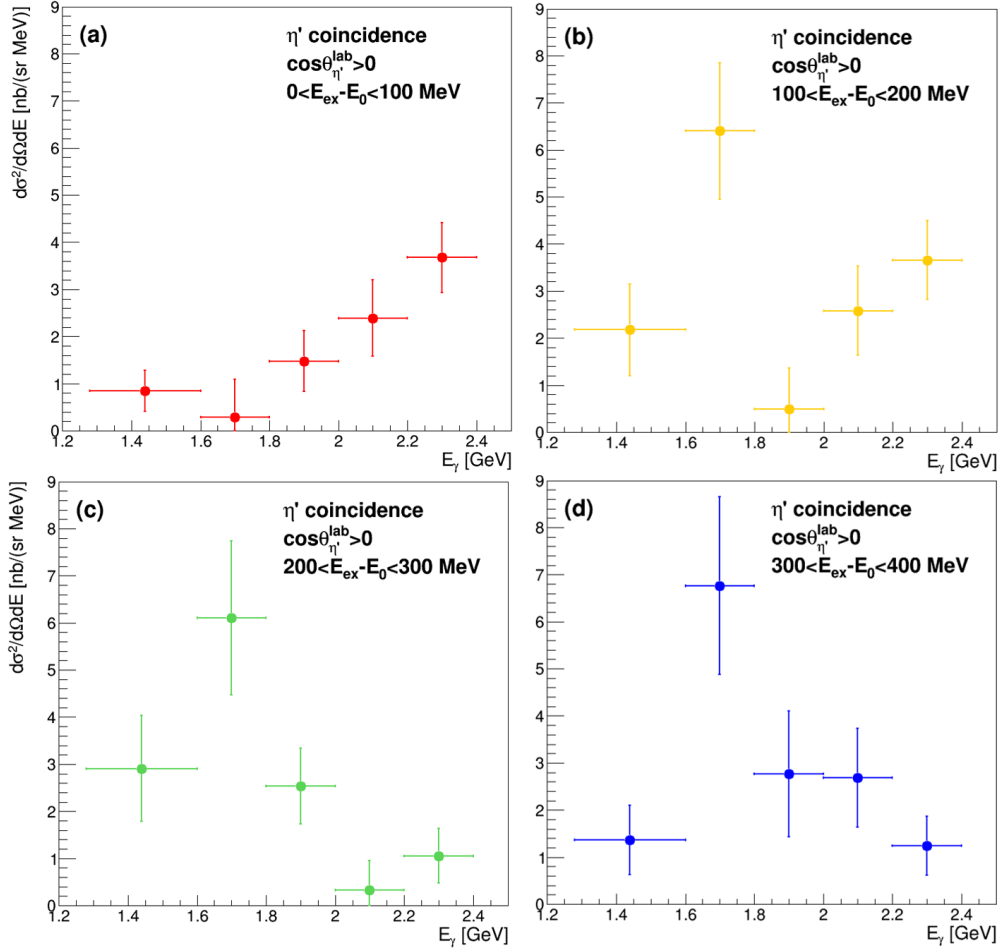


Figure H.2: The  $E_\gamma$  dependence of the  $\eta'$  coincidence cross section in different excitation energy region.

is ambiguous. Because of the Fermi motion, we have events in  $\cos\theta_{\eta'}^{CM} < -1$  if we use the definition above. The cut condition of CBELSA/TAPS is explained as “backward” in the text and “ $-1 < \cos\theta_{\eta'}^{CM} < 0$ ” in figures [34]. It is not clear whether they included events in  $\cos\theta_{\eta'}^{CM} < -1$  when they calculated the cross section. In our data points, events in  $\cos\theta_{\eta'}^{CM} < -1$  are included. Thirdly, there is no data point at  $\eta'$  kinetic energy  $> 500$  MeV in the measurement by the CBELSA/TAPS collaboration. In the BGOegg data, we have several events with  $\eta'$  kinetic energy  $> 500$  MeV. The difference might come from the difference of the definition of  $\cos\theta_{\eta'}^{CM}$ . As can be seen in Fig.H.3, the cross sections measured by the CBELSA/TAPS and our cross sections were consistent within the statistical error, except for the lowest energy bin where the definition of  $\cos\theta_{\eta'}^{CM}$  is ambiguous. The systematic error of the cross section of the CBELSA/TAPS measurement is 17%.

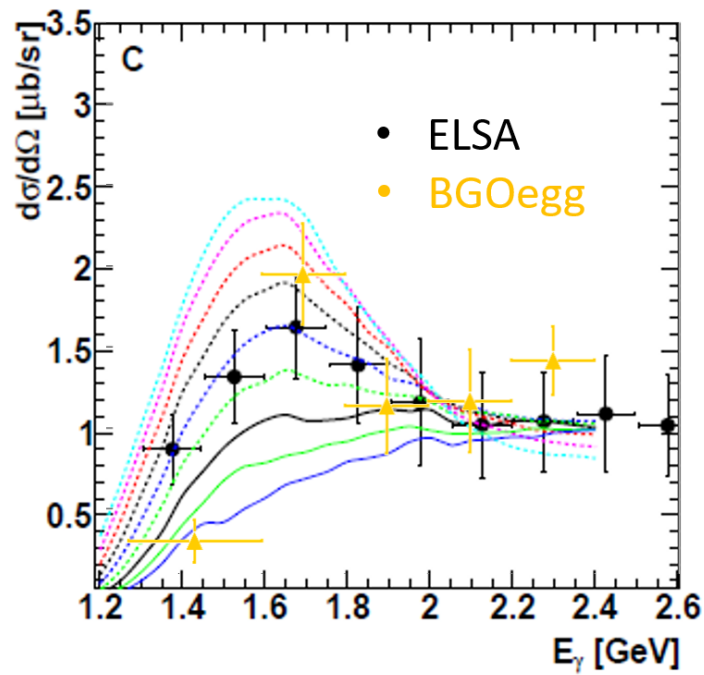


Figure H.3: The  $E_\gamma$  dependence of the cross section of our measurement (yellow) and the measurement by CBELSA/TAPS collaboration (black), integrated over all the excitation energy region. The figure is from [34].

# Bibliography

- [1] M. Tanabashi and others (Particle Data Group), Phys. Rev. D **98**, 030001 (2018).
- [2] Y. Nambu, Phys. Rev. Lett. **4**, 380 (1960).
- [3] D. Jido, T. Hatsuda, and T. Kunihiro, Phys. Lett. B **670**, 109 (2008).
- [4] D. Jido, H. Nagahiro, and S. Hirenzaki, Phys. Rev. C (R) **85**, 032201 (2012).
- [5] D. Jido, S. Sakai, H. Nagahiro, S. Hirenzaki, and N. Ikeno, Nucl. Phys. A **914**, 354 (2013).
- [6] H. Nagahiro and S. Hirenzaki, Phys. Rev. Lett **94**, 232503 (2005).
- [7] H. Nagahiro, M. Takizawa, and S. Hirenzaki, Phys. Rev. C **74**, 045203 (2006).
- [8] H. Nagahiro, S. Hirenzaki, E. Oset, and A. Ramos, Phys. Lett. B **709**, 87 (2012).
- [9] S. Friedrich *et al.*, Eur. Phys. J. A **52**, 297 (2016).
- [10] Y. Nambu and G. Jona-Lasinio, Phys. Rev. **122**, 345 (1961).
- [11] Y. Nambu and G. Jona-Lasinio, Phys. Rev. **124**, 246 (1961).
- [12] M. Kobayashi and T. Maskawa, Prog. Theor. Phys. **44**, 1422 (1970).
- [13] M. Kobayashi, H. Kondo, and T. Maskawa, Prog. Theor. Phys. **45**, 1955 (1971).
- [14] P. Costa, M. C. Ruivo, C. A. de Sousa, and Y. L. Kalinovsky, Phys. Rev. D **71**, 116002 (2005).
- [15] P. Rehberg, P. Klevansky, and J. Hufner, Phys. Rev. C **53**, 410 (1996).
- [16] S. Afanasiev *et al.*, Nucl. Phys. B (Proc. Suppl.) **219-220**, 255 (2011).
- [17] A. Budzanowski *et al.*, Phys. Rev. C **79**, 012201(R) (2009).
- [18] S. Sakai and D. Jido, Phys. Rev. C **88**, 064906 (2013).
- [19] S. D. Bass and A. W. Thomas, Phys. Lett. B **634**, 368 (2006).

- [20] A. Kawamoto, Master thesis, Nara Women Univerisity (2018).
- [21] Y. K. Tanaka *et al.*, Phys. Rev. C **97**, 015202 (2018).
- [22] Y. K. Tanaka *et al.*, Phys. Rev. Lett. **117**, 202501 (2016).
- [23] O. Morimatsu and K. Yazaki, Nucl. Phys. A **435**, 727 (1985).
- [24] K. Itahashi *et al.*, Prog. Theor. Phys. **128**, 601 (2012).
- [25] T. Harada and T. Hirabayashi, Nucl. Phys. A **759**, 143 (2005).
- [26] T. Harada, R. Honda, and Y. Hirabayashi, Phys. Rev. C **97**, 024601 (2018).
- [27] T. Motoba, H. Bando, R. Wünsch, and J. Žofka, Phys. Rev. C **38**, 1988 (1988).
- [28] J. Hüfner, S. Lee, and H. A. Weidenmüller, Nucl. Phys. A **234**, 429 (1974).
- [29] A. Boussy, Nucl. Phys. A **290**, 324 (1977).
- [30] T. Nishi *et al.*, Phys. Rev. Lett. **120**, 152505 (2018).
- [31] E. Y. Paryev, J. Phys. G: Nucl. Part. Phys **40**, 025201 (2013).
- [32] M. Nanova *et al.*, Phys. Lett. B **727**, 417 (2013).
- [33] M. Nanova *et al.*, Phys. Rev. C **94**, 025205 (2016).
- [34] M. Nanova *et al.*, Eur. Phys. J. A **54**, 182 (2018).
- [35] B. Krusche *et al.*, Eur. Phys. J. A **22**, 277 (2004).
- [36] T. Mertens *et al.*, Eur. Phys. J. A **38**, 195 (2008).
- [37] M. Kotulla *et al.*, Phys. Rev. Lett. **100**, 192302 (2008).
- [38] T. Ishikawa *et al.*, Phys. Lett. B **608**, 215 (2005).
- [39] T. Kunihiro, Phys. Lett. B **219**, 363 (1989).
- [40] T. Csörgő and R. Vértési and J. Sziklai, Phys. Rev. Lett. **105**, 182301 (2010).
- [41] S. Adler *et al.*, Phys. Rev. Lett. **93**, 152302 (2004).
- [42] J. Adams, Phys. Rev. C **71**, 044906 (2005).
- [43] E. Oset and A. Ramos, Phys. Lett. B **704**, 334 (2011).
- [44] H. Nagahiro, JPS Conf. Proc. **13**, 010010 (2017).
- [45] “SPRING-8 web site,” <http://www.spring8.or.jp/>.

- [46] K. Kawase *et al.*, Nucl. Instrum. Methods. Phys. Res. Sect. A **592**, 154 (2008).
- [47] N. Kumagai, SPring-8 Annual report **3, No.5**, 1 (1998).
- [48] A. D'Angelo *et al.*, Nucl. Instrum. Methods. Phys. Res. Sect. A **455**, 1 (2000).
- [49] “Kuraray, Plastic Scintillating Fibers, Plastic Imaging Fibers,” <http://kuraraypsf.jp/>.
- [50] T. Ishikawa *et al.*, Nucl. Instrum. Methods. Phys. Res. Sect. A **837**, 109 (2016).
- [51] N. Tomida *et al.*, JINST **9**, C10008 (2014).
- [52] N. Tomida *et al.*, JINST **11**, C11037 (2016).
- [53] Y. Kawashima and Y. Ohashi, SPring-8/SACLA information **13, No.1**, 28 (1998).
- [54] I. Nagasawa *et al.*, ELPH annual report 2011-2013 , 194 (2013).
- [55] T. Ishikawa *et al.*, ELPH annual report 2011-2013 , 175 (2013).
- [56] “PSTAR,” <https://physics.nist.gov/PhysRefData/Star/Text/PSTAR.html>.
- [57] K. Niita, S. Chiba, T. Maruyama, T. Maruyama, H. Takada, T. Fukahori, Y. Nakahara, and A. Iwamoto, Phys. Rev. C **52**, 2620 (1995).
- [58] T. Kinoshita *et al.*, Phys. Lett. B **639**, 429 (2006).
- [59] M. Mertens *et al.*, Eur. Phys. J. A **38**, 195 (2008).
- [60] K. Garrow *et al.*, Phys. Rev. C **66**, 044613 (2002).
- [61] P. Lava, M. C. Martínez, J. Ryckebusch, J. A. Caballero, and J. Udías, Phys. Lett. B **595**, 177 (2004).
- [62] O. Hen *et al.*, Phys. Lett. B **722**, 63 (2013).
- [63] S. Agostinelli *et al.*, Nucl. Instr. Meth. A **506**, 250 (2003).
- [64] T. Ishikawa, PhD thesis, Kyoto University (2005).
- [65] R. D. Cousins and V. L. Highland, Nucl. Instr. and Meth. **320**, 331 (1992).
- [66] T. Harada and Y. Hirabayashi, Nucl. Phys. A **744**, 323 (2004).
- [67] Y. Morino *et al.*, Prog. Theor. Exp. Phys. , 013D01 (2015).
- [68] V. Crede *et al.*, Phys. Rev. C **80**, 055202 (2009).
- [69] H. Nagahiro, S. Hirenzaki, E. Oset, and A. Ramos, Phys. Lett. B **709**, 87 (2012).

[70] “SPring-8 web site,” [http://www.spring8.or.jp/en/users/operation\\_status/schedule/bunch\\_mode](http://www.spring8.or.jp/en/users/operation_status/schedule/bunch_mode).

[71] R. Brun and F. Rademakers, Nucl. Inst. Meth. in Phys. Res. A **389**, 81 (1997).